FLORIDA STATE UNIVERSITY

COLLEGE OF ARTS AND SCIENCES

PHOTOPRODUCTION OF THE $\eta\pi^0$ SYSTEM OFF A PROTON TARGET AT $E_\gamma = 8.5$ GEV

By

LAWRENCE NG

A Dissertation submitted to the
Department of Physics
in partial fulfillment of the
requirements for the degree of
Doctor of Philosophy

2023

Lawrence Ng defended this dissertation on April 7, 2023.
The members of the supervisory committee were:

Sean Dobbs

Professor Directing Dissertation

Ettore Aldrovandi

University Representative

Volker Crede

Committee Member

Simon Capstick

Committee Member

Ted Kolberg

Committee Member

The Graduate School has verified and approved the above-named committee members, and certifies that the dissertation has been approved in accordance with university requirements.

To my Family, Friends, and Honey

ACKNOWLEDGMENTS

I started out my graduate school application with the phrase, "here be dragons", which represent uncharted lands. Similarly, the journey through the Ph.D. navigates through the unknown. In this case, the strange land is described by quantum chromodynamics with all its complexities.

This journey would not have been possible without the guidance of my advisor, Sean Dobbs. You have provided me with guidance and mentorship that has allowed me to become the researcher that I am today. You have always enabled me to perform at my best and provided me with the resources I needed to execute these ideas. Thank you for all your support. To Malte Albrecht and Colin Gleason, thank you for all the countless exchanges we had.

To my family. There is really nothing more I can say that you do not already know. Thank you. To my new family member and wife, Jing Lu, you have become an additional sunshine in my life. Of course, Honey (our dog) deserves credit here also as she kept me physically and mentally healthy.

Of course, thank you to all my fellow students here at FSU. You have made this a fantastic adventure. Through our interactions, you have made me grow as a scientist and as a person. We had a lot of great times, didn't we!?

TABLE OF CONTENTS

LIST OF TABLES

LIST OF FIGURES

xxvii

ABSTRACT

The reaction, $\gamma p \to \eta \pi^0 p$, is studied in this dissertation at $E_\gamma = 8.5$ GeV at GlueX. The $\eta\pi$ decay channel is one of the "golden channels" to search for the π_1 spin-exotic meson. The yield of the π_1 is expected to be only a few percent of the $a_2(1320)$ yield, which dominates the $M(\eta\pi^0)$ spectrum observed at GlueX. Exotic signatures from the π_1 can also be mimicked by the double Reggeon exchange (DREx) process. Therefore, searching for the π_1 in the $\eta\pi^0$ channel necessitates a detailed understanding of nearby $a_2(1320)$ meson and the DREx process. A measurement will be presented in this dissertation to characterize each of these features.

An analysis will be presented of the first measurement of the differential photoproduction cross section, $d\sigma/dt$, of the $a_2(1320)$ meson at photon beam energies of $8.2 - 8.8$ GeV and in the four-momentum transfer range of 0.1 to $1.0\,\text{GeV}^2$ is performed. A full partial wave analysis is carried out in the $\eta\pi^0$ invariant mass region around $1.3\,\text{GeV}/c^2$ using amplitudes that depend on the polarization of the incoming photon beam, which allows us to separate the contributions of natural and unnatural parity exchange to the differential cross section. The partial wave analysis suggests that the $a_2(1320)$ differential cross section contains a dip around $-t \approx 0.5$ GeV^2 with total cross-section equal to $68.3 \pm 4.6 \pm 7.1$ nb over the measured interval. These values correspond to the central estimate, the statistical uncertainty, and the systematic uncertainty.

Additionally, an analysis will be presented of this reaction beyond the resonance region at $M(\eta\pi) > 1.6$ GeV where the DREx process contributes significantly. As input for the development of models to describe polarized photoproduction in this mass range at GlueX energies, we measure the Σ beam asymmetry for individual η and π mesons for the above reaction, Σ_η and Σ_π, as functions of several kinematic variables including baryon sensitive ones. This allows a separation of contributions of the DREx process from baryon production. The measurements performed at large $M(\eta\pi)$ can be used to constrain the contributions of the DREx process in the resonance region where the π_1 is expected to populate. A comparison is made to measurements of the complementary reaction, $\gamma p \to \eta \pi^- \Delta^{++}$.

CHAPTER 1

INTRODUCTION

1.1   Quantum Chromodynamics

So far, physics has come to characterize four fundamental forces of nature: electromagnetism, the weak and strong forces, and gravity. All, except gravity, have been unified under a quantum field theory (QFT) known as the *Standard Model*. In this theory, particles are excitations in a quantum field that can propagate through spacetime and interact with each other by the exchange of force carrier particles, known as the gauge bosons: g (gluon), γ (photon), Z, and W. The range of a force is given by the Compton wavelength of the gauge boson, $\lambda = 1/m$ [1]. Gluons and photons are themselves massless and should therefore have an infinite range, whereas the massive W and Z bosons, with a mass of 80 and 91 GeV respectively, are short-range carriers. The elementary particles in the standard model can be seen in Figure 1.1.

Quantum Electrodynamics details the interaction of charged objects through exchanges of the chargeless spin-1 gauge boson known as the photon. This is the quantum theory of the electromagnetic force. The photon is massless, giving this force an essentially infinite range. The strength of this interaction is characterized by the fine structure constant, $\alpha \approx 1/137$. The small value for this interaction makes it amenable for perturbation theory to perform calculations. That is, higher order (more complicated) processes contribute less and less as extra factors of α are introduced.

Quantum Chromodynamics characterizes the interaction of color-charged objects through exchanges of the color-charged spin-1 gauge boson known as the gluon. Color charge comes in three main types: red, blue, and green. Intuitively, mixing those three colors produces something that is white or, in this case, *colorless*. This is as far as the additive color analogy takes us, as there are an associated set of anti-colors that are also available. Mixing a color with an anti-color is also colorless. The description of a quark involves a single color charge, whereas gluons are described by a color and an anti-color. In total, quarks can take on 1 of 3 color states, whereas gluons can take on 1 of 8 color states. Only *colorless* states have been observed experimentally. There is no analytic proof based on QCD that color has to be confined in a colorless state, though *quark confinement* is an experimental fact and is well-accepted in the physics community.

1

Standard Model of Elementary Particles
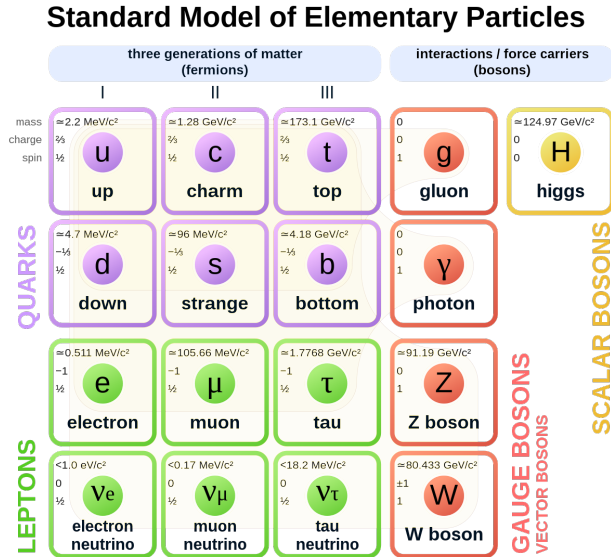
Figure 1.1: Particles in the standard model separated into several classes: leptons, quarks, gauge bosons, and a scalar boson. Taken from https://en.wikipedia.org/wiki/Standard_Model.

The fact that the mediator of the strong force itself is color charged creates some interesting phenomena, such as color confinement and asymptotic freedom. The strong coupling constant, α_s, sets the strength of the strong interaction just like α for the electromagnetic force. α_s can vary depending on the energy scale. Figure 1.2 shows calculations of α_s as a function of the energy scale. At high energies or small distances, the quarks inside a hadron behave as free particles; this feature is known as asymptotic freedom [2]. Here, it is possible to apply perturbation theory to make precision calculations. Conversely, the coupling grows stronger at larger distances / lower energies and confines color charges to be within a system. Perturbation theory is less useful at these scales, as higher order terms in the expansion are needed to achieve similar precision and may not even converge.

This effect can be modeled with a combination of a coulomb-like potential with a string-like term that exhibits a constant tension, k

$$V(r) = -\frac{4\alpha_s}{3r} + kr \tag{1.1}$$

This is known as the *Cornell potential* [4]. When two color-charged particles move further apart the energy density grows until it is enough to pair produce a new quark-antiquark pair from the vacuum. The confinement of color-charged particles inside hadrons can be seen as a consequence of this, but
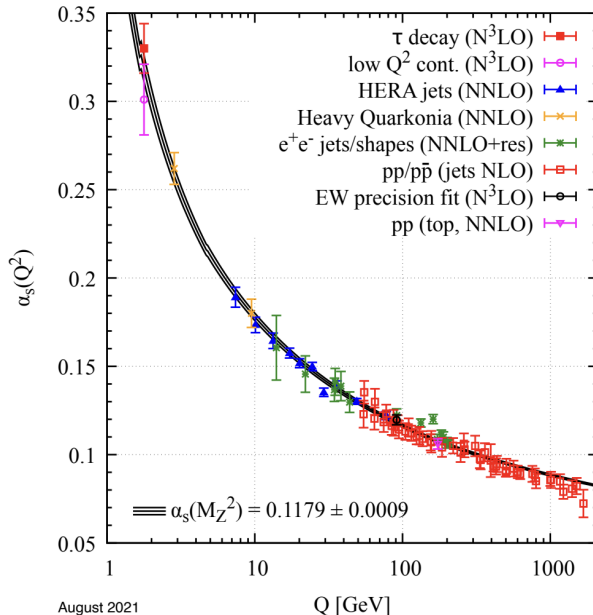
Figure 1.2: Measurements [3] of α_s at various energy scales extracted from QCD perturbation theory. The included order of expansion is denoted by the number of N's.

the exact mechanism of how it arises from QCD is not well understood. Hadrons are color-singlet states of QCD, where rotations in color space do not change the state. Colorless states can be formed from 3 valence quarks, where each quark takes on a different color, as in a baryon. Another possibility is to pair a quark and an anti-quark with a given color and anti-color, as in a meson. Mesons and baryons are simple cases of colorless systems. One can imagine other colorless states like the tetraquark (consisting of a bound diquark and anti-diquark) and pentaquarks (consisting of four quarks and an anti-quark). Molecular versions of tetraquark and pentaquark states can also exist. These consist of a meson-meson or a meson-baryon system, respectively, bound together by long-range inter-nuclear forces.

Gluonically excited states can also exist, such as hybrids (consisting of a quark and an anti-quark neutralized in color by an excited gluonic field), and glueballs (consisting entirely of excited gluonic fields). A picture of hybrid mesons, that is consistent with lattice QCD, has an excited flux tube connecting the quark-anti-quark pair. In this scheme, a normal meson would then have the flux tube in the ground state. Section 1.2 expands on this description.

These features of QCD, in principle, should be encoded in the QCD *Lagrangian* given by

3

$$\mathcal{L}_{QCD} = \bar{\psi}_i (i\gamma^\mu (D_\mu)_{ij} - m\delta_{ij})\psi_j - \frac{1}{4}G^a_{\mu\nu}G^{\mu\nu}_a \qquad (1.2)$$

where ψ_i is the quark field and $G^a_{\mu\nu}$ is the gauge invariant gluon field strength tensor given by

$$G^a_{\mu\nu} = \partial_\mu A^a_\nu - \partial_\nu A^a_\mu + g f^{abc} A^b_\mu A^c_\nu \qquad (1.3)$$

where A^a_μ are the gluon fields. It is a SU(3) non-abelian gauge theory. The non-abelian nature of the Lagrangian is what gives the gluon a color charge. Getting this seemingly innocuous equation to characterize confinement and asymptotic freedom has been a tremendous undertaking. One way to understand QCD is through hadron spectroscopy, which aims to map the masses and decays of hadrons. This should in turn illuminate the nature of QCD, much like how mapping the energy levels of a hydrogen atom lead to a better understanding of quantum electrodynamics. Section 1.2 introduces the constituent quark model (CQM) that was first introduced to explain the source of the myriad particles that were being experimentally observed at particle accelerators. Section 1.3 introduces *Regge theory*, which is another phenomenological model, that was developed alongside CQM. Section 1.4 introduces an ab initio method, known as lattice QCD, that makes use of modern computational resources to obtain quantitative measures of the non-perturbative regime of QCD. The measurements performed in this dissertation form the basis to search for a particular hybrid meson, the π_1, by informing the development of reaction models needed for the search. Previous experimental results in regard to the π_1 will be discussed in Section 1.5. Section 1.6 introduces photoproduction and how the GlueX experiment fits in the overall thrust to understand QCD. The π_1 is expected to be produced at GlueX within the $\eta\pi^0$ final state, which this dissertation explores.

1.2   Constituent Quark Model

Scattering experiments began revealing the inner structure of the atom in the early 20th century. These systems were composed of electrons electromagnetically bound to a positive nucleus, which was itself a collection of protons and neutrons bound together by the strong force. Particle accelerators and cosmic ray experiments later showed the existence of an entire zoo of strongly interacting half-integer spin and integer spin particles known as baryons and mesons respectively and are known as hadrons collectively.

In searching for some underlying substructure to describe the complexity of this zoo, Gell-Mann and Zweig suggested that these hadrons are composed of more fundamental particles known as

quarks or and aces. This theory, postulated the existence of the up, down, and strange quarks which carry different electrical charge, isospin, and strangeness. Strangeness is conserved in interactions involving the strong force. *Isospin symmetry* turned out to be an approximate symmetry of QCD due to the similarity in mass between the up and down quarks. This equality can be extended to incorporate strange quarks to obtain a *flavor symmetry*, which is a weaker approximate symmetry of QCD. This description is known as Gell-Mann's *eightfold way.*

Together, these quarks unified much of the then known hadron zoo under the same phenomenology. The idea gained credence when a predicted baryon, the Ω^-, was discovered in 1964 [5] at Brookhaven with the expected properties consistent with this quark picture of the hadron. Evidence for these point-like fundamental particles (quarks) were found when the Stanford Linear Accelerator (SLAC) showed through electron scattering experiments that the proton was composed of point-like constituents, later called partons by Feynman. In the 1970s, experiments were revealing the existence of heavier quarks which required extra quantum numbers (charm, bottomness) to describe.

In general, quark models describe the properties of hadrons as arising from constituent valence quarks. This dissertation will focus on light meson physics where only u, d, and s quarks are involved. Mesons are generally sorted into groups containing the same J^{PC} quantum numbers, where J is the total angular momentum, P is the parity quantum number, and C is the charge conjugation quantum number. These quantum numbers are conserved in strong interactions. The total spin, S, and relative orbital angular momentum between the quark and anti-quark, L, combine to form the total angular momentum

$$J = L \oplus S \tag{1.4}$$

The parity operation flips the spatial coordinates such that $P[\psi(\vec{r})] = \psi(-\vec{r}) = \eta_p \psi(\vec{r})$. η_p can only be ± 1 as two applications of parity must return the same state. The parity operation affects the wave function by reflecting the spherical harmonics, $P[Y_L^M] \rightarrow (-1)^L Y_L^M$. η_p is then equal to $(-1)^L$. The parity quantum number of a quark and an anti-quark are opposite, therefore the composite meson-system has parity

$$P = (-1)^{L+1} \tag{1.5}$$

The charge conjugation quantum number swaps all particles with their antiparticles. The total wave function is a function of position and spin. Swapping particles/antiparticles has the effect of a spatial flip and therefore contributes a factor of $(-1)^{L+1}$, the same as the parity operation. The

Charge conjugation operation also flips the spin wave function, picking up a factor of $(-1)^{S+1}$. The charge conjugation quantum number is then

$$C = (-1)^{L+S} \tag{1.6}$$

Applying the charge conjugation operation on charged particles results in a different state, therefore only neutral particles can be eigenstates of C. Charged particles can be eigenstates of the G-parity operator which applies the C operator followed by a rotation in isospin, $(-1)^I$, bringing the particle back to the original state. G-parity quantum number takes the form

$$G = C(-1)^I = (-1)^{L+S+I} \tag{1.7}$$

Isospin, I, is a vector quantity that counts the difference between the number of up and down quarks. Hadrons with the same J^{PC} quantum numbers can be distinguished experimentally by their total isospin. Up and anti-down quarks have $I=1/2$ and $I_3 = +1/2$ whereas anti-up and down quarks have $I_3 = -1/2$. That is,

$$I_3 = \frac{1}{2}(n_u - n_d + n_{\bar{d}} - n_{\bar{u}}) \tag{1.8}$$

It turns out that not all combinations of the J^{PC} quantum numbers are allowed. It is convenient to split the allowed J^{PC} into two series based on naturality, as some measurements are sensitive to the difference. Naturality is defined as $\eta = P(-1)^J$. From here it is possible to tabulate the possible meson J^{PC} quantum numbers separated by naturality as shown in Table 1.1. Some of the natural parity states are the 0^{++} scalar mesons (such as the f_0 and a_0 mesons) and the 1^{--} vector mesons (such as ρ and ω mesons). The 0^{-+} psuedoscalar mesons (such as the π and η) and the 1^{+-} axial-vector (such as the h meson) are some unnatural parity states. From the table, it is clear that some combinations of J^{PC} are missing, i.e. 1^{-+}.

	Allowed J^{PC} quantum numbers
Natural Parity States	$0^{++}, 1^{--}, 2^{++}, ...$
Unnatural Parity States	$0^{-+}, 1^{+-}, 1^{++}, 2^{--}2^{-+}, ...$

Table 1.1: Allowed J^{PC} quantum numbers in the Quark model

Flavor symmetry is described by the symmetry group $SU(3)_{\text{flavor}}$. Combining a $SU(3)_{\text{flavor}}$ quark triplet with the anti-quark triplet results in an octet and a singlet: $3 \otimes \bar{3} = 8 \oplus 1$. Together
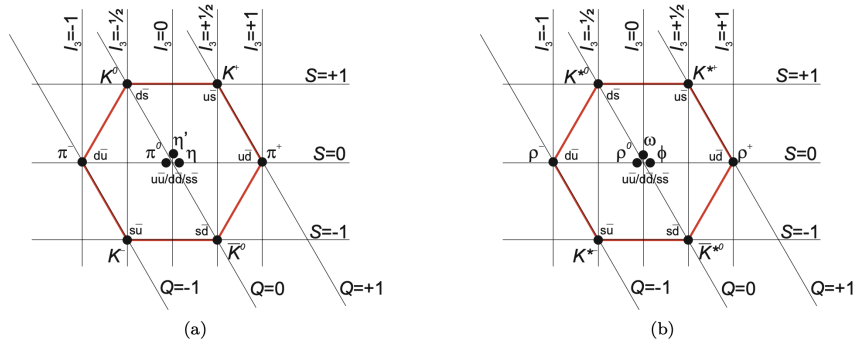
Figure 1.3: Figure as it appears in [1]. (a) is the psuedoscalar nonet and (b) is the vector meson nonet.

they form a nonet. The pseudoscalars and vector mesons belong to two distinct nonets as shown in Fig. 1.3. Every meson J^{PC} has its own nonet.

This simple formula of describing the spectrum of hadrons using constituent valence quarks has been quite successful, but nowhere does the quark model use *confinement* nor use gluons. One can imagine states that are completely composed of gluons or meson systems where gluons directly contribute to the wavefunction as a *valence gluon*. These states are known as *glueballs* and *hybrids*. As time passed, more states than can be supported by the quark model and mesonic states that do not carry $q\bar{q}$ quantum numbers have been identified. These revelations show that in order to understand the meson spectrum, the gluon must be considered.

The bag model [6] was the first model that predicted the existence of mesons with exotic quantum numbers. In this model, quarks and gluons are confined (by boundary conditions) inside a bag. Hybrid mesons arise from the inclusion of a transverse-electric(TE) or a transverse-magnetic(TM) gluon with 1^{+-} and 1^{-+} quantum numbers to a $q\bar{q}$ system with total spin equal to 0 or 1. The inclusion of a TE gluon creates 4 almost degenerate hybrid meson nonets with quantum numbers: 1^{--}, 0^{-+}, 1^{-+} and 2^{-+}. Early predictions put the mass for the 1^{-+} nonet between 1.0 and 1.4 GeV. Including a TM gluon gives four heavier nonets with quantum numbers: $= 1^{++}$, 0^{+-}, 1^{+-}, and 2^{+-}.

Extending the quark model to include contributions from gluonic excitations, via a flux tube, show the existence of states which directly engage with gluons. Yoichiro Nambu introduced the idea of flux tube formation as a way of explaining the phenomenological observations of a linear dependence between a hadrons' squared mass to their spin [7]. This is known as a *Regge trajectory* and will be the topic of Section 1.3. Later, lattice Quantum Chromodynamics confirms this

7
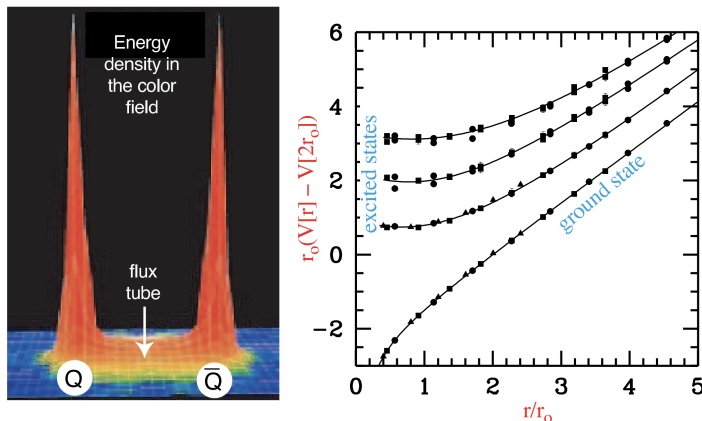
Figure 1.4: (Left) Lattice QCD calculation showing the energy density of the color field between a heavy quark and a heavy anti-quark. (Right) The corresponding potential between the quarks. The ground state potential evolve from a $1/r$ dependence to a linear dependence as a function of distance. From Reference [10].

interpretation that the gluonic field is indeed confined between the quarks while studying the heavy quark sector. A depiction of this model can be found in Figure 1.4.

Hybrid mesons can arise when the flux tube acquires angular momentum. Two degenerate excitations can exist, one where the flux tube is rotating clockwise and another where it is rotating counter-clockwise. A linear combination of these can be formed such that the state can take on definite J^{PC} quantum numbers. In the case of a single unit of angular momentum, the flux tube can contribute J^{PC} quantum numbers of 1^{-+} and 1^{+-} to the underlying meson. If the underlying meson has L=0 then eight hybrid nonets can be formed where three of them have exotic quantum numbers. These eight nonets are degenerate in the flux tube model, though lattice QCD points to the 1^{-+} nonet being the lightest. Close and Page extended a flux-tube model introduced by Isgur [8] and were able to determine the decay width of hybrid mesons [9]. For the π_1 ($J^{PC} = 1^{-+}$) hybrid, the relative ratios are computed and are shown in Equation 1.9. The ordering of decay modes is in agreement with recent lattice calculations, which will be introduced later in Section 1.4. More information on hybrids arising from the flux tube model can be found in Reference [10].

$$\pi b_1 : \pi f_1 : \pi \rho : \eta \pi : \eta' \pi$$
$$170 : 60 : 5 - 20 : 0 - 10 : 0 - 10 \tag{1.9}$$

A question might be asked: if the goal is to study the gluon, why not look for glueballs? Unfortunately, models suggest that the lightest glueballs do not have exotic quantum numbers.

8

Having the same quantum numbers as normal mesons allows for mixing to occur and thus becomes difficult to separate their contributions. Therefore, the existence of a glueball in a spectrum has typically been inferred in supernumerary resonances. The lightest glueball with exotic quantum numbers is expected to be the 2^{+-} near 4 GeV.

1.3 Regge Phenomenology

1.3.1 Regge Trajectories and the Flux Tube Model

Chew and Frautschi [11] noticed that hadrons can be organized into groups where there exists a linear dependence between the spin (J) and it's squared mass (M)

$$J(M) = \alpha(0) + \alpha' M^2 \tag{1.10}$$

where α' is known as the *Regge trajectory*. This regularity hinted at some underlying substructure. Nambu introduced the flux tube model in response to the observation [7]. This model contains massless quarks that are tethered by a relativistic string with a constant energy density, σ_0. The system rotates about its center. The energy (or mass) and total angular momentum of a string element is given by

$$dE = dM = \gamma(r)\sigma_0 dr$$
$$dJ = r\beta(r)\gamma(r)\sigma_0 dr \tag{1.11}$$

where $\gamma = \left[1 - \beta^2\right]^{(-1/2)}$ is the *Lorentz factor* and β is the ratio of v over c. Integrating these equations and reorganizing gives the following expression for the total angular momentum of the string

$$J = \frac{M^2}{2\pi\sigma_0} = \alpha' M^2 \tag{1.12}$$

where $\alpha' = \frac{1}{2\pi\sigma_0}$ is the *trajectory* from this model. Figure 1.5 shows a Chew-Frautsci plot for the radial ground state mesons organized into three groups with the same I, S, and P, while J increases by 2 units. Mesons on the blue line are characterized by $S = 1$ and natural parity, whereas mesons along the green line are described by S=0 and unnatural parity.

The α' for the blue line is 0.917 ± 0.016 GeV^{-2} and corresponds to the string tension $\sigma_0 = 0.880 \pm 0.016$ GeV/fm. This value is in good agreement to the one extracted from fits to the energy levels of heavy quarkonia. The intercept, $\alpha(0)$, is equal to 0.440 ± 0.011. Radially excited states can be found to lay on trajectories with similar slopes, only shifted to higher masses. These are known as *daughter trajectories*.
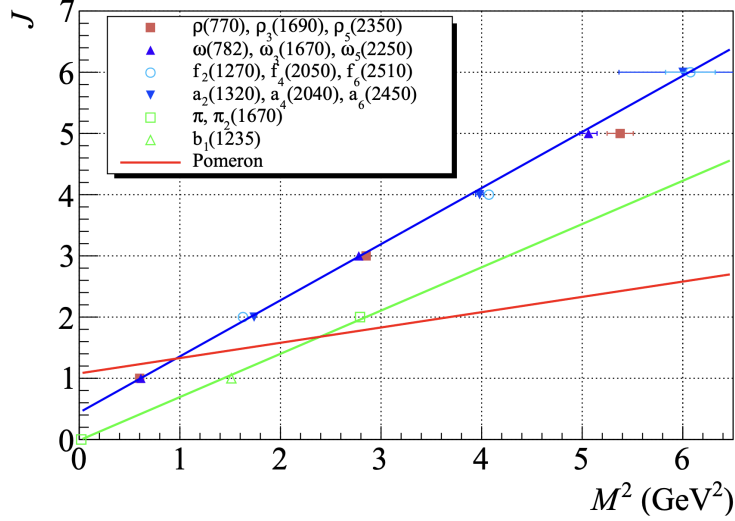
Figure 1.5: Chew-Frautschi plot showing the linear dependence between the spin and squared mass of radial ground state mesons [1].

The red line is known as the *Pomeron trajectory* and is described as $\alpha(M^2) = 1.08 + \alpha' M^2$ where $\alpha' = 0.25$ GeV^2. This trajectory was introduced to compensate for a discrepancy between Regge theory predictions of the total hadronic cross section and the experimentally measured results. This will be described in more detail below. The Pomeron has the quantum numbers of the vacuum. Currently, there is no associated particle for the Pomeron. Glueballs are a plausible candidate, but they remain elusive. If this is the case, it could explain the dramatically different slope of the Pomeron trajectory as compared to meson Regge trajectories.

1.3.2 Scattering and Regge Theory

In 1958, Stanley Mandelstam introduced the s, t, and u variables. These variables are useful in describing two-to-two body scattering. They are defined as

$$s = (p_1 + p_2)^2 = (p_3 + p4)^2$$
$$t = (p_1 - p_3)^2 = (p_4 - p_2)^2 \qquad (1.13)$$
$$u = (p_1 - p_4)^2 = (p_3 - p_2)^2$$

The corresponding diagrams depicting a s, t, and u channel exchange are shown in Figure 1.6. For two-to-two scattering of identical mass particles, the s-channel physical region is given by $s > 4m^2$ and $t < 0$. The t-channel physical region is given by $t > 4m^2$ and $s < 0$ and is seen as the shaded regions on the right side of Figure 1.6.

10
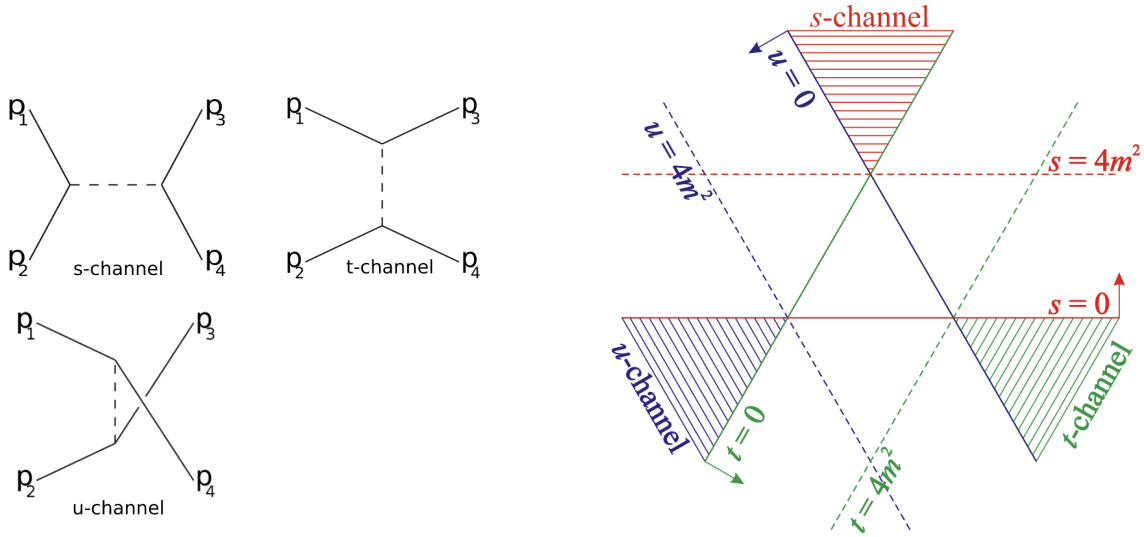
Figure 1.6: s, t, u Mandelstam variables for two-to-two scattering. Source for left plot https://en.wikipedia.org/wiki/Mandelstam_variables. Source for right plot from Reference [1].

Scattering of some initial state to some final state is described by an amplitude, M_{fi}. This amplitude can be expanded as a *partial wave series*. Each term of the series corresponds to different angular momentum components. The theory behind partial wave analysis(PWA) will be discussed in significantly more detail in Chapter 4. At low energies, scattering in the s-channel is dominated by intermediate state resonances, which populate specific partial waves. In these cases, a limited set of partial waves are enough to describe the reaction. High-s scattering is dominated by multi-particle exchanges, which makes the series non-convergent. There is a duality between high-s scattering and t channel exchanges of color singlet objects that can be exploited to describe this.

Yukawa's one-pion exchange description of interacting hadrons is a particular case of the more general Regge theory. An important result of this theory is that the cross section at high s and low $-t$ is given by

$$\sigma \sim s^{J-1} \tag{1.14}$$

scaling as a power law. For the exchange of a pion ($S=0$) the corresponding cross section should decrease like s^{-1}. The exchange of a $\rho(770)$ ($S=1$) meson would then be predicted to be constant. Experimentally, this does not quite match the measured total cross sections, shown in Figure 1.7, which tend to decrease until around 2 GeV and then begins to rise. Instead, the total cross section in a high-s scattering process should be described by the exchange of entire families of particles in the t-channel.

11
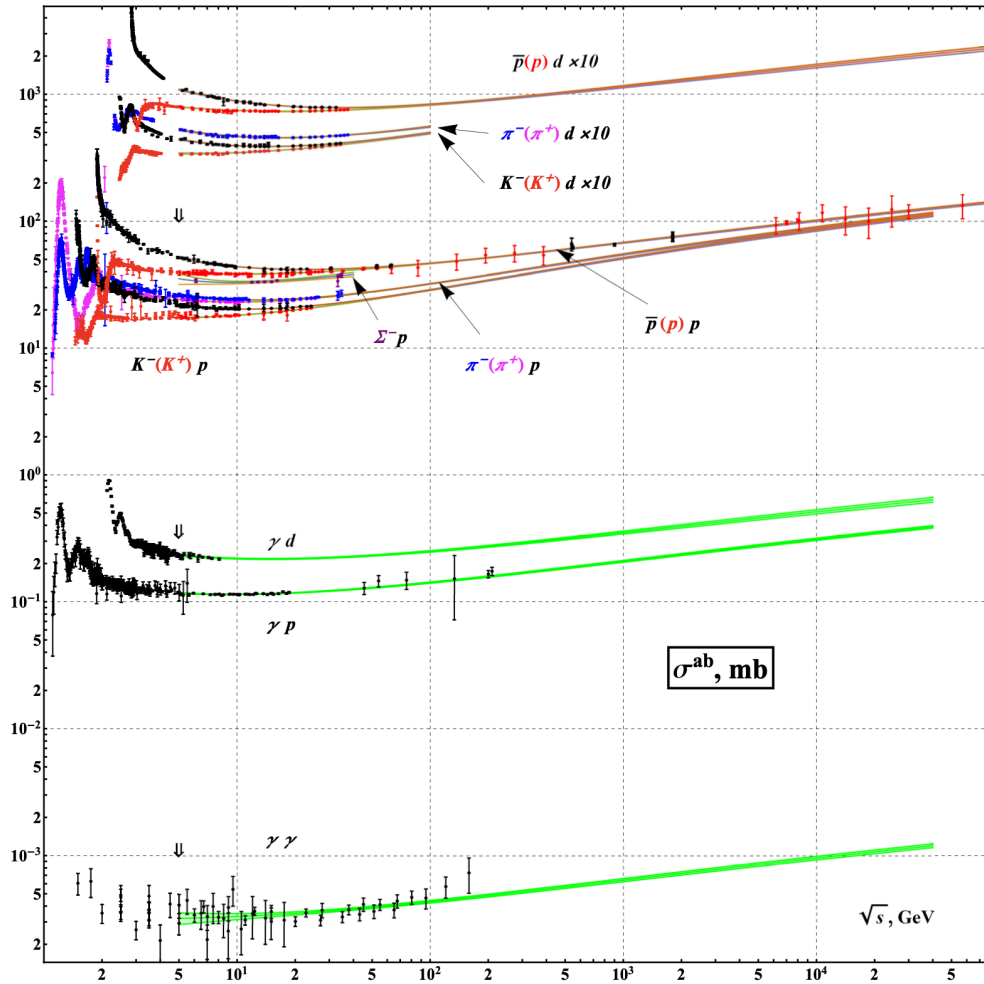
Figure 1.7: Total cross sections for hadronic, γp, and $\gamma\gamma$ as a function of center of mass energy, $\sqrt{s}$ [12].

To describe large s and small $-t$ scattering processes, the t-channel partial wave expansion begins in the t-channel physical region, $t > 4m^2$ $s < 0$, where the partial wave series converges. t is then moved into the complex plane. The amplitude is analytically continued to large s. The scattering cross section, as in 1.14, is now given by

$$\sigma \sim s^{\alpha(0)-1} \tag{1.15}$$

The amplitude contains a number of poles, known as *Regge poles* or *Reggeons*. They are given by $\alpha_i(t)$. The path traced out by $\alpha_i(t)$ is known as a *trajectory* which was defined Section 1.3.1. The amplitude is primarily driven by trajectories that pass near integer values of angular momentum at a given $t = t_0$ such that $\alpha(t_0) \approx J$ and where t_0 corresponds to the squared mass of the associated resonance with spin J.

Figure 1.7 can now be explained as follows. Reggeons, corresponding to a family of particles (or trajectory), are exchanged. Meson trajectories have $\alpha(0) < 0.5$ so the cross section should decrease. This describes the data points at low $\sqrt{s}$ where valence quarks dominate. The inflection at $\sqrt{s} \sim O(1)$ is due to the exchange of the Pomeron trajectory with $\alpha(0) \sim 1$ which has a roughly constant cross section. This is where sea quarks and gluons begin to prevail. The logarithmic rise at even higher $\sqrt{s}$ is due to multi-pomeron exchanges. It was in 1992, that Donnachie first used similar arguments to construct a model to fit a number of total hadronic cross section plots. The model contained a third of the number of parameters that were previously used while obtaining a similar χ^2 [13].

A final note: scattering through intermediate resonances in the s-channel or the t-channel are dual ways to describe the same dynamics. Any reaction occurring through the s-channel can be described as an infinite sum of partial waves in the s-channel. Experimentally, a truncation of partial waves has to occur, which leads to effective background terms like the Deck effect and double Regge exchanges. These effects can be modeled as exchanges in the t-channel and can populate numerous partial waves. This contamination can be significant, especially if one is looking for weak signals in specific partial waves, like the π_1 in the $\eta\pi$ channel (see Equation 1.9 and Section 1.10). Part of this dissertation studies this particular type of background. It will be discussed in Chapter 5. A more in-depth discussion of Regge theory can be found in Reference [1].

1.4   Lattice QCD

Lattice QCD is a non-perturbative method of solving QCD where calculations are performed on a discrete grid in Euclidean space-time. The grid spacing, a, acts as a momentum cut-off and acts to regularize the theory. Quark fields are situated at the lattice sites and gluon fields are located on the edges. Numerical calculations are performed by averaging Monte Carlo sampled field configurations that require significant computational power. To reduce the computational burden and to limit the variety of scattering, a heavier up/down quark mass is used (summarized by the pion mass). In the end, extracting a physical result involves taking several limits: shrinking the lattice spacing, extending to the infinite space-time volume, and taking the physical quark mass limit. One way to relate the finite-volume energy levels to the infinite-volume scattering matrix can be done by following the method prescribed by Lüscher [14].

Through a series of papers, the HADSPECT Collaboration has developed a description for a complete nonet of scalar and tensor mesons which is partly summarized in [15]. These resonances decay through multiple channels, so all possible scatterings must be included. These studies showed that lattice QCD can expose non-trivial resonance physics. The remainder of this section will highlight some of their works as it can provide a coherent picture of the light meson states, including the lightest exotic hybrid meson, that will be important in disentangling the $\eta\pi^0$ spectrum at GlueX.

Fig. 1.8 shows a spectrum of masses for the ground state mesons extracted on the lattice by the HADSPECT Collaboration. In this study, the authors did not consider the scalar mesons, 0^{++}, as they have more complicated phenomenology. Though the calculation was done at a higher unphysical pion mass, the level ordering, level count, and the existence of non-$q\bar{q}$ quantum numbers(rightmost set of states) are interesting. The spectra show numerous overlapping states that can potentially mix with other states with the same J^{PC} quantum numbers.

The orange outlined states in Fig. 1.8 contains a significant chromomagnetic gluonic component in their wave function and can be interpreted as the lightest hybrid meson super-multiplet. The lightest exotic hybrid meson is predicted to belong to the $J^{PC} = 1^{-+}$ nonet and would be the π_1 isovector state. The predicted isoscalar states in the 1^{-+} nonet are slightly heavier. The study uses an artificial 392 MeV pion. It is important to note that this is a qualitative depiction of the light meson spectrum but it gives an expectation for the level structure. Numerous calculations have been previously performed to estimate the π_1 mass at different pion masses. Figure 1.9 plots several
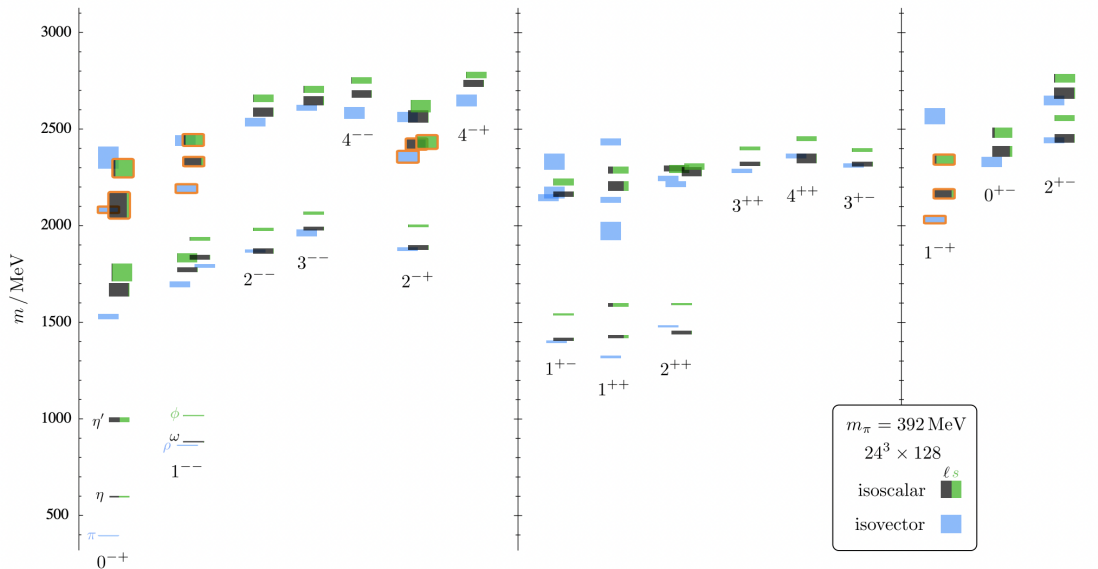
Figure 1.8: Isoscalars (green/black) and isovectors (blue) spectrum from lattice QCD as determined in [16]. The vertical width of the bars denotes the statistical uncertainty. The pion mass was set to 392 MeV and was performed on a 24^3x128 lattice. States with orange outlines have a large chromomagnetic gluonic component in their wave function and can be interpreted as the lightest hybrid meson supermultiplet. The rightmost column of states contains exotic quantum numbers.

predictions as a function of the pion mass used. An approximately linear pion mass dependence can be seen and intercepts with the physical pion mass somewhere between 1.5 and 1.7 GeV.

Recently, the branching fractions of the π_1 exotic hybrid meson have been determined on the lattice while working with $SU(3)_\text{flavor}$ symmetry and coupling eight different decay channels [25]. The analysis showed that the main decay mode of the 1^{-+} is through the $b_1\pi$ with much smaller decays to $f_1\pi$, $\rho\pi$, $\eta'\pi$, and $\eta\pi$. This is shown in Fig. 1.10. This relative ordering of the partial widths is in agreement with a flux tube model introduced in Section 1.2. Previous experimental results, which we will introduce in the next section, have shown significant evidence for the π_1 in searches involving its decay to $\eta'\pi$ and $\eta\pi$. These channels may be heavily suppressed. This suppression can be compensated by the fact that the $\eta^{(\prime)}\pi$ channels are easier to analyze due to the simpler pseudoscalar decays and smaller final state multiplicity when compare to the vector-pseudoscalar channels that the π_1 mostly decays into.

Lattice QCD also hints at potential molecular states. The isovector scalar $a_0(980)$ meson has been primarily observed as an enhancement in $\eta\pi$ final states (including in the GlueX data that is used in this dissertation) close to the $K\bar{K}$ threshold around 1 GeV. This proximity necessitated
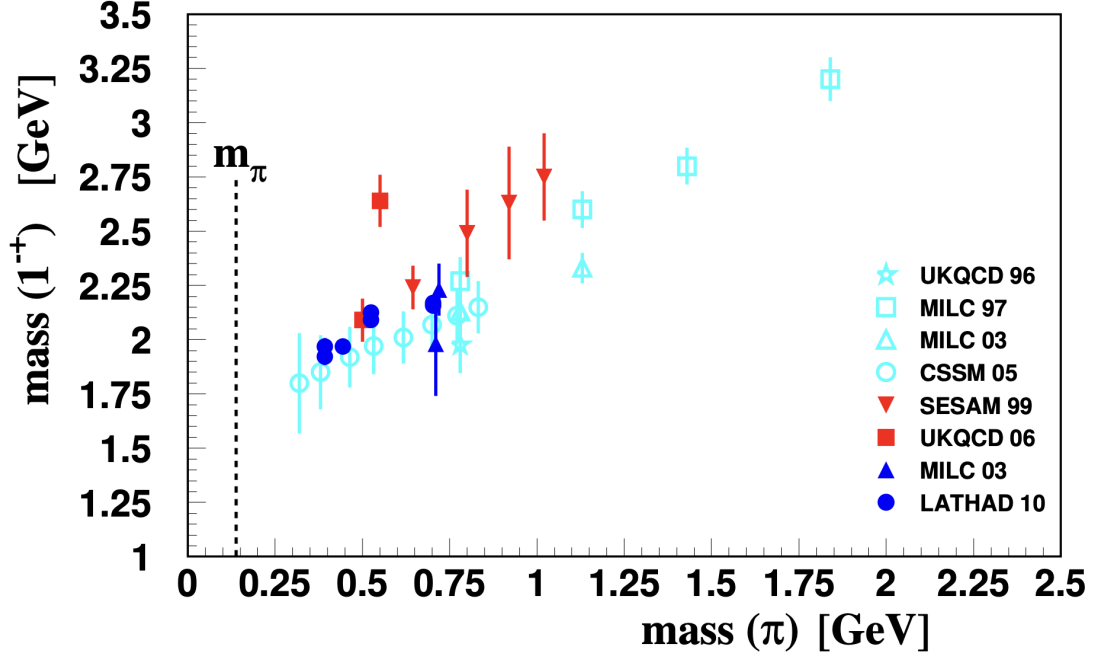
Figure 1.9: Predictions for the mass of the 1^{-+} as a function of the pion mass. The open symbols are from calculations that do not include $q\bar{q}$ loops (quenched approximation) whereas the solid symbols are from calculations that do. The references in the legend (from top to bottom) are [17][18][19][20][21][22][19][23]. Figure is taken from Reference [24].
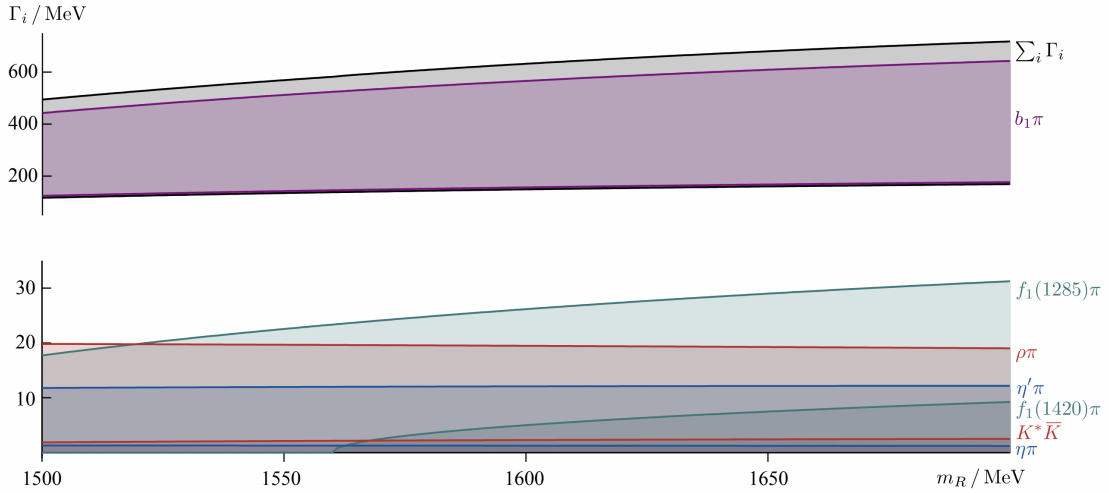
Figure 1.10: Partial widths as a function of the π_1 pole mass as determined in [25].

16

a coupled-channel analysis and is detailed in Ref. [26]. The isoscalar scalar $f_0(980)$ and isoscalar tensor mesons $f_2(1270)$ and $f'_2(1525)$ have been studied in [15]. With these lattice results, it is suggested that the $a_0(980)$ and $f_0(980)$ could originate from the same source (or pole, see Section 1.3.2), that is, an isovector and isoscalar manifestation of a $K\bar{K}$ molecule.

1.5   Experimental observations of π_1 in $\eta\pi$

The π and η mesons are well studied pseudoscalar mesons with $J^{PC} = 0^{-+}$, see Section 1.2. The total spin of a $\eta\pi$ system is 0 since both the constituents are spinless. Therefore, the total angular momentum of the system is equal to the relative orbital angular momentum between them. The parity quantum number of the system is equal to $(-1)^l$. Note, that since these are bosons there is no additional factor of -1 that is included, as in Equation 1.5. The charge conjugation quantum number of the system is strictly positive. The series of J^{PC} quantum numbers accessible by an $\eta\pi$ system is: 0^{++}, 1^{-+}, 2^{++}, 3^{-+}, ..., where all sets of quantum numbers with odd-J are manifestly exotic. Experimentally, the spin of the meson can be determined by studying the angular distributions of the decay products. For instance, if the decay products are two spin-0 states, then the relative angular momentum between the two daughter particles must equal to the spin of the parent. This is typically referenced in spectroscopic notation where S, P, and D... wave decays refer to 0, 1, and 2 units of angular momentum that is carried away in relative angular motion. A decay through the S-wave would appear to be flat in $\cos(\theta)$ whereas a D-wave contains two nodes.

Mode	Experiment	Mass (GeV)	Width (GeV)	Events	Ref.
$\pi^0(\eta \to \pi^+\pi^-\pi^+)$	E852	1.257 ± 0.02	0.354 ± 0.064	23,492	[27]
$\pi^0(\eta \to \gamma\gamma)$	E852	-	-	45,000	[28]
$\pi^0(\eta \to \gamma\gamma)$	Crystal Barrel	1.36 ± 0.025	0.22 ± 0.090	269,087	[29]
$\pi^-\eta$	GAMS	1.406 ± 0.02	0.180 ± 0.030	-	[30]
$\pi^-\eta$	E852	$1.370 \pm 0.016^{+0.050}_{-0.030}$	$0.385 \pm 0.040^{+0.065}_{-0.105}$	47,235	[31]
$\pi^-\eta'$	E852	$1.597 \pm 0.010^{+0.045}_{-0.010}$	$0.340 \pm 0.040 \pm 0.050$	5,765	[32]
$\pi^-\eta + \pi^-\eta'$	JPAC (COM-PASS Data)	$1.564 \pm 0.024 \pm 0.86$	$0.492 \pm 0.054 \pm 0.102$	155,000	[33]

Table 1.2: Reported masses and widths of the π_1 with $J^{PC} = 1^{-+}$ from select experiments, including the number of events. Experiments reporting on the $\eta\pi^0$ channel is in the top section. Note that the Crystal Barrel results looked at the $\eta\pi^0\pi^0$ final state. Reports for $\eta^{(\prime)}\pi^-$ is on the bottom section.

There is experimental evidence for the π_1. Most of these experiments, like E852 and COMPASS, used a π^- beam and mainly revolve around the negatively charged π_1. Historically, there has been

(a) (CBAR) $M(\eta\pi^0)$ where $\eta \to 2\gamma$

(b) (E852) $M(\eta\pi^0)$ where $\eta \to \pi^+\pi^-\pi^0$

(c) (E852) $M(\eta\pi^0)$ where $\eta \to 2\gamma$
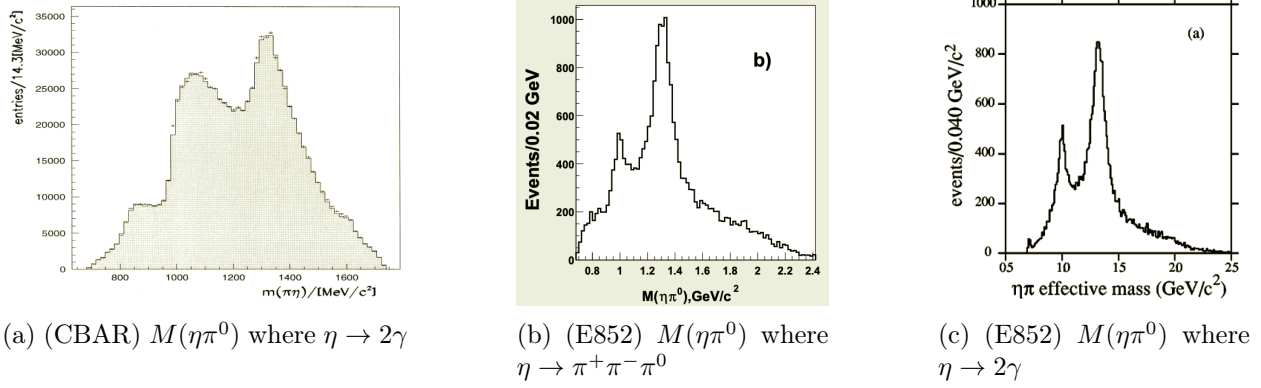
Figure 1.11: $M(\eta\pi^0)$ distribution where $\eta \to 2\gamma$ in Crystal Barrel (a) and in E852 where $\eta \to 3\pi$ (b) and $\eta \to 2\gamma$ (c). The analysis from the Crystal Barrel Collaboration looked at the final state $\eta\pi^0\pi^0$ whereas the analysis from the E852 Collaboration looked at the final state $\eta\pi^0$.

some confusion about the nature of this meson. This problem arose when multiple groups measured a P-wave resonance around 1.4 GeV and 1.6 GeV which correspond to the claimed $\pi_1(1400)$ and $\pi_1(1600)$. Table 1.2 shows the reported masses and widths from select groups. In general, the 1^{-+} exotic P-wave is seen in the $\eta\pi$ final state at around 1.4 GeV and in the $\eta'\pi$ final state at around 1.6 GeV. The observed intensity at some experiments near 1.4 GeV is problematic since lattice QCD predicts a larger mass value for the π_1, see Section 1.4. The $\pi_1(1600)$ has a much richer set of observations and statistics and whose mass is closer to the expected range predicted by lattice. For a more complete history of this resonance and the experiments behind these determinations, see [34]. Fig. 1.11 shows the $M(\eta\pi^0)$ distribution from the Crystal Barrel, GAMS, and E852 Collaborations. GAMS reported the first observation of a state with exotic quantum numbers $= 1^{-+}$ when looking at the reaction $\pi^-p \to p\eta\pi^-$. Crystal Barrel analyzed the reaction $\bar{p}p \to \pi^0\pi^0(\eta \to 2\gamma)$. E852 analyzed the reaction $\pi^-p \to \pi^0\eta$ where the $\eta \to 2\gamma$ and $\eta \to 3\pi$.

The COMPASS Collaboration published results on exclusively produced $\pi^-\eta$ where the $\eta \to \pi^+\pi^-\pi^0(\pi^0 \to \gamma\gamma)$ along with results for $\pi^-\eta'$ where the $\eta' \to \pi^+\pi^-\eta(\eta \to \gamma\gamma)$. The pion beam is operated at 191 GeV. The data set they analyzed is the largest published data set looking at the $\pi\eta$ final state. The analyses shared the same $\pi^-\pi^-\pi^+\gamma\gamma$ final state. The $\pi^-\eta$ and $\pi^-\eta'$ data set contain 116,000 and 39,000 events. Fig. 1.12 shows the $M(\eta^{(\prime)}\pi^-)$ and $M(\eta^{(\prime)}\pi^-)$ vs $\cos\theta_{GJ}$ distributions on the left and right-hand side, respectively. A clear double-lobed D-wave is present in the $M(\eta^{(\prime)}\pi^-)$ vs $\cos\theta_{GJ}$ distribution corresponding to the spin-2 $a_2(1320)$ meson. This D-wave is not seen in $\eta'\pi$ due to its proximity to the 1.1 GeV threshold of this system. In the $\eta\pi$ channel, there is an absence

18

(a) $m(\eta\pi^-)$

(b) $m(\eta'\pi^-)$

(a) $m(\eta\pi^-)$ vs. $\cos\vartheta_{\mathrm{GJ}}$

(b) $m(\eta'\pi^-)$ vs. $\cos\vartheta_{\mathrm{GJ}}$
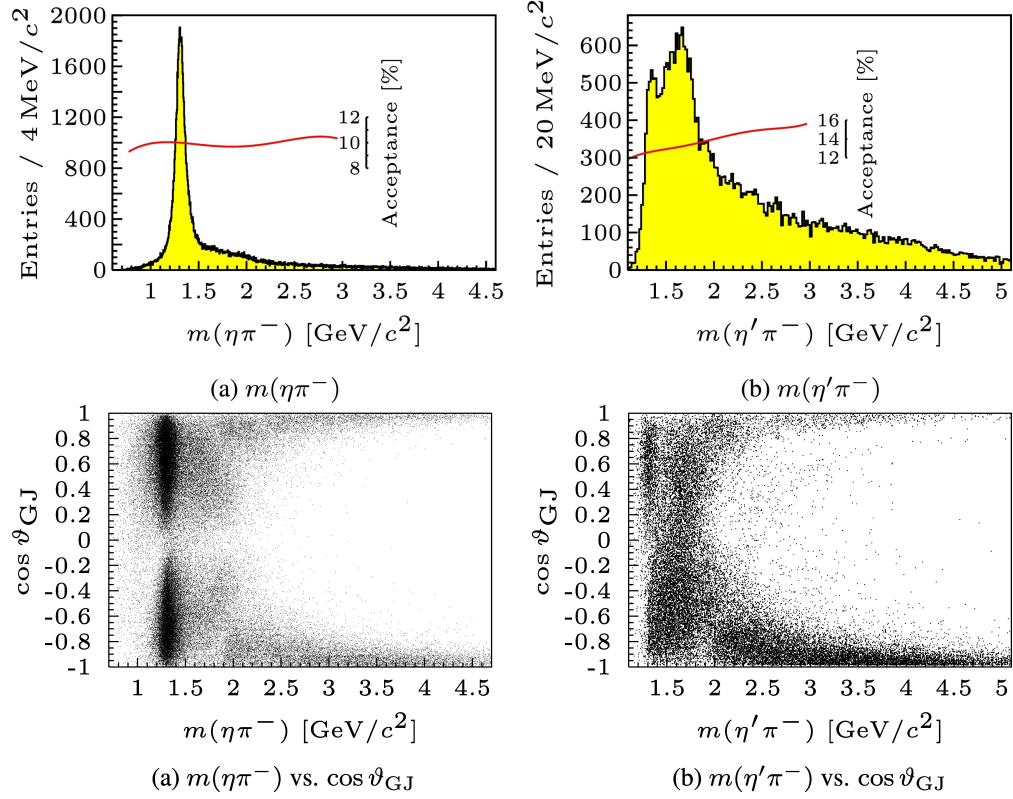
Figure 1.12: (Top) $M(\eta^{(\prime)}\pi^-)$ and (Bottom) $\cos(\theta_{GJ}$ vs $M(\eta^{(\prime)}\pi^-)$ data from the COMPASS experiment. A prominent double-lobed a_2 resonance can be seen in $\eta\pi$ but is too close to threshold (1.1GeV) to be seen in $\eta'\pi$. The forward/backward asymmetry is visibly larger in $\eta'\pi$ [35].
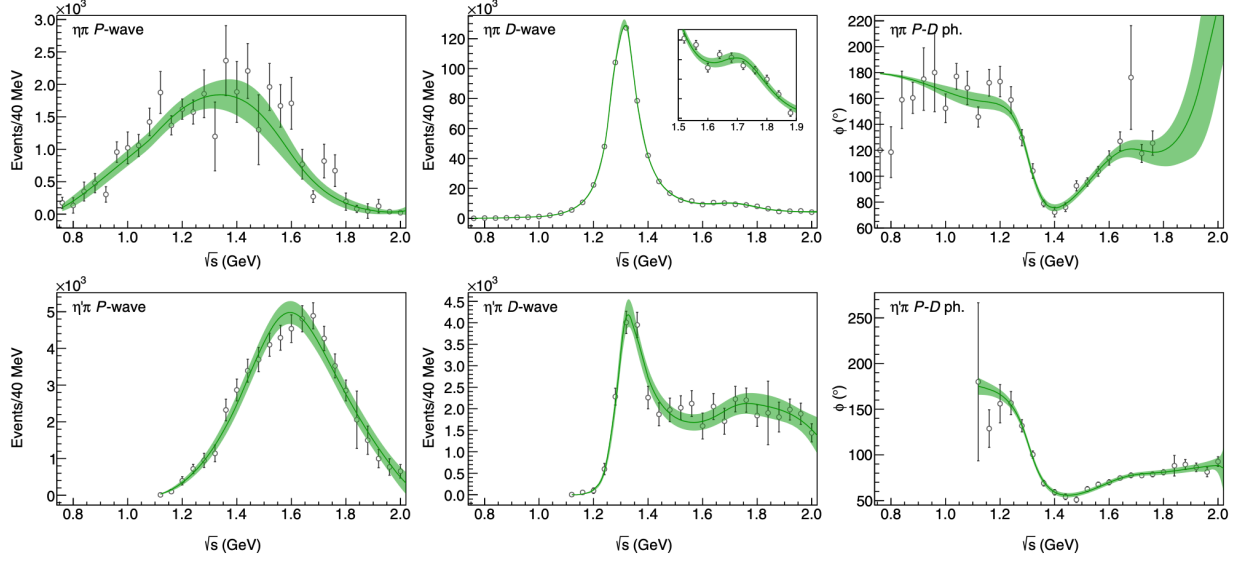
Figure 1.13: Coupled channel fit to $\eta\pi$ (upper half) and to $\eta'\pi$ (lower half) data from COMPASS. The intensities of the P(left) and D(center) waves and relative phases (right) are shown. The green bands show the 2σ confidence level calculated from the bootstrap analysis technique [33].

of a signature for the $a_0(980)$ meson that was observed in other experiments. This feature is due to the fact that Pomeron exchange dominates at the higher energies that COMPASS operates. The Pomeron has the quantum numbers of the vacuum and will not permit the production of an a_0 due to parity conservation. The forward/backward asymmetry, which can indicate coherent P and D wave interference, is visibly larger in $\eta'\pi$ than $\eta\pi$. Performing a PWA on both the reactions shows a peak at 1.4 GeV and 1.6 GeV in the exotic P-wave for the $\pi^-\eta$ and $\pi^-\eta'$ respectively. It is important to note the existence of the strong feature at large angles that appear to become more narrow as a function of M($\eta\pi$). The next section will briefly expand on the source and how a measurement made in this dissertation can help construct models for it.

A more comprehensive analysis by the JPAC Collaboration has been performed for the two

20

channels $\eta^{(\prime)}\pi$ using the data collected by the COMPASS experiment [33]. They completed a coupled channel analysis in which they extracted a single exotic π_1 pole, thus providing a resolution to the observed mass differences in previous experiments. The mass and width of the pole is $1564 \pm 24 \pm 86$ MeV and $492 \pm 54 \pm 102$ MeV. The two cited errors are for the statistical and systematic error, respectively. Fig. 1.13 shows the fits to the P and D waves and their relative phase for the $\eta\pi$ and $\eta'\pi$ data. Large phase motion is seen, which indicates the P-wave is resonant. The difference in the masses is explained as a combination of final state interactions and production processes. Another analysis using a K-matrix approach (a different description of the dynamics) has been performed on data from Crystal Barrel, COMPASS, and 11 different $\pi\pi$ scattering datasets. The results agree with the JPAC findings for a single π_1 pole [36]. Coupled channel analyses represent the gold standard in how similar analyses should proceed.

The π_1 is just one member in a nonet of $J^{PC} = 1^{-+}$ mesons. Determining the properties (i.e. mass and width) of the other members will be important in validating/invalidating theoretical predictions for the nonet. The isoscalar partners are expected to be slightly heavier, see Figure 1.8. Recently, BESIII has observed evidence for a 1^{-+} isoscalar partner, the η_1 in the $J/\psi \to \gamma\eta\eta'$ where $\eta_1 \to \eta\eta'$. The authors compared models, with and without an η_1 contributing in the P-wave. Figure 1.14 shows fits with these two models to the observed angular moments strongly favoring a need for the η_1 with a mass and width of around 1.855 GeV and 188 MeV, respectively. The authors estimate a statistical significance greater than 19σ. This is the first evidence for this exotic hybrid meson.
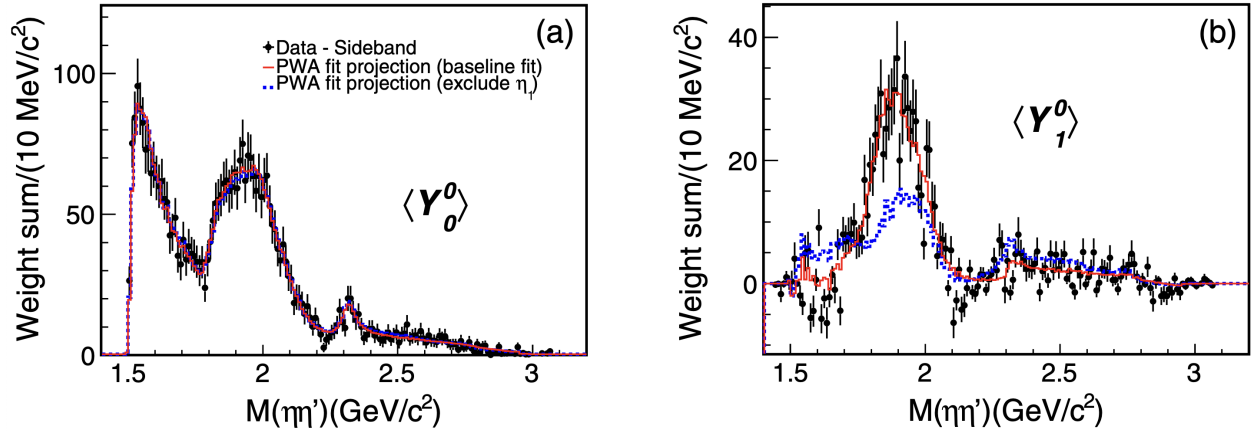
Figure 1.14: Partial wave analysis results of $J/\psi \to \gamma\eta\eta'$ radiative decays from BESIII Collaboration [37]. Y_l^0 is the l-th moment which characterizes the spin of contributing $\eta\eta'$ resonances. The background-subtracted data is in black. The fit results shown in red includes a contribution from the η_1 whereas the fit results in blue does not. The Y_1^0 moment has a clear preference for a hypothesis including the η_1. The estimated statistical significance was estimated to be greater than 19σ.

1.6 Photoproduction at GlueX

Much of the data on the π_1 comes from hadron production experiments. Signals can be produced in different ways depending on the production mechanism. Confirming the existence of the π_1 in another production mechanism, like photoproduction, will help verify the existence and properties of the π_1. The GlueX experiment is one such experiment whose goal is to map the meson spectrum including the hybrid mesons. Observing the π_1 in photoproduction will lay the foundation for future hybrid meson searches at GlueX. GlueX uses a linearly polarized photon beam with around 35% polarization at 8.5 GeV. Linear polarized photon beams have many benefits. The polarization is important in the determination of the J^{PC} quantum numbers, is essential in determining the production mechanism, and can be used to filter exotics once the production mechanism is isolated [38]. Chapter 2 will introduce the GlueX experiment.

Based on previous experiments, the golden channels to search for the π_1 are $\eta\pi$ and $\eta'\pi$. These states are relatively easy to reconstruct, are generally clean channels, and have narrow signatures. A resonant signature for the π_1 is expected to be seen around 1.4 GeV in the $\eta\pi$ channel. The expected yield of the π_1 in the $\eta\pi$ channel is expected to be small. The $\eta\pi$ invariant mass spectrum, as measured by GlueX, has features similar to Figure 1.11c (showing a peak for the $a_0(980)$ and a peak for the $a_{(}1320)$) and Figure 1.12 (showing strong intensity at $\cos\theta = \pm 1$ at large $M(\eta\pi)$).

22

Chapter 3 will discuss how the data is processed into $\eta\pi^0$ physics events and the resulting mass and angular distributions. This dissertation will introduce a study of the $\eta\pi$ system at GlueX broken up into two main thrusts related to these two features.

It is predicted that the cross section for the $a_2(1320)$ and the π_1 should be of similar size [39]. The expected branching ratio for π_1 to $\eta\pi$ is much smaller than in $a_2(1320)$ to $\eta\pi$, see Figure 1.10. The expected yield for the π_1 is then anticipated to be much smaller than that of the nearby $a_2(1320)$. Therefore, it is crucial to understand the production of the $a_2(1320)$ due it's larger yield, its relatively narrow width, and as it can act as a phase reference to establish any resonant contributions from the π_1. The first thrust then is to measure the differential cross section for the $a_2(1320)$. Chapter 4 will introduce previous studies of this meson and detail the differential cross section measurement made for this dissertation.

The second thrust is to understand the source of the strong intensity at $\cos\theta = \pm 1$ at large $M(\eta\pi)$. These "wings" can be modeled as a double Regge exchange process, which can contribute to intensity in the exotic partial waves of this channel. To aid the development of theoretical models to describe this type of process, measurements will be made to determine the relative contributions of natural to unnatural exchanges to the $\eta\pi^0$ cross section. In particular, Σ beam asymmetries are measured in various kinematic bins and will be discussed in Chapter 5.

CHAPTER 2

THE GLUEX EXPERIMENT

2.1 Continuous Electron Beam Accelerator Facility

Thomas Jefferson National Accelerator Facility, Jefferson Lab for short, is located in Newport News, VA. Jefferson Lab hosts the Continuous Electron Beam Accelerator Facility (CEBAF). In 1984, a consensus in the nuclear science community had been reached to construct a new electron beam facility to study the interface between nuclear physics and QCD at an initial maximum energy of 4 GeV [40][41]. Construction on this accelerator began in 1987 along with three experimental halls that it would service: A, B, and C. CEBAF started operations in 1994 and by the 2000s the beam energy had increased to nearly 6 GeV. In 2012, the facility began a major upgrade, which doubled the maximum energy of its electron beam to 12 GeV and included a new hall, Hall D. The 12 GeV CEBAF era began in 2014 when the project was granted CD-4A or Start of Initial Operations that July [42]. It took another 2 years to fully deliver this energy to Hall D. Figure 2.1 shows a schematic of the current layout of the facility.

The beam begins at the injector, where a pulsed near-infrared laser ejects bunches of electrons off of a gallium arsenide photocathode via the photoelectric effect [41]. These bunched electrons are passed through a Wien filter to homogenize the beam energy, a chopper to separate the bunches, and a set of cryomodules to increase their energy to 123 MeV. These bunches of electrons can be polarized (or not) by using (or not using) a polarized laser source. The frequency of the laser pulse is made such that beam bunches arrive at Hall D in 4 ns intervals.

These electrons are now injected into the CEBAF accelerator, which is formed from two linear accelerators (linacs) joined together by recirculating arcs. The linacs accelerate the electrons using superconducting niobium radio-frequency (RF) cavities cooled to 2-4K. Superconducting RF cavities are used to minimize resistive energy loss. RF cavities accelerate charged particles by setting up an oscillating electromagnetic field such that the particles always experience a positive accelerating force [43]. Each time the electron beam passes through a linac, its energy is increased by $\sim$1.1 GeV or $\sim$2.7 MeV/m. After getting accelerated by one linac the electrons can be sent through a recirculating arc which uses magnets to redirect the path of the beam into another linac, finally
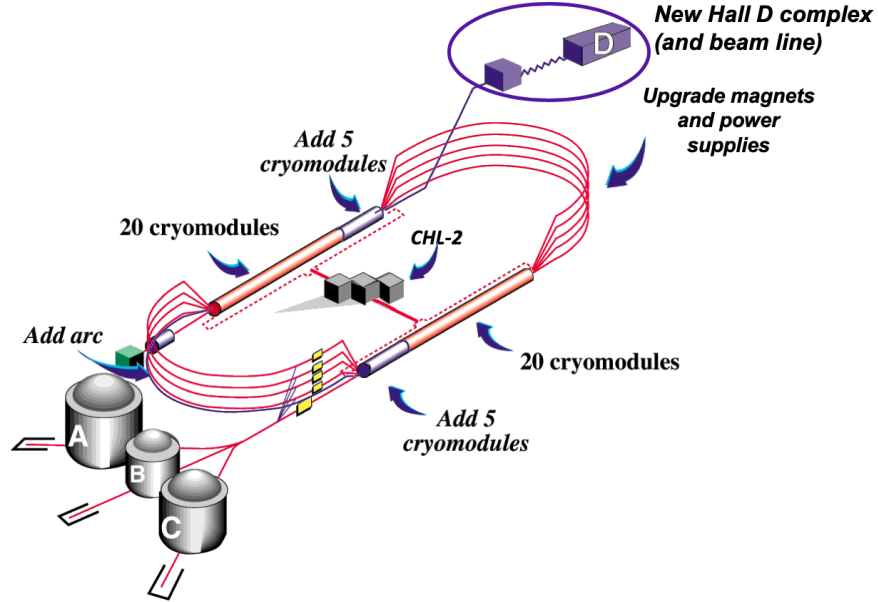
Figure 2.1: Schematic of the Continuous Electron Beam Accelerator Facility at Jefferson Lab [44].

completing the orbit in a racetrack configuration. These electrons are extracted at two points: one for Halls A, B, and C, and another for Hall D which includes an extra linac pass. In total, the electron beam will recirculate 5 1/2 times before entering Hall D. CEBAF was designed to deliver up to 5 μA current to Hall D. The typical currents arriving at Hall D for data taking is around 100-200 nA for GlueX-I.

2.2   Hall D Beamline

Most of the following information about the Hall D beamline and detector is derived from Reference [44]. When the electron beam enters the Hall D complex, it first enters the tagger hall. The electron beam is first passed through a thin radiator which produces linearly polarized photons via coherent bremsstrahlung. The energy of the photons is determined by the tagger system by measuring the scattered electron. The photon beam is then passed through the collimator to increase the degree of polarization. The polarization spectrum of the photon beam is determined by the triplet polarimeter. The photon flux is determined by the pair spectrometer. Figure 2.2 shows a schematic of the beamline.
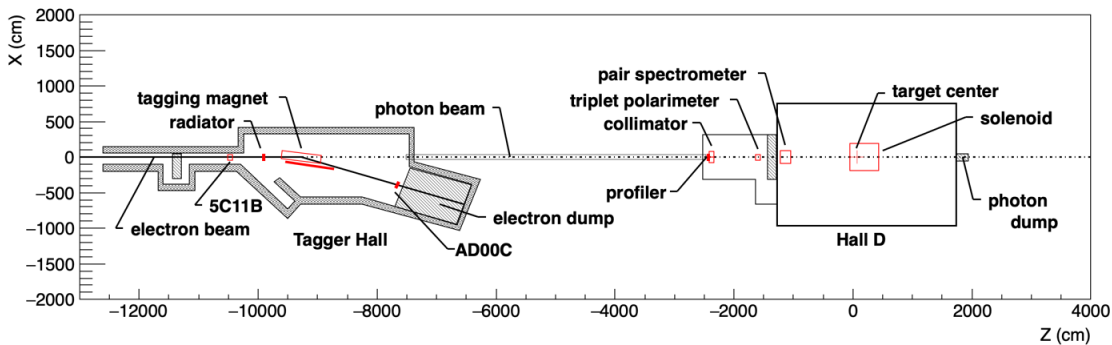
Figure 2.2: Diagram of the Hall D beamline [44].

2.2.1 Radiators and Polarization

A diamond radiator is used to convert the electron beam to a beam of linearly polarized photons via coherent bremsstrahlung. The energy of the photons is determined by the tagger system that can tag photons with energies around $3-12$ GeV. For coherent bremsstrahlung, the energy spectrum and the corresponding degree and angle of linear polarization are dependent on the angle between the electron beam direction and the (2,2,0) crystal plane of the diamond radiator. The momentum transfer must be an integer multiple of the reciprocal lattice vector which leads to discrete electron recoil momentum that can be transferred to the crystal lattice and therefore a well-defined photon energy [45]. Incoherent bremsstrahlung can also occur with a diamond radiator when an electron recoils against one particular nucleus(or electron). The coherent process results in a "coherent" peak and additional secondary peaks in the photon energy spectrum.

The orientation of the diamond radiator can be modified to produce a coherent peak energy up to the energy of the photon beam and to adjust the degree or direction of linear polarization. A 9 GeV primary peak with a maximum degree of polarization of around 40% was found to be optimal for GlueX. Data is typically taken in two pairs of perpendicular polarization directions in order to control for instrumental acceptance effects: $\{0°, 90°\}$ and $\{45°, 135°\}$ pairs.

The beam of bremsstrahlung photons are then passed through a collimator to increase the degree of linear polarization. It is able to do this due to the fact that incoherently produced photons have a wider angular spread compared to coherently produced photons. The collimator is made of a lead block with 3.4 mm and 5.0 mm openings. The collimator is placed 75 meters downstream from the radiator. The 50 μm diamond radiator can be swapped with a 30 μm aluminum radiator, which

26
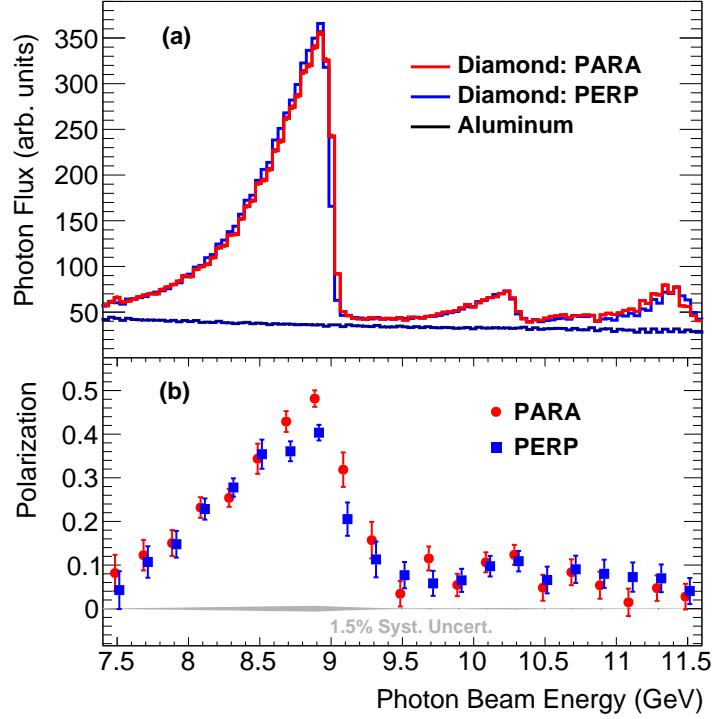
Figure 2.3: (a) Photon beam intensity vs beam energy as measured by the pair spectrometer.(b) Photon Beam polarization vs beam energy as measured by the triplet polarimeter. The flux and polarization spectra are shown for 0 (PARA) and 90 (PERP) degree orientations [44]. 0 (PARA) and 90 (PERP) degrees correspond to a particular pair of orthogonal polarization orientations.

only produces incoherent bremsstrahlung. Fig. 2.3 shows how the beam intensity and degree of polarization vary as a function of beam energy.

2.2.2 Measuring the Photon Flux, Energy and Polarization

Measuring Photon Energy. The tagger system consists of a dipole magnet, the tagger hodoscope (TAGH), and the tagger microscope (TAGM). Figure 2.4 shows a schematic of the system. The magnet deflects the scattered electrons from the bremsstrahlung process into the two tagging systems where the radius of curvature is directly proportional to their momenta. Scintillators are placed at varying radii to intercept the bent electrons. The bremsstrahlung photons are "tagged" by these recoiled electrons. Higher position resolution corresponds to higher energy resolution of the scattered electrons, which leads to higher energy resolution for the tagged photon. Electrons that did not interact with the radiator are sent to the beam dump.

The TAGM consists of an array of scintillating fibers. For a 12 GeV beam, the TAGM system measures energies in the coherent peak from 8.2-9.2 GeV and provides an energy resolution of around

27
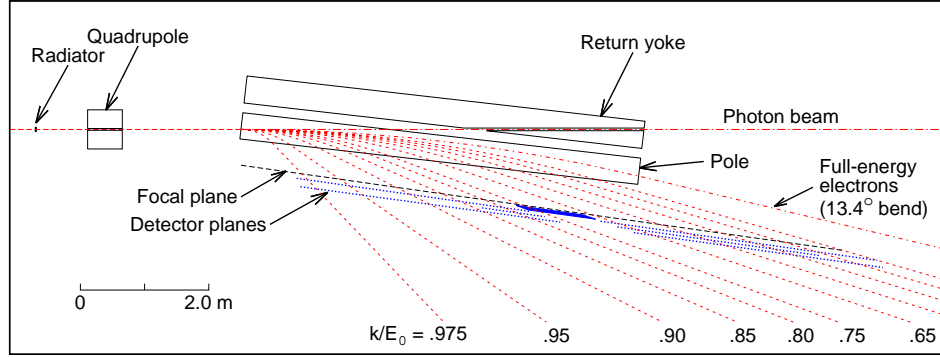
Figure 2.4: Schematic of the tagger system. The path of the electrons (incident beam and the scattered electrons) are shown as red dashed lines. The resulting photon beam is depicted as a red dash-dotted line. The TAGH and TAGM focal plane detectors are shown in blue, with the denser portion representing the TAGM [44].

12 MeV. The TAGH system consists of scintillator counters that are read out by photomultipliers tubes. These counters have coarser spacing than the TAGM scintillating fibers but for a 12 GeV beam, it measures energies from around 3-12 GeV, excluding the coherent peak region. Most of the counters below 5.5 GeV were off for the majority of the run period. The energy resolution of the TAGH is between 10-30 MeV. The timing resolution of both the TAGM and the TAGH is around 200 ps. This temporal resolution is enough to determine which 4 ns beam bunch the tagged photon belongs to.

Measuring Photon Flux.   The photon beam is passed through a thin 75 μm beryllium foil after collimation. A small fraction of the photons pair produce e^+e^- pairs off the beryllium nuclei. Another small fraction pair produce off the atomic electron, which will be described in the next section for photon polarization measurements. The recoil of the nucleus is negligible. The produced pairs then travel to the Pair Spectrometer (PS) system, which consists of a 1.8 T dipole magnet that deflects the charged pairs to the set of fine and coarse grain scintillator arrays of the pair spectrometer system [46].

Figure 2.5 shows a schematic of the Pair Spectrometer system. PS-A and PS-B are high-resolution hodoscopes that consist of stacked scintillator tiles that are read out by silicon photomultipliers connected to wavelength-shifting fibers. PSC-A and PSC-B are coarse-grained counters and are read out by photomultiplier tubes. A coincidence in the PSC is used to trigger the fine-grained PS for the actual energy measurement. This reduces backgrounds from $e^{+/-}$ interactions inside
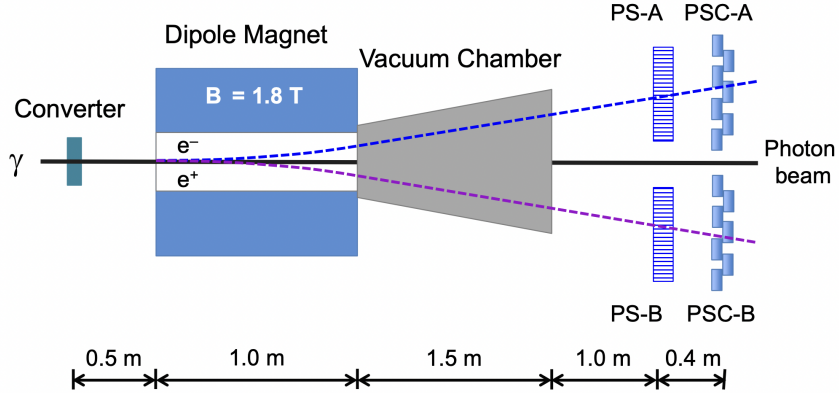
Figure 2.5: Schematic of the pair spectrometer system [46].

the magnet pole edges. The fraction of pair production conversions is dependent on the thickness of the beryllium foil and the efficiency and acceptance of the PS detector. The efficiency of the Pair Spectrometer is determined in special low-current TAC runs. The total absorption counter, TAC, is a lead glass calorimeter with a height and width of 20 cm and a length of 40 cm [47]. The TAC can be inserted immediately upstream of the photon beam dump and is sensitive to nearly the full photon beam energy spectrum. During the TAC runs, data is taken in both the TAC and PS systems, which allows for the determination of an absolute flux calibration. The PS system has 120 ps timing resolution and is used as a trigger for the polarization measurement system, discussed next.

Measuring Photon Polarization. The beam photons can also interact with an atomic electron of the beryllium foil in a process known as "triplet photoproduction" [48]. A polarized photon beam can interact with the electric field of an atomic electron in the target and pair produce e^+e^- pairs. The energy of the recoil (triplet) atomic electron is small but large enough to be measured, allowing it to obtain a large polar scattering angle, and is nearly independent of the incident photon's energy. The pair-produced leptons are higher energy and will be detected in the PS system for triggering. The cross section for triplet production is given by

$$\sigma_{\text{triplet}} = \sigma_0(1 - P\Sigma\cos(2\phi)) \tag{2.1}$$

where σ_0 is the unpolarized cross section, P is the degree of polarization, Σ is the beam asymmetry of the process (which can be determined to high precision through QED calculations) and ϕ is the

29

azimuthal angle of the recoiling electron's trajectory. By measuring the angular distribution of recoiled electrons from triplet production, the degree of polarization can be determined.

The Triplet Polarimeter (TPOL) is a 1 mm-thick silicon strip detector that is azimuthally segmented into 30 bins. The yields in each bin can be fit to an equation similar to the form of the equation above to determine the degree of polarization. The PS system measures the pair produced e^+e^- pair while the TPOL detects the slow recoiling atomic electron. See Ref. [49] for more details.

2.3   GlueX Spectrometer

A description of the GlueX spectrometer will be given for the GlueX-I run period. The beam photons enter the GlueX spectrometer, which surrounds a liquid hydrogen (LH$_2$) target. The spectrometer is instrumented in the barrel and the forward regions. The barrel region contains the central drift chamber (CDC) and the barrel calorimeter (BCAL) which are both cylindrical structures built concentrically around the target, in the order mentioned. In the forward direction is the forward drift chamber (FDC), the time-of-flight detector (TOF), and the forward calorimeter (FCAL) which is also built outward in the sequence mentioned. These systems allow for the reconstruction and identification of charged and neutral particles. A diagram of the spectrometer can be found in Figure 2.6.

2.3.1   Solenoid

The photon beam travels along the axis of a superconducting solenoid. The solenoid is capable of producing a 2T field at the nominal current of 1350 A. The magnet was first constructed for the LASS experiment at SLAC and has since been refurbished and modified for GlueX. The magnet consists of four superconducting coils and is constructed from a superconducting composite of niobium-titanium filaments in a copper substrate, each cooled with a cryostat. A map of the magnetic field is made with a 2D field calculator [44] and was compared to in-situ measurements. The field deviation from the calculated field along the solenoid axis does not exceed 0.2%. A maximum deviation of 1.5% exists downstream at large radii. The typical deviations are smaller than the charged particle track momentum resolution of the GlueX spectrometer, which is larger than 1% and is dominated by multiple scattering and the spatial resolution of position measurements.
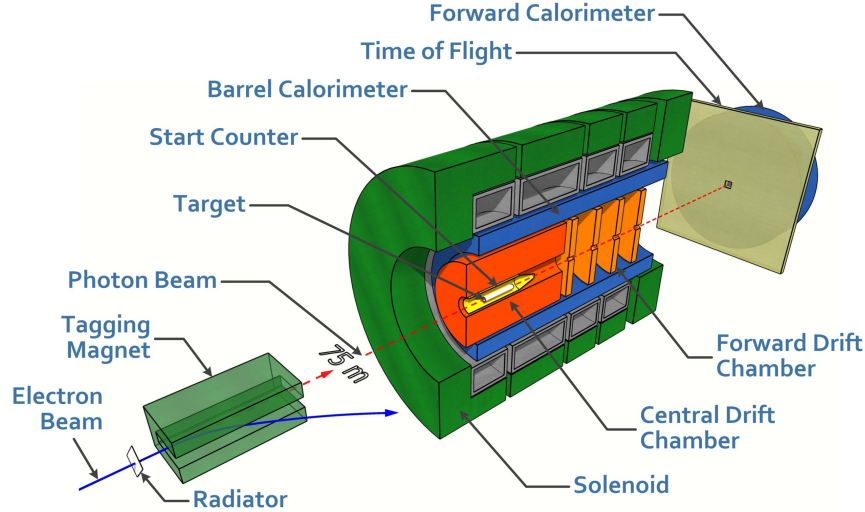
Figure 2.6: GlueX spectrometer and the Hall D beamline [44].

2.3.2 Target and the Start Counter

Liquid hydrogen is used as a target and is contained within a target cell that is 30 cm long with a diameter of roughly 1.6 cm. The target cell is contained within a vacuum chamber and is kept around 18K and 18 psi. Empty target runs are used for systematic studies.

The target is enveloped by the start counter (SC) which consists of 30 tapering plastic scintillator paddles. Figure 2.7 shows a schematic of the start counter enveloping the target cell. The tapering on the downstream end increases the angular coverage at larger boosts, covering around 90% of the solid angle for particles originating from the center of the target. The energy deposition in the paddle, dE/dx, can be used in conjunction with the flight time for charged particle identification. Figure 2.7 shows the dE/dx vs p for the SC. The curved band is from protons, whereas the horizontal band is from e, π, and K. There is good separation between protons and π for momenta less than 0.9 GeV/c. Silicon photomultipliers are used for readout, as they are largely unaffected by large magnetic fields. As the name suggests, this system gives a measure of the primary interaction time with a resolution in the range of 500-800 ps (FWHM) making it effective at determining the bunch of the beam electrons an event belongs to. The resolution of the SC does not contribute to the resolution of the flight time, as it mainly determines which 4ns beam bucket initiated a reaction. See Ref. [50] for more details about the start counter.

(a)   (b)
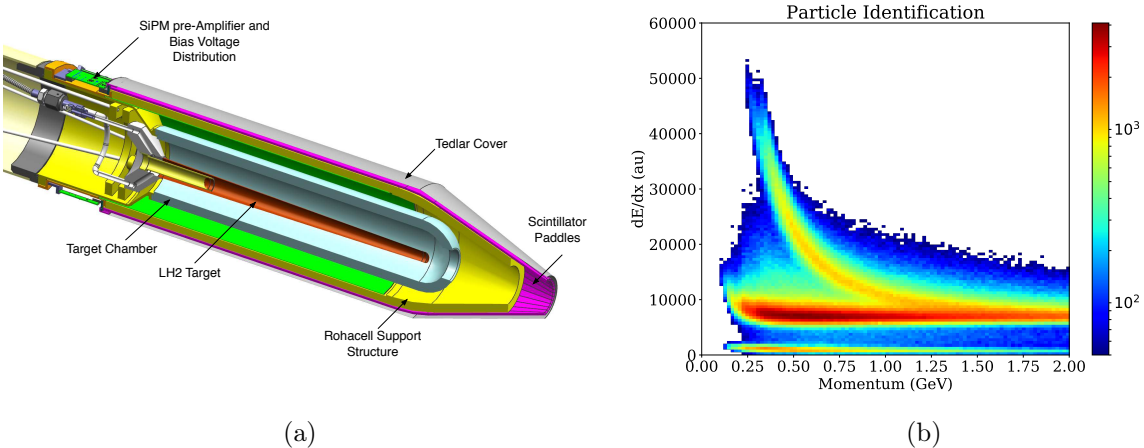
Figure 2.7: (a) Start counter and the target cell. (b) dE/dx vs p for the start counter. Source [44].

2.3.3   Tracking System

Charged particles move in a helix inside a magnetic field, such that the radius of curvature is proportional to the momentum, charge, and field strength. Tracking detectors measure the path the track takes and therefore give access to the momentum. GlueX employs two drift chambers to do charged particle tracking, one in the barrel section and the other in the forward region.

Central Drift Chamber (CDC).   The CDC is a system of 3522 straw tubes that are held at +2125V between their cylindrical Mylar shell and their central 20 μm gold-plated tungsten anode wire. The central wire is held under tension to prevent sagging due to its own weight. The tubes are filled with a 50:50 mixture of carbon dioxide and argon. Each straw tube is 1.5 m long with a diameter of 1.6 cm. The straw tubes are organized into 7 super layers, each containing 4 layers. Layers 1,4, and 7 are the axial straws and are oriented parallel to the beam and the rest are alternately oriented at stereo angles of ±6°. The CDC has an active volume with an inner radius from 10 cm up to an outer radius of 56 cm, corresponding to polar angles between 6 and 168 degrees.

A charged particle passing through one of the straw tubes would leave an ionization signal consisting of electron-ion pairs. The electrons are accelerated towards the anode wire, which subsequently frees additional electrons due to the extra energy which it picks up along the way. This electrical avalanche produces a much stronger signal that is collected by the anode wire. The signal gets sent through readout cables to preamplifiers, which produce the final output signal. If one assumes some propagation model, the distance of the closest approach, DOCA, for an ionization

32
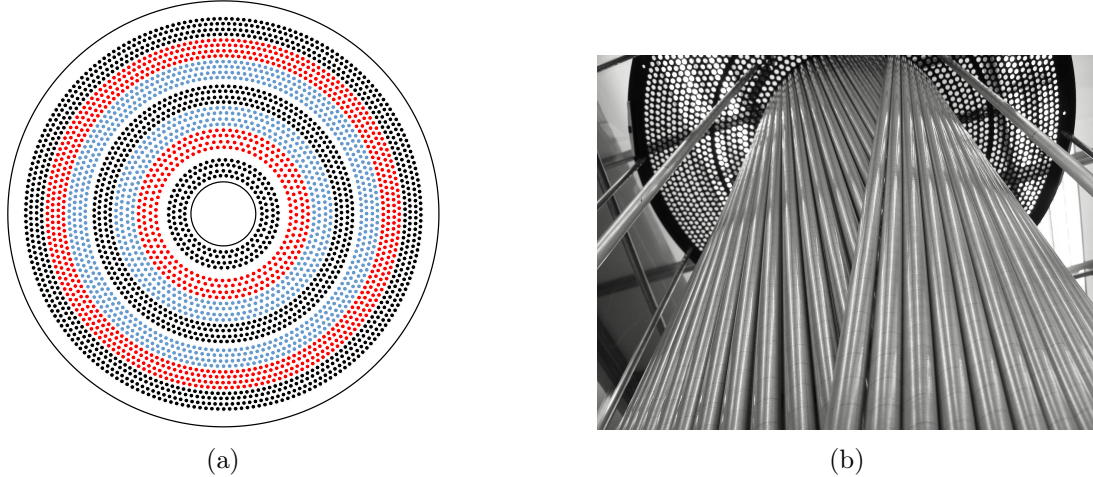
Figure 2.8: (a) Schematic of the CDC straw positions. The axial straws are shown in black. The +6 degree stereo straws are shown in red. The -6 degree stereo straws are shown in blue. [51] (b) Picture of a partially completed layer of the CDC stereo straws covering a layer of stereo straws in the opposite angle [44].

cluster can be determined and thus a cylindrical shell of possible locations can be defined. With the DOCA from multiple straws, a track can be reconstructed.

The CDC has optimal coverage of polar angles between 29 and 132 degrees. The CDC has a DOCA-dependent hit efficiency and position resolution. The hit efficiency is >95% for DOCA less than 0.7 cm. The position resolution reaches down to around $70\mu m$ for DOCA greater than 3.5 mm [51]. The CDC can also provide energy deposition information (dE/dx) which is useful in particle identification. Ionization loss is given by a Bethe-Bloch type formula, which describes the energy loss as a function of the particle's mass. The dE/dx in the CDC is useful in separating protons and π^+ up to around 1 GeV. More information about the CDC can be found in Ref. [51].

Forward Drift Chamber. The FDC is a cathode strip chamber that is comprised of 4 packages, 1 m in diameter. Each package consists of 6 chambers. Each chamber contains a wire plane sandwiched between two grounded cathode planes spaced 5 mm apart from each other. A wire plane is a system of alternating sense (20 μm diameter) and field wires (80 μm diameter) placed 5 mm apart. The sense wires are held at +2200V and are connected to readout electronics. The field wires are set to a negative potential of 0.5 kV and are used to maintain the cylindrical symmetry of the field around the sense wires. A 40% argon / 60% carbon dioxide gas mixture fills the chamber.
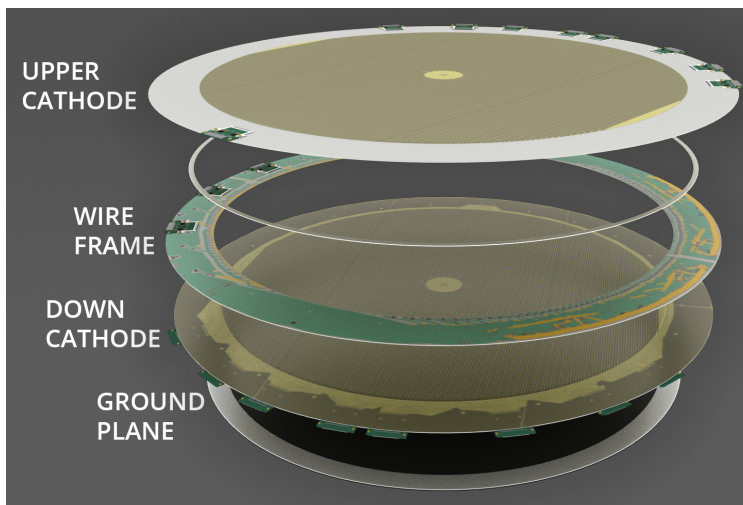
Figure 2.9: One cell of the forward drift chamber [44].

The cathodes are made from $2\mu m$ thick copper strips. One plane is rotated by 75 degrees relative to the anode wires whereas the other is rotated by 105 degrees. The basic operating principle is the same as the CDC, where an ionization signal produces a measurable signal by creating an electrical avalanche. Here, the pulse height, from the induced charge, along these copper strips are measured, and factoring in the timing measurement of the sense wires, it is possible to determine a 3D position in each cell.

The FDC is able to measure tracks with polar angles between 1 and 10 degrees with all chambers with partial coverage up to 20 degrees. The hit position resolution of the FDC is between 140 and 240 μm depending on the distance to a wire. See Ref. [52][53] for more information.

Track Reconstruction. The goal now is to reconstruct all tracks given the information provided by the drift chambers in order to extract particle momenta and charges. Reconstruction occurs in a series of stages.

First Stage: Hits in adjacent CDC straws and FDC chambers are linked to form track segments. Multiple track segments in each subsystem are then linked together to form CDC and FDC track candidates, assuming a simple helical model. Candidates that originate from within the target region and pass through the FDC and CDC between 5 and 20 degrees in polar angle are also linked together.

Second Stage: A Kalman Filter [54] is used to estimate charged track parameters at the position of the closest approach of a track to the beam line. The process starts by incorporating hits that are

34

furthest from the beam and incrementally working inward. At this stage, energy loss and multiple scattering are included according to a map of the magnetic field. Tracks are assumed to be from a pion except for tracks with momentum less than 0.9 GeV/c (which are assumed to be a proton).

Third Stage: Fitted tracks are matched to either the SC, TOF, BCAL, or FCAL so that the start time for a given track, and thus the drift time to each wire, can be determined. The drift times are then incorporated in another, more refined, fit using a Kalman filter again. At this stage, various particle hypotheses are also considered, i.e. $\{e^{\pm}, \pi^{\pm}, K^{\pm}, p^{\pm}\}$.

Performance of the Tracking System. The momentum resolution can be parameterized as follows

$$\frac{\sigma_p}{p} = \frac{1}{B\sin\theta}\left(\frac{a}{\beta} \oplus bp\right) \tag{2.2}$$

where θ is the polar angle, p is the momentum, B is the magnetic field strength, a and b are parameters representing the strength of multiple scattering and uncertainty in position measurements respectively. Figure 2.10 shows the momentum and angular resolution of protons and pions as a function of momentum and polar angle. Momentum resolution is optimal for pions with momenta around 1 GeV/c and for protons around 1.5 GeV/c. Angular resolution improves as track momentum increases.

The target walls and the exit window of the target vacuum chamber provide a way to measure the vertex resolution of the tracking system. Pairs of tracks during empty target runs can be used to reconstruct the location of these features in the target system. The z-position resolution is estimated to be 3 mm.

2.3.4 Calorimetry

The goal of the calorimetry systems is to measure the energy and position of electromagnetic showers to reconstruct neutral particles like the photon. High-energy photons lose energy primarily through e^+e^- pair production. The resulting high-energy electrons and positrons mainly lose energy via bremsstrahlung. This cascade is known as an electromagnetic shower. The characteristic length that a shower loses 1-1/e $\approx$ 63% of its energy is known as the radiation length. The BCAL and FCAL employ different technologies to infer the total energy of a shower. The BCAL uses scintillating fibers that emit a light signal due to the passage of charged particles (electrons/positrons). The FCAL produces a light signal via Cherenkov radiation, which is a result of a particle traveling faster
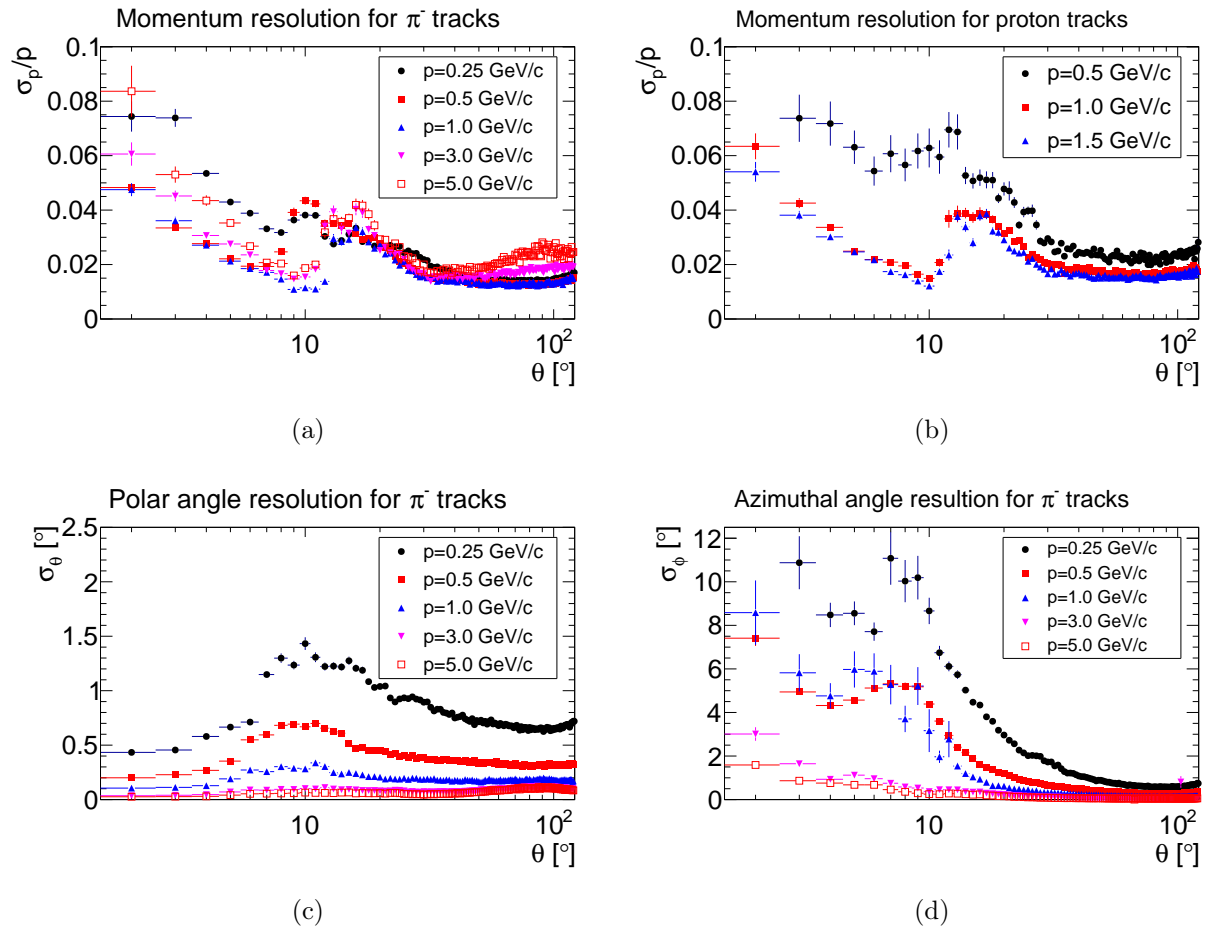
Figure 2.10: Momentum resolution as a function of angle and magnitude for (a) pion (b) proton. (c) Polar (d) Azimuthal angular resolution as a function of angle and magnitude for a charged pion [44].
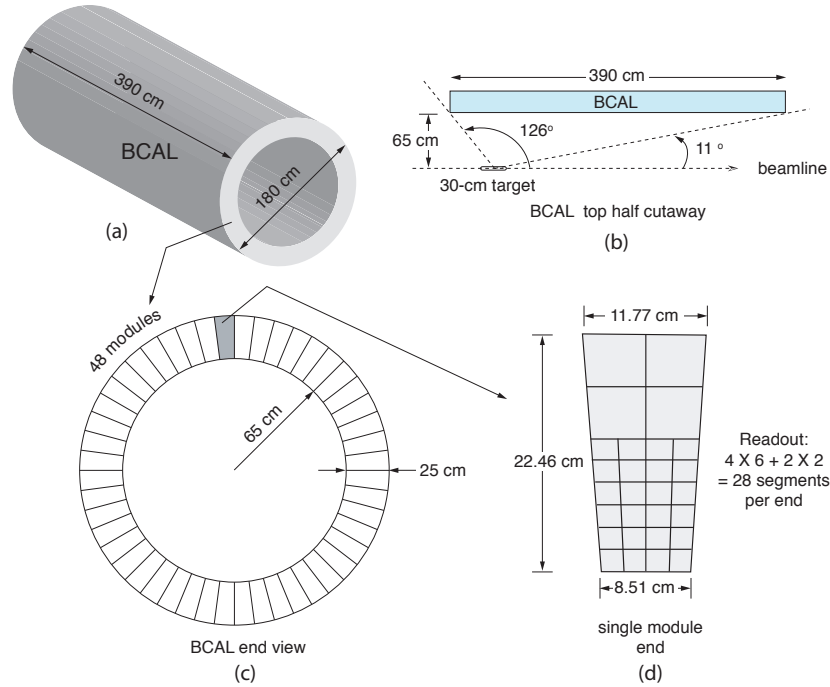
Figure 2.11: Barrel Calorimeter [55].

than the speed of light in a medium. The light signal can then be amplified and collected. Below, I first introduce the specifications of the calorimeter systems and then discuss their performance.

Barrel Calorimeter. The BCAL is a sampling calorimeter that is formed from a fused matrix of 1 mm diameter scintillating fibers and stacked 0.5 mm thick lead plates. The fibers at slotted into half cylinder-shaped grooves cut into the lead plates. There are 48 modules segmented in azimuthal angle, ϕ, and 10 times in the radial, r, direction. Each module has approximately 185 layers and 15,000 fibers. There are silicon photomultipliers on both sides of the scintillating fibers, allowing for position determination along the length by measuring the timing difference in the scintillation light signal. The BCAL covers polar angles between 11 and 126 degrees for photons originating from the target. There is complete azimuthal coverage. Figure 2.11 shows the specifications.

The BCAL has a thickness of 15.3 radiation lengths for particles traversing normal to the calorimeter face and up to 67 radiation lengths at shallower angles. Readout is done in a 1,2,3,4 fashion in which layer 1 is read out, the next 2 layers are read out together, the next 3 layers are read out together, and the final 4 layers are read out also together. This scheme attempts to take into account a typical electromagnetic shower's deposition profile.
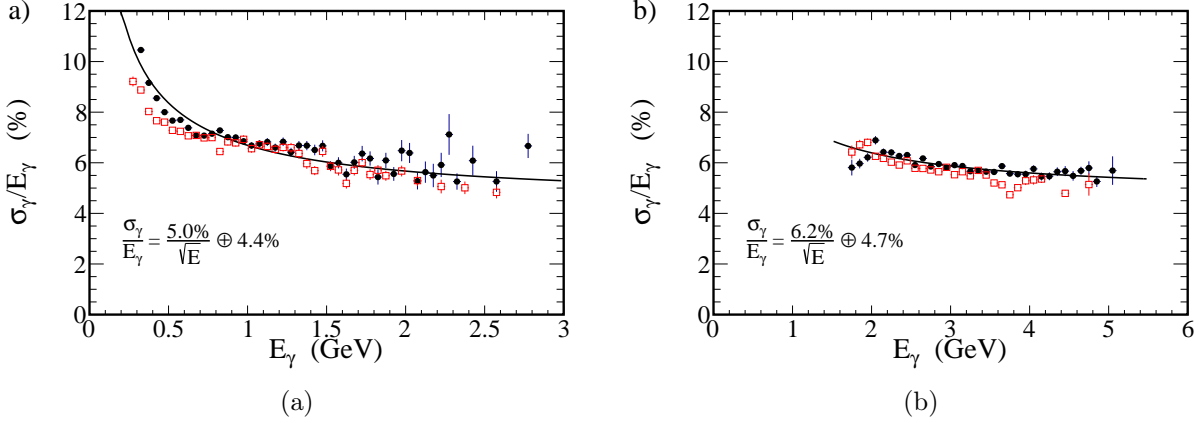
Figure 2.12: Single-photon energy resolution, σ_E/E, vs E of (a) BCAL (b) FCAL. Solid black circles are data, open red squares are from simulation, and the curve is from a fit that includes the stochastic and constant terms. More details on how the resolution was obtained can be found in [44].

Forward Calorimeter.   The FCAL is a homogeneous calorimeter consisting of 2800 lead glass blocks stacked in a single layer taking on a circular pattern of 2.4 m in diameter. Each block has dimensions $4 \times 4 \times 45$ cm. Cherenkov light produced during an electromagnetic shower is measured by a photo-multiplier attached to the back of the block. The amount of light is proportional to the energy deposited in the block, and each shower can spread out to nearby blocks. Shower profiles and energies can then be determined given some clustering scheme. The shower profile contains information on particle species, e.g. photons produce Gaussian-like shower shapes whereas charged pions usually do not. Most of the PMTs and the lead glass blocks were refurbished from the decommissioned E852 experiment at Brookhaven National Laboratory [56] and from the RadPhi experiment at JLab [57]. More information about the FCAL can be found in Ref. [58].

There is a square hole centered on the beamline to allow the beam particles to pass. Even though the FCAL is several meters downstream of the solenoid, stray fields can still affect the performance of the PMTs' magnetically sensitive photocathode. A dual layer of soft iron and mu-metal is used to attenuate these residual fields. The FCAL measures photons from 100 MeV up to a few GeV from polar angles of 1 degree up to 11 degrees.

Performance of the Calorimetry System.   The energy resolution is typically parameterized as
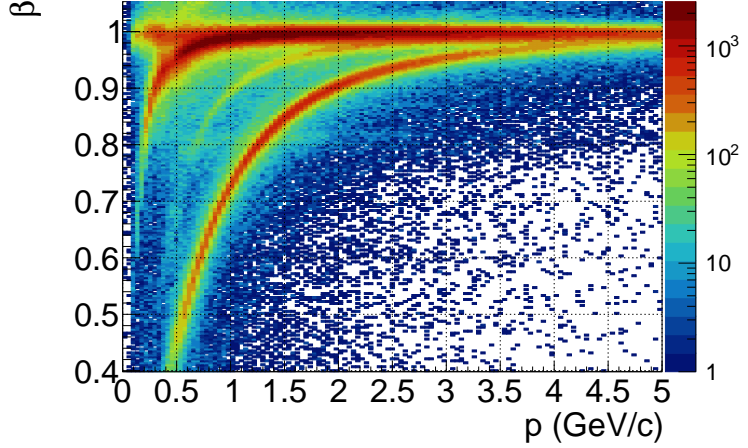
Figure 2.13: (a) Picture of the time-of-flight detector. (b) Velocity, β of positively charged tracks, vs p [44].

$$\frac{\sigma_E}{E} = \frac{a}{\sqrt{E}} \oplus \frac{b}{E} \oplus c \qquad (2.3)$$

where a describes the stochastic nature of the number of photons generated, b parameterizes the electrical noise, and c accounts for calibration and leakage. The energy resolution of the calorimeters was determined by selecting clean samples of $\eta \to 2\gamma$ and $\pi^0 \to 2\gamma$ where the daughter particles have approximately the same energy. The single-photon energy can then be related to the resolution of the invariant mass distributions and the opening angle resolution. Gaussian fits are performed to extract the η and π^0 mass resolutions. The resulting single-photon resolutions agree between the two channels and the fractional resolution, σ_E/E, vs E for the BCAL and FCAL are shown in Figure 2.12.

2.3.5 Time-of-Flight

The time-of-flight, TOF, detector is just upstream of the FCAL. It is made of two layers of 46 scintillating paddles with PMTs on each end to allow determination of position along the length. The majority of the paddles are 252 cm long, 2.54 cm thick, and 6 cm wide. Some paddles are made shorter to create room for a 12x12cm^2 aperture along the beamline for the beam to pass through. The layers are rotated 90° relative to each other. The timing resolution of the paddles is around 100 ps.

Figure 2.13 shows a picture of the TOF detector on the left and on the right is a picture representing its particle identification, PID, capability plotting the particle velocity, β, vs momentum, p. There are 4 clear curves representing electrons, pions, kaons, and protons in order of how closely the curve hugs the top-left corner. The TOF detector is capable of π/K separation up to 2 GeV/c and π^+/proton separation up to 4.5 GeV/c.

2.3.6 Triggering and Data Acquisition

Writing out all the produced data is impractical and wasteful, as not all events are interesting(i.e. cosmics). The set of criteria that is required for an event to be written out is known as the trigger conditions. Signals from the detector enter the front-end crates and are digitized by flash analog-to-digital converters, fADC. The Tagger, SC, FDC, BCAL, SC, and TOF detectors all use time-to-digital converters, TDC, for more precise timing measurements. The CDC and FCAL only use fADCs. The trigger has to operate quickly to make these decisions and accept hadronic events with high probability. fADCs help with the former requirement as they allow readout and digitization to occur independently.

GlueX uses two main types of triggers. The first is a trigger that looks for a coincidence of hits in the two arms of the PS detector to identify e^+e^- pairs. The second is a physics trigger that is based on the energies registered in the calorimeters and is defined as

$$1) \quad 2 \cdot E_{\text{FCAL}} + E_{\text{BCAL}} > 1 \text{ GeV and } E_{\text{FCAL}} > 0 \text{ GeV}$$

$$2) \quad E_{\text{BCAL}} > 1.2 \text{ GeV}$$

Alongside these triggers, there is also a random trigger that aims to determine experimental background signals which can then be used in Monte Carlo. Additionally, there are triggers for LED monitoring systems.

The events that pass the trigger enter the data acquisition system. The triggered signals from the front-end crates are sent to readout controllers (ROC) and are subsequently shuttled to data concentrators (DC) where partial events are reconstructed from a subset of crates. These partial events are sent to the event builder (EB) to construct complete events, which are then written to local data storage by the event recorder (ER). Figure 2.14 shows a schematic of the DAQ system. All DAQ nodes are connected to a 40 Gb Ethernet switch and a 56 Gb Infiniband switch. The Ethernet network is exclusively used for the acquisition of data, whereas the Infiniband network is
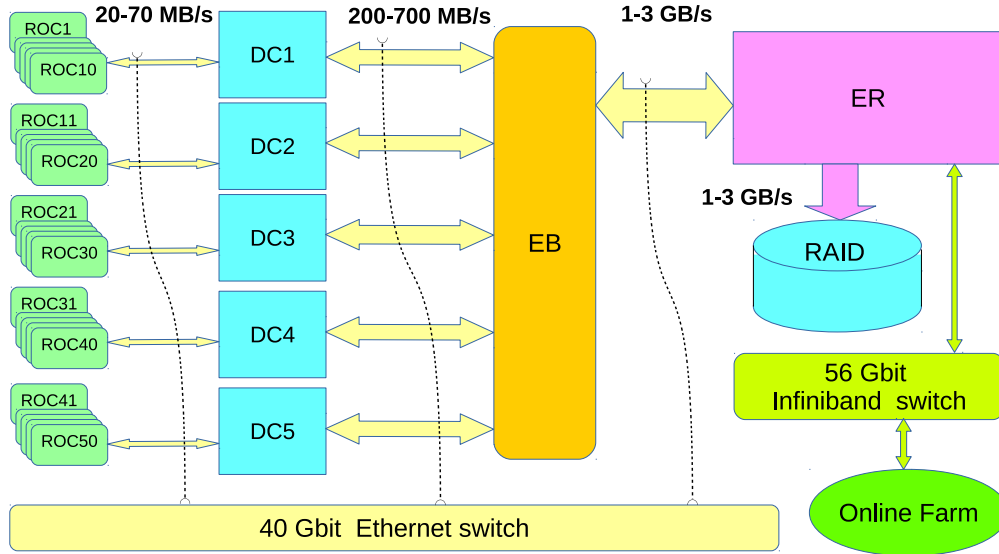
Figure 2.14: Data acquisition system [44].

used to transfer data to the monitoring system. The monitoring system processes a small fraction of the data stream, about 10% for low-level occupancy plots, and about 2% are fully reconstructed for high-level analysis plots. This data stream is also used for calibrations.

2.4   Monte Carlo Simulations

Events of interest are generated with an event generator that produces 4-vectors of the reaction. The event specification is then sent to a full simulation of the GlueX detector, performed with the GEANT4 framework, which tracks particles through the experimental setup and records deposition and timing information from the active elements. The experimental conditions, i.e. beam polarization/intensity and magnetic field map, are run-dependent. The simulations retrieve this information from the calibrations database which hosts all time-dependent geometry, magnetic field, and calibration data. These simulated event signals are then passed through a smearing step that produces signals that are faithful representations of real detector outputs. Some of the steps included in the smearing are to apply corrections to the hits that include detector inefficiencies and resolution. Backgrounds sampled by the random trigger are also folded in at this time. From here, the simulated detector response can be reconstructed in the same fashion as the data. The final result is in a reconstructed event storage, or REST, format. Figure 2.15 shows a schematic of the Monte Carlo simulation framework.

41
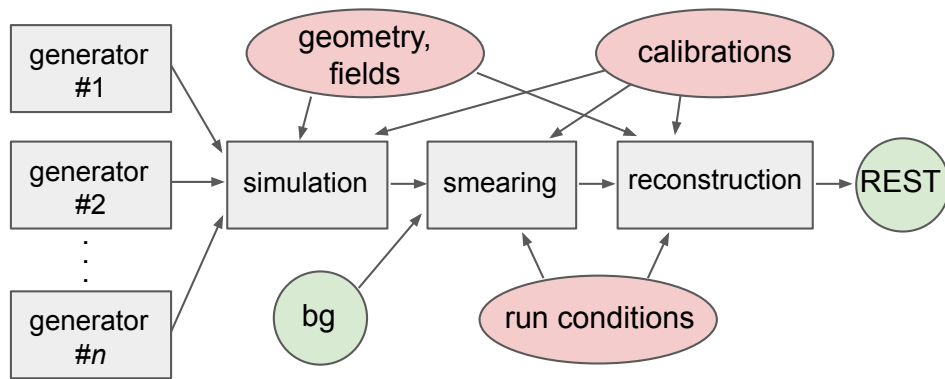
Figure 2.15: Monte Carlo simulation framework [44]. Run-dependent calibrations and conditions provide a configuration for simulation, smearing, and reconstruction. Backgrounds from the random trigger, bg, are overlaid on simulated events.

CHAPTER 3

EVENT RECONSTRUCTION AND MONTE CARLO SIMULATIONS

3.1 Reaction of Interest

The reaction of interest in this dissertation is $\gamma p \to \eta \pi^0 p \to 4\gamma p$ and a diagram of it can be seen in Fig. 3.1. An intermediate resonance, X, is produced via t-channel exchange between the beam photon and the target proton. At GlueX center-of-mass energies, t-channel exchange dominates the cross section [1]. X subsequently decays to a π^0 and η which both decay to a pair of photons. The target proton recoils due to the momentum transferred to it. All final state particles are measured.

First, the datasets used in this dissertation will be introduced. Next, the selections that are used to select a set of final state particles that correspond to this reaction are presented. Finally, techniques to reduce backgrounds from other reactions will be shown.
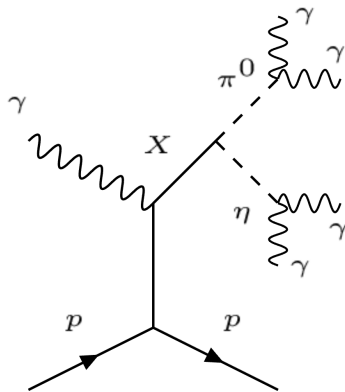
Figure 3.1: Diagram of the reaction $\gamma p \to \eta \pi^0 p \to 4\gamma p$.

3.2 Data Collected and Simulated

GlueX data was taken in 2 phases. Each phase is taken in a series of run periods each containing a set of ≈ 2 hour-long runs. The Phase-I data will be used in this dissertation, which was taken over three run periods: spring 2017, Spring 2018, and Fall 2018 runs. During these run periods, a total of 49.6, 146, and 77.5 billion triggers were acquired in those run periods, respectively. This roughly corresponds to a 1:3:2 ratio.

The polarization of the photon beam is typically cycled between $\phi = 0$, 45, 90, and -45 degrees using a *coordinate system* in which the z-axis points downstream along the beamline, and the y-axis is perpendicular to the floor of the experimental hall. The right-hand coordinate system then defines the x-axis. The GlueX detector is designed to be azimuthally, ϕ, symmetric but deviations can exist, e.g. from extra material from cables and electronics. For some measurements, these potential ϕ-dependent detector effects can be canceled by analyzing perpendicular pairs of the polarized datasets, i.e. $0°/90°$ and $45°/-45°$. Further details can be found in the beam asymmetry analysis in Chapter 5.

The process to reconstruct physics events, described in Chapter 2, is performed centrally and released in *reconstruction launches*. At this stage, each event has a set of reconstructed charged and neutral particle hypotheses. An *analysis launch* can then be performed where events are first selected given that it can support a given reaction topology (i.e. having the minimum number of charged/neutral hypotheses) through loose timing and kinematic selections. All potential combinations are then formed. For this analysis, events are required to have at least 4 photons and at least one charged track (up to 3) in the final state.

3.2.1 Monte Carlo Data Samples

Monte Carlo simulations are used to numerically determine the efficiency of the detector and to quantify the performance of event selections. The momentum transfer distribution in MC must re-

Run Period	Run Range	Version Set	Analysis Version Set
Spring 2017	30274-31057	recon-2017_01-ver03_31.xml	analysis-2017_01-ver51.xml
Spring 2018	40856-42577	recon-2018_01-ver02_22.xml	analysis-2018_01-ver02.xml
Fall 2018	50677-51768	recon-2018_08-ver02_21.xml	analysis-2018_08-ver02.xml

Table 3.1: Phase space simulation specifications for the three different run periods of the GlueX Phase-I dataset.

semble the distribution seen in the data as the formulation of the amplitudes used in the partial wave analysis of the $a_2(1320)$ meson does not contain terms for the description of the t-channel exchange process, see Section 4.4.1. Therefore, simulations should be made such that the t-distributions are similar in shape between data and MC. This can be done in various ways, but a simple approach is to formulate an accept-reject scheme.

Simulations are generated for each run period of the Phase-I dataset with the specifications seen in Table 3.1. This ensures that the data and the Monte Carlo are reconstructed in the same fashion. Events are produced with the `gen_amp` generator which uses a simplified model based on an exponential behavior for the t-dependence which is not sufficient to describe the distribution seen in the data. These events are produced flat in $\eta\pi$ mass up to 3 GeV with a t-slope of 1[1]. All other angular variables, including polarization, are uniform. This particular t-slope was chosen such that the acceptance corrected t-distribution of the GlueX data falls slightly faster. Choosing a reasonable t-slope to generate the simulations with will determine the efficiency of the accept-reject algorithm, which turns out to be ∼40% in this setup.

An accept-reject algorithm is implemented to sample the simulations after the `mcsmear` step on the `hddm` files, before the analysis trees are constructed. The probability, p, of accepting an event with momentum transfer, t, is given by

$$p(t) = \frac{N * Q_{\text{acc. corr. data}}(t)}{Q_{\text{MC}}(t)} \tag{3.1}$$

where $Q_{MC}(t)$ is the probability density function, pdf, of t for the Monte-Carlo sample described in the previous paragraph, $Q_{acc.corr.data}(t)$ is the pdf of t for the acceptance corrected GlueX data, and N is the smallest scaling factor such that $Q_{MC}(t)$ is (almost) always greater than $Q_{acc.corr.data}(t)$. Applying this procedure requires the knowledge of the acceptance, which has to be determined beforehand. This filtered data is then used to construct analysis trees, where the reconstructed events will be put through the same analysis procedure as the data. Figure 3.2 shows the $Q_{MC}(t)$, $Q_{acc.corr.data}(t)$, and the resulting acceptance function for these datasets.

3.2.2 Initial Selections

The event is then passed through a series of selections that can support the reaction of interest. This is done by the `ReactonFilter`[59] plugin. Events are limited to having up to 3 charged tracks and up to 15 showers per event. Timing and dE/dx (rate of energy loss in a drift chamber)

---

[1]`gen_amp` generator with the flags `-f -u 3 -t 1`
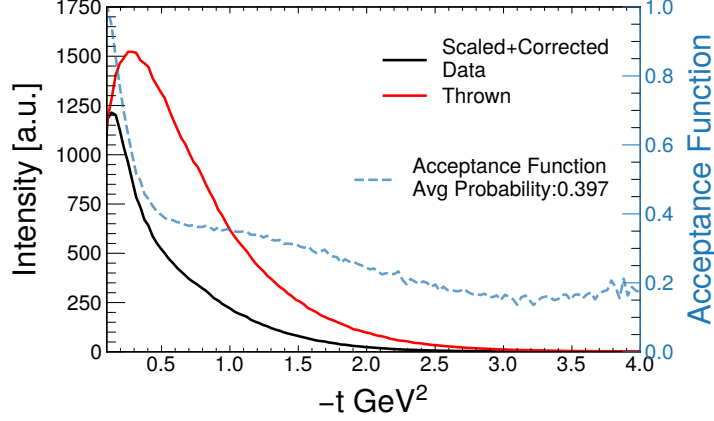
Figure 3.2: (Red) is t-distribution of the generated MC, $Q_{MC}(t)$. (Black) is the scaled and corrected GlueX data, $Q_{acc.corr.data}(t)$. (Blue) show the acceptance function.

information will be used to select a good proton candidate. Timing information will be used to select good photon candidates. We label the final state photons such that the π^0 and η candidates are formed from $\gamma_1\gamma_2$ and $\gamma_3\gamma_4$ photon pairs respectively. An additional selection is made to loosely enforce exclusivity as all particles are measured. The selections are:

- Minimum final state photon energy > 100 MeV

- γ $|\Delta t|$ BCAL/RF < 1.5 ns

- γ $|\Delta t|$ FCAL/RF < 2.5 ns

- proton $|\Delta t|$ BCAL/RF < 1.0 ns

- proton $|\Delta t|$ TOF/RF < 0.6 ns

- proton $|\Delta t|$ FCAL/RF < 2.0 ns

- proton $|\Delta t|$ SC/RF < 2.5 ns

- dE/dx in the central drift chamber consistent with proton hypothesis

- $0.08 <\ M(\pi^0 = \gamma_1\gamma_2)\ < 0.19$ GeV

- $0.35 <\ M(\eta = \gamma_3\gamma_4)\ < 0.75$ GeV

- $|\text{MMSq}| < 0.1$ GeV^2

where Δt is the difference between observed and expected particle arrival time to a subsystem. The observed particle arrival time is the elapsed time between some start time, which is the expected

arrival time of the photon bunch to the center of the target, and some stop time, determined by the subsystem of interest. The expected particle arrival time is determined from the particle velocity (which assumes a particle hypothesis). These timing selections and dE/dx energy loss information provide a loose filter on particle identities. Missing mass squared is calculated as

$$\text{MMSq} = (P_{\gamma_{beam}} + P_{\text{target}} - \sum_{i=0}^{4} P_{\gamma_i} - P_{\text{recoil}})^2 \tag{3.2}$$

where *recoil* refers to the recoiled proton *target*.

3.2.3 Constructing combinations

Recall from the track reconstruction stage (Section 2.3.3), all charged particle identities are considered potential hypotheses. A positively/negatively charged particle can be a $\pi^{+/-}$, $K^{+/-}$, $e^{+/-}$, or a proton/antiproton.

Recall from the previous section, that each event can have up to 3 charged tracks and up to 15 showers. For each event, all possible combinations with a single charged track and two pairs of neutral showers are made. The two pairs of neutral showers are consistent with the mass of the π^0 and η, see Section 3.2.2. The exclusivity selections, which will be described later, are efficient in rejecting events with extra particles.

Tagged beam photons from 4 adjacent out-of-time beam bunches are included during the construction of possible combinations along with all in-time beam photons. These additional out-of-time beam bunches are kept for the *accidental subtraction* procedure that will be detailed in Section 3.3.1 which aims to statistically determine the contribution from the signal-generating photon.

A larger set of combinations are made by combining the set of tagged beam photons and the set of spectroscopic combinations such that each element of the new set has a single charged track, two pairs of neutral showers, and a single tagged beam photon.

3.2.4 Kinematic Fitting

So far, we have simply assembled all potential combinations of particle hypotheses that match our reaction of interest and have applied a set of loose selections. We can improve our measurements of the final state particle's four-momentum and reject backgrounds from other final states by including information of the GlueX detector's resolution and imposing physical constraints, such as four-momentum conservation, through *kinematic fitting*. Every combination is kinematically fitted, separately.

Let $\mathbf{y_{meas}}$ be our measured four-momenta, $\mathbf{y_{fit}}$ be the fitted four-momenta, $\mathbf{V}$ be the covariance matrix that encodes the detector resolution, and $\mathbf{F}$ which encodes the physics constraints. In this analysis, only the conservation of four-momentum is included. Then, we can define

$$\chi^2 = (\mathbf{y_{fit}} - \mathbf{y_{meas}})^T \mathbf{V^{-1}} (\mathbf{y_{fit}} - \mathbf{y}_{meas}) + 2\lambda^{\mathbf{T}}\mathbf{F} \tag{3.3}$$

as our metric to minimize. The first term attempts to improve our resolution, whereas the second enforces a reaction hypothesis by the use of Lagrange multipliers. Minimization is typically done as an iterative procedure. If the input variables are uncorrelated with Gaussian errors, then the resulting χ^2 values should be distributed as

$$f_{\mathrm{NDF}}(x) = \frac{x^{(\mathrm{NDF}/2-1)}}{2^{(\mathrm{NDF}/2)}\Gamma(\mathrm{NDF}/2)} e^{-x/2} \tag{3.4}$$

where NDF is the number of degrees of freedom. NDF can be calculated by

$$NDF = N_m - 3N + 4 + N_c \tag{3.5}$$

where the 4 is from the inclusion of conservation of four-momentum, N_c is the number of additional constraints, N is the number of particles, and $N_m \leq 3N$ is the number of measured particle properties [60]. Since this analysis does not include any extra constraints and measures all particles, we have NDF=4. An additional selection is now imposed requiring the kinematic fit to properly converge for each combo. In the end, every combination will have an associated χ^2 value. This dissertation will use kinematically fitted values unless otherwise stated. The same selections from 3.2.2 are re-applied using the improved momentum and vertex information.

3.2.5 Exact Dataset Specifications

The construction of combinations and handling of the kinematic fit is done by the `ReactionFilter` plugin. The trees used in this analysis only enforce conservation of four-momentum and are produced given the name `pi0eta__B4_M17_M7_Tree`. B represents the number of out-of-time beam bunches to include on either side of the prompt peak; 4 in this case. M refers to a flag to leave the masses unconstrained in the kinematic fit for the Geant PIDs η=17 and π^0=7. The corresponding reconstruction and analysis launches are tabulated in Table 3.2.

Run Period	Run Range	Analysis Version Set
Spring 2017	30274-31057	analysis-2017_01-ver52.xml
Spring 2018	40856-42577	analysis-2018_01-ver02.xml
Fall 2018	50677-51768	analysis-2018_08-ver02.xml

Table 3.2: GlueX Phase-I dataset specifications

3.3 Event Selections

The dataset at hand now consists of all potential combinations (over all events in the GlueX Phase-I data) that are largely consistent with the reaction: $\gamma p \to \eta \pi^0 p \to 4\gamma p$. A set of refined selections will now be made on the charged tracks, the neutral showers, and on the exclusivity. Finally, the treatment of final state combinatorics and cross-channel backgrounds will be discussed. Since all the final measurements will utilize beam polarization, the very first selection that will be made is to select a region of beam energy that has a large flux and polarization fraction. These distributions were shown in Figure 2.3. The standard selection is made to select the coherent peak by requiring

$$8.2 < E_\gamma < 8.8 \text{ GeV} \tag{3.6}$$

3.3.1 Tagged Beam Photon Combinatorics

Recall that the CEBAF accelerates bunches of electrons spaced 4 ns apart, which in turn radiates bunched photons after scattering off the radiator. Multiple tagged beam photons within the same beam bunch could have passed our event selections. Only one photon could have initiated the reaction but it is not possible to discern which. Additionally, due to the inefficiency of the tagger, there can be events in which the beam photon initiating the reaction is never tagged. Instead, the effect of these "accidental" photons is removed in a process known as *accidental subtraction*.

Tagged beam photons from 4 adjacent beam bunches (out-of-time) were additionally considered in addition to the prompt peak when forming combinations. All beam photons are produced independently, and thus there is no difference between accidental photons produced in-time and out-of-time photons. Combinations with an in-time photon are given a weight of 1. Combinations with out-of-time photons are weighted with a negative value equal to the ratio of the considered phase space size of the signal to that of the out-of-time background. Accidental subtraction is a specific use case of the general subtraction procedure known as *sideband subtraction*. With N adjacent

49
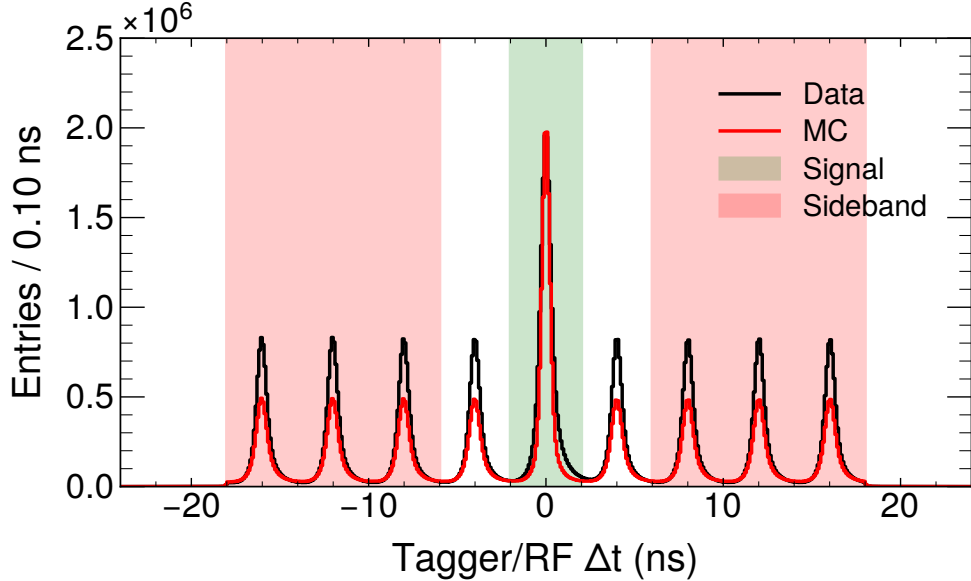
Figure 3.3: Distribution of the tagger time with respect to the RF time. Events in the coherent peak have been selected.

beam bunches, weights given to out-of-time photons are $-1/N$. 6 beam bunches are considered in this analysis, 3 to the left and 3 to the right of the signal peak.

$$\text{Signal}: \ |RF_{\text{time}}| \leq 2 \text{ ns} \qquad \text{Sideband}: 6 < |RF_{\text{time}}| < 18 \text{ ns} \tag{3.7}$$

The nearest beam bunch to the prompt peak is skipped to limit the amount of potential leakage from the large prompt signal. Fig. 3.3 shows the timing spectrum of the beam photons and the corresponding signal and sideband regions where the standard proton, photon, and loose exclusivity selections have been applied. This picture of accidental subtraction is almost sufficient in removing this type of background. It turns out that the accidental tagger background underneath the prompt timing peak does not scale one-to-one with the accidental hits in the side peaks [61]. A run-dependent scaling factor, or *accidental scaling factor*, needs to be introduced to account for this difference. The accidental hits in the side peaks require around a 5% upscaling. Accidentals will be subtracted for the rest of the distributions shown in this dissertation.

3.3.2 Charged Track Selections

We start by requiring the charged track to be consistent with being a proton. The production vertex is defined solely by the charged track. This track is required to originate from within the

50
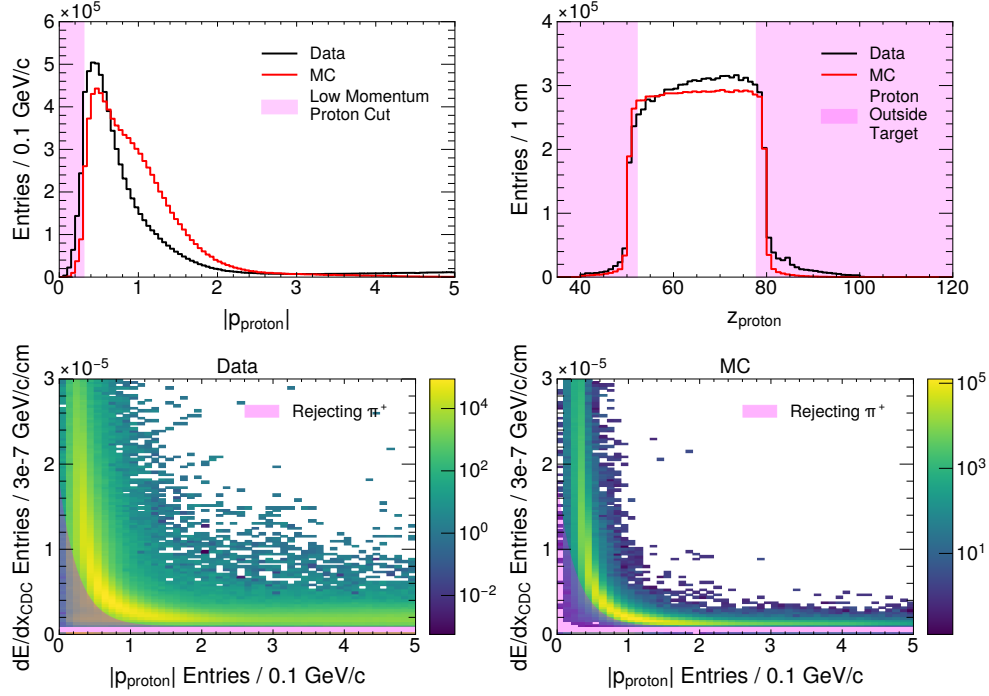
Figure 3.4: Distributions of variables related to the charged track / proton hypothesis. The data distribution corresponds to the spring 2017 run. The MC distributions are arbitrarily scaled to overlap the data. No selections are applied to the data. The shaded regions denote places where events are rejected. Two clusters of events for low proton momenta can be seen in the bottom-left plot. In this region, small dE/dx corresponds to tracks generated by charged pions.

cylindrical target region, which is chosen to be within $z \in [52, 82]$ cm and $R < 2$ cm in the cylindrical GlueX coordinate system. To ensure that the charged track has enough momentum to travel significant distances to be measured in the CDC, the magnitude of the momentum is required to be at least 0.3 GeV. One final selection is made by considering the fact that charged pions and protons lose energy at different rates in the CDC. The energy loss per distance in the CDC, dE/dx, is given by the Bethe-Bloch formula, which is momentum and mass dependent. Protons experience a much larger dE/dx loss at lower energies than pions do, but becomes difficult to distinguish at larger momenta. A selection[2] is made such that

$$\frac{dE}{dx} \geq 10^{-6}(0.9 + e^{3-3.5(|P|+0.05)/0.93827}) \tag{3.8}$$

Fig. 3.4 shows the distribution of these variables. The detailed selection regions are shown. A comparison between the data and Monte-Carlo simulations of this reaction is also shown.

---

[2]This selection is tighter than the one used in the spring 2017 analysis launch. See Appendix A.1
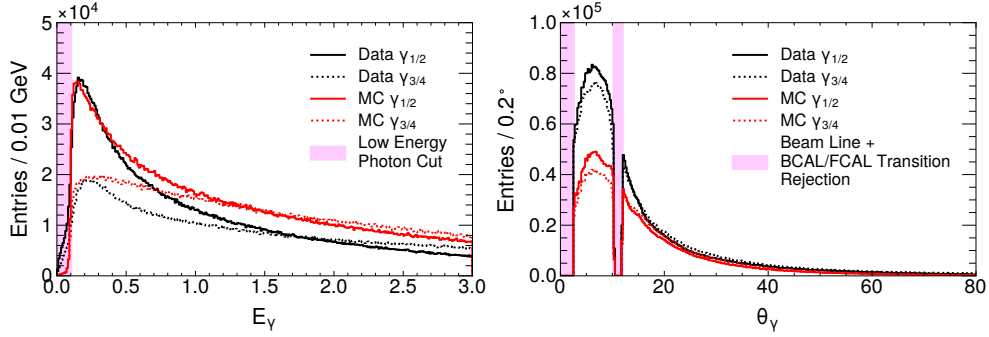
Figure 3.5: Distributions instead of photon energy, E_γ, and photon polar angle, θ_γ are shown. The data distribution corresponds to the spring 2017 run. The MC distributions are arbitrarily scaled to overlap the data. Charged track related selections have been applied to the data. The shaded regions denote places where events are rejected.

3.3.3 Neutral Shower Selections

To select combinations with good photons, all four photons' energies must have at least 100 MeV as lower energy photons are more likely to be spurious. If a photon lands in the BCAL/FCAL transition region or lands near the beamline, then the combination is also rejected. This is done by requiring that the polar angle of all photon showers satisfy

$$2.5^\circ < \theta < 10.3^\circ \quad \text{or} \quad 11.9^\circ > \theta \tag{3.9}$$

Fig. 3.5 shows the distribution of these variables where selections on the charged track have already been applied. The distributions differ depending on whether its parent particle lay within the π^0 or the η mass region. A comparison between the data and Monte-Carlo simulations of this reaction is also shown. See 3.2.3 for more details on the photon labeling scheme.

3.3.4 Exclusivity

We measure the exclusive reaction, as all particles in $\gamma p \to 4\gamma p$ can in principle be measured. We begin by performing two simple selections to reduce the backgrounds from final states with extra showers. When forming the set of final state photons, it may turn out that not all shower energy that was deposited onto the calorimeters is used. Unused energy is defined as the sum of the neutral shower energy in an event that is not used in the combination. Thus, for this all-neutral final state with no expected missing particles, zero unused energy is expected. Similarly, combinations with a non-zero missing mass(MM) are also rejected. In practice, this means that selections are made by requiring the unused energy=0 GeV and $|\text{MM}|^2 < 0.05 \text{ GeV}^2$.

52
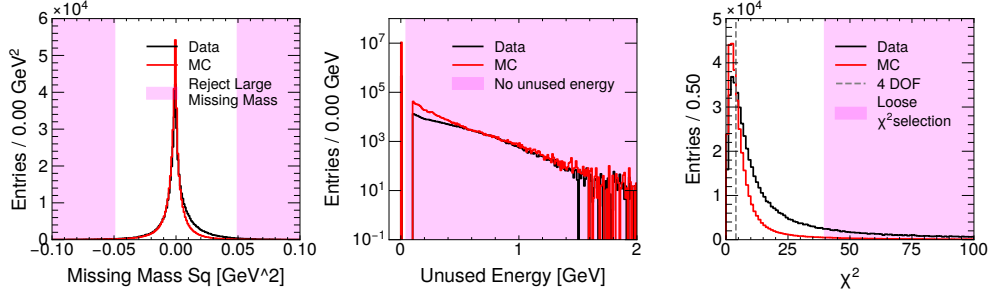
Figure 3.6: Distributions of variables related to exclusivity. Selections related to charged tracks and neutral showers have been applied. Additionally, for each distribution, the selection on the other variables has been applied. For example, for the missing mass distribution, the selections have been placed on both the unused energy and the χ^2. The data distribution corresponds to the spring 2017 run. The MC distributions are arbitrarily scaled to overlap the data. The shaded regions denote places where events are rejected.

The kinematic fit χ^2 also helps quantify the exclusivity, as it enforces the conservation of four-momentum. χ^2 is a powerful discriminator, so a loose selection is first applied to require $\chi^2 <$ 40 before systematically tightening the selection to some optimal value later. Fig. 3.6 shows the distribution of these exclusivity variables where the selection on the charged track and neutral showers have already been applied. Due to the correlations between these variables, the distributions of one variable include additional selections on the two other variables. Combinations are thrown away if they lie in the shaded regions. A comparison between the data and Monte-Carlo simulations of this reaction is also shown.

At this point, basically, all the standard event selections have been detailed. The resulting 1D invariant mass plots, $M(\gamma_1\gamma_2)$ and $M(\gamma_3\gamma_4)$ are shown in Fig. 3.7 (in log-scale) with the event selections, described above, applied in succession. Fig. 3.8 shows these invariant mass distributions and the correlation between them with the selections described thus far.

The optimal χ^2 threshold can be determined by looking at how the significance of the signal changes as a function of the χ^2 selection. The significance metric that will be used here is given by $\sqrt{2(s+b)\log(1+s/b)-2s}$. This metric contains the $\frac{s}{\sqrt{b}}$ metric in the small $\frac{s}{b}$ (or $s << b$) limit and is seen to perform better when this condition is not met [62].

To perform this analysis, a succession of tighter χ^2 selections are applied. For each iteration, a fit is performed on the $M(\gamma_3\gamma_4)$ distribution to extract the signal and background yields to be used for the calculation of the significance. The choice of fitting the $M(\gamma_3\gamma_4)$ distribution only is done for simplicity and because more background lay underneath the $M(\gamma_3\gamma_4)$ peak, see Figure

53
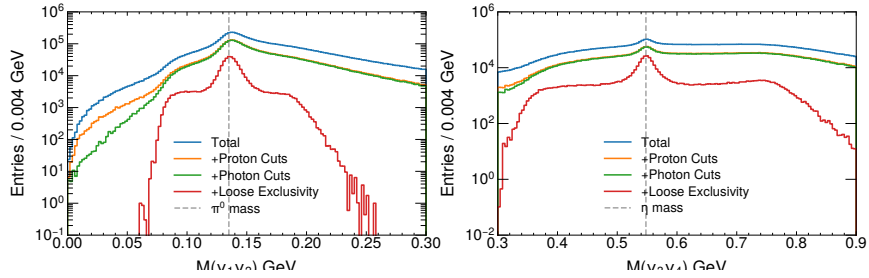
Figure 3.7: Invariant mass distributions, $M(\gamma_1\gamma_2)$ and $M(\gamma_3\gamma_4)$ are shown with groups of selections applied in turn. +Photon Selection would include the photon selections AND all the selections above it, in this case, the proton cuts. These distributions correspond to the spring 2017 run.
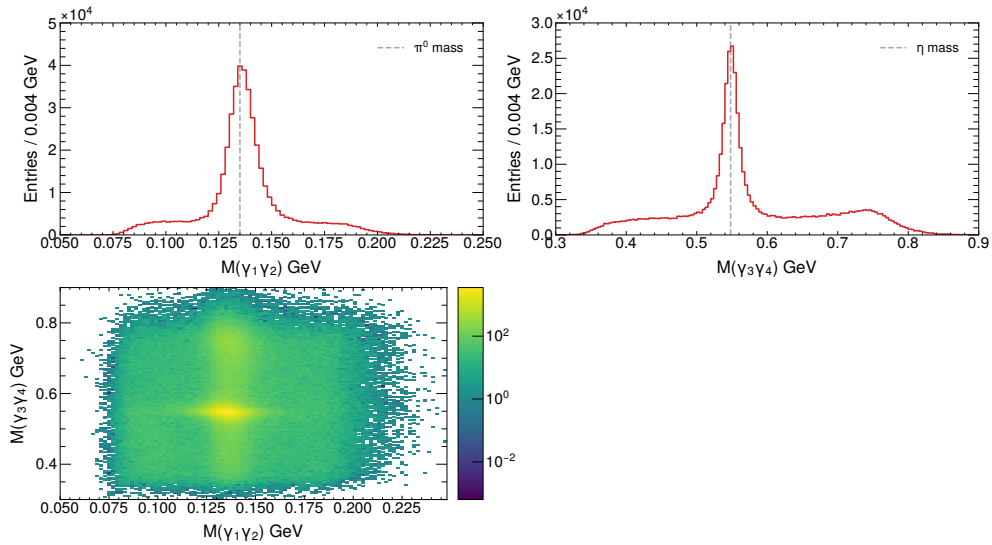
Figure 3.8: Invariant mass distributions, $M(\gamma_1\gamma_2)$, $M(\gamma_3\gamma_4)$, and their correlation(log-scale), are shown with the current selections: proton, photon, and loose exclusivity selections. These distributions correspond to the spring 2017 run.

54

3.8. The signal is described by two Gaussians that share the same mean. The background is a 2nd-order polynomial. Fig. 3.9 shows the fit results. The signal and background yields are determined by integrating the relevant distributions between $\pm 3\sigma$. σ is the weighted average of the standard deviations for the two-Gaussian signal. The averaging is based on the integrated yield of the Gaussian components.

Fig. 3.10 shows the significance as a function of $\chi^2/$NDF in two regions of $M(\eta\pi)$. The first bin, $1.04 < M(\eta\pi) < 1.72$ GeV, will be the region of interest for the measurement of the differential cross section of the $a_2(1320)$ in Chapter 4. The second bin, $1.6 < M(\eta\pi) < 2.8$ GeV, is the region of interest for the measurement of the single-particle beam asymmetries in Chapter 5. The optimal value for the χ^2 selection should attempt to maximize the significance which appears to be roughly 13 in both mass regions. It turns out that with 4 DOF (in the kinematic fit) a χ^2 value of 13.3 represents a 0.01 confidence level. A selection requiring $\chi^2 < 13.3$ is made. The purity is around 85% in the $1.04 < M(\eta\pi) < 1.72$ GeV region and around 93% in the higher mass region.

(a) $1.04 < M(\eta\pi) < 1.72$ GeV

(b) $1.6 < M(\eta\pi) < 2.8$ GeV

Figure 3.9: Plot of fits vs the χ^2 selection threshold in different regions of $M(\eta\pi)$.
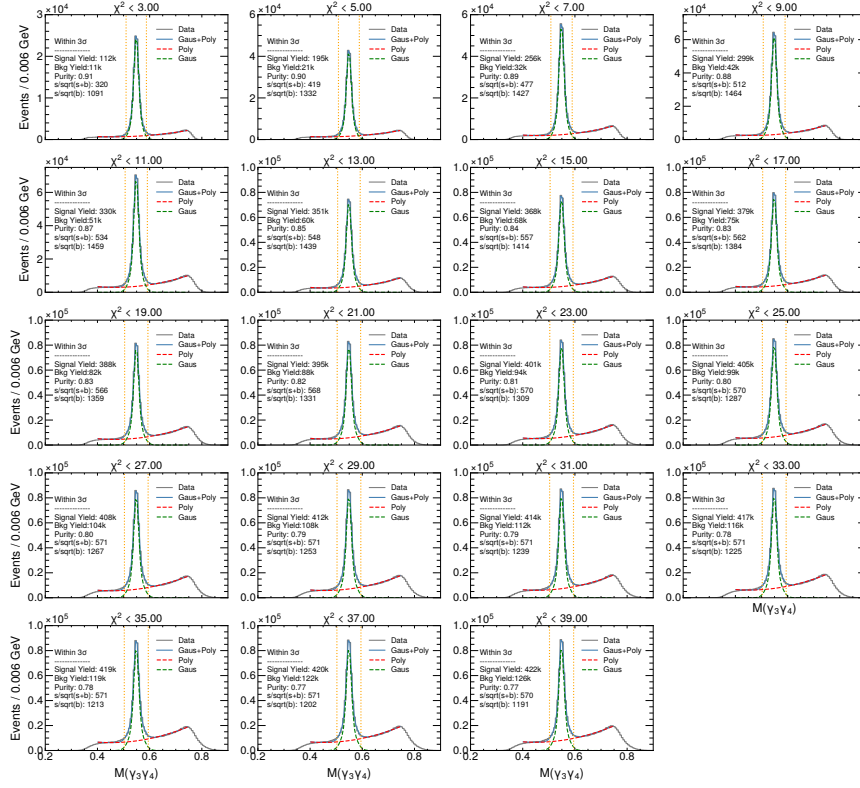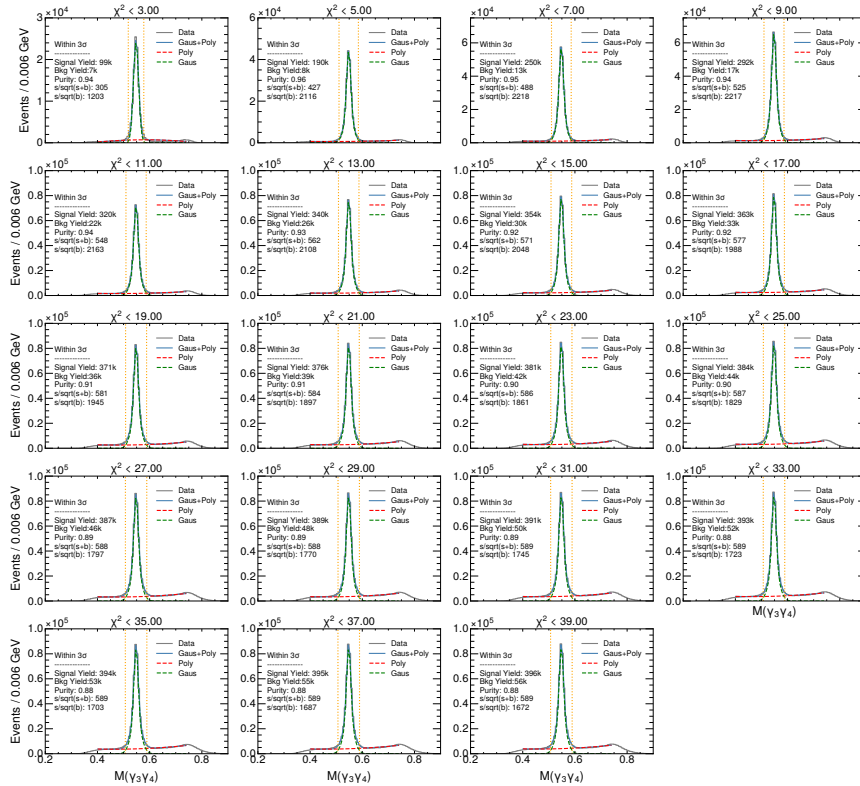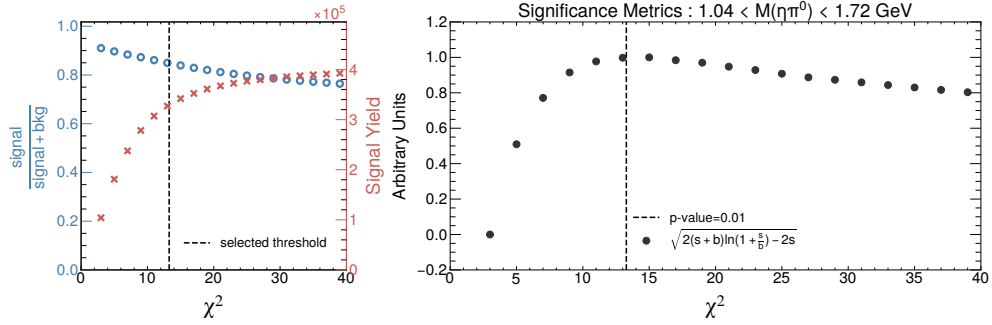
(a) $1.04 < M(\eta\pi) < 1.72$ GeV
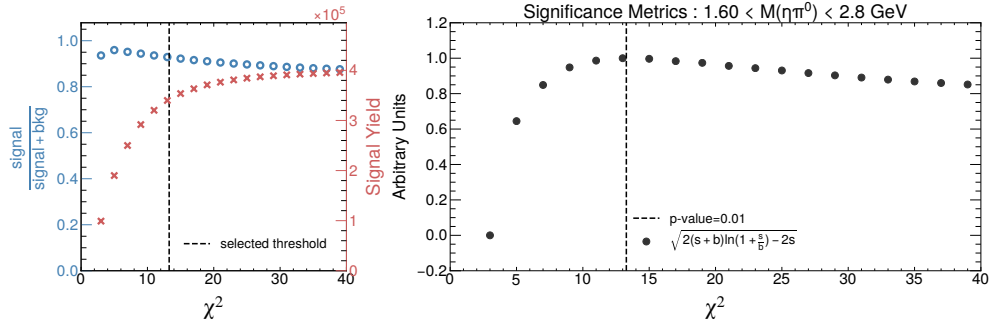
(b) $1.6 < M(\eta\pi) < 2.8$ GeV

Figure 3.10: (Left) plot shows the the purity, $\frac{s}{s+b}$, and the signal yield as a function of the χ^2 selection. (Right) plot shows significance vs the χ^2 selection. These metrics are shown for different regions of $M(\eta\pi)$ corresponding to the two different regions studied in this dissertation.

3.4   Final State Combinatorics and Background Suppression

At this point, all standard event selections have been applied to all potential combinations for all events. After all these selections, there remains a "combinatorial" background. As the candidate η and π^0 share the same 2γ final state, alternative combinations of photon pairs can also pass all event selections. Background processes with a different $N\gamma$ final state can also end up in the selected dataset by losing or gaining some number of photons. Alternative combinations from these background processes can also show up in the selected dataset, just like an $\eta\pi^0$ signal. Two techniques will be studied to remove these types of backgrounds.

The general strategy that is used here is to turn to simulation to study and validate the proposed techniques. The MC sample that was described in Section 3.2.1 is used here. This sample is generated flat in $\eta\pi$ mass and without any angular dependence in its decay. This setup evenly distributes the events to populate as much phase space as possible. The events can be passed through the simulation of the GlueX detector and are then fully reconstructed, following a similar pathway as actual data would. These combinations can then be matched back to the true particle decay chain, where we can check the performance of the subtraction schemes.

Section 3.4.1 will look into *sideband subtraction* to deal with these final state photon combinatorics. Section 3.4.3 will discuss an alternative method known as Q-Factors, which will be studied in an attempt to deal with some drawbacks of sideband subtraction. The performance of sideband subtraction will be compared to that of the Q-Factors approach. In Section 3.5 a Monte Carlo study will be examined in order to determine the performance of the current event selections and the chosen subtraction schemes.

3.4.1   Sideband Subtraction

An event can produce numerous showers in the calorimeters. After the unused energy selection (see Section 3.3.4), the event can only have 4 showers that can be used as photon candidates. There are 3 unique ways of forming two pairs of photons, where only one is the correct pairing. The correct combination should be much more likely to produce pairs of $M(2\gamma)$ near the π^0 and η peaks. Wrong combinations should be smoothly distributed over a much larger range. Two important features are important there. More background appears outside the η peak, which is attributed to the $b_1(1235) \to \omega\pi^0 \to \gamma 2\pi^0 \to 5\gamma$ process leaking into this channel with an undetected photon. Figure 3.11 shows an estimate of the leakage from this background channel and how it influences

58
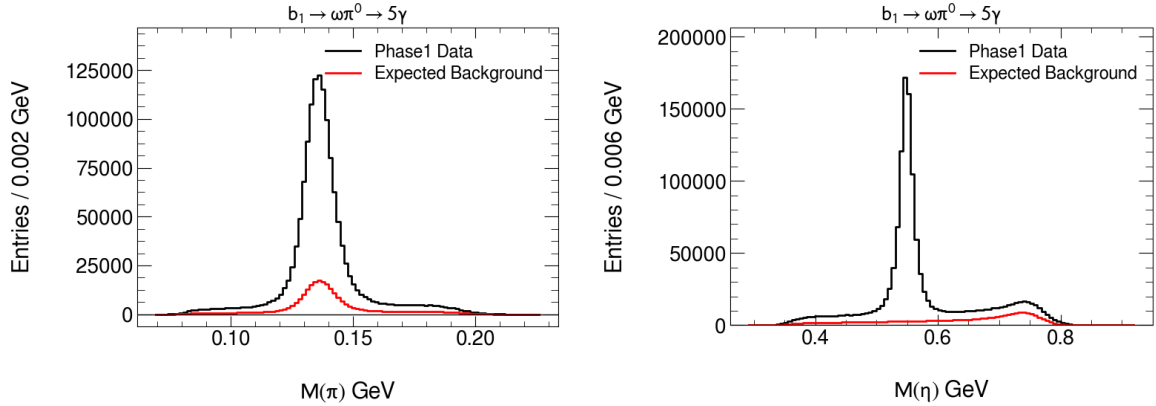
Figure 3.11: Distributions of $M(\eta)$ and $M(\pi^0)$ for the GlueX Phase-I dataset. The η and π^0 signal regions have been selected. These regions are detailed in 3.3. The red distribution is an estimate of the leakage from the $b_1(1235) \to \omega\pi^0 \to \gamma 2\pi^0 \to 5\gamma$ process.

the $M(2\gamma)$ distributions. The details of this estimation are shown in Section 3.5 which showcases a Monte Carlo study that is used to determine the extent of leakage from select channels. Another feature that can be seen here is that there appears to be a slight correlation between the $M(2\gamma)$ pairs (bottom-left plot), which can be attributed to the kinematic fit. This will become important when Q-Factors are introduced in section 3.4.3.

Sideband subtraction will be used to handle these final state photon combinatorics, similar to the way accidentals are handled. The idea, again, assumes that wrong combinations underneath the $\eta\pi$ signal peak look similar to wrong combinations that form outside the peak. This assumption will not hold in certain situations and will be discussed in the coming sections. For now, two independent sideband subtractions can be performed to subtract out the candidate π^0 candidate sidebands and the candidate η candidate sidebands. A fit is performed to the η or π^0 lineshape using a signal distribution formed from two Gaussians that share the same mean on top of a linear background. The signal region is defined by ± 3 weighted-σs where the σ's are combined based on the relative integrals between the Gaussians. The sideband regions are chosen to be in approximately linear regions of data. The signal and sideband regions are shown in Table 3.3.

For each dimension, the sideband weights for combos in the signal region are equal to 1. The weights for combos in the sidebands are equal to the ratio of span of the signal region to that of the sideband region times -1. Combinations not in the signal region nor the sideband region are rejected. The total sideband weight is then simply the two independent sideband weights multiplied

π^0 peak	0.135881 GeV
η peak	0.548625 GeV
$\sigma(\pi^0)$	0.0076 GeV
$\sigma(\eta)$	0.0191 GeV
π^0 signal region:	$M(\gamma_1\gamma_2) - \pi^0$ peak $< \mathrm{abs}(3\sigma)$
η signal region:	$M(\gamma_3\gamma_4) - \eta$ peak $< \mathrm{abs}(3\sigma)$
π^0 sideband region:	$\mathrm{abs}(4\sigma) < M(\gamma_1\gamma_2) - \pi^0$ peak $< \mathrm{abs}(5.5\sigma)$
η sideband region:	$\mathrm{abs}(4\sigma) < M(\gamma_3\gamma_4) - \eta$ peak $< \mathrm{abs}(6\sigma)$

Table 3.3: Table of values that determine the sideband regions of $M(\gamma_1\gamma_2)$ and $M(\gamma_3\gamma_4)$.

together. Figure 3.12 show the signal and sideband regions for the candidate π^0 and η on the top row. The bottom-left plot shows the effects of the subtraction. An additional selection is introduced in the next section to address the false cusp-like feature that is created by the subtraction of mass sidebands.

3.4.2 Low mass alternative combinations

With the current definitions, sideband subtraction performs poorly near the $M(\eta\pi)$ threshold. The next section details a Monte Carlo study that aims to understand the performance of the current selections and the strategy for dealing with combinatorics. In particular, in section 3.5, it will be shown that the cusp-like feature near the $M(\eta\pi)$ threshold (see Figure 3.12) is reproduced by improperly reconstructed $\omega \to 3\gamma$ events faking as an $\eta\pi^0 \to 4\gamma$ event. The simulations suggest that the actual efficiency for this leakage is very low, around 0.03%, but it still poses as a significant background due to the large cross section for ω photoproduction which is measured to be around 1.3 μb[63] at GlueX. It is interesting then to look at the invariant masses of the alternative photon pairing (pairs that are not used to form the candidate π^0 nor η): $M(\gamma_1\gamma_3)$, $M(\gamma_1\gamma_4)$, $M(\gamma_2\gamma_3)$ and $M(\gamma_2\gamma_4)$. These low mass alternative combinations are removed with box cuts. The selection requires:

$$(M(\gamma_1\gamma_3) < 0.15 \text{ GeV}) \ \& \ (M(\gamma_2\gamma_4) < 0.15 \text{ GeV})$$

$$(M(\gamma_1\gamma_4) < 0.15 \text{ GeV}) \ \& \ (M(\gamma_2\gamma_3) < 0.15 \text{ GeV})$$

$$(M(\gamma_1\gamma_3) < 0.12 \text{ GeV}) \ \& \ (M(\gamma_2\gamma_3) < 0.12 \text{ GeV})$$

$$(M(\gamma_1\gamma_4) < 0.12 \text{ GeV}) \ \& \ (M(\gamma_2\gamma_4) < 0.12 \text{ GeV})$$
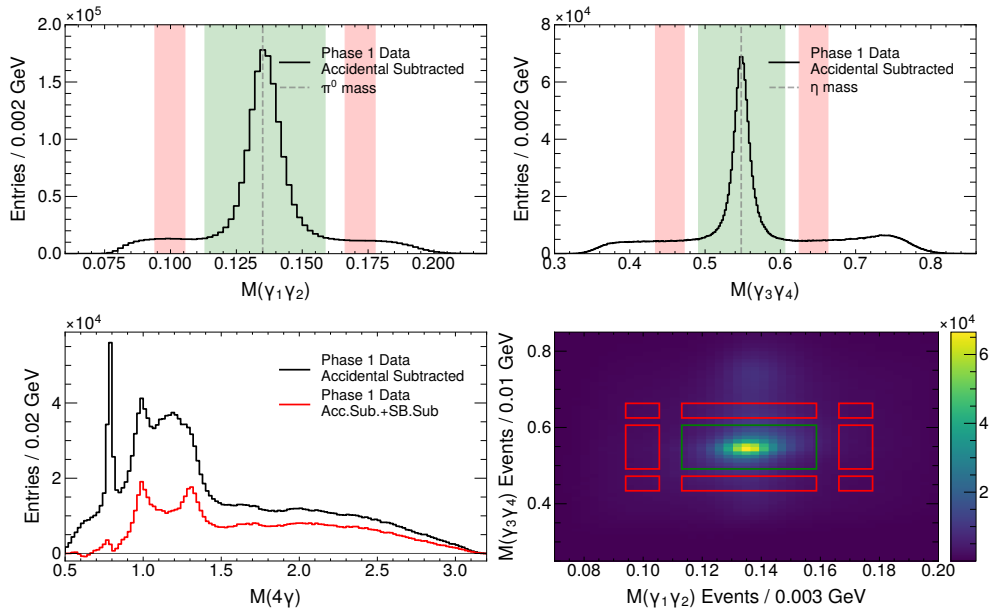
Figure 3.12: Top row and the bottom-right figures highlights the signal and sideband regions used to sideband subtract the final state photon combinatorics. The 3 regions of each $M(2\gamma)$ distribution combines to form the 9 rectangular regions in the 2D, bottom-right, plot. The bottom-left plot shows in black the GlueX Phase-I data with accidental subtraction applied. The overlaid red distribution shows the effects of sideband subtraction.
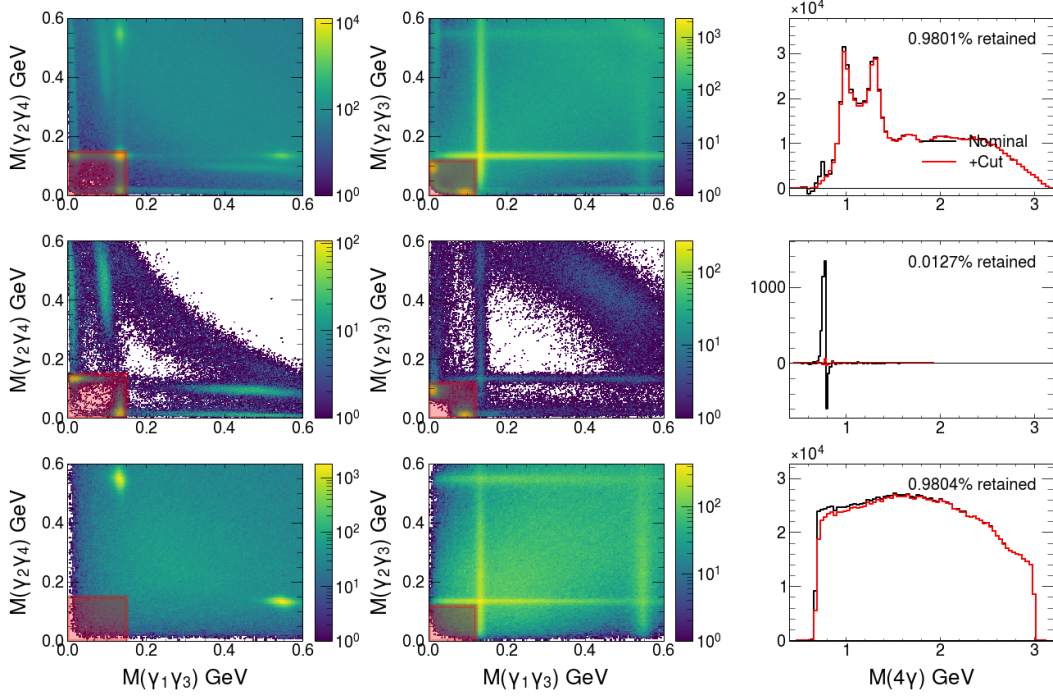
Figure 3.13: Distributions showing the performance of the LMAC selection. The red regions in the left and middle column plots depict the rejection regions. The column on the right show $M(4\gamma)$ before and after including the selection.

Figure 3.13 shows the performance of this selection. The columns from left to right are $M(\gamma_2\gamma_4)$ vs $M(\gamma_1\gamma_3)$, $M(\gamma_2\gamma_3)$ vs $M(\gamma_1\gamma_3)$, and $M(4\gamma)$. The top row corresponds to the GlueX Phase-I data. The middle and bottom rows are from $\omega \to \pi^0\gamma \to 3\gamma$ and $\eta\pi^0 \to 4\gamma$ Monte Carlo events both being reconstructed under a $\eta\pi^0 \to 4\gamma$ hypothesis. The red regions in the 2D plots depict this low-mass alternative combination, LMAC, selection. The red curves in the rightmost column include the LMAC selection on top of the nominal selections. This selection also rejects alternative combinations that are consistent with a $2\pi^0$ scenario.

The inclusion of this selection cleans up the threshold region nicely while leaving the higher mass region relatively untouched. $\sim 3\%$ of the signal is rejected, mostly near the threshold. The measurements made in this dissertation are carried out at significantly higher masses. Therefore, this selection is only used for illustration purposes here when the behavior of the spectrum near-threshold is of interest.

62

3.4.3   Q-Factors

The use of sideband subtraction in this channel required the introduction of an additional threshold-focused selection, see 3.4.2. It will also be shown in the next section that the $b_1 \to \omega\pi^0 \to 5\gamma$ reaction is the largest expected background and that sideband subtraction performs well here but leads to some minor over and under-subtraction. This section introduces the Q-Factors approach as an alternative method to address these deficiencies and cross-check the sideband subtraction procedure. A comparison will be made to the sideband subtracted results and their performance will be tested on Monte Carlo simulations.

The Q-factor method is a multivariate sideband subtraction technique using probabilistic weights [64]. The phase space of a given reaction is labeled by some set of coordinates. A subset of these coordinates are chosen as reference coordinates where the signal and background distribution must be known. In the space defined by the non-reference coordinates, k nearest neighbors are determined for each event under some metric (typically Euclidean or L2 norm). An unbinned maximum likelihood (MLE) fit is performed on the reference coordinates of the k nearest neighbors. The Q-factor is defined to be the signal fraction/probability from the resulting fit. This value becomes the weight assigned to a given event and can be used in subsequent analyses such as partial wave analysis (PWA). The Q-Factors technique has been applied sucessfully in numerous measurements [65][66][67][68][69].

An implementation of the algorithm is developed for this dissertation [70][71] for use at GlueX. Q-Factors is a computationally expensive technique requiring one to search for nearest neighbors and perform an unbinned MLE fit for each event. The current implementation is written and compiled in C++ with a python driver script. Unbinned MLE fits are done in RooFit. Multiple processes can be requested. Nearest neighbors are determined by using a priority queue. Auxillary programs are included to conveniently draw variables of interest and to diagnose individual fit results. This program has also been used by several GlueX collaborators.

The largest background, as will be shown in Section 3.5, is expected to be from the $b_1(1235)$ meson decaying into $\omega\pi^0 \to 5\gamma$. Therefore, a dedicated Monte Carlo dataset was produced for the b_1 channel and is reconstructed under the $\eta\pi^0 \to 4\gamma$ hypothesis. The simulation described in Section 3.2.1 is used as signal MC for reference. The datasets were added together, reconstructed, and the default selections were applied. Figure 3.14 shows the initial MC sample split among the two datasets in various kinematic variables. $\cos\theta_{hel}$ and ϕ_{hel} are the helicity angles [72] defined in the $\eta\pi$ rest frame. Recall that $\gamma_1\gamma_2$ form the π^0 candidate and $\gamma_3\gamma_4$ form the η candidate. Let $M(\eta)$
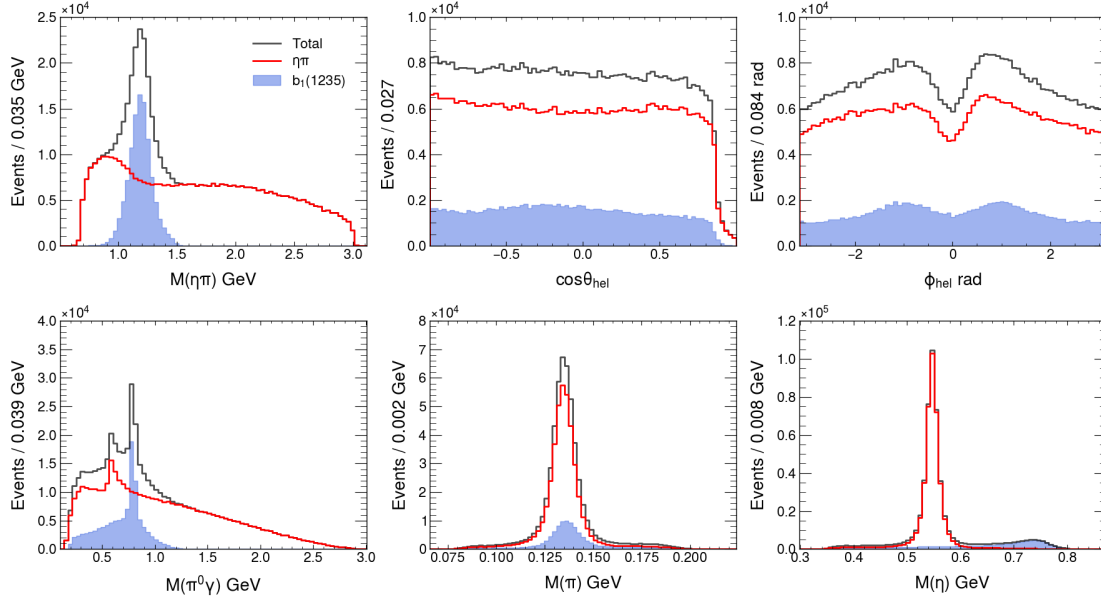
Figure 3.14: Distributions of the merged MC sample consisting of photoproduced $b_1(1285) \rightarrow \omega\pi^0 \rightarrow 5\gamma$ and $\eta\pi^0$ events (generated flat in $M(\eta\pi)$) reconstructed under a $\eta\pi^0 \rightarrow 4\gamma$ hypothesis. The first 4 variables are included in the metric used for distance calculation. The last two will be the reference variables. All Final state combinatorics are included.

and $M(\pi^0)$ denote the mass of the η and π^0 candidate. $M(\pi^0\gamma_3)$, and $M(\pi^0\gamma_4)$ are 3γ invariant masses that incorporate the π^0. This variable is sensitive to background contributions that contain an ω. The samples include all selected final-state combinatorics.

The Q-Factors are extracted for all combinations. The current setup uses 200 neighbors and performs a 2D unbinned maximum likelihood fit to the $M(\eta)$ vs $M(\pi)$ distribution of those neighbors.

In the Q-Factor procedure, a natural place where one can incorporate accidental subtraction would be in the construction of the distribution to be fitted. For each combination, $M(\eta)$ vs $M(\pi)$ is filled with all its neighbors with their associated accidental weights. This construction decouples the photon beam combinatorics from the final state photon combinatorics, such that the final weight for the combination can be constructed simply as a product of the accidental subtraction weights and the Q-Factor (analogous to combining the accidental and sideband subtraction weights). Alternatively, the dataset can be split in two: one that considers only in-time beam photons and another that considers only out-of-time beam photons. The Q-Factors can be extracted for each dataset and the final results can be combined. This particular study will use the former approach,

but an additional comparison will be made at the end considering the latter prescription.

The neighbors are determined in a 5 dimensional phase space using the l^2, Euclidean, norm. The phase space is $\cos\theta_{hel}$, ϕ_{hel}, $M(\eta\pi)$, $M(\pi\gamma_3)$, and $M(\pi\gamma_4)$. Including the three mass variables increases separation power between b_1 and $\eta\pi$ events, as b_1 events are localized in $M(\eta\pi)$ and are likely to appear with peaks in $M(\pi\gamma)$ around the ω mass, which can be seen in Figure 3.14. The $\eta\pi$ simulations are not produced with any photon polarization, but if they were, then another variable should be included in the metric that takes incorporates it. For instance, $(\phi_{proton})_{cm} - \Phi_\gamma$. To simplify the notation of the probability density functions (pdf), $M(\eta)$ and $M(\pi)$ will be referred to as y and x in the following pdf functions. The signal is described by a bivariate Gaussian

$$\frac{1}{2\pi\sigma_X\sigma_Y\sqrt{1-\rho^2}}\exp\left(-\frac{1}{2(1-\rho^2)}\left[\left(\frac{x-\mu_X}{\sigma_X}\right)^2 - 2\rho\left(\frac{x-\mu_X}{\sigma_X}\right)\left(\frac{y-\mu_Y}{\sigma_Y}\right) + \left(\frac{y-\mu_Y}{\sigma_Y}\right)^2\right]\right)$$
(3.10)

with correlation ρ and widths σ_X and σ_Y. The kinematic fit introduces a slight correlation between the $M(\eta)$ and $M(\pi)$ which ρ can attempt to capture. The background is given by

$$\left[a(c \cdot b_{0,1}(x) + d \cdot b_{1,1}(x)) + (1-a)N(x; \mu'_X, \sigma'_X))\right][e \cdot b_{0,1}(y) + f \cdot b_{1,1}(y)]$$
(3.11)

where $b_{\nu,n} = \binom{n}{\nu}x^\nu(1-x)^{n-\nu}$ is known as a *Bernstein polynomial* and is strictly positive on the domain [0,1]. Bernstein polynomials are useful in the construction of probability densities. $b_{0,1}(x)$ and $b_{1,1}(x)$ are a Bernstein polynomial basis of degree 1 and are equal to $1-x$ and x. $N(x; \mu'_X, \sigma'_X)$ is a normal distribution with mean and width equal to μ'_X and σ'_X. a is a pdf fraction between the polynomial and Normal background distributions in x and takes on values between [0,1]. This specific construction for the background in x is chosen since the largest expected combinatorial background to the $\eta\pi^0$ channel is from the $b_1(1235) \to \omega\pi^0 \to 5\gamma$ where it is likely that the π^0 candidate is real. c, d, e, f are coefficients of the Bernstein polynomials and also take on values between [0,1]. The final fit distribution is the sum of signal and background pdfs. A sample fit is shown in Figure 3.15 which contains significant contributions from b_1 events, as can be seen in a rising tail at large $M(\gamma_3\gamma_4)$ coupled with the presence of a real pion.

Figure 3.16 shows the separation of signal and background for four invariant mass plots, two of which are the reference variables. It can be seen that the majority of the events from the b_1 process are separated out. Combinatorial backgrounds from $\eta\pi$ events are also separated out which can be clearly seen in the differences in the $M(\pi^0\gamma)$ distributions around 0.6 GeV in Figures 3.16 and 3.14.
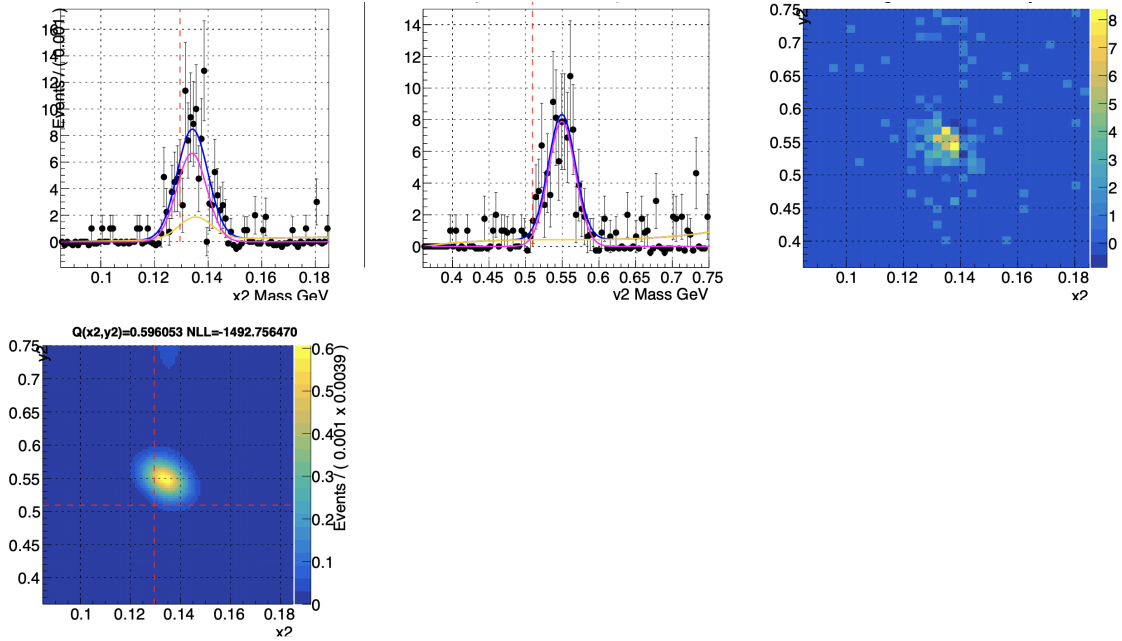
Figure 3.15: Sample 2D Q-Factor fit of the $M(\eta)$ vs $M(\pi)$ distribution for a single event. Top-left and top-middle plots show the projections of the data and pdfs onto $M(\pi^0)$ and $M(\eta)$ respectively. The blue, orange, and magenta lines correspond to the best fit, background, and signal functions respectively. The top-right plot shows the 2D data that is fitted. The bottom-left plot depicts the fitted pdf. The red dashed lines correspond to the current event's mass values. A rising tail can be seen in the candidate $M(\eta)$ distribution which is a signature of leakage from the b_1 process. The Q-Factor for this event is 0.596.
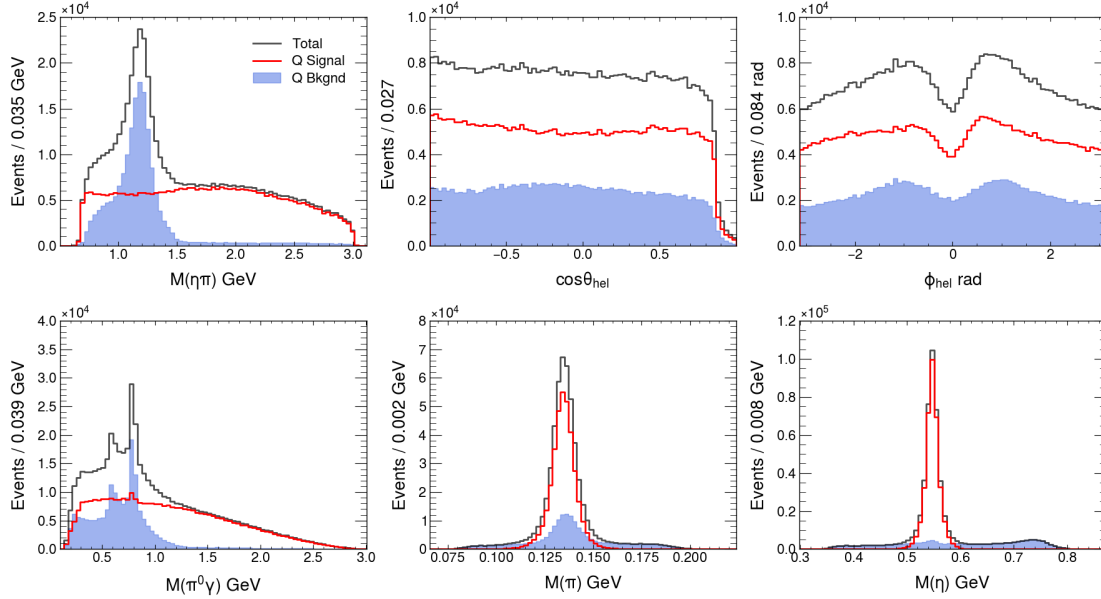
Figure 3.16: Q-Factor results separating signal from background for various distributions. Each figure consists of 3 plots: total, signal, and background such that total-backgroud=signal. In practice, the signal is constructed as a weighted histogram filled with the Q-Factors. The background distribution is filled with 1 minus the Q-Factors.

In particular, the 0.6 GeV peak comes from a real η and low energy photon, which implies the π^0 candidate is not genuine.

Figure 3.17 shows a comparison of the signal extracted from Q-Factors to the signal extracted from sideband subtraction on top of the distribution from matched thrown events. There appears to be little difference in the final results between the subtraction schemes, except in $M(\pi^0\gamma)$ where a clear bump near the ω mass is seen (which is indicative of b_1 leakage). This mass distribution suggests that the Q-Factors have not completely separated out all b_1 events. Obtaining the Q-Factors is a computationally expensive operation, whereas obtaining the weights from sideband subtraction is essentially free. For these reasons, sideband subtraction will be used in the rest of the dissertation instead of Q-Factors. The Q-Factor procedure remains an interesting alternative when sideband subtraction performs poorly.

Treatment of Accidentals. Although Q-Factors will not be used, a discussion regarding the treatment of accidentals is important to return to as it can affect the performance of the algorithm. The prescription discussed so far can be phrased in the context of conditional probabilities. The joint probability for a combination to have a given (Q)-factor and (A)ccidental weight can be written
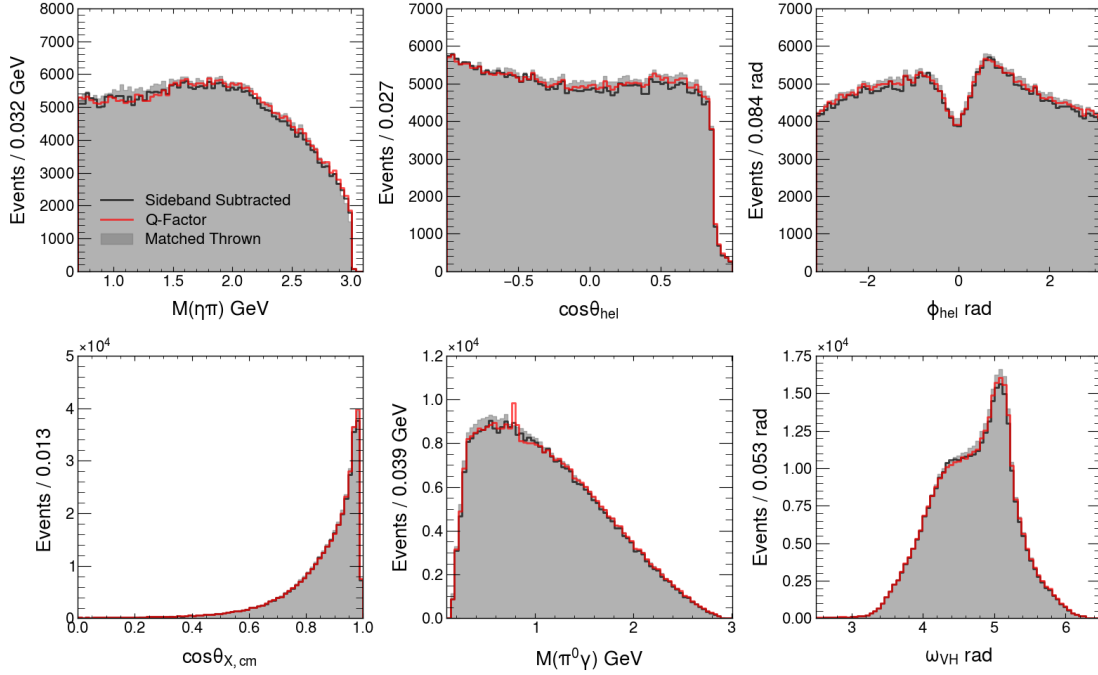
Figure 3.17: Comparing resulting signal events after applying Q-Factors (red) or sideband subtraction (blue) to the matched thrown events (shaded gray). Matched-thrown events are events that have been matched to the particles that were thrown in the simulation. *hel* represents the helicity frame, X is the $\eta\pi$ system, *cm* is the center of mass frame, and ω_{VH} is the Van Hove angle [73][74].

as $P(Q, A)$. The probability for a combination to have an accidental weight is then $P(A)$ and is strictly a property of the beam. The probability for a combination to have a given Q-factor is $P(Q|A)$ such that the three probabilities are related by

$$P(Q, A) = P(Q|A)P(Q) \tag{3.12}$$

If Q and A are uncorrelated, then $P(Q|A)$ is just $P(Q)$. This is not the case here. Accidental beam photons directly contribute to the final $M(\eta)$ and $M(\pi)$ spectrum by broadening the peak, as beam photons with slightly deviated energies can leak in. The effects of the accidentally tagged beam photons can be removed by accidental subtraction and can be used to decouple the extracted Q-factor from their contributions. Let's call this method the 'conditional' approach. An alternative method, that does not modify the methodology introduced in the original paper, is to split the dataset in two so that individual sets of Q-Factors could be calculated for combinations that have in-time beam photons from combinations that use the out-of-time beam photons. The datasets can then be combined. The procedure is denoted as the 'separate' approach.

Two sets of Q-Factors are determined following these two methodologies, and the subtracted results can be compared to the matched thrown events, similar to what was shown above. Figure 3.18 shows the subtracted results comparing the two methodologies to the matched thrown events. The two approaches perform very similarly, but the conditional approach appears to agree with the matched thrown distribution slightly better.
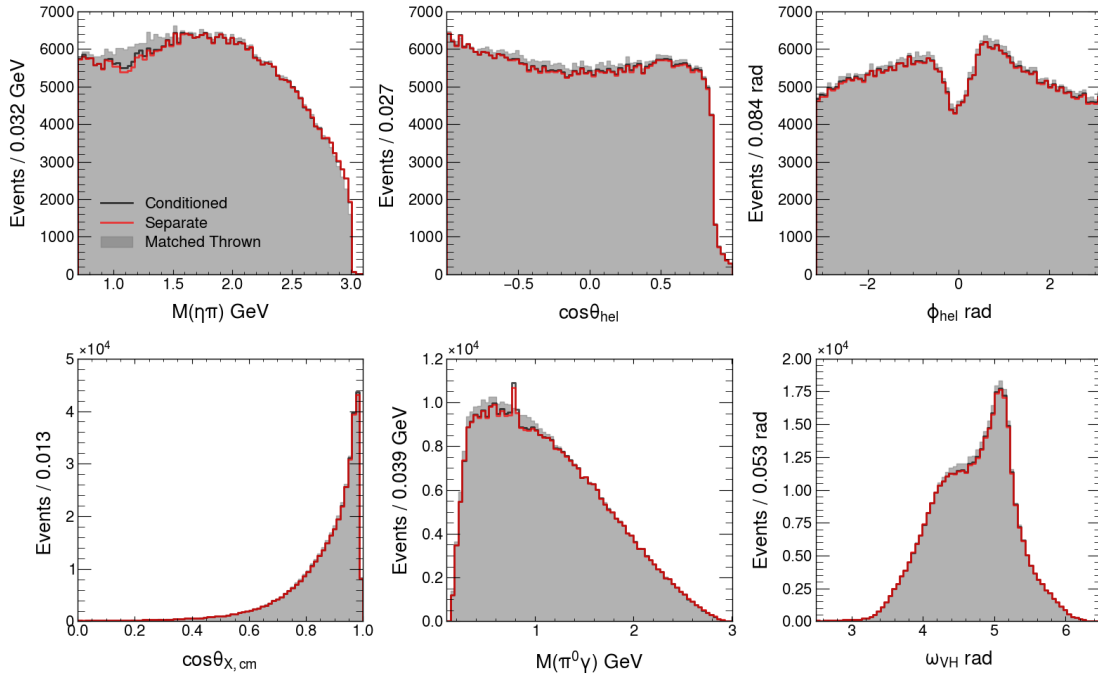
Figure 3.18: Comparing the resulting signal events after applying Q-Factors extracted through the 'conditional' approach (black), Q-Factors extracted through the 'separation' approach (red), and the matched thrown events (shaded gray). Matched-thrown events are events that have been matched to the particles that were thrown in the simulation. *hel* represents the helicity frame, X is the $\eta\pi$ system, *cm* is the center of mass frame, and ω_{VH} is the Van Hove angle [73][74].

3.5 Monte Carlo Background Study

3.5.1 Generic Photoproduction Monte Carlo Study

An initial study is carried out to study the performance of the event selections and subtraction techniques detailed in the previous sections. A generic photoproduction generator[3] is used to simulate a variety of final states which can then be sent through the detector simulation, reconstructed, and passed through all event selections and subtraction schemes. The relative yields in the different final states of the simulation are not representative of GlueX data. Rather, these simulations can provide guidance on which final states to consider when developing more dedicated studies.

Figure 3.19 shows a stacked histogram of $M(\eta\pi)$ separated into contributions from only the five leading background final states which accounts for $> 99\%$ of the remaining simulated yield in both histograms. The percentage of events in each channel is shown in brackets. The blue histogram is the $\eta\pi^0$ signal channel. The ω channel only contributes near the $\eta\pi$ threshold. The $3\pi^0$ channel backgrounds are significantly reduced after sideband subtraction. The largest remaining backgrounds in this simulation are from the $\pi^0\pi^0$ final state. The $\omega\pi^0$ channel is seen to contribute also. Even though the $\omega\pi$ and ω channels do not appear to contribute significantly after sideband subtraction, the cross sections for their production are much larger than the $\pi^0\pi^0$ reaction. The expected leakage from several reactions that decay to a $N\gamma$ final state, including the ω, $\omega\pi^0$, and $\pi^0\pi^0$ channels, will be studied in the next section.

3.5.2 Expected Leakage from Different Nγ Final States

It is interesting to see how the current event selections and strategy to handle combinatorics perform on removing leakage from other multi-photon channels, i.e. by not detecting a set of final state photons or by the inclusion of spurious low energy photons. Studying how these Nγ channels leak in can provide insight into how pure the current dataset is and how might these backgrounds be removed.

Based on an internal GlueX study [75] the ω, $f_2(1270)$, b_1, and η resonances are seen to be the dominant contributions of 3, 4, 5, and 6 photon final states respectively. Preliminary photoproduction cross sections for these resonances at GlueX have already been measured at GlueX: $b_1(1232)$ [76], ω [63], η [77]. An estimation of the $f_2(1270) \to 2\pi^0$ cross section is made in Appendix A.3. There are a few other decay channels of interest with a 6 photon final state that are seen to

---

[3]`bggen`
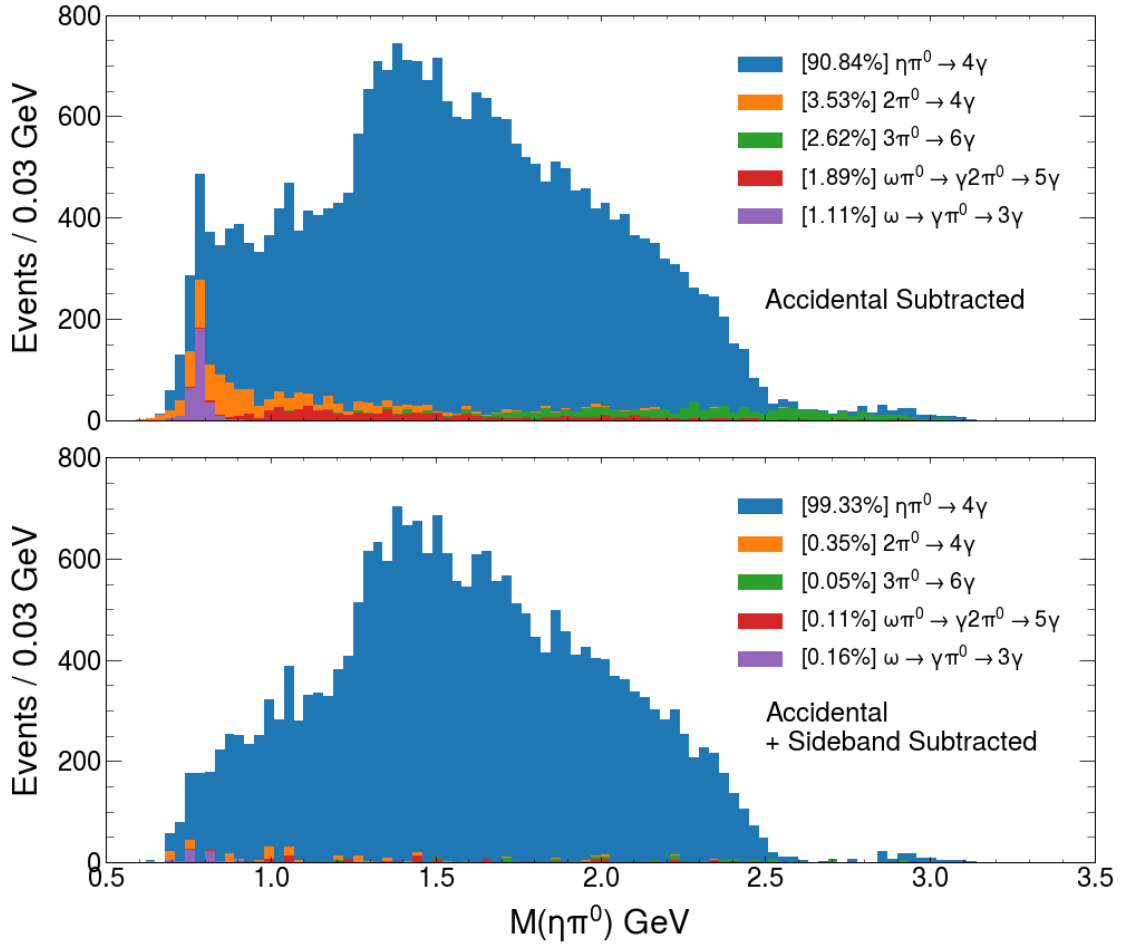
Figure 3.19: Stacked histogram of $M(\eta\pi)$ separating out the contributions from different final states. The histogram on the top has only accidental subtracted whereas the bottom histogram also includes sideband subtraction. The percentage of events in each channel is shown in brackets.

Decay	Estimated Cross Section of Meson Production at 8.5 GeV [nb]	Product of Decay Branching Fractions
$b_1 \to \omega\pi^0 \to (\pi^0\gamma)\pi^0 \to 5\gamma$	1390.89	0.082
$\omega \to \pi^0\gamma \to 5\gamma$	1299.67	0.082
$\eta \to 3\pi^0 \to 6\gamma$	36.20	0.31
$f_1 \to \eta\pi^0\pi^0 \to 6\gamma$	36.20	0.2
$f_2 \to \pi^0\pi^0 \to 4\gamma$	12.72	0.82
$\eta' \to \eta\pi^0\pi^0 \to 6\gamma$	29.44	0.086
$a_2\pi^0 \to \eta\pi^0\pi^0 \to 6\gamma$	36.20	0.056
$a_2 \to \eta\pi^0 \to 4\gamma$	68.36	0.056

Table 3.4: Table containing average cross sections for the production of select mesons at 8.5 GeV at GlueX. Since the cross section for f_1 and $a_2\pi$ have not yet been measured, the η cross section is used instead. The cross sections for the f_2 and a_2 mesons are determined for $-t \in [0.1, 1.0]$ GeV^2.

be produced in significant quantities: η', $f_1(1285)$, and $a_2\pi^0$. The cross sections for the $f_1(1285)$ and $a_2\pi^0$ channels have not been measured yet but are likely upper-bounded by the η. This is determined by comparing the relative intensities in Reference [75] and relative products of decay branching ratios between channels. The cross section for η' is determined in Reference [78]. Table 3.4 shows the average measured cross sections for these mesons from the above analyses. For comparison, the cross section for the $a_2(1320)$ determined in this dissertation for $-t \in [0.1, 1.0]$ GeV^2 is included.

Simulations of all the channels discussed are made, propagated through the detector, reconstructed, and analyzed following the same procedure that was done for the $\eta\pi^0$ data. With these simulations, the efficiency of a particular channel to leak into the $\eta\pi^0$ channel can be estimated. The integrated flux for the Phase-I data and the target thickness are known. Leakage estimates can be made by plugging all these values into the equation

$$N_{X \to n\gamma} = \sigma_X \times \text{Target Length} \times \text{Tagged Flux} \times \Gamma(X \to n\gamma) \times \epsilon \tag{3.13}$$

Figure 3.20 shows the expected background leakage from each channel overlaid with the Phase-I data where accidentals are subtracted and the η and π signal region are selected. $b_1 \to 5\gamma$ can be seen to be the most significant potential background channel, populating an important region of space between the $a_0(980)$ and $a_2(1320)$ resonances. $\omega \to 3\gamma$, $\pi^0\pi^0$ and the 6γ final state channels have essentially no expected contribution.
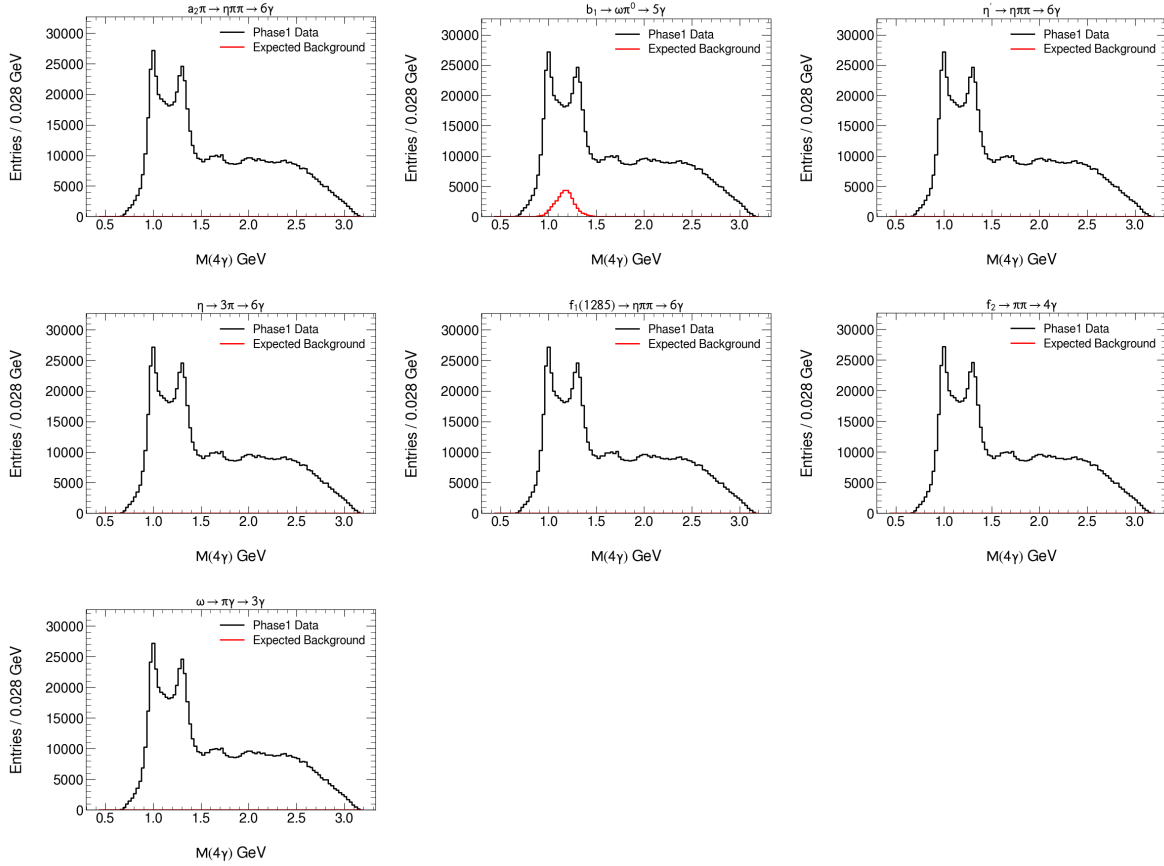
Figure 3.20: Expected leakage from other multi-photon final state channels. The estimated background is overlaid on top of the Phase-I $\eta\pi^0$ dataset. This estimation takes the central yield estimates and adds 3 times the stat. errors on top of it. Only accidentals are subtracted.
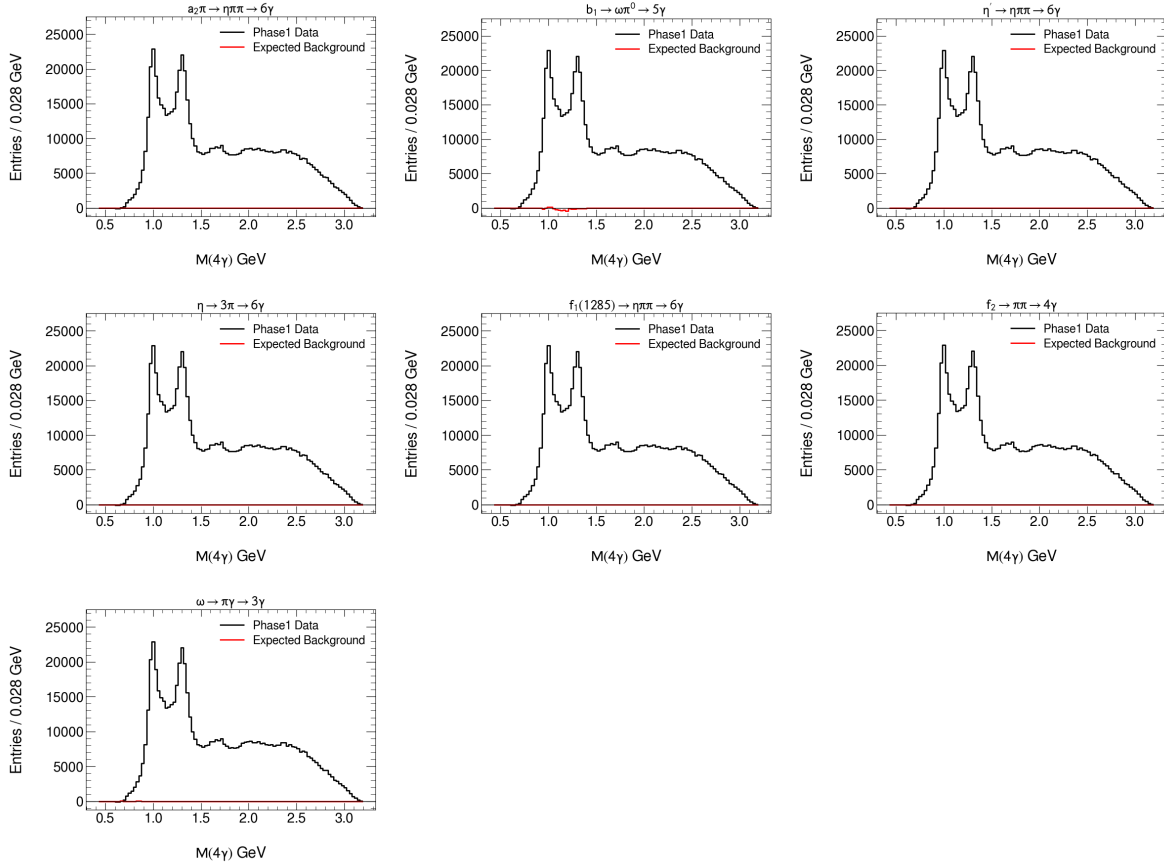
Figure 3.21: Expected leakage from other multi-photon final state channels. The estimated background is overlaid on top of the Phase-I $\eta\pi^0$ dataset. This estimation takes the central yield estimates and adds 3 times the stat. errors on top of it. Accidentals and $M(2\gamma)$ sidebands are subtracted.
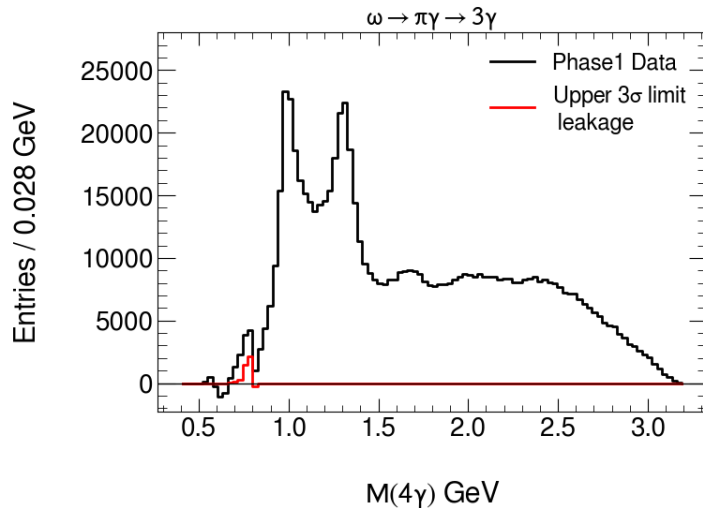
Figure 3.22: Figure showing the performance of the LMAC selection. The red distribution shows the expected leakage from $\omega \to \pi^0\gamma \to 3\gamma$ into $\eta\pi^0 \to 4\gamma$. This estimation takes the central yield estimates and adds 3 times the statistical errors on top of it. The black distribution is the Phase-I data with the same selection applied.

Figure 3.21 show the expected background leakage from each channel overlaid with the Phase-I data where accidentals and $M(2\gamma)$ sidebands are subtracted. Subtracting the mass sidebands significantly reduces the leakage from the b_1 channel. Additional details regarding the branching ratios of the decay chain and the values for the efficiency and integrated flux can be found in Appendix A.4.

Figure 3.22 shows the expectations from the $\omega \to \pi^0\gamma$ channel where the LMAC selection, showcased in Section 3.4.2, is not applied. The leakage from the ω channel after sidebands and accidentals are subtracted roughly reproduces what is seen in data. The remaining dip at the lowest masses is most likely due to $\pi^0\pi^0$ contributions below the $f_2(1270)$, perhaps from the $f_0(980)$. $\pi\pi$ contributions can be seen in data, as shown in Figure 3.13, and can be separated by the LMAC selection. The threshold region can be important if one wishes to study the $a_0(980)$ but is outside the region of interest for this dissertation.

3.6 Summary of Event Selections

Analysis Library Selections	Default Selections: see Section 3.2.2
Beam Energy Selections	$8.2 < E_\gamma < 8.8$ GeV
Charged Track Selections	$\left\|\vec{P}\right\| \geq 0.3$ GeV $\cdot c^{-1}$ 52 cm $\leq d_z \leq 78$ cm $\frac{dE}{dx}\|_{\text{CDC}} \geq 10^{-6}\left(0.9 + e^{3.0 - \frac{3.5[\|\vec{P}\|+0.05]}{0.93827}}\right)$
Neutral Shower Selections	$E \geq 0.1$ GeV $2.5^o \leq \theta \leq 10.3^o \qquad \theta > 11.9^o$
Exclusivity Selections	Unused Energy $= 0.0$ GeV Missing Mass Squared ≤ 0.05 GeV^2 $\chi^2 \leq 13.3 \qquad with\ 4\ DOF$
Event Counting	Accidental Subtraction: see Equation 3.7 Sideband Subtraction: see Table 3.3

Table 3.5: Table of Event Selections
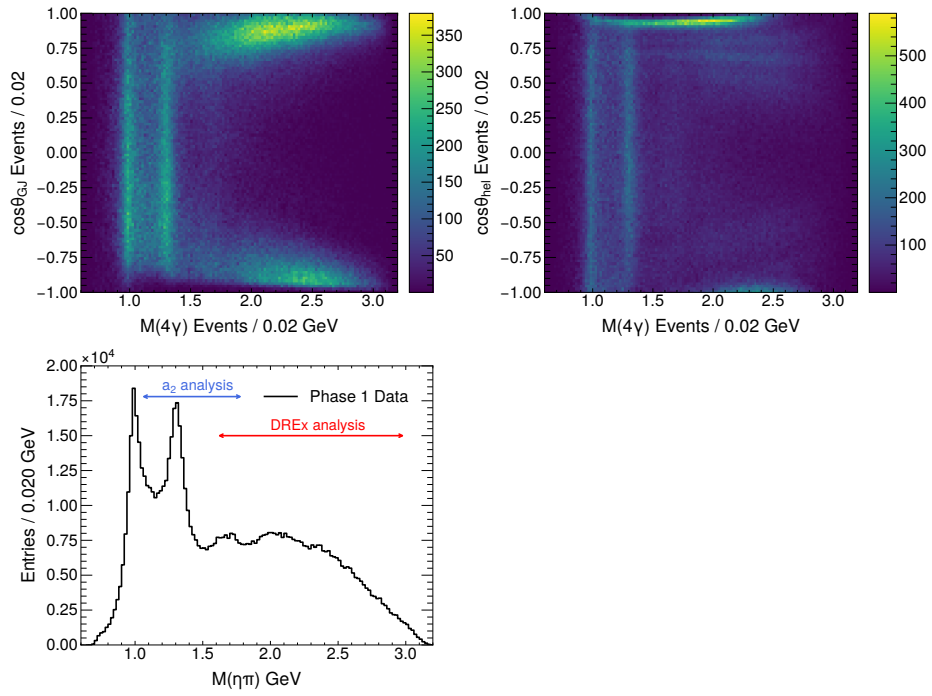
Figure 3.23: Distributions of $\cos\theta_{GJ}$ vs $M(4\gamma)$, $\cos\theta_{hel}$ vs $M(4\gamma)$, and $M(4\gamma)$.

3.7 Kinematic Distributions and Baryonic Contributions

Fig. 3.23 shows the current $\cos\theta_{GJ}$ vs $M(\eta\pi)$, $\cos\theta_{hel}$ vs $M(\eta\pi)$, and $M(\eta\pi)$ distributions. θ_{GJ} and θ_{hel} refers to the polar angle of the η in the Gottfried-Jackson or Helicity systems [72], which are in the $\eta\pi$ rest frame(Section 4.3 discusses this further). Several peaks and shoulders can be seen in the $M(\eta\pi)$ distribution, similar to previous experiments discussed in Section 1.5.

From here, the dissertation diverges into two separate but complementary analyses that aim to build the foundation for future searches of the π_1. The first analysis focuses in on a region around 1.3 GeV where the $a_2(1320)$ is dominant. Since the π_1 is expected to be a broad resonance peaking around 1.4 GeV in this channel, studying the nearby $a_2(1320)$ is important as it can act as a reference in determining any exotic contributions. The $a_2(1320)$ has been extensively studied in the past, which can provide guidance and verification of analysis procedures. To this end, Chapter 4 will discuss the measurement of the differential cross section of the $a_2(1320)$.

The second analysis studies the $M(\eta\pi) > 1.6$ GeV region. The main feature of this region can be seen in the angular distribution where most events are concentrated near $\cos(\theta_{GJ}) \approx \pm 1$. This region can be described by double Regge exchanges, see Section 1.3.2. Chapter 5 introduces the measurement of the top-vertex beam asymmetries, which will shed light on the relative contributions of natural and unnatural parity exchange (see Section 1.2). Knowing the relative contributions will aid in the development of theoretical models that can be used to understand this process's contribution to the exotic partial waves that the π_1 should occupy.

In both of these studies, baryon contributions are expected to be significant. Figure 3.24 show the reaction of interest along with diagrams depicting examples of the double Regge exchange process and of baryon production. Figure 3.25 shows distributions for the momentum transfer t, $M(\pi p)$, and $M(\eta p)$ as seen in the Phase-I data. There are 4 prominent peaks in the $M(\pi^0 p)$ distribution, the main one being the $\Delta(1232)$. The strongest resonance in the ηp system is the $N(1535)$ which only appears at large $M(\eta\pi)$. The red curve denotes the region where a_2 will be studied, whereas the blue curve signifies the region where the double Regge process will be studied. A section will be dedicated to the discussion of baryons in their respective Chapters.
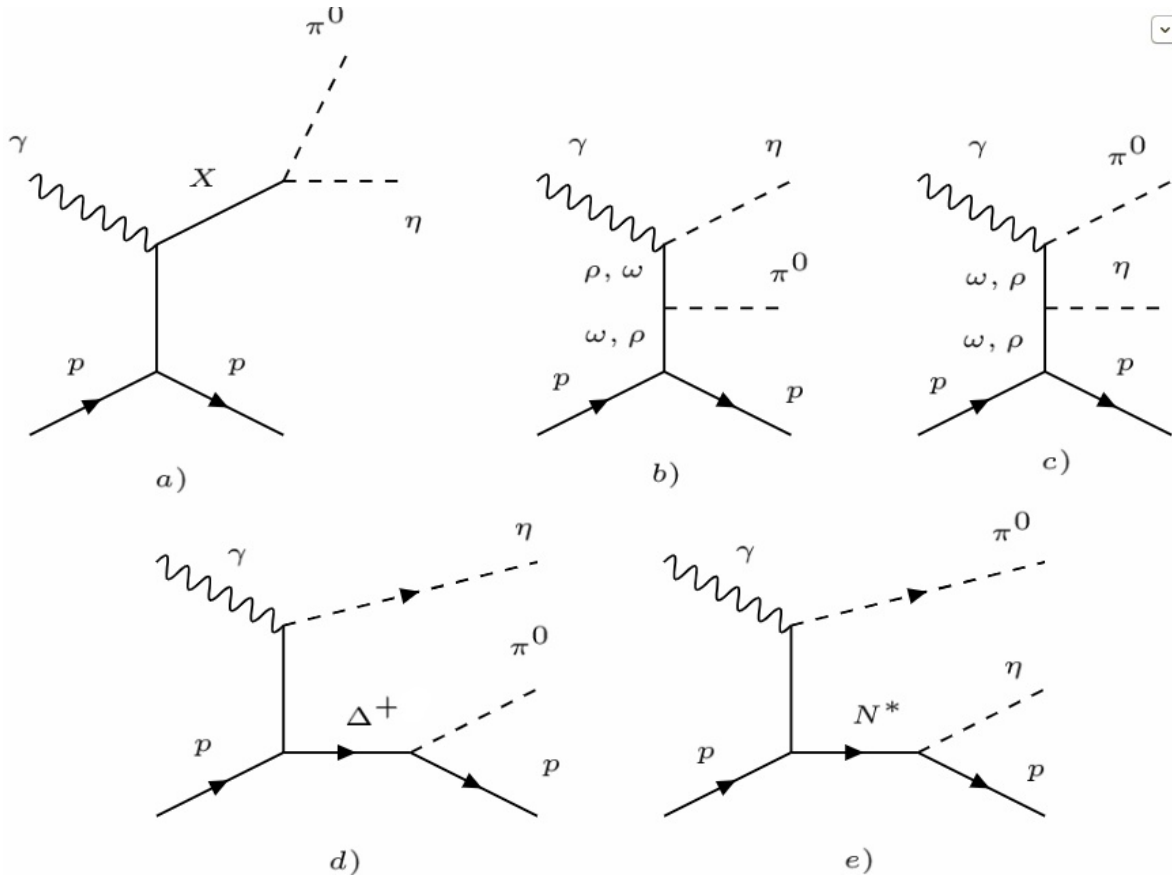
Figure 3.24: Diagram of the reaction of interest,$\gamma p \to \eta \pi^0 p \to 4\gamma p$, along with potential backgrounds that share the same final state. Figures (b)(c) are examples of double Regge exchange diagrams where the η or π^0 is produced at the upper vertex. Figure (d) is an example of a baryon resonance in the $\pi^0 p$ system, i.e. Δ^+. Figure (e) is an example of a baryon resonance in the ηp system.
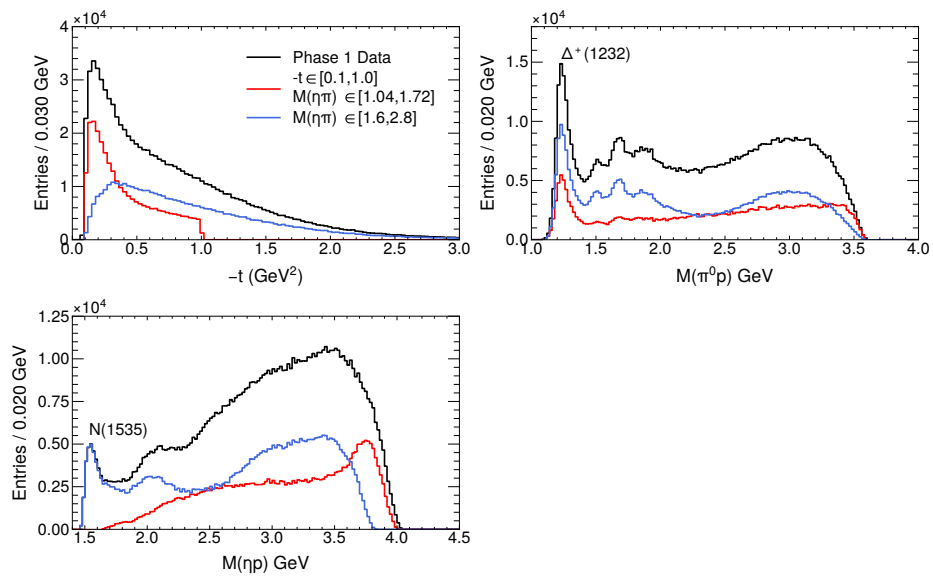
Figure 3.25: Distributions of the momentum transfer, $M(\pi p)$ and $M(\eta p)$ for the Phase-I data (black), for low-t meson production region for the a_2 study (red), and for the double Regge study that will be performed at high $M(\eta\pi)$.

CHAPTER 4

PRODUCTION OF THE $a_2(1320)$ MESON

4.1 Introduction

The two strongest resonances that are seen in the GlueX $\eta\pi^0$ spectrum are the $a_0(980)$ and $a_2(1320)$ mesons. There is a feature around 1.7 GeV that is likely to be a contribution from the $a_2(1700)$. The $a_0(980)$ takes on a complicated lineshape as a function of $M(\eta\pi)$ as it is right on top of the $K\bar{K}$ threshold. The Flatté lineshape is typically used in those cases as was done in Ref. [79]. The $a_0(980)$ is also a spin-0 particle that produces isotropic decay products which can be more easily imitated by other backgrounds. These complications are minimized in the case of the $a_2(1320)$ meson. There are no nearby threshold openings and being a spin-2 particle, the decay has distinct decay angular distributions. As a relatively isolated resonance, a standard relativistic Breit-Wigner parameterization can be used to describe the lineshape. The first thrust of this dissertation is to study the production of $a_2(1320)$ meson. Understanding its production will be essential in extracting exotic signatures for the π_1, which are expected to be small in intensity and close by in mass, around 1.4 GeV in this channel. To this end, the differential cross section for the photoproduction of the $a_2(1320)$ meson will be measured in 5 t-bins from $-t \in [0.1, 1.0]\text{GeV}^2$ at GlueX.

4.1.1 Brief History of the a_2 Mesons

Historically, resonances that were observed decaying to $\pi^+\pi^-\pi^+$ around 1 GeV were given the name, A[81]. Bubble chamber experiments in the 1960s, studying the π^+p reaction scattering into $\pi^+\pi^-\pi^+p$, saw evidence for a broad resonance around 1.27 GeV originally designated the $A(1270)$ decaying into $\rho\pi$ [82]. Additional bubble chamber experiments were able to resolve the broad resonance into two separate states [83][84], the A_1 and the A_2. These resonances are now known as the $a_1(1260)$ and the $a_2(1320)$, respectively, after the Particle Data Group (PDG) introduced a systematic method of naming hadrons in 1984 [85]. In this system, the a mesons would have $I = 1$, $S = 1$ and odd-L. Since then, the $a_2(1320)$ has been studied extensively and has been primarily observed in the 3π, $K\bar{K}$, $\eta'\pi$, and $\eta\pi$ final states. The lineshape of this resonance is well described by a relativistic Breit-Wigner. Numerous experiments have determined the resonance parameters
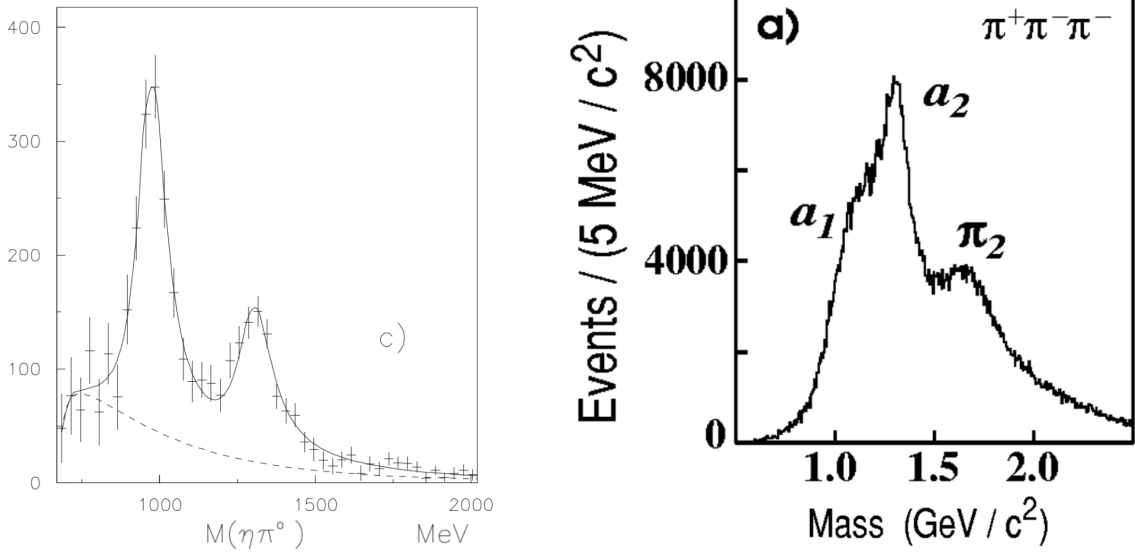
Figure 4.1: (Left) The acceptance corrected invariant mass spectrum for centrally produced $\eta\pi^0$ events as observed in the WA102 experiment[79]. (Right) Acceptance corrected $\pi^+\pi^-\pi^-$ invariant mass distribution as observed in the E852 experiment[80].

for a_2 decaying into the $\eta\pi$ final state, i.e. Refs. [79][86][80][87]. Figure 4.1 shows an example invariant mass spectrum from pp central production by WA102 Collaboration and pion production by the E852 Collaboration.

The coupled channel analysis of the COMPASS data by JPAC, shown in Figure 1.13, provides a sophisticated determination of the resonance parameters of the $a_2(1320)$, $a_2(1700)$, and the π_1. This analysis studies the poles of the amplitude in the complex plane, s_P, which can then be related to the mass, $m = \mathrm{Re}\sqrt{s_P}$, and width, $\Gamma = -2\,\mathrm{Im}\sqrt{s_P}$. Figure 4.2 shows the position of the poles, and therefore their resonance properties, and are identified as the $a_2(1320)$, $a_2(1700)$, and the π_1.

Evidence for an excited a_2 was seen by the Crystal Barrel experiment in 1994 in their analysis of the $\pi^0\pi^0\eta$ Dalitz plot [87] and was observed in their partial wave analysis of the $\pi^0\eta\eta$ final state [88] around 1660 MeV. In a follow-up to both these analyses, a coupled channel analysis was performed including $\pi^0\pi^0\pi^0$ data with the previous two reactions [89] and found that the mass of the excited a_2 was around 1700 MeV. This analysis is currently the only study that the PDG uses in their average to determine the resonance parameters for the $a_2(1700)$. The $a_2(1320)$ and $a_2(1700)$ share the same quantum numbers and therefore can populate the same set of partial waves. Isolating the contributions from only the $a_2(1320)$ to determine its cross section would require modeling for the $a_2(1700)$.
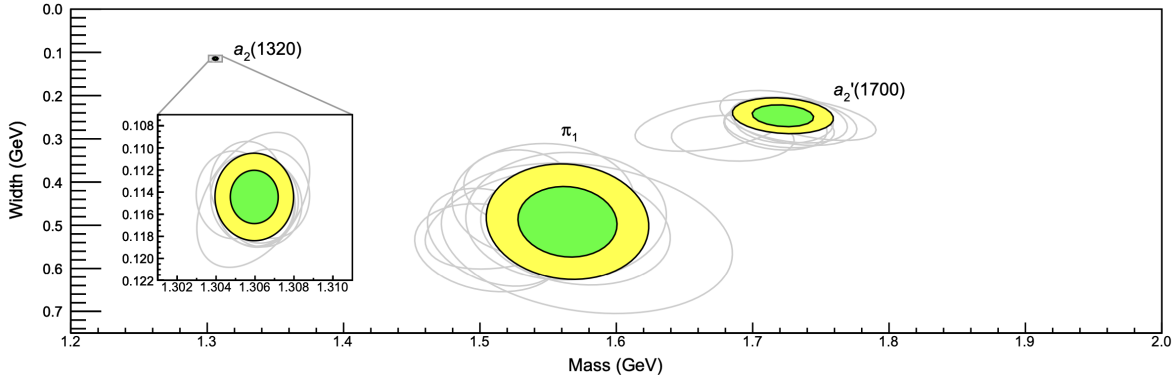
Figure 4.2: Positions of the poles identified as the $a_2(1320)$, π_1, and $a_2(1700)$. The inset shows the position of the $a_2(1320)$. The green and yellow ellipses show the 1σ and 2σ confidence levels, respectively. This figure is reproduced from Reference [33]

4.1.2 Previous Photoproduction Cross Section Measurements

Photoproduction cross section data for $\gamma p \to \eta \pi^0 p$ exists for low energies (<2.5 GeV). The data was collected by multiple experiments: GRAAL [93], Crystal Ball [94], CB-ELSA [95], and the A2 Collaboration [96], to name a few. The spectrum is mainly dominated by baryon resonances, but around $E_\gamma \sim 2$ GeV the $a_0(980)$ begins to appear. The only photoproduction cross section data that currently exists for this channel at the higher energies where meson production is dominant were measured by CLAS [90]. The beam was unpolarized. Their spectrum contains contributions from the $a_0(980)$ and also the $a_2(1320)$. The differential cross section for the $a_2^0(1320)$ was measured in the 4-5 GeV energy range. Figure 4.3 shows $d\sigma^2/dt dM$ as a function of the $\eta \pi^0$ invariant mass. A clear signature for the $a_2(1320)$ can be seen. The differential cross section, $d\sigma/dt$, is obtained by integrating the resonance term in each kinematic bin. The results are shown in Figure 4.4.

Based on these results, a model based on Regge theory was developed by the Joint Physics Analysis Center (JPAC) [91] that describes the features of the cross sections of the a_2^0 and f_2 where the f_2 cross sections have been extracted from the CLAS $\pi^+\pi^-$ partial wave analysis results [97]. Predictions for the cross section, parity asymmetry, and partial wave contributions in the production of these tensor mesons are made for $E_\gamma = 8.5$ GeV using the so-called "minimal" and "tensor meson dominance" (TMD) models. These models differ in the form of the Regge couplings which describe the interaction between the beam photon, the tensor meson, and an exchanged vector meson. The "minimal" model, which draws inspiration from effective field theories (EFTs), prescribes neglecting terms involving particle momenta due to their correspondence to higher derivative interactions in
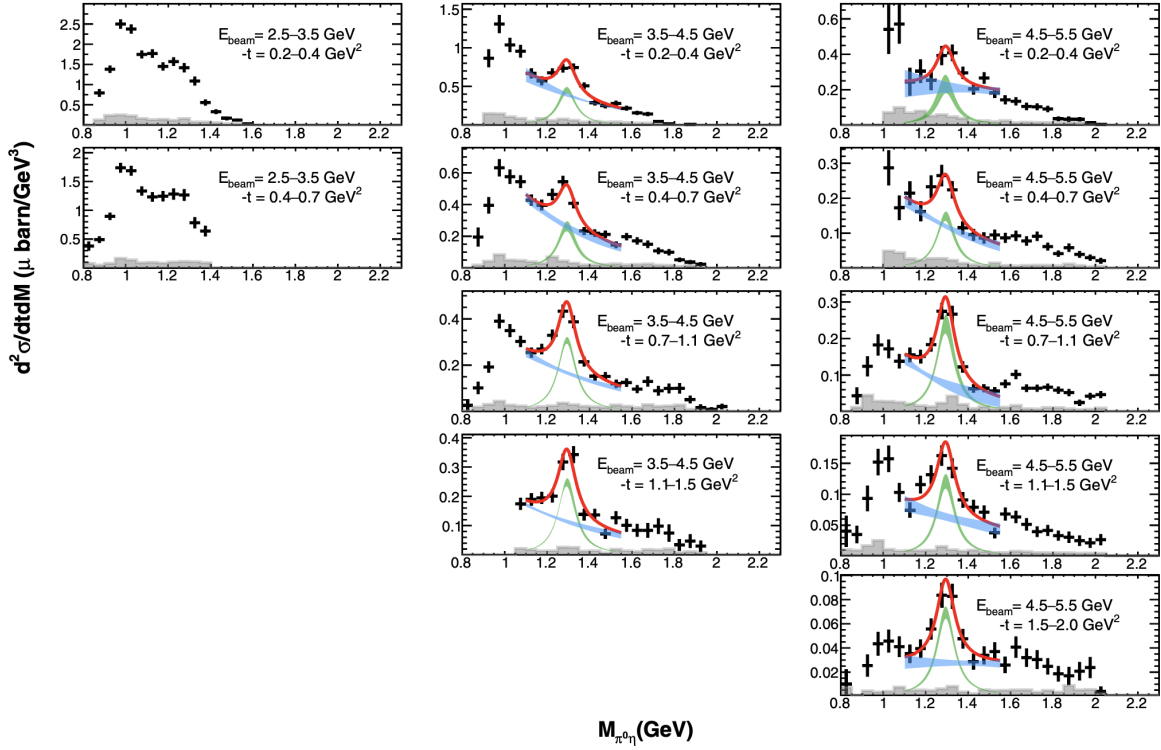
Figure 4.3: Differential cross section for the reaction $\gamma p \rightarrow \eta \pi^0 p$ as observed by CLAS. Each histogram reports the reaction differential cross-section $d\sigma^2/dtdM$ as a function of the $\eta \pi^0$ invariant mass for the specific E_{beam} and $-t$ bin reported in the same panel. The bottom gray-filled area in each panel shows the systematic uncertainty. The red curve is the result of the best fit performed with the model described in the text. The green and blue areas correspond, respectively, to the contribution of the a2 resonance and of the background, here, reported as the $\pm 1\sigma$ systematic uncertainty bands around the central value. These have been scaled vertically by a factor of x2 for better readability. This figure is reproduced from Ref. [90].
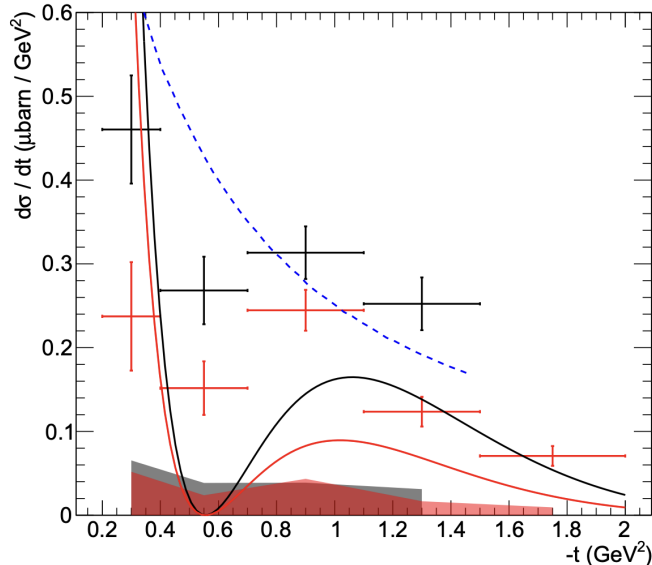
Figure 4.4: Differential cross section $\frac{d\sigma}{dt}$ for the reaction $\gamma p \rightarrow a_2(1320)p$ for $E_\gamma = 3.5 - 4.5$ GeV (black) and $E_\gamma = 4.5 - 5.5$ GeV (red). The continuous lines are predictions from the JPAC model [91], computed respectively for a beam energy of 4 GeV (black) and 5 GeV (red). The blue dashed line is the prediction from the model by Xie et al. [92], for beam energy 3.4 GeV. For better readability, this was scaled vertically by a factor $\times 0.5$. This figure is reproduced from Ref. [90].

the EFT Lagrangian. The TMD model assumes the tensor meson couples to a vector field through the stress-energy tensor[98].

Previous GlueX beam asymmetry, Σ, measurements have shown a strong dominance of natural parity exchange in the production of neutral mesons, see Section 5.5. The minimal model suggests overwhelming production of a_2 through unnatural parity exchange, which is contrary to these previous measurements. The TMD model has a better description of the a_2 cross section measurements by CLAS and predicts a dominance of natural parity exchange. The measured differential cross section at GlueX will be compared to the TMD predictions and the lower energy CLAS data.

4.2   Additional Event Selections

4.2.1   Restricting $M(\eta\pi)$

From the PDG, the a_2 is seen to have a mass of around 1.317 GeV with a width of 111 MeV as seen in $\eta\pi$ channel. For the measurement of the a_2 cross section, the region $1.04 < M(\eta\pi) < 1.72$ GeV is chosen as a general selection. The lower bound is chosen to include most of the a_2 lineshape, but also to exclude the a_0 peak. The upper bound is chosen to include a wide enough area to accommodate
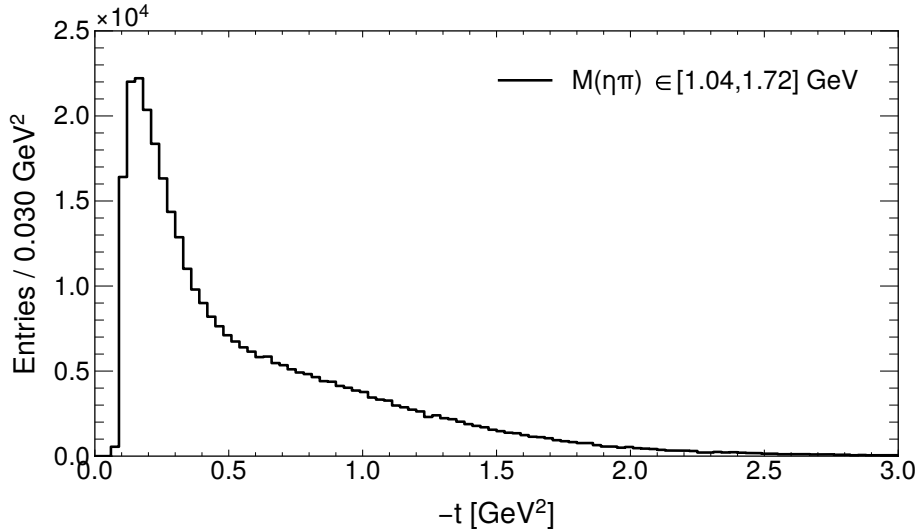
Figure 4.5: Momentum transfer, $-t$, distribution in the Phase-I dataset.

the presence of the $a_2(1700)$ while avoiding the higher mass region where double Regge and baryon process become more predominant.

4.2.2 Meson production

At GlueX energies, the production of the $a_2(1320)$ is expected to proceed through the exchange of Reggeons. These diffractive reactions are characterized by small values of momentum transfer, t[1]. Figure 4.5 shows the t distribution for the GlueX Phase-I dataset. As we aim to measure the differential cross-section in the range $-t \in [0.1, 1.0]$ GeV^2, the following selection is made

$$0.1 \text{ GeV}^2 < -t < 1.0 \text{ GeV}^2 \tag{4.1}$$

4.2.3 Baryon Removal

Baryons are an important background that needs to be kinematically separated. Figure 3.24 shows the reaction of interest, potential baryon diagrams, and potential double Regge exchange processes that lead to the same $\eta\pi p$ final state. The black curves of Figure 4.7 show the $M(\pi p)$ distribution binned in momentum transfer. Several Δ resonances can be seen. The $\Delta^+(1232)$ can be somewhat efficiently removed, with a selection requiring $M(\pi^0 p)$ to be greater than 1.4 GeV. On the other hand, the heavier Δ's share the $M(\pi p)$ region with a significant signal underneath making a threshold selection quite wasteful.
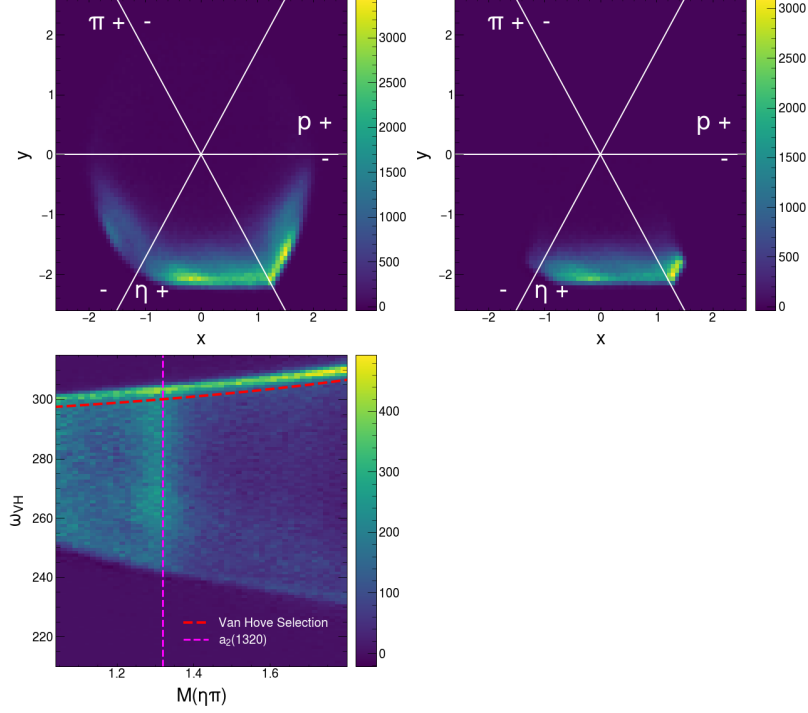
Figure 4.6: Top row shows a Van Hove plot for the selected GlueX $\eta\pi^0$ data with(right) and without(left) an extra selection on $1.04 < M(\eta\pi) < 1.72$ GeV. The bottom plot shows a mass-dependent Van Hove selection to remove $\pi^0 p$ baryons.

Longitudinal Momentum Space. The distribution of momenta among final state particles is process dependent. One way, proposed back in 1969 by Leon Van Hove, was to make selections based on the longitudinal phase space [99]. The idea was that at high center of mass energies, final state particle momenta are dominated by longitudinal components, allowing for the transverse components to be ignored. The Van Hove plot is made in the center of the mass frame with the z-axis aligned to the beam momentum. For 2-to-3 body scattering, a Van Hove plot is described in polar coordinates with radius $q = (q_1^2 + q_2^2 + q_3^2)^{1/2}$ and polar angle ω satisfying the equations

$$
\begin{aligned}
q_1 &= \sqrt{\frac{2}{3}} q \sin(\omega), \\
q_2 &= \sqrt{\frac{2}{3}} q \sin(\omega + \frac{2}{3}\pi), \\
q_3 &= \sqrt{\frac{2}{3}} q \sin(\omega + \frac{4}{3}\pi)
\end{aligned}
\tag{4.2}
$$

Zero longitudinal momenta, $q_i = 0$, lines divide the two-dimensional space into 6 triangular sectors, each spanning 60 degrees. The top row of plots of Figure 4.6 shows a Van Hove plot for the

selected GlueX $\eta\pi^0$ data with(right) and without(left) an extra selection on $1.04 < M(\eta\pi) < 1.72$ GeV. A line exists for each final state particle where forward-going and backward-going are on opposite sides. The sector defined by $300 < \omega < 360$ has a backward-going π, a backward-going proton, with a forward-going η. $\pi^0 p$ resonances, like the $\Delta^+(1232)$, recoiling against an η would typically populate this region. The sector defined by $240 < \omega < 300$ has forward-going π and η recoiling against a backward-going proton. The production of a resonance that decays to $\eta\pi$ would typically populate this region, i.e. the a_2. ηp resonances, like the $N(1535)$ would populate the sector defined by $240 < \omega < 300$. In the $1.04 < M(\eta\pi) < 1.720$ region of interest, it appears that only $\pi^0 p$ baryons exist. A Van Hove analysis of the photoproduction of another two pseudoscalar system, K^+K^-, in regard to the double Regge exchange process can be found in Reference [100].

Heavier resonances can leak out into neighboring sectors due to the larger phase space it can have access to. Therefore, a simple sector selection can be too aggressive. A mass-dependent longitudinal phase space selection is developed in Reference [101] to separate out hyperon decays from the production of meson resonances in the two pseudoscalars K^+K^- system. Their approach modifies the sector selection to be between $\rho_{low} < \rho < \rho_{up}$ where ρ takes into account the potential isobar mass. Performing a selection for meson production combined with another selection to reject baryon production provides a significant improvement over a simple sector selection. For the analysis of the a_2, several Δ resonances can be seen in Figure 4.7, but the resonances appear shifted and significantly overlapping. Since these isobar masses are an input to the procedure, it can be hard to properly determine the ρ sectors.

A data-driven approach is taken here and is shown in the bottom plot of Figure 4.6 where ω is plotted against $M(\eta\pi)$. A few features can be seen in the region of interest. The $a_2(1320)$ can be seen as a vertical band spanning basically the entire meson production sector, $240 < \omega < 300$. A strong band appears above $\omega > 300$ corresponding to Δ resonances which can be removed by requiring

$$\omega < -29.0 \operatorname{atan}(-1.05 * M(\eta\pi) + 2.78) + 328 \tag{4.3}$$

The results of the selection can be seen in Figure 4.7 and is binned in momentum transfer, t. The heavier Δ resonances and the $\Delta(1232)$ are removed with this Van Hove selection.

Figure 4.8 show the $cos\theta_{GJ}$ and $cos\theta_{hel}$ vs $M(4\gamma)$ and $M(4\gamma)$ after applying the selections on t and Van Hove angle. Compared to Figure 3.23, much of the features in the forward direction($cos\theta$=+1) have been removed.
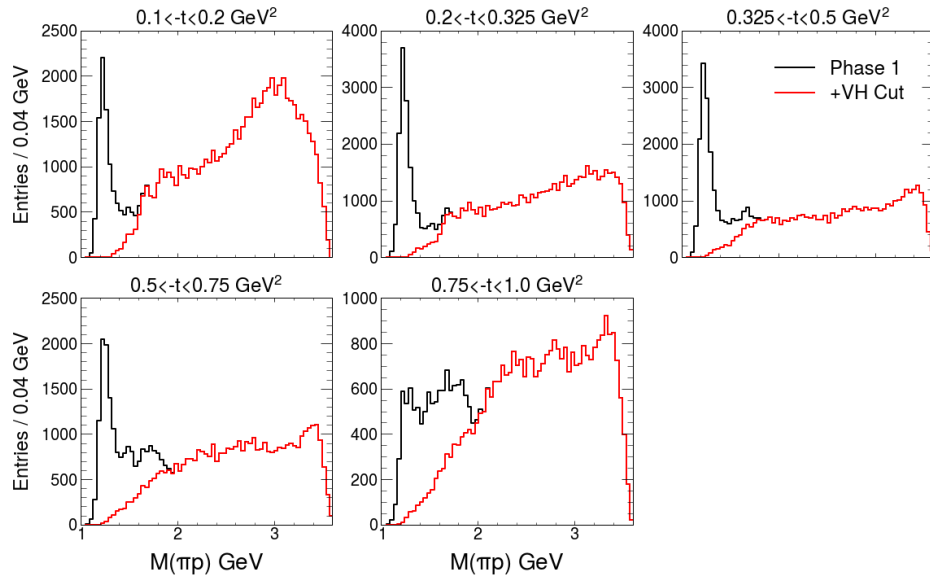
Figure 4.7: Distributions of $M(\eta\pi)$ in five bins of momentum transfer with and without a selection on the Van Hove angles.
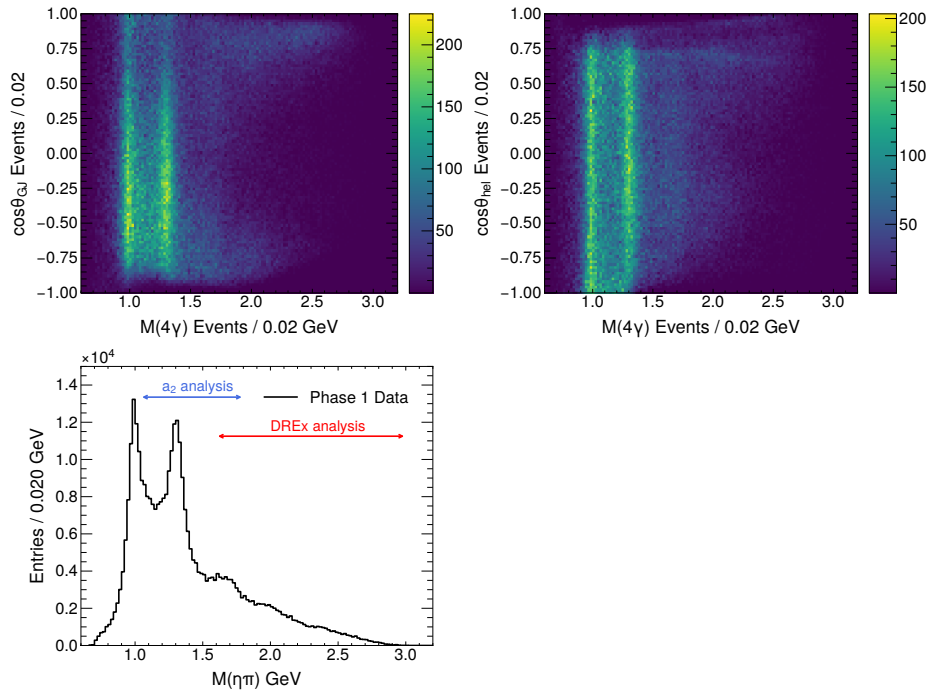
Figure 4.8: Distributions of $\cos\theta_{GJ}$ vs $M(4\gamma)$, $\cos\theta_{hel}$ vs $M(4\gamma)$, and $M(4\gamma)$ after selecting on $-t < 1$ and performing the Van Hove selection.

4.3 Coordinate Systems

The so-called helicity system and Gottfried-Jackson (GJ) system are in the reference frame where the intermediate resonance, X, is at rest. They simply differ by a rotation. A diagram of the helicity frame is shown in Fig. 4.9. The z-axis is aligned in the direction of the momentum of X. The y-axis is defined by the normal of the reaction plane. The reaction plane is the plane that is spanned by the momentum of the incident photon beam and the momentum of the recoiling proton. ϵ is the beam polarization angle and Φ is the angle between the polarization angle and the reaction plane. η and ϕ are the polar and azimuthal angles. For the GJ system, the z-axis is aligned in the direction of the momentum of the beam.
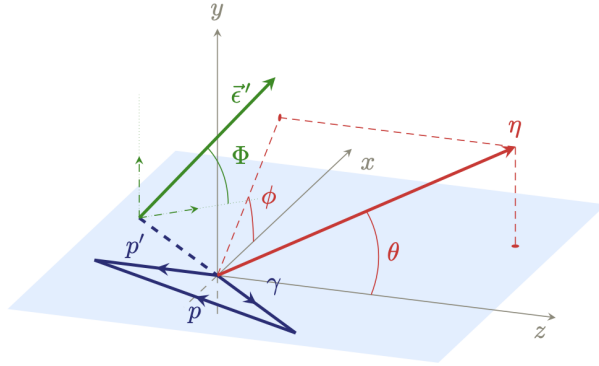
Figure 4.9: Depiction of the helicity frame as seen in [102].

4.4 Partial Wave Analysis

A general overview of partial wave analysis is presented in Reference [1]. Some important points will be discussed here. The intensity distribution of events produced in a reaction with an n-body final state with total invariant mass, m_X, and momentum transfer, t', is given by

$$I(m_X, t', \tau_n) = \frac{\mathrm{d}N}{\mathrm{d}m_X \, \mathrm{d}t' \, \mathrm{d}\Phi_n(m_X, \tau_n)} \propto m_X |M_{fi}(m_X, t', \tau_n)|^2 \tag{4.4}$$

where $t' = t - t_{min}$ represents the momentum transfer shifted by the minimum value of t. The shift is given by $t_{min} = m_1^2 + m_3^2 - 2(E_1 E_3 \mp |\boldsymbol{p_1}||\boldsymbol{p_2}|)$ following the notation given in Fig. 4.10.

N is the number of produced events and the differential phase space element is defined as

$$\mathrm{d}\Phi_n(m_X, \tau_n) = \rho_n(m_X, \tau_n) \, \mathrm{d}\tau_n \tag{4.5}$$

with $\rho_n(m_X, \tau_n)$ being the phase space density and τ_n as the phase space variables. The amplitude, M_{fi}, can be factorized into three parts: a production amplitude that characterizes the production of X, a dynamical part that represents its propagation, and a decay amplitude that represents its decay. This is given by

$$M_{fi}(m_X, t', \tau_n) = P(m_X, t') D_X(m_X) \Psi(m_X, \tau_n) \tag{4.6}$$

The production amplitude, $P(m_X, t')$, for the resonance X depends on the process and is only partly known. An approximate production amplitude can be used where the rest of the unknowns features are absorbed into a coupling amplitude, $C_X(t')$. Partial wave contributions from the decays of resonances that have the same final state need to be coherently summed. The amplitude can be rewritten as

$$M_{fi}(m_X, t', \tau_n) = P(m_X, t') \sum_i^{N_{waves}} \left[\sum_{k \in S_i} C_{ki}(t') D_X(m_X) \right] \Psi(m_X, \tau_n) \tag{4.7}$$
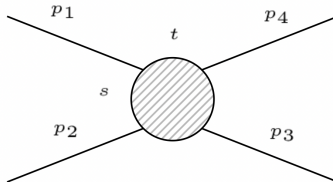
Figure 4.10: Generic 2-to-2 scattering where $p_1 + p_2 \rightarrow p_3 + p_4$. Mandelstam variables s,t are defined such that $s = p_1 + p_2$ and $t = p_3 - p_1$.

where i sums over the partial waves and k sums over the subsets of resonances that decay into a given partial wave. Equations 4.4 and 4.7 can be combined to obtain

$$I(m_X, t', \tau_n) = \left| \sum_{i}^{N_{waves}} \sqrt{(m_X)} P(m_X, t') \left[\sum_{k \in S_i} C_{ki}(t') D_X(m_X) \right] \Psi(m_X, \tau_n) \right|^2 \qquad (4.8)$$

The dynamical part for isolated isobar resonances can be approximated by a relativistic Breit-Wigner amplitude with dynamical width given by

$$\mathcal{D}_X^{\text{BW}}(m_X; m_0, \Gamma_0) = \frac{m_0 \Gamma_0}{m_0^2 - m_X^2 - i m_0 \Gamma(m_X)} \quad \text{with} \quad \Gamma(m_X) = \sum_{j}^{\substack{\text{decay} \\ \text{modes}}} \Gamma_j \frac{q_j}{m_X} \frac{m_0}{q_{j,0}} \frac{F_{L_j}^2(q_j)}{F_{L_j}^2(q_{j,0})} \qquad (4.9)$$

where m_0 and Γ_0 are the nominal mass and total width of the resonance, X. F_{L_j} is the barrier factor which encodes the centrifugal barrier from the orbital angular momentum L_j between the decay products. For the decay into two spinless particles, the decay amplitude reduces to

$$\widetilde{\Psi}_{X \to 1+2}(m_X, \vartheta_{\text{GJ}}, \phi_{\text{GJ}}) = \alpha_{X \to 1+2} F_J(m_X) Y_J^M(\vartheta_{\text{GJ}}, \phi_{\text{GJ}}) \qquad (4.10)$$

where α encodes the strength and relative phase of the decay mode, F is again the barrier factor where $L_j = J$, Y_L^M are the spherical harmonics, and GJ represents the Gottfried-Jackson frame. From here it is possible to perform a global fit. There can be difficulties in accomplishing this in that, generally, the set of resonances, the resonance parameters, and the coupling parameters are generally unknown. It is possible to include insights from previous experiments, as will be done for the measurement done in this dissertation.

4.4.1   Polarized amplitudes

The formalism for the polarized decay amplitudes that are used in this dissertation is described in [102][103]. These amplitudes were developed to study the $\eta\pi$ angular distributions in polarized photoproduction at GlueX. The production amplitude is not explicitly modeled but should not significantly affect the results as we bin in beam energy and t. A brief summary is given below.

The differential cross section is given by

$$I(\Omega, \Phi) = \frac{d\sigma}{dt \, dm_{\eta\pi} \, d\Omega \, d\Phi} \qquad (4.11)$$

where t is the momentum transfer, $m_{\eta\pi}$ is the $\eta\pi$ invariant mass, Ω is the solid angle, and Φ is the angle between the polarization plane and reaction plane. This can be rewritten explicitly as

$$I(\Omega, \Phi) = I^0(\Omega) - P_\gamma I^1(\Omega)\cos2\Phi - P_\gamma I^2(\Omega)\sin2\Phi \tag{4.12}$$

where $P_\gamma \in [0,1]$ is the fraction of linear beam polarization and

$$I^0(\Omega) = \frac{\kappa}{2}\sum_{\lambda,\lambda_1,\lambda_2} A_{\lambda,\lambda_1,\lambda_2}(\Omega)A^*_{\lambda,\lambda_1,\lambda_2}(\Omega)$$

$$I^1(\Omega) = \frac{\kappa}{2}\sum_{\lambda,\lambda_1,\lambda_2} A_{-\lambda,\lambda_1,\lambda_2}(\Omega)A^*_{\lambda,\lambda_1,\lambda_2}(\Omega) \tag{4.13}$$

$$I^2(\Omega) = i\frac{\kappa}{2}\sum_{\lambda,\lambda_1,\lambda_2} \lambda A_{-\lambda,\lambda_1,\lambda_2}(\Omega)A^*_{\lambda,\lambda_1,\lambda_2}(\Omega)$$

Here, κ contains kinematical factors and are irrelevant to the intensity as the intensity will be renormalized during the fit procedure. λ is the photon beam helicity and A is the $\eta\pi^0$ amplitude. The helicity partial wave amplitudes, T_{lm}, follow the relation

$$A_{\lambda,\lambda_1,\lambda_2}(\Omega) = \sum_{lm} T_{\lambda m;\lambda_1\lambda_2}Y_l^m(\Omega) \tag{4.14}$$

where Y_l^m are the spherical harmonics. It is convenient to change the helicity amplitudes to the reflectivity, ϵ, basis. At high energies, amplitudes with ϵ=+1(-1) are dominated by t-channel with naturality, η, equal to +1(-1). This is given by,

$$^\epsilon T_{\lambda m;\lambda_1\lambda_2}^l = \frac{1}{2}[T_{+1m;\lambda_1\lambda_2}^l - \epsilon(-1)^m T_{-1-m;\lambda_1\lambda_2}^l] \tag{4.15}$$

These amplitudes are invariant under parity such that

$$^\epsilon T_{m;-\lambda_1-\lambda_2}^l = \epsilon(-1)^{\lambda_1-\lambda_2}\,^\epsilon T_{m;\lambda_1\lambda_2}^l \tag{4.16}$$

allowing two sets of partial waves, corresponding to nucleon helicity flip and non-flip, to be defined and are given by

$$[l]_{m,0}^{(\epsilon)} = {}^{(\epsilon)}T_{m,++}^l$$
$$[l]_{m,1}^{(\epsilon)} = {}^{(\epsilon)}T_{m,+-}^l \tag{4.17}$$

$[l]$ is the total spin of the $\eta\pi$ system. Inserting Equations 4.14, 4.15, and 4.17 into Equation 4.13 one arrives at

$$I(\Omega, \Phi) = 2\kappa\sum_k \left((1-P_\gamma)\left[\sum_{l,m}[l]_{m;k}^{(-)}\mathrm{Re}[Z_l^m(\Omega,\Phi)]\right]^2 + (1-P_\gamma)\left[\sum_{l,m}[l]_{m;k}^{(+)}\mathrm{Im}[Z_l^m(\Omega,\Phi)]\right]^2 \right.$$

$$\left. +(1+P_\gamma)\left[\sum_{l,m}[l]_{m;k}^{(+)}\mathrm{Re}[Z_l^m(\Omega,\Phi)]\right]^2 + (1+P_\gamma)\left[\sum_{l,m}[l]_{m;k}^{(-)}\mathrm{Im}[Z_l^m(\Omega,\Phi)]\right]^2 \right) \tag{4.18}$$
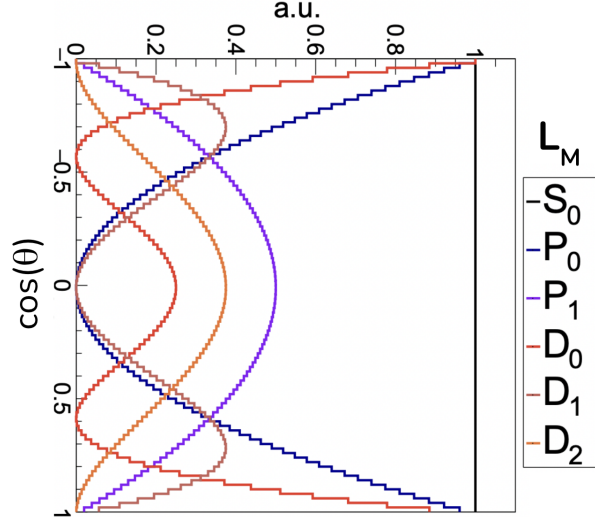
Figure 4.11: $\cos(\theta)$ distribution for select partial waves.

where a phase-rotated spherical harmonic, $Z_l^m(\Omega, \Phi) = Y_l^m e^{-i\Phi}$, has been substituted in. Here, k denotes the nucleon helicity flip and non-flip and there exist $2\ell+1$ complex partial waves for each. During the expansion, the intensity function was split into terms with definite reflectivity as sums over products of opposite reflectivity vanish. The current GlueX dataset does not permit a separation between the nucleon spin flip/non-flip. For this analysis, one k is assumed to be dominant.

In practice, the detector observes some number of signal events, $\mathbf{x}$. The probability density function is given by

$$P(\mathbf{x}; \Omega, \Phi) = I(\mathbf{x}; \Omega, \Phi)\eta(\mathbf{x}) \tag{4.19}$$

where η represents the probability that an event, with some kinematics, will be detected by the detector and pass all event selections. Figure 4.11 shows the $\cos(\theta)$ distribution for select partial waves in spectroscopic notation: S: $\ell = 0$, P: $\ell = 1$, D: $\ell = 2$, ..., etc. An S-wave decay results in a flat angular distribution whereas D-wave decay has two nodes. The angular distribution around the $a_2(1320)$ mass region in the GlueX Phase-I data, see Figure 4.8, is similar in shape to a D_2 partial wave.

95

4.4.2 Mass Dependence Formulation

Equation 4.18 does not include a dependency on the mass of the resonance. This is the case if the data can be finely binned such that the local mass dependence is flat. The data can be subsequently fitted to extract binned partial wave amplitudes. This is known as a *mass independent fit* and is a model-independent approach to describe the dynamics of the region of interest. This approach is typically more complicated as there can be a large number of degrees of freedom overall and can lead to non-smooth bin-to-bin results.

On the other hand, if there is good reason to, a *mass dependent fit* can be performed. We can rewrite Equation 4.18 to explicitly depend on the mass of the $\eta\pi$ system, M, as

$$
\begin{aligned}
I(\Omega, \Phi, M, \vec{x}) = 2\kappa \sum_k \Bigg(& (1 - P_\gamma) \left[\sum_{l,m} [l]_{m;k}^{(-)} F_l^{(}(M, \vec{x}) \operatorname{Re}[Z_l^m(\Omega, \Phi)] \right]^2 \\
& + (1 - P_\gamma) \left[\sum_{l,m} [l]_{m;k}^{(+)} F_{l,m;k}^{(+)}(M, \vec{x}) \operatorname{Im}[Z_l^m(\Omega, \Phi)] \right]^2 \\
& + (1 + P_\gamma) \left[\sum_{l,m} [l]_{m;k}^{(+)} F_{l,m;k}^{(+)}(M, \vec{x}) \operatorname{Re}[Z_l^m(\Omega, \Phi)] \right]^2 \\
& + (1 + P_\gamma) \left[\sum_{l,m} [l]_{m;k}^{(-)} F_{l,m;k}^{(-)}(M, \vec{x}) \operatorname{Im}[Z_l^m(\Omega, \Phi)] \right]^2 \Bigg) \quad (4.20)
\end{aligned}
$$

where $\vec{x}$ contains additional parameters that characterize the mass distribution, F.

4.5   Methodology

The experimental acceptance of the detector, introduced as $\eta(\mathbf{x})$ in the previous section, does not have a closed form description. To account for the acceptance, a large Monte-Carlo sample is required in the fitting procedure. The generation of the MC sample was discussed in Section 3.2.1. This sample is split into two datasets, `genmc` and `accmc`. The `genmc` sample contains the kinematics of the generated events. The `accmc` sample contains the kinematics of the corresponding events that has been passed through the GlueX detector simulation, reconstructed, and filtered by the event selections laid out in Chapter 3.

Partial wave analysis of the polarized datasets is carried out by performing an extended unbinned maximum likelihood fit. The `accmc` sample is weighted by the partial wave amplitudes (to be

optimized for) to match the observed data. This naturally incorporates the acceptance of the detector. The GlueX Phase-I data is also split into two datasets. The `data` sample contains all the events in the signal region as defined in the accidental and mass sideband subtraction procedure. The `bkgnd` sample contains all the events in the sideband regions. This prescription is implemented in the `AmpTools` framework.

$$-2\ln\mathcal{L}(\boldsymbol{\theta}) = -2\left(\sum_{i=1}^{N}\ln\mathcal{I}\left(\mathbf{x}_i;\boldsymbol{\theta}\right) - \int\mathcal{I}(\mathbf{x};\boldsymbol{\theta})\eta(\mathbf{x})d\mathbf{x}\right) \tag{4.21}$$

For numerical reasons, it is typical to minimize to $-2\ln\mathcal{L}$ instead of maximizing the likelihood, $\mathcal{L}$. Equation 4.21 shows the form of the log-likelihood function that is minimized. The intensity, $\mathcal{I}\left(\mathbf{x}_i;\boldsymbol{\theta}\right)$, is the model-predicted number of signal events per unit phase space. $\eta(\mathbf{x})$ is acceptance function. $\int\mathcal{I}(\mathbf{x};\boldsymbol{\theta})\eta(\mathbf{x})d\mathbf{x}$ is impossible to analytically compute as the acceptance function does not have a closed form description in general. Instead, Monte-Carlo integration is used to compute the integral. More information on the derivation of the likelihood and how weighted events are handled can be found in the `AmpTools User Guide` [104].

4.5.1 Mass Dependence Parameterization

Mass independent fits are model independent whereas mass depdendent fits are biased towards the model choice. For this analysis, a semi-mass independent fit approach is taken to describe the $1.04 < M(\eta\pi) < 1.72$ GeV region of interest. This region is completely dominated by the $a_2(1320)$ resonance and so a relativistic Breit-Wigner formulation for F in equation 4.20 is a good approximation. Equation 4.9 shows the form of the Breit-Wigner distribution used. $\vec{x}$ would be the mass and width of the resonance.

The $a_2(1320)$ peak sits on top of some background which is likely from the tail of the $a_0(980)$ and from additional non-resonant production processes. The exact mass dependence of this background is not assumed and will be modeled by a piecewise constant function, thereby mimicking the model independent nature of a mass independent fit for this contribution. The piecewise S-wave parameterization used in this measurement contains 40 MeV bins on the $1.04 < M(\eta\pi) < 1.72$ GeV interval chosen for this analysis. The piecewise function contains a single complex parameter for each mass bin. The bins centered on 1.22 act as the "anchor" and is set to be real for both reflectivities to remove the phase ambiguity in each reflectivity component.

Waveset. The $a_2(1320)$ and $a_2(1700)$ are spin-2 resonances. There are five different m-projections and two different reflectivities to consider, totaling 10 different potential waves each resonance could populate. The combinatorial nature of this problem makes it difficult to select a particular waveset as the nominal configuration. The JPAC TMD model, introduced in Section 4.1.2, suggests a particular waveset to use for the a_2: D_{-1}^-, D_0^-, D_1^-, D_0^+, D_1^+, D_2^+. This is the TMD waveset and will be taken as the nominal fit configuration to describe both a_2's. Additionally, a S^+ and S^- piecewise amplitude is used. These amplitudes will be used to model the tail of the $a_0(980)$, additional non-resonant contributions, and help collect residual backgrounds.

Resonance Parameters. A relativistic Breit-Wigner resonance model is used in this analysis to describe both a_2's. The resonance parameters for the $a_2(1700)$ have large associated uncertainties with a small apparent signal in the data. These parameters will be fixed to the nominal Particle Data Group, PDG, values. On the other hand, the resonance parameters of the $a_2(1320)$ are well constrained and is the dominant signal. The fits are initialized to the nominal PDG value for the $a_2(1320)$ mass with an additional Gaussian constraint to incorporate the associated uncertainty. The PDG uncertainty for the $a_2(1320)$ width turns out to be actually smaller than the mass resolution that GlueX observes for this channel. The $a_2(1320)$ width parameter in the fit is Gaussian constrained to be centered on PDG value but the associated standard deviation for this constraint is set to the GlueX $M(\eta\pi)$ resolution which is estimated in Section B.3 to be roughly 5.5 MeV. Table 4.1 details the nominal model configuration.

Table of Nominal Model Configuration. Table 4.1 shows the nominal model configuration.

Waveset	$S_0^\pm, D_{-1}^-, D_0^\pm, D_1^\pm, D_2^+$
Piecewise S-wave	40 MeV bins from $1.04 < M(\eta\pi) < 1.72$
Piecewise Anchor Bin	Piecewise bin at 1.22 GeV is Fixed to be real
$a_2(1320)$ Breit-Wigner Resonance Parameters	$M = 1.3182 \pm 0.0006$ and $\Gamma = 0.1111 \pm 0.0055$ GeV
$a_2(1700)$ Breit-Wigner Resonance Parameters	$M = 1.698$ and $\Gamma = 0.265$ GeV both Fixed

Table 4.1: Nominal Model Configuration. The uncertainty on the $a_2(1320)$ resonance parameters are incorporated via a Gaussian constraint.

Combined Fit of Polarized Datasets. GlueX produces a linearly polarized photon beam by scattering an electron beam off a diamond radiator. The polarization angle is dependent on the orientation of the diamond radiator. Data is taken at four polarization angles: 0, 45, 90, -45(135) degrees. These orientations are typically sequentially cycled over during a run period.

A combined fit of the polarized datasets can be performed where the partial wave amplitudes are shared. Each dataset's polarization magnitude and angle are fixed to their respective nominal values. The polarization magnitude for each run period is measured by the Triplet Polarimeter[105]. After applying the event selections detailed in Chapter 3, the yields of the Spring 2017, Spring 2018, and Fall 2018 run periods are roughly in a 1:3:2 proportion. A weighted average can be taken to produce the average polarization magnitudes for the Phase-I dataset with their associated uncertainties listed below. The nominal polarization angles are taken to be 0, 45, 90, and -45(135).

$$P_{\gamma,0°} = 0.35062 \pm 0.00397 \tag{4.22}$$

$$P_{\gamma,45°} = 0.34230 \pm 0.00412 \tag{4.23}$$

$$P_{\gamma,90°} = 0.34460 \pm 0.00404 \tag{4.24}$$

$$P_{\gamma,-45°} = 0.35582 \pm 0.00420 \tag{4.25}$$

Search for Global Minimum. The mass dependent fit in this analysis can incorporate $O(100)$ free parameters. Searching for a good (hopefully similar to a global) minimum requires finding a set of initial conditions that can allow the minimizer to descend appropriately. The current search uses roughly 300 fits with randomized initial parameters to search for a good minimum.

4.5.2 Mass-Independent Fits and Importance of $a_2(1700)$

Before diving into the results of the procedure outlined in the previous sections, it is interesting to study the importance of the $a_2(1700)$. For this intermediate study, the model is set to the nominal configuration laid out in Table 4.1 but has been restricted to $1.04 < M(\eta\pi) < 1.56$ GeV to focus in on the $a_2(1320)$. Two sets of mass-dependent fits were performed to study the significance of an $a_2(1700)$ resonance: one with and one without an additional set of amplitudes for the excited a_2. A set of mass independent fits are also performed on the same $1.04 < M(\eta\pi) < 1.56$ GeV region with 40 MeV bin widths matching the piecewise S-wave amplitudes in the mass dependent fits. The same set of 8 waves are chosen for these fits, where the S-waves act as the anchor for all bins.

Figures 4.13 and 4.12 show a comparison between the mass-dependent fits with and without an explicit contribution from the $a_2(1700)$ respectively. Only positive reflectivity waves are shown. The coherent sum of the two a_2's (if applicable) in the mass dependent fits are the orange shaded histograms (the uncertainties are not shown). Mass independent fit results are the black points
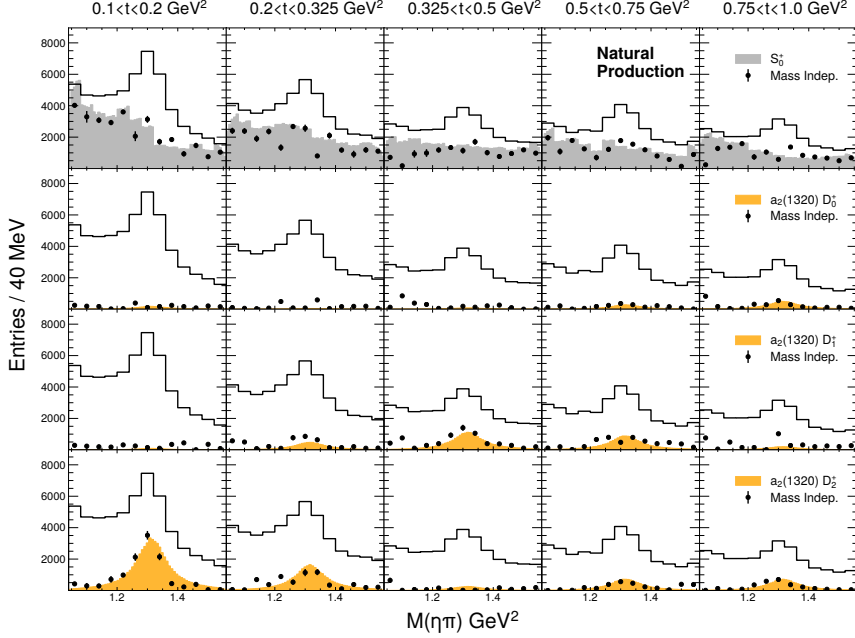
Figure 4.12: Mass dependent fit with piecewise constant S-waves and a single Breit-Wigner for the $a_2(1320)$. The orange-shaded histograms correspond to D-wave contributions. The black points are the results of the mass independent fits. Only partial waves corresponding to natural parity exchange are shown.

with uncertainties taken from Minuit. The solid line is the data. Each column represents a different t-bin and each row represents a different partial wave.

Visually, the fits that include the presence of an $a_2(1700)$ compare much better to the mass-independent fit results. To analyze the actual significance, it is important to note that the simpler mass-dependent model's parameters actually live in a subspace of the more complex model that includes contributions for the $a_2(1700)$. A likelihood ratio is therefore a powerful test statistic to be used here and is given by $2\Delta\ell$ where ℓ is the log-likelihood. The likelihood ratio is χ^2 distributed with degrees of freedom, DOF, equal to the difference in the models' DOFs. The likelihood ratio between the two mass-dependent models for the 5 different t-bins in ascending order are [124.72, 52.23, 353.82, 100.88, 333.50]. The more complex model contains 14 more degrees of freedom. In all cases the simpler model is rejected as the p-values are essentially zero. It is clear from this study that including a description for the $a_2(1700)$ is preferred.
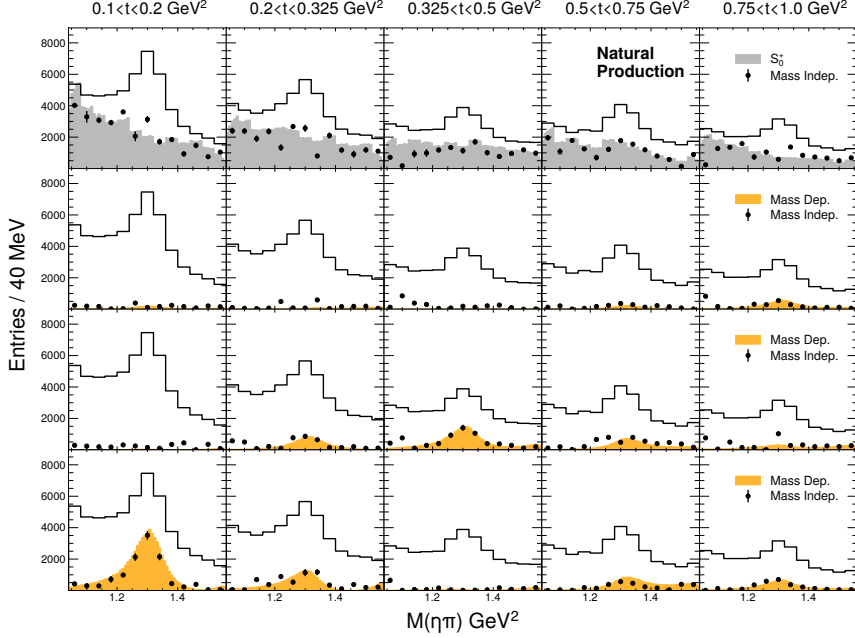
Figure 4.13: Mass dependent fit with piecewise constant S-waves and two Breit-Wigners: one for the $a_2(1320)$ and another for the $a_2(1700)$. The orange-shaded histograms correspond to D-wave contributions, coherently summing contributions from both a_2's. The black points are the results of the mass independent fits. Only partial waves corresponding to natural parity exchange are shown.

4.5.3 Quality of Fits

Figures 4.14, 4.15, 4.16, 4.17, 4.18 show the quality of fits with the nominal procedure outlined in Section 4.5 for the 5 t-bins in ascending order. θ and ϕ are given in the helicity angles. Φ is the angle between the polarization and production planes. Ψ is equal to $\phi - \Phi$. t is the momentum transfer. The beam energy and momentum transfer are not part of the fit. The simulations are passed through a accept/reject scheme to sculpt their t-distribution to resemble that of the data, see Section 3.2.1. The fit can capture the relevant distributions well in the first, second, and fifth t bins. The biggest discrepancies are seen in the third and fourth bins which are likely due to the production of baryons which can contribute to partial waves not present in the current waveset including angular asymmetry producing odd-l waves. These contributions, along with double Regge exchange processes, typically populate the regions near $\cos(\theta) \pm 1$. The sensitivity of the differential cross section measurement on $M(\pi^0 p)$ will be studied in Section 4.6.

101
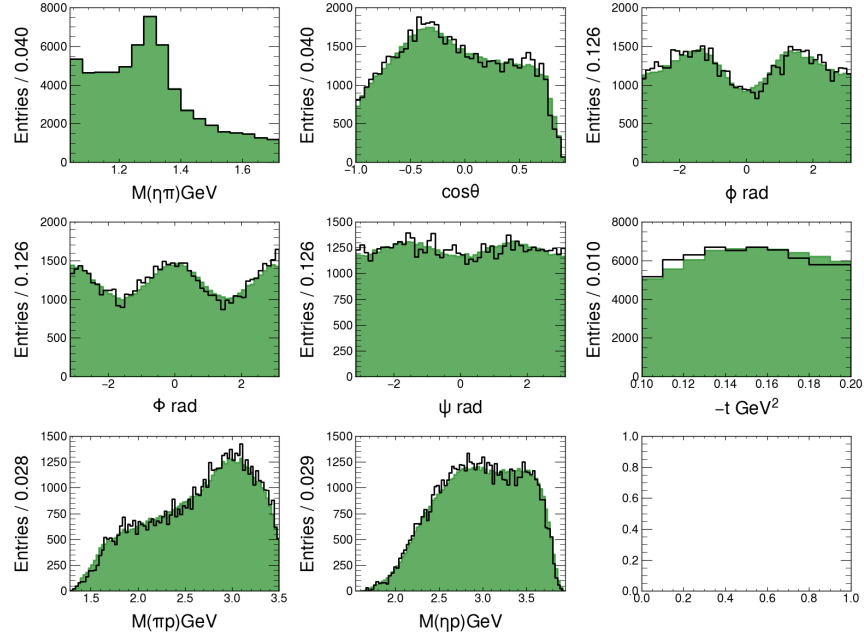
Figure 4.14: Fit quality in $0.1 < -t < 0.2$ GeV^2 bin. Black lines are the data. Green shaded region are the fit results.
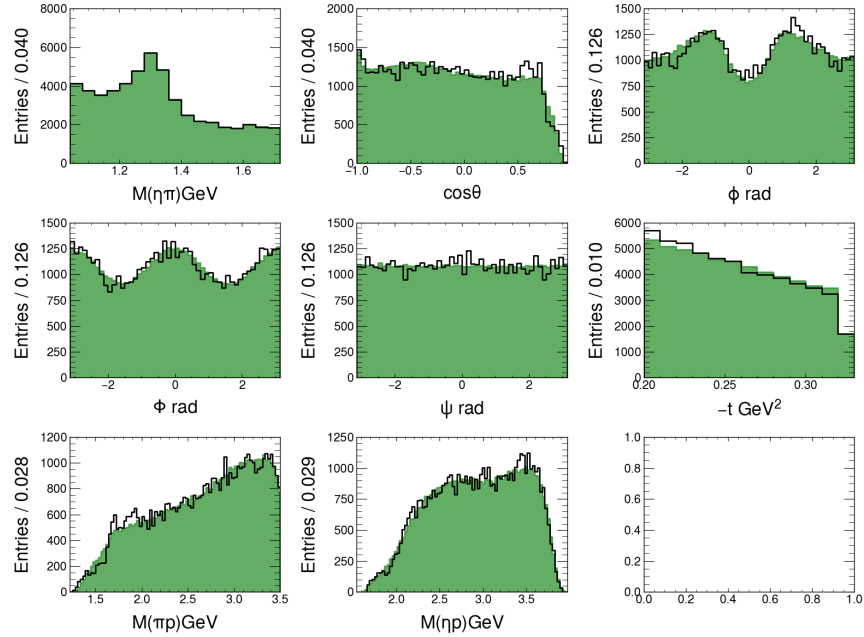
Figure 4.15: Fit quality in $0.2 < -t < 0.325$ GeV^2 bin. Black lines are the data. Green shaded region are the fit results.
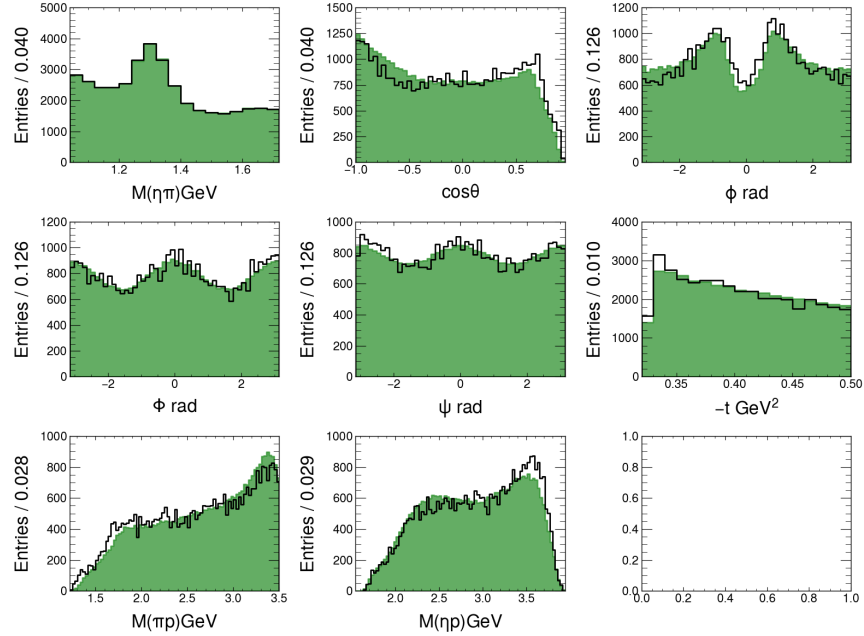
Figure 4.16: Fit quality in $0.325 < -t < 0.50$ GeV^2 bin. Black lines are the data. Green shaded region are the fit results.
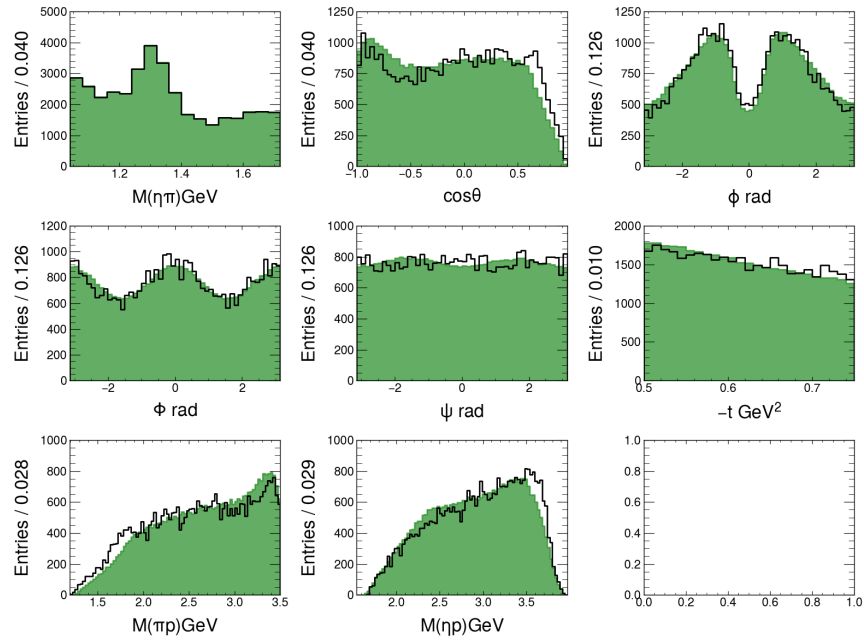
Figure 4.17: Fit quality in $0.50 < -t < 0.75$ GeV^2 bin. Black lines are the data. Green shaded region are the fit results.
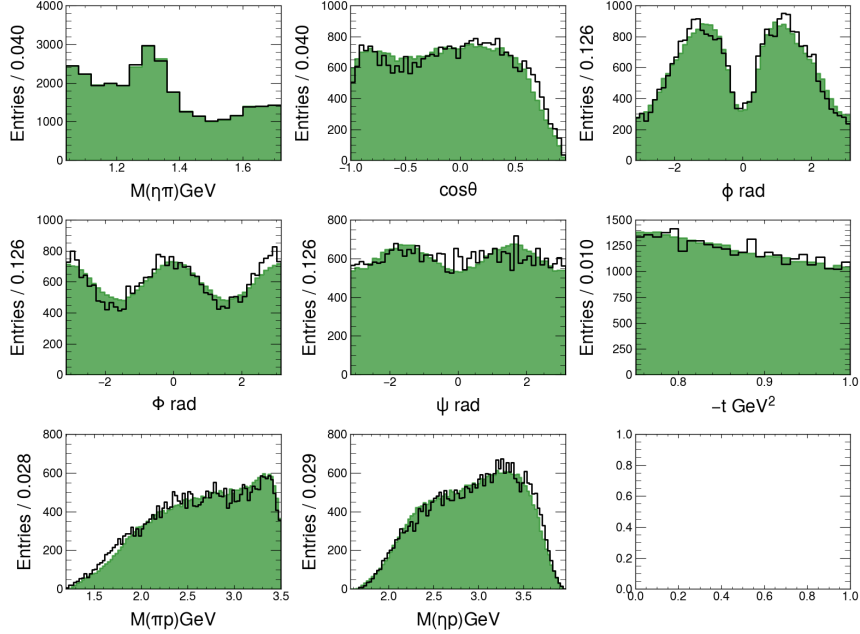
Figure 4.18: Fit quality in $0.75 < -t < 1.0$ GeV^2 bin. Black lines are the data. Green shaded region are the fit results.

4.5.4 Partial Wave Intensities

Partial wave contributions as a function of t are shown in Figures 4.19 and 4.20, for the positive and negative reflectivity contributions, respectively. The individual $a_2(1320)$ and $a_2(1700)$ Breit-Wigner contributions are separated in the Figure. The TMD model predictions for the relative contributions of the partial waves as a function of t are denoted by the green Breit-Wigner lineshape which is scaled to match the yield of the D_2^+ wave in the lowest t-bin. The $a_2(1700)$ is seen to contribute significantly to some partial waves. The piecewise S-wave is mostly smooth across the entire mass and momentum transfer regions studied. There are obvious differences between the measured partial waves and the theoretical predictions, e.g. the missing D_2^+ intensity for $0.325 < -t < 0.5$ GeV^2. It is important to note that the TMD model was fitted to the CLAS a_2 differential cross section data only. CLAS did not perform a partial wave analysis, and the beam is not polarized. Figures 4.21 and 4.22 show the coherent sum between the two a_2's.
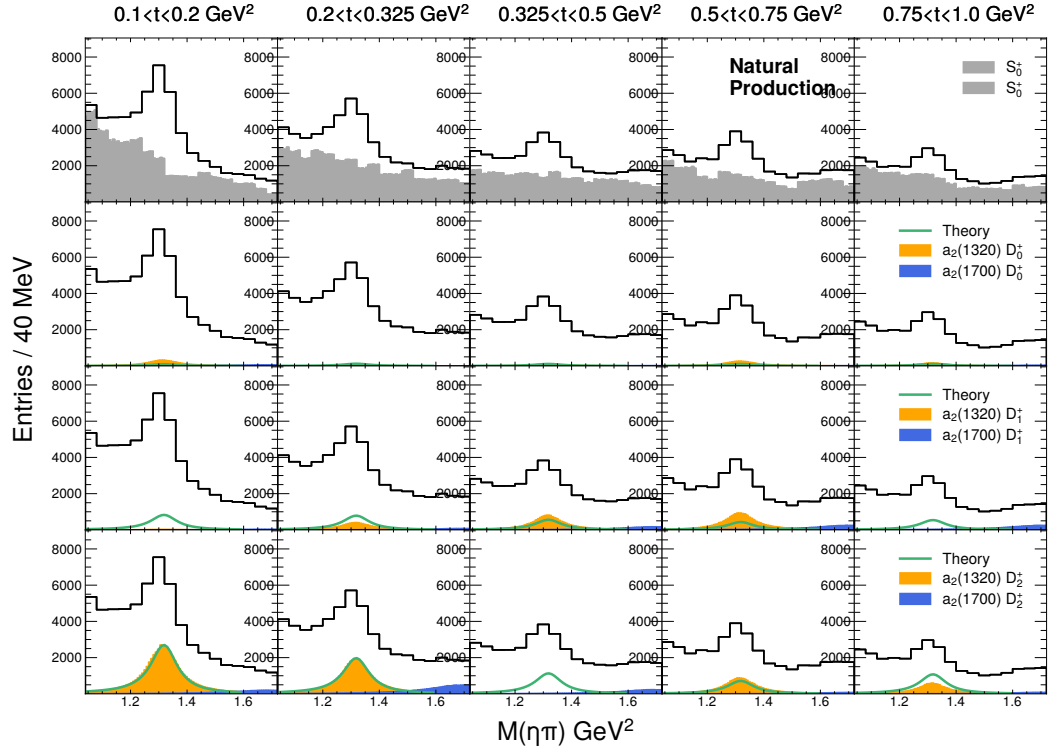
Figure 4.19: ((Natural Parity Exchange)Mass dependent fit results in 5 bins of t (columns) for the S, D_0, D_1, and D_2 waves (rows). S-wave is parameterized by a piecewise constant mass function whereas the D-waves are parameterized by two Breit-Wigner distributions representing the $a_2(1320)$ and $a_2(1700)$.
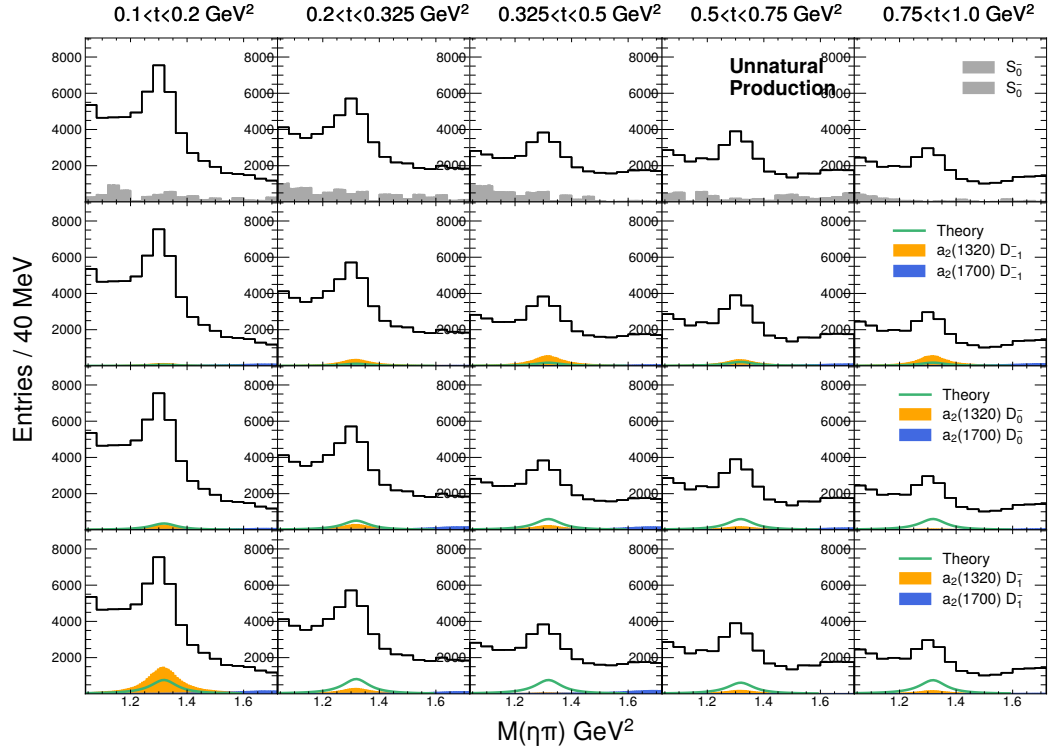
Figure 4.20: (Unnatural Parity Exchange)Mass dependent fit results in 5 bins of t (columns) for the S, D_0, D_1, and D_2 waves (rows). S-wave is parameterized by a piecewise constant mass function whereas the D-waves are parameterized by two Breit-Wigner distributions representing the $a_2(1320)$ and $a_2(1700)$.
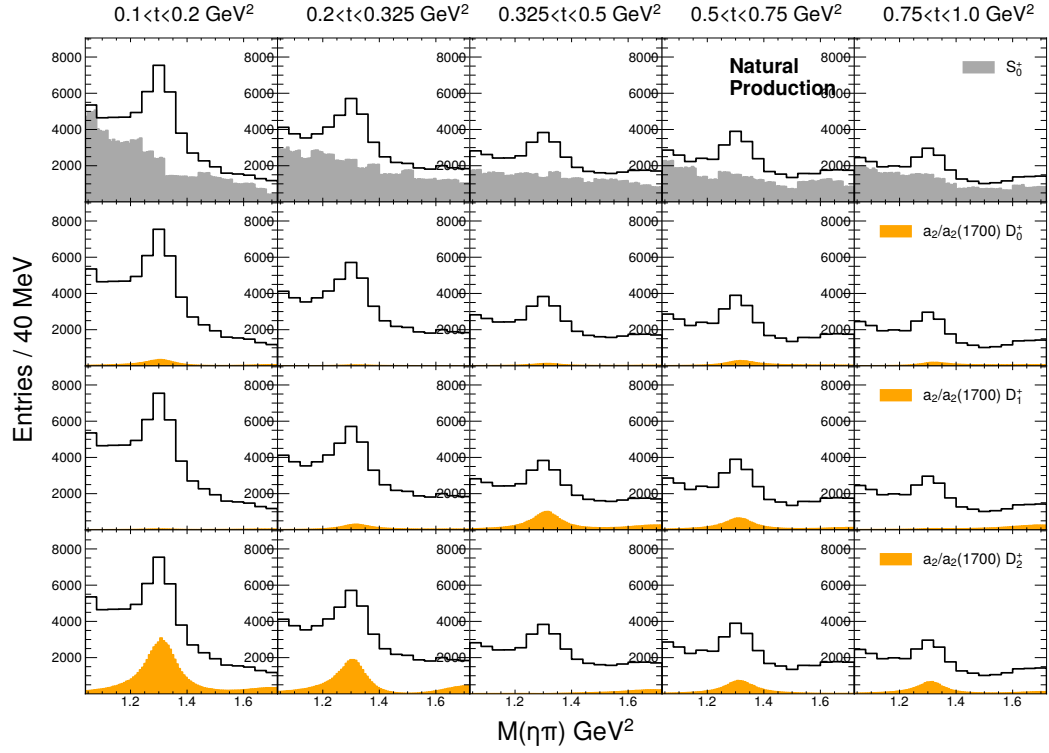
Figure 4.21: (Natural Parity Exchange)Mass dependent fit results in 5 bins of t (columns) for the S, D_0, D_1, and D_2 waves (rows). S-wave is parameterized by a piecewise constant mass function. The D-waves show the coherent sum of the two Breit-Wigner distributions representing the $a_2(1320)$ and $a_2(1700)$.
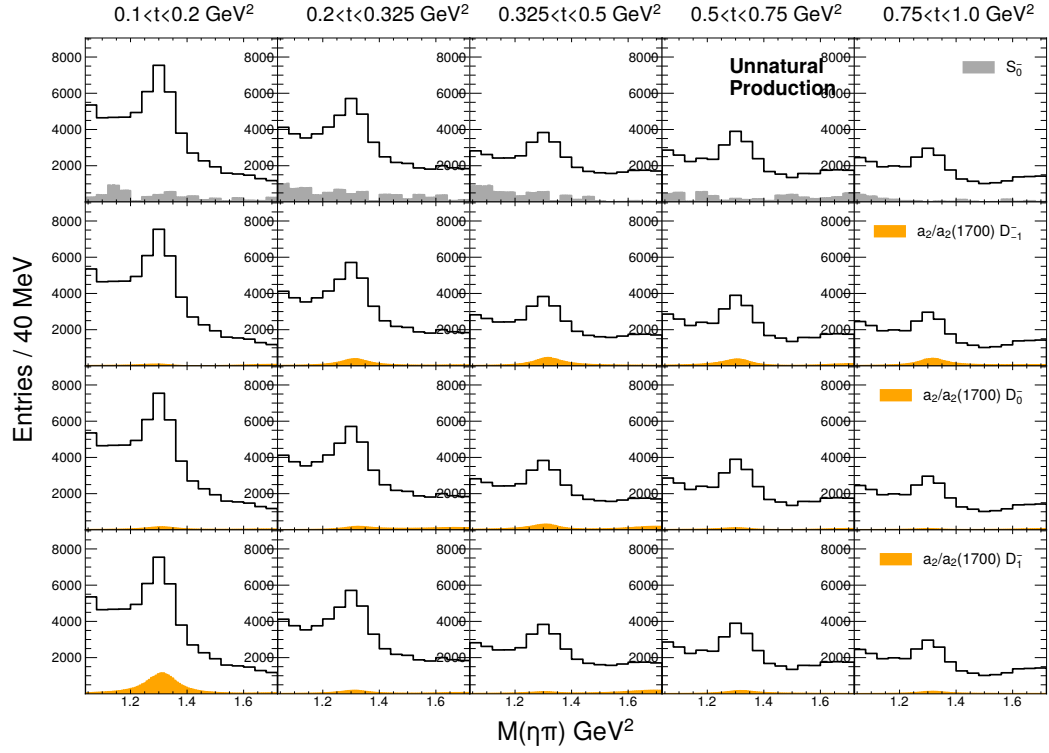
Figure 4.22: ((Unnatural Parity Exchange)Mass dependent fit results in 5 bins of t (columns) for the S, D_0, D_1, and D_2 waves (rows). S-wave is parameterized by a piecewise constant mass function. The D-waves show the coherent sum of the two Breit-Wigner distributions representing the $a_2(1320)$ and $a_2(1700)$.

4.5.5 Cross Section Results

$$\sigma = \frac{N}{\epsilon \times \text{Flux} \times \text{Target} \times \mathcal{B}(a_2(1320) \to \eta\pi^0) \times \mathcal{B}(\eta \to 2\gamma) \times \mathcal{B}(\pi^0 \to 2\gamma)} \tag{4.26}$$

Equation 4.26 is used to calculate the cross-section. N is the yield of the a_2 (coherently summed over all partial wave contributions), ϵ is the efficiency, Flux is the total polarized tagged flux, $\mathcal{B}$ is the branching fractions following the decay chain $\gamma p \to a_2(1320)p \to \eta\pi^0 p \to 4\gamma p$ and is equal to 0.0565±0.0047%. The individual branching fractions are taken from the Particle Data Group(PDG) and are tabulated in Table 4.2. Target is the target thickness. $\frac{N}{\epsilon}$ is the acceptance corrected yield.

The total polarized tagged luminosity (which incorporates both the tagged flux and the Target) for the GlueX Phase-I dataset is determined using the `plot_flux_ccdb.py` program in `hd_utilities`[106]. The `-pol` flag can be set equal to AMO to obtain the unpolarized flux and when subtracted from the total, the polarized flux can be obtained. The commands used for the Spring 2017, Spring 2018, and Fall 2018 datasets can be found in Appendix B.2. The total polarized tagged luminosity of the Phase-I dataset in the coherent peak is 103.634 pb^{-1}.

Decay	Branching Fraction %
$a_2(1320) \to \eta\pi^0$	14.5±1.2
$a_2(1700) \to \eta\pi^0$	3.6±1.1
$\eta \to 2\gamma$	39.41±0.2
$\pi^0 \to 2\gamma$	98.823±0.034

Table 4.2: Branching fractions of relevant decays taken from the Particle Data Group [107].

The differential cross section is shown in black in Figure 4.23. Including polarization in the fits allows separation in positive and negative reflectivity waves, which correspond to the production of the $a_2(1320)$ through natural and unnatural parity exchange. Predictions from the TMD model are overlaid in green, with the shaded area representing its uncertainty. The predictions from theory tend to overestimate the measured values. A more detailed discussion about the measurements will be returned to after the systematic uncertainties have been characterized.

4.5.6 Parity Asymmetry Results

The reflectivity, ϵ, of a partial wave is equal to the naturality of the exchanged particle, $\eta_{exc.}$, since the naturality of $\eta\pi$ system is +1. The equation relating these quantities is given by

$$\epsilon = \eta_{\eta\pi}\eta_{\text{exch.}} \tag{4.27}$$
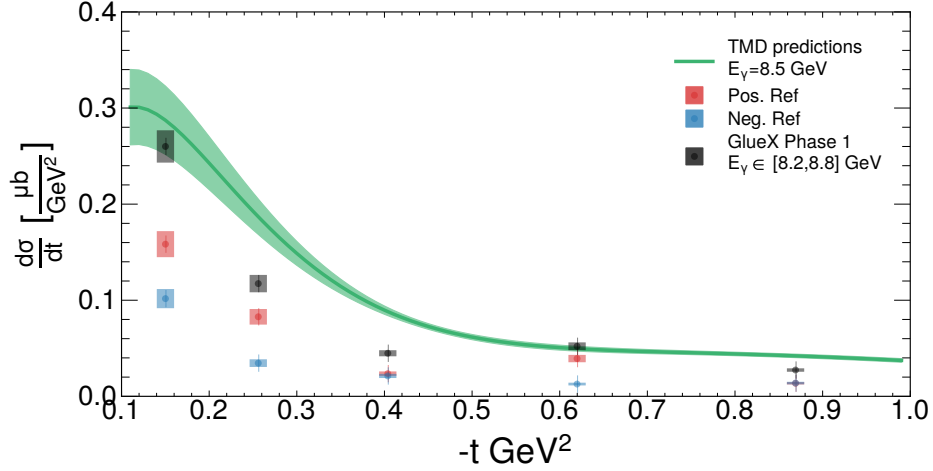
Figure 4.23: The differential cross section for the production of $a_2(1320)$ is shown in black. Errors are statistical only and are taken from `Minuit`. Incorporating polarization allows a separation of the cross section into positive and negative reflectivity components, which represents production through natural and unnatural parity exchange. Predictions from the TMD model are overlaid.
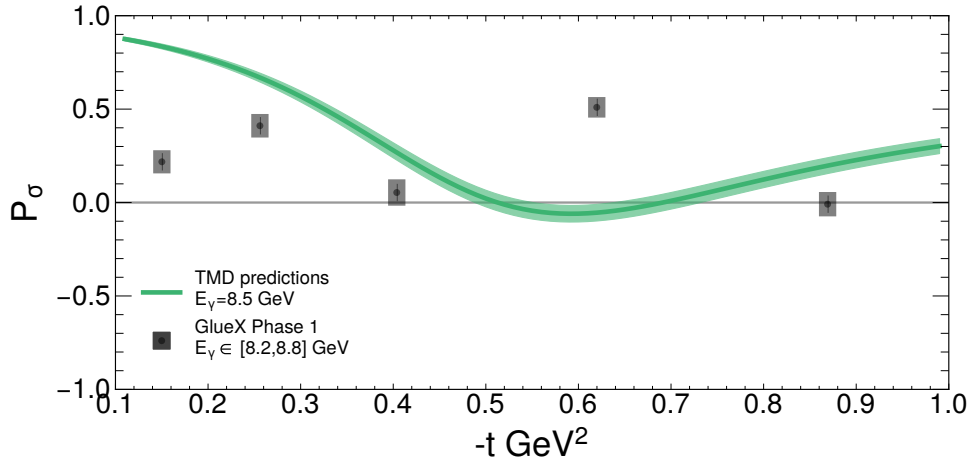
Figure 4.24: The parity asymmetry for the production of $a_2(1320)$ is shown in black. Errors are statistical only and are taken from Minuit. Values close to +1/-1 indicate dominance of natural/un-natural exchange production. Predictions from the TMD model are overlaid.

It is useful to quantify the relative contributions of these types of exchanges. The parity asymmetry is defined as

$$P_\sigma = \frac{\frac{d\sigma^+}{dt} - \frac{d\sigma^-}{dt}}{\frac{d\sigma^+}{dt} + \frac{d\sigma^-}{dt}} \tag{4.28}$$

P_σ takes on a value between -1 and 1. In this formula, $\frac{d\sigma^{+/-}}{dt}$ indicate positive and negative reflectivity components of the differential cross section, respectively. A value at the extremes indicates production purely through unnatural and natural parity exchange, respectively. Figure 4.24 shows P_σ as a function of momentum transfer. A slight dominance of natural parity exchange is seen.

4.5.7   Direct Fits to $M(\eta\pi)$ distribution
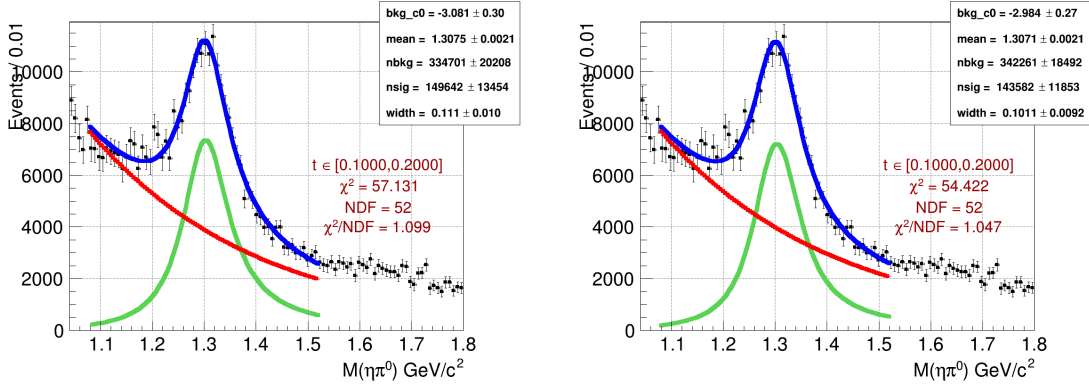
(a) Breit-Wigner plus exponential background fit to the acceptance corrected invariant mass distribution with $0.1 < -t < 0.2$ GeV^2

(b) Voigtian plus exponential background fit to the acceptance corrected invariant mass distribution with $0.1 < -t < 0.2$ GeV^2

Figure 4.25: Direct fit to the acceptance corrected yield.

It is useful now to compare the differential cross section results obtained by the presented partial wave analysis and the values that come out of a direct fit to the acceptance corrected invariant mass distribution. Figure 4.25 shows an example fit to the acceptance corrected invariant mass distribution with $0.1 < -t < 0.2$ GeV^2 using a Breit-Wigner and a Voigtian signal distribution. A Voigtian is the convolution of a Breit-Wigner with a Gaussian distribution and is typically used to incorporate the mass resolution of the detector. An estimate of mass resolution is determined in Section B.3 and is used in the fit. The reduced-χ^2's are both close to 1 with a favoring towards the Voigtian signal distribution. The integral of the green curve of Figure 4.25 the acceptance corrected yield which can then be propagated to obtain a cross section.

Figure 4.26 shows a comparison between the differential cross section obtained through partial wave analysis and the values obtained from the direct fit. In the direct fits, both parameterizations of the a_2 signal agree with each other but some tension exists when compared to the partial wave analysis results. This discrepancy is due to the fact that potential contributions from the $a_2(1700)$
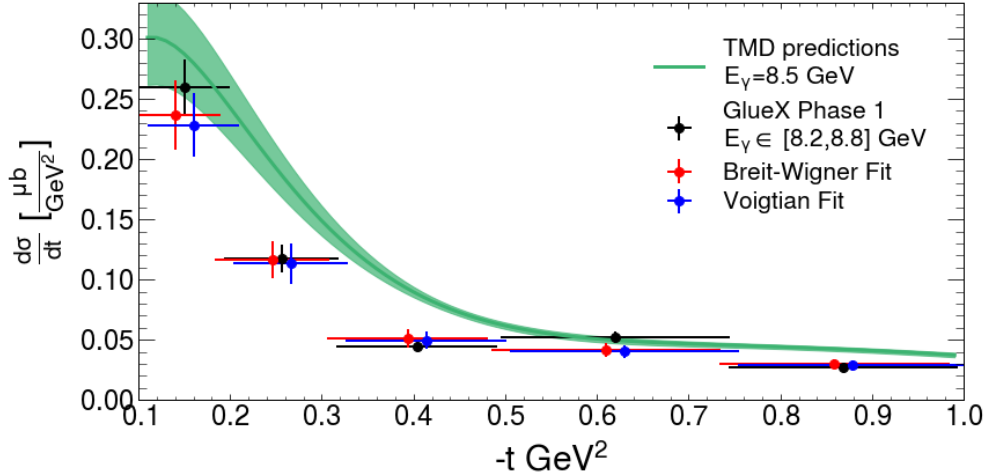
Figure 4.26: Comparison of cross section results obtained with the presented (black pints) partial wave analysis and from a direct fit of the invariant mass distribution.

are not included in the direct fits. An underestimation of the yield can occur due to the two a_2 mesons destructively interfering. This can be seen when comparing Figures 4.19 and 4.21.

4.5.8 Bootstrapped Statistical Uncertainties

The uncertainties on the partial wave amplitudes that are extracted by `Minuit` can be poorly estimated due to the high correlations that can exist between the fitted parameters. The calibration of these uncertainties can be determined by doing an input/output test, see Appendix B.7.1. Alternatively, the uncertainties can be estimated through the bootstrap procedure. Bootstrapping is a resampling technique that allows for a variety of statistical quantities to be determined, i.e. confidence intervals, percentiles, and standard deviations. New sets of samples are generated by resampling the data with replacement. A fit can be performed on each set of samples, resulting in a distribution of parameter values from which the statistic quantity of interest can be determined.

The procedure is as follows. To find the associated uncertainties around the nominal minimum, bootstrap samples are generated by resampling he `data`, `bkgnd`, and `accmc` dataset inputs to `amptools`. The generated samples are subsequently fitted with the initialization of the parameters set to the nominal fit results. This is done N times, where $N \sim O(100)$. N depends on the complexity of the data/model and should be significantly larger[108] but a compromise between computational resources and statistical accuracy has to be made. In the end, the ensemble

of measurements should be smoothly distributed. See Appendix B.4 for more information on the convergence of the bootstrap which suggests the parameter uncertainties have converged.

From here, the uncertainties on various quantities can be extracted by using the set of N bootstrapped "measurements". As will be done with the systematic uncertainties, the uncertainties are first determined for the positive and negative reflectivity components first. These uncertainties can then be propagated to the cross section and the parity asymmetry. The bootstrapped statistical uncertainties for the differential cross section and the parity asymmetry measurements is shown in Figure 4.27 and 4.28, respectively. There is roughly a factor of 2 between the bootstrap and `Minuit` uncertainties from the previous section.
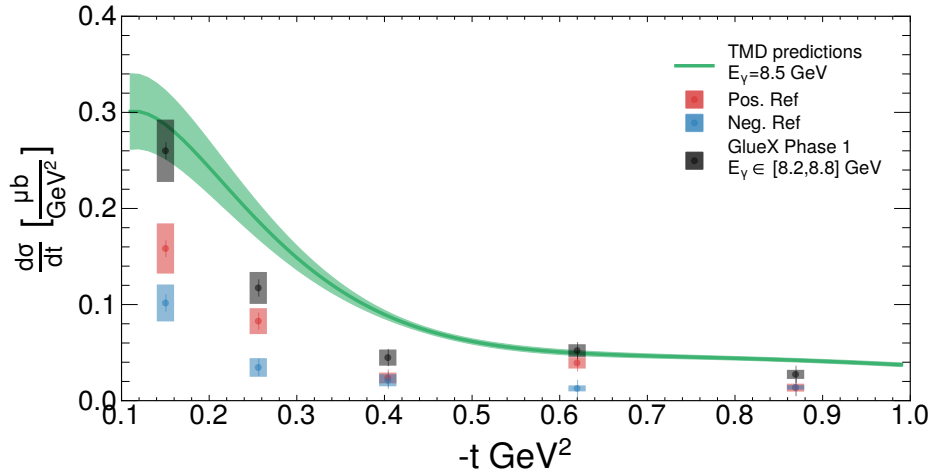
Figure 4.27: The differential cross section for the production of $a_2(1320)$ is shown in black. Errors are statistical only and are estimated from the bootstrap procedure. Incorporating polarization allows a separation of the cross section into positive and negative reflectivity states, which represents production through natural and unnatural parity exchange. Predictions from the TMD model is overlaid.
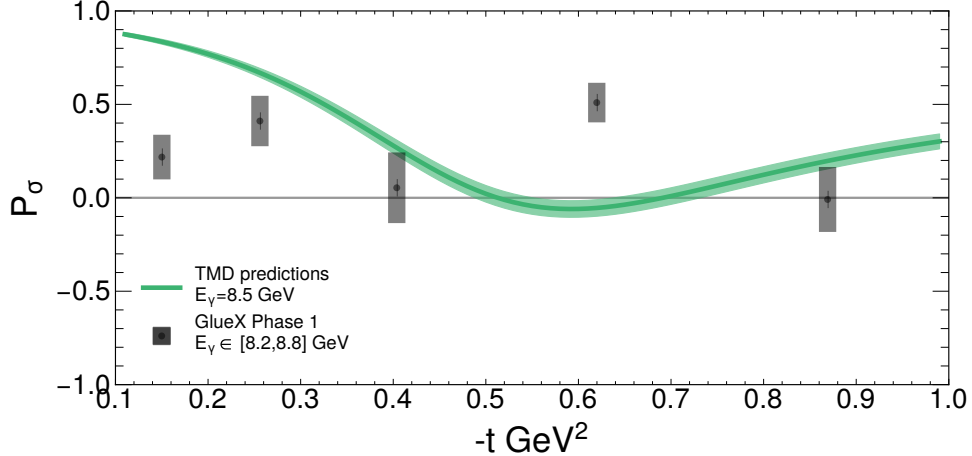
Figure 4.28: The parity asymmetry for the production of $a_2(1320)$ is shown in black. Errors are statistical only and are estimated from the bootstrap procedure. Values close to $+1/-1$ indicate a dominance of natural/unnatural exchange production. Predictions from the TMD model is overlaid.

4.6 Systematic Uncertainties

We perform several studies in order to identify sources of potential systematic uncertainties. A systematic trend can be observed if there is a mismatch between how an event selection performs on data and how it performs on simulations. Systematics of this type will be discussed in Section 4.6.2 which will consider the significance of a variation taking into account the variation of statistics. Additionally, there are good motivations for the nominal model that the data is fitted under (TMD waveset, Breit-Wigner, constraints, etc...) but other model choices could fit the data just as well. Systematics of this type will be discussed in Section 4.6.3. Additional measurements of the differential cross section can be made with varied selections and models to quantify the scale of these discrepancies. The deviation and significance of these variations will be shown in the following sections. Additional plots of the fit fractions for each wave and select coherent sums can be found in Appendix B.6. Groups of variations are formed and the maximum deviation in each group is taken to be the associated systematic uncertainty. The systematic uncertainty in each group is added in quadrature to obtain the total systematic uncertainty. Tables 3.5 and 4.1 detail the standard event selections and nominal model configuration, respectively. Section 4.2 showed additional selections performed for the study of the $a_2(1320)$.

An estimate of the systematic uncertainty will be determined in the following sections for each reflectivity component of the differential cross section. The total uncertainty for each component

is found by adding the statistical and systematic uncertainties in quadrature. These uncertainties can then be propagated to the differential cross section and the parity asymmetry measurements.

One can also conduct an input/output test on simulated data to study whether the experimental methodology extracts results that are consistent with generated inputs and to determine whether these systematic variations do not introduce significant artifacts that affect the cross section measurements. This kind of study is performed in Appendix B.7.

4.6.1 Perturbation Scans for Fit Convergence

The procedure to determine the significance/magnitude of systematic variations requires the initialization of a new fit with the nominally converged parameters as we wish to quantify the associated uncertainties at the nominal minimum. Due to the complexity of the fits and the large computational resources they take to perform, there would be no guarantee that we could arrive at a similar minimum if the parameter initialization or set of parameter initializations were different. With this procedure, a substantial fraction of fits fails to converge due to the error matrix being non-positive-definite. This is a peculiarity of `Minuit` as it estimates uncertainties as it descends in the likelihood surface but is unable to travel significantly as the minimizer has been initialized to a local minimum. As a result, the uncertainty cannot be trusted. A perturbation scan is performed to search for convergence by slightly perturbing the production coefficient with the largest intensity. The scale of these perturbations starts from zero (no perturbation) and increments/decrements up to ±5%. In some rare cases, this scan requires up to 10 percent variation. In even rarer cases, this method is still unable to find a converged fit. Only 2 variations in total never find convergence and are denoted with an X in the systematic overview plots. The failed fits and the converged fits found by the perturbation scan give essentially the same parameter values but the uncertainties can be half the size of the failed fits.

4.6.2 Barlow Significance: Variations of Statistics

To determine the significance of variations that change the statistics of the sample, i.e. event selection related variations, this analysis will follow the prescription detailed by R. Barlow[109]. Suppose the nominal measurement returns a value of $x \pm \sigma_x$ and that a specific variation produces a measurement of $y \pm \sigma_y$. Here, σ_x and σ_y are the statistical uncertainties. Since these two measurements are very similar, i.e. only varying one particular element of the event selection or analysis procedure, the values and uncertainties should also be very similar. Define $\Delta = y - x$ and

$\sigma_\Delta^2 = \sigma_y^2 - \sigma_x^2$. It is computationally prohibitive to perform the bootstrap procedure to obtain more accurate statistical uncertainties for every systematic variation. Therefore, the `Minuit` uncertainties will be used when calculating σ_Δ. A test of a variation's significance is to check the condition: $\frac{|\Delta|}{\sigma_\Delta} > X$. Systematic variations with discrepancies, X, greater than 4 are all included in the calculation of the systematic uncertainty. It is useful to divide Δ and σ_Δ by the nominal value to obtain a percent deviation and a "normalized/unit-less" uncertainty. This puts the variations for the five different t-bins on the same scale.

Figure 4.29 contains histograms of all the event selection variables that will be systematically varied. The variations are chosen such that they do not change the statistics by more than 10%, otherwise, a variation can be significantly affected by the difference in statistics. To be precise, the statistic of interest is the number of candidate 4γ events which are determined post-accidental-subtraction. Each scanned variable will generally choose a looser and a tighter selection to survey. In some cases, the nominal selection is already quite loose. Two tighter selections will be chosen for these.

$-t$ GeV^2	Variation	(+)Diff. [nb]	(+)N_{Barlow}	(-)Diff. [nb]	$(-)N_{Barlow}$
$0.1 < -t < 0.2$	$E_\gamma > 0.13GeV$	0.00035	0.06946	-0.00523	4.71925
$0.1 < -t < 0.2$	$53 < z_{proton} < 77cm$	0.00616	0.96804	-0.00947	4.93012
$0.1 < -t < 0.2$	$\chi^2 < 11$	-0.01910	6.27729	-0.03441	6.54606
$0.2 < -t < 0.325$	$|MMsq| < 0.01GeV^2$	-0.00285	1.18798	-0.00238	9.44436
$0.325 < -t < 0.5$	$M(\pi p) > 1.7$	-0.00206	11.15650	-0.00103	1.45386
$0.325 < -t < 0.5$	$M(\pi p) > 1.8$	-0.00330	10.41414	-0.00048	0.30924
$0.5 < -t < 0.75$	$E_{unused} < 0.17GeV$	0.00270	7.17983	-0.00056	1.09679
$0.5 < -t < 0.75$	$\chi^2 < 12$	0.00090	4.56111	0.00126	1.30019
$0.5 < -t < 0.75$	$M(\pi p) > 1.8$	0.00118	6.02017	0.00498	2.51047
$0.75 < -t < 1.0$	$\theta_{\gamma,trans}$ cut $[10.1, 12.1]°$	-0.00086	4.35860	0.00034	0.54891

Table 4.3: ($N_{\text{barlow}} > 4$) Table of systematics for each t-bin and variation combo where at least one reflectivity component is significant. (+/-) corresponds to (positive/negative) reflectivity. Diff. is the difference between the differential cross section of the variation and the nominal in units of microbarns/GeV^2. N_{barlow} is the significance of this particular variation.

Figure 4.30 shows how significant each variation is to the differential cross section measurement for GlueX data. Each panel corresponds to a different t bin. The red/blue bars correspond to positive/negative reflectivity components. The x-axis is the percent deviation of a particular variation (y-axis) when compared to the nominal. The width of each bar is the normalized uncertainty, $\frac{\sigma_\Delta}{x}$. The discrepancy of a variation, N, is then the distance its corresponding bar is away from 0. For reference, the nominal `Minuit` statistical errors are also illustrated and are denoted by lines near
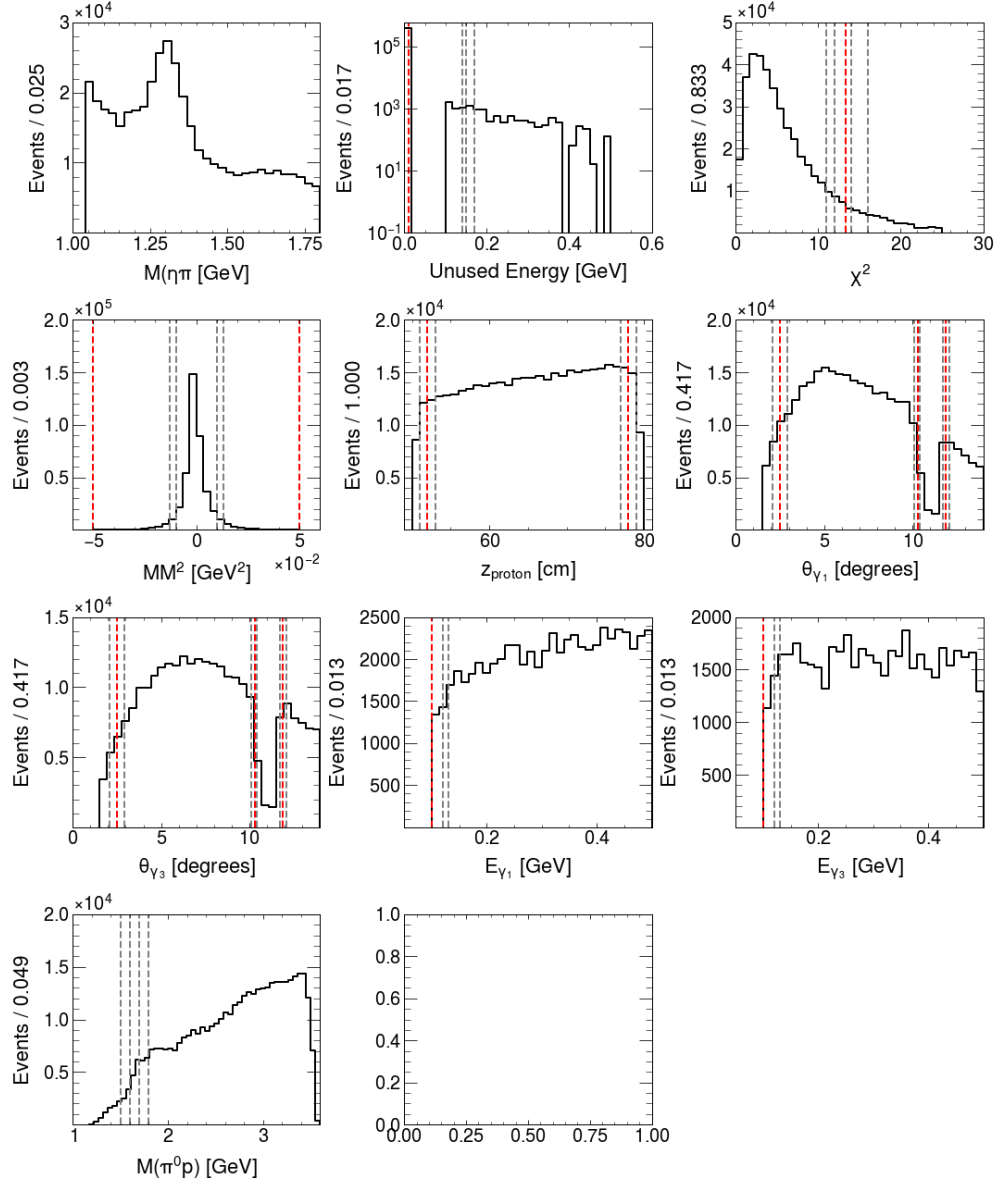
Figure 4.29: Histograms of variables that are systematically varied. The red dashed line denotes the nominal selection. The gray dashed line denotes one limit of a variation.

the bottom of the graph. Most variations are consistent with the nominal measurement. Black horizontal lines that span the 5 different subplots are used to roughly separate groups of variations into ones related to event selections and sideband subtraction. Each group will be discussed sequentially below. The maximum deviation of the significant variations will be taken as the associated systematic uncertainty for each group.
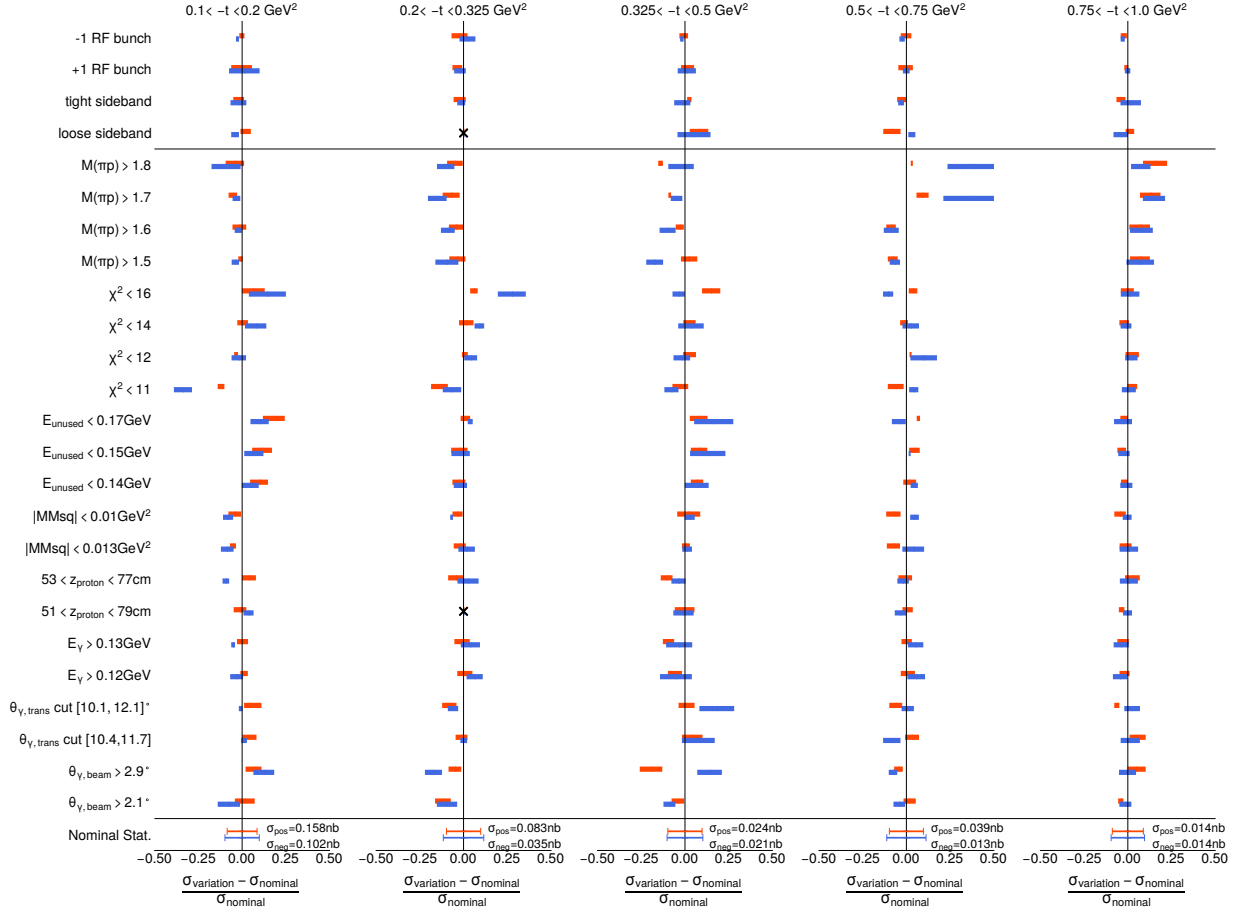
Figure 4.30: Systematics overview for variations that change the sample statistics. Each panel corresponds to a different t bin. The red/blue bars correspond to positive/negative reflectivity components. The x-axis is the percent deviation of the cross section between a particular (y-axis) variation, $\sigma_{\text{variation}}$, when compared to the nominal, σ_{nominal}. The width of each bar is the normalized uncertainty, $\frac{\sigma_\Delta}{x}$. The discrepancy of a variation, N, is then the distance its corresponding bar is away from 0. For reference, the nominal Minuit statistical errors are also illustrated and are denoted by lines near the bottom of the graph. Black horizontal lines that span the 5 different subplots are used to roughly separate groups of variations into ones related to event selections and sideband subtraction.

Event Selections. Most of the variations made on the fiducial selections do not produce significant variations. The significant variations, with $N_{\text{barlow}} > 4$, are shown in Table 4.3. Only three variations are seen to significantly affect the lowest and highest t bins. Part of the trend seen in χ^2 and unused energy, E_{unused}, are likely due to a mismatch between data and simulations. This mismatch is shown in Appendix B.1 where a comparison between data and MC for the unused energy selection is made. Some variations of $M(\pi p)$ are seen to be significant and appear to only

118

affect the region from $-t = [0.325, 0.75]$ GeV^2.

Sideband Subtraction. For this measurement, sideband subtraction has been used to statistically select good $\eta\pi^0$ candidates. There are heuristics to choose the signal and sideband regions but there remains some level of ambiguity. To assess how the particular choice of the regions affect the outcome of the measurement, two variations are performed. One set of selections shrinks all regions. Another set expands all regions. Figure 4.31 shows these additional variations. These particular choice of sideband regions is not significant. The specific choice of sidebands will not contribute to the systematic uncertainty.

Additionally, accidental subtraction has been used to statistically select good beam photon candidates. Recall that the nominal scheme involves skipping the inner most RF bunch due to potential leakage from the large prompt signal. A tighter variation, removing another inner beam bunch, is studied. In this variation, only 2 bunches exist to the left and right of the prompt peak. A looser variation is also studied. This variation reincorporates the nearest beam bunch to the left and right of the prompt peak. Both variations are not significant to the outcome of the measurement. The specific choice of the accidental subtraction scheme will not contribute to the systematic uncertainty.
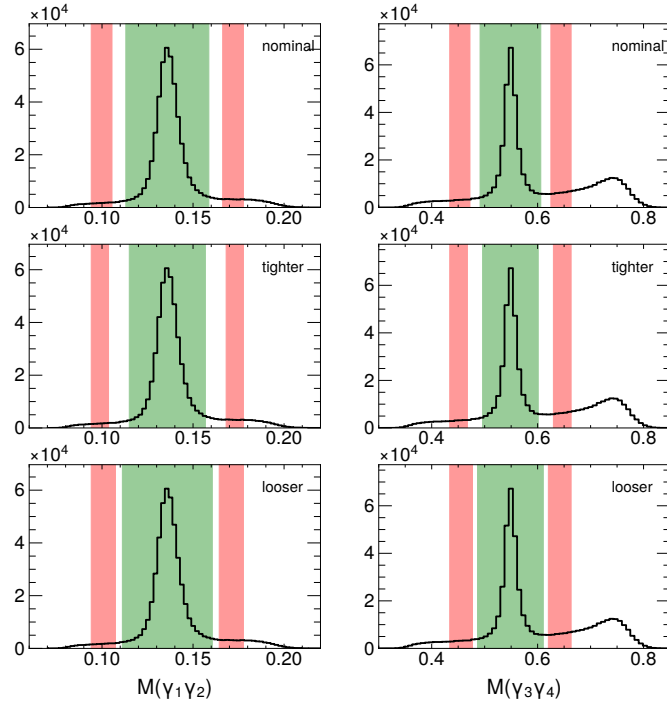
Figure 4.31: Systematically varied regions for the sideband subtraction procedure. The nominal selection is shown on the top row. A tighter set of regions is shown in the middle row. A looser set of regions is shown in the bottom row. The left column shows the invariant mass of the candidate π^0. The right column show the invariant mass of the candidate η.

4.6.3   Model Parameterization

Model variations are performed to study its effect on the results. These model variations do not change the statistics of the sample. Figure 4.32 shows an overview plot in a similar format to what was shown in the previous section. Here, the width of the bars are the `Minuit` statistical uncertainty of the variation instead of σ_Δ. The black lines separate the variations into roughly independent groups that modify distinct parts of the model. These groups of variations are related to the: a_2 Breit-Wigner parameterization, piecewise S-wave parameterization, fit range, and polarization. Each group will be discussed individually below. The maximum deviation in each group will be taken as the associated systematic uncertainty.

Breit-Wigner Parameterization.   The nominal setting for the resonance parameters were shown in Table 4.1. The constraints on the resonance parameters are modified to study the depen-
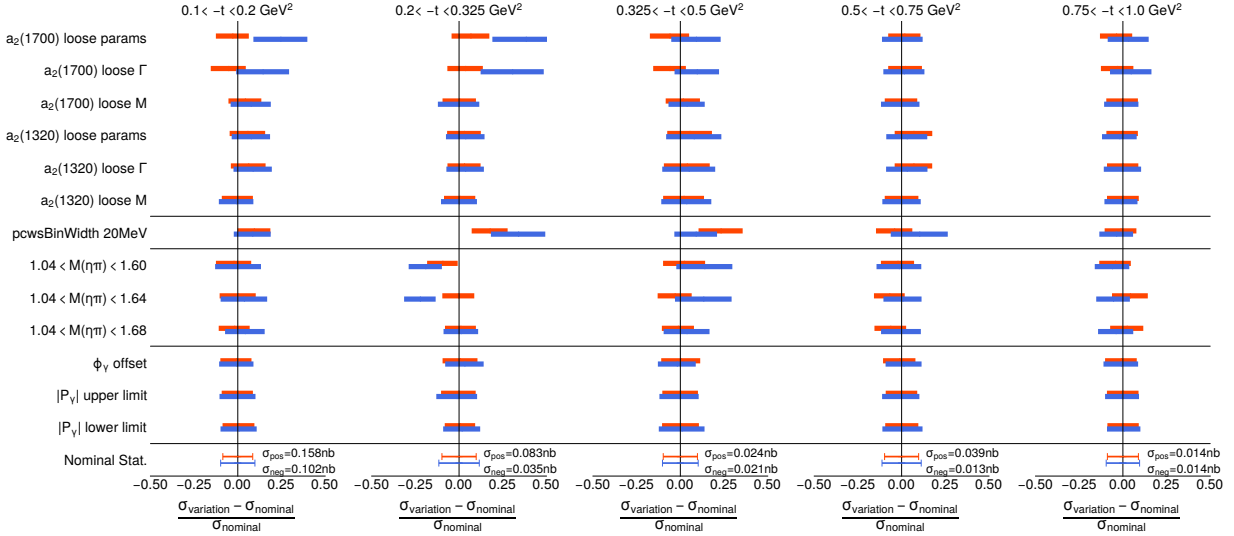
Figure 4.32: Systematics overview for variations of the model. Each panel corresponds to a different t bin. The red/blue bars correspond to positive/negative reflectivity components. The x-axis is the percent deviation of the cross section between a particular (y-axis) variation, $\sigma_{\text{variation}}$, when compared to the nominal, σ_{nominal}. The width of each bar is the `Minuit` statistical uncertainty. For reference, the nominal `Minuit` statistical errors are also illustrated and are denoted by lines near the bottom of the graph. Black horizontal lines that span the 5 different subplots are used to roughly separate groups of variations.

dence of the differential cross sections on these particular choices. Three variations are performed for each a_2 meson. For the $a_2(1320)$, the constraint uncertainty can be increased by a factor of 3 for the mass, the width, and the mass and width together. A similar process can be repeated for the $a_2(1700)$ but instead of the parameter(s) being fixed, the parameter(s) can be Gaussian constrained to the PDG uncertainties.

Piecewise S-wave Parameterization. The number of bins used by the piecewise S-wave amplitudes can be made smaller allowing for a more flexible description. Each bin can be split into an integer number of equal parts so that the complex value can be reused. This will leave the initial functional output completely unchanged. Since the nominal measurement uses 40 MeV bins, only 20, 13.333, 10, ... MeV bins are allowed in this scheme. Technically, the only viable option is the 20 MeV bin width as other elements of the series allow the piecewise S-wave to capture too much variance. These variations seem to affect the $0.2 < t < 0.5$ GeV^2 region significantly.

Additionally, there is an overall phase ambiguity for each reflectivity when performing these fits. A particular, but equally valid, solution would be to arbitrarily fix the phase of a component in each

reflectivity of the model. The nominal selection fixes the bin centered on $M(\eta\pi) = 1.22$ GeV to be real. This particular selection was chosen since the $a_2(1320)$ phase is rapidly changing here. The position of the anchor can be varied to disparate points along the $a_2(1320)$ lineshape. No variation is seen.

Fit Range. To modify the $M(4\gamma)$ window both the input datasets and the piecewise S-wave amplitude need to be altered the match the variation. A natural way to truncate the $M(4\gamma)$ region is to truncate at 40 MeV intervals to match the piecewise binning. In this way, the model still has full information on the sub-region of interest. Four variations are performed, truncating the upper mass limit from 1.72 down to 1.60 GeV.

These variations show some significant drift in the cross section in some t-bins at tighter $M(4\gamma)$ windows. It is important to note that tightening the $M(\eta\pi)$ selection can make it more difficult to constrain the contributions from the $a_2(1700)$ as the fit sees less of the lineshape. Some variation could be expected due to this.

Polarization Magnitude and Offset. The fits are performed at fixed polarization magnitudes, P_γ, and polarization angles, Φ_γ. There is a small statistical uncertainty associated with P_γ which can be incorporated in the scans. These values can be found in Equation 4.25. The intensity depends on these polarization variables beyond a simple scaling factor. Fit variations are performed to "propagate" the polarization uncertainty and offset to quantify its affect on the cross section measurements.

A variation can be performed where the nominal P_γ values can be modified to their associated upper and lower limits. These fit variations do not produce significant shifts to the differential cross section measurements. The polarization offset is varied in a similar way. The nominal fit sets the polarization angle of the four datasets to be exactly 0, 45, 90, and -45 degrees. It is known that the physical polarization angles are not correct and that an offset is required[110]. These offsets are extracted from detailed studies of $\rho(770)$ decay asymmetries. The measured offset to the nominal values are 1.77, 2.85, 4.50, and 3.43 degrees respectively. Shifting the nominal polarization angles to include these offsets do not produce significant changes to the differential cross section measurement. The measured deviations are negligible.

4.6.4 Table of Systematic Uncertainties

Table 4.4 shows the systematic uncertainty of $d\sigma/dt$ in each t bin for both reflectivities.

Systematic Study	Reflectivity	$d\sigma/dt$ Systematic Uncertainty $[\frac{\mu\mathrm{b}}{\mathrm{GeV}^2}]$				
Event Selections	$+$	0.0191	–	0.0033	0.0027	0.0009
	$-$	0.0344	0.0024	-	–	–
Polarization	$+$	0.0017	0.0004	0.0001	0.0005	0.0001
	$-$	0.0009	0.0011	0.0004	0.0001	0.0002
Fit Range	$+$	0.0038	0.0079	0.0008	0.0028	0.0006
	$-$	0.0041	0.0077	0.0029	0.0002	0.0009
Piecewise S-wave Parameterization	$+$	0.0146	0.0145	0.0054	0.0017	0.0002
	$-$	0.0084	0.0117	0.0019	0.0013	0.0005
Breit-Wigner Parameterization	$+$	0.0095	0.0054	0.0015	0.0027	0.0005
	$-$	0.0248	0.0132	0.0020	0.0004	0.0006

Table 4.4: Table of absolute systematic uncertainties. The systematic uncertainty columns show the maximum absolute deviation for each t-bin in ascending order from left to right. Entries with hyphens do not have an associated systematic uncertainty as no variations were significant.

4.6.5 External Systematics

Here, we consider external systematics which are systematic deviations coming from the efficiency of the detectors. The average detection efficiency of the pair spectrometer, which determines the flux, is around 95%[111]. Therefore, a conservative 5% systematic uncertainty will be taken for the flux normalization. An additional indication that this estimate is reasonable and conservative is based on the flux systematic studies performed for the PrimeX experiment which uses the GlueX experimental setup [112]. A 3% systematic uncertainty will be taken for the proton reconstruction efficiency.

Photon Reconstruction Efficiency. The largest external systematic is expected to be from the photon reconstruction efficiency. A more detailed study will be performed here.

Method 1. The detection efficiency for the FCAL is around 97% whereas the detection efficiency for the BCAL is around 95% [113]. This bias can be incorporated into the simulations to test the agreement between the data and MC as a probe to understand the uncertainty of the MC-determined efficiency. There are four photons in the final state which are detected in the BCAL or the FCAL resulting in 16 potential permutations. The left-hand side of Figure 4.33 shows the number of occurrences for each permutation as observed in the Phase-I dataset. The majority of events, FFFB and FFBF, detect the $\gamma_1\gamma_2 := \pi^0$ in the FCAL and one photon from the η candidate is detected in the FCAL and the other is detected in the BCAL. The total inefficiency of each permutation is shown on the right-hand side where the inefficiency is given by

$$\epsilon = \sqrt{(0.03 \times N_{\text{FCAL}})^2 + (0.05 \times N_{\text{BCAL}})^2} \tag{4.29}$$

where N_{FCAL} is the number of final state photons detected in the FCAL and $N_{\text{BCAL}} = 4 - N_{\text{FCAL}}$. The weighted average of the inefficiency is 11.37% and is the estimated systematic uncertainty from this method.
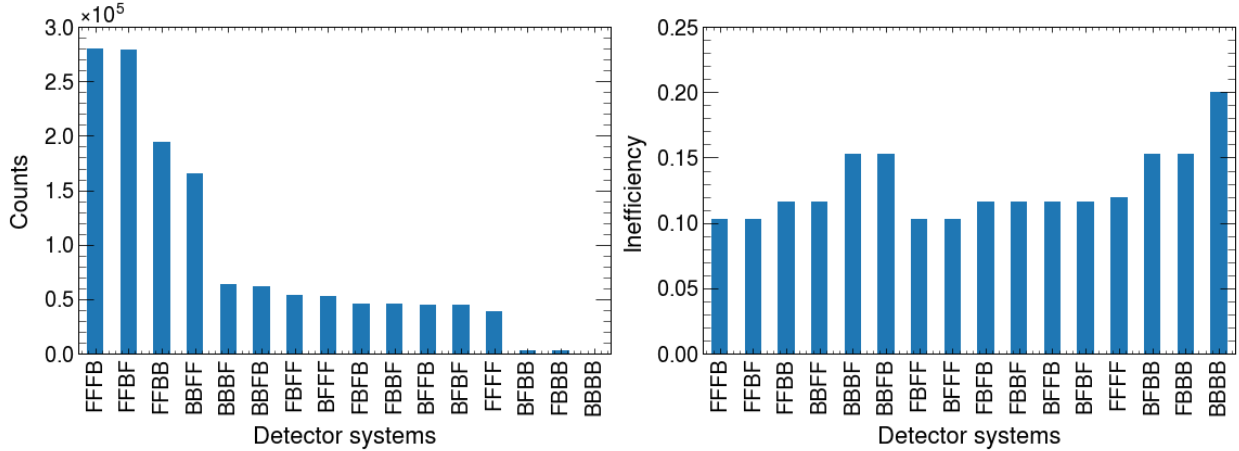
Figure 4.33: (Left) Number of events found in all possible detector systems that the final state photons can be measured by. F/B are short for FCAL/BCAL. The four letters are in the same order as the final state photons. (Right) The inefficiency for each permutation.

Method 2. Another method to study the photon reconstruction systematic is to systematically reduce the efficiency of the FCAL by up to 3% or BCAL by up to 5%. Figure 4.34 shows the results of these variations in 1% reduction increments. For t-bins reducing the FCAL efficiency leads to bigger deviations than similar reductions to the BCAL efficiency. The maximum deviation in each t bin is shown in Table 4.5. Overall the systematic uncertainty determined in the first method appear to be larger than those obtained from the second method.

$-t$ GeV^2	Systematic Uncertainty Pos.Ref. [%]	Systematic Uncertainty in Neg.Ref. [%]
$0.1 < -t < 0.2$	9.61	11.81
$0.2 < -t < 0.325$	9.79	13.28
$0.325 < -t < 0.50$	9.88	9.34
$0.50 < -t < 0.75$	7.76	9.35
$0.75 < -t < 1.0$	9.98	10.95

Table 4.5: Table of t-dependent total photon reconstruction inefficiency in the positive and negative reflectivity components of the differential cross section based on the second method.

124
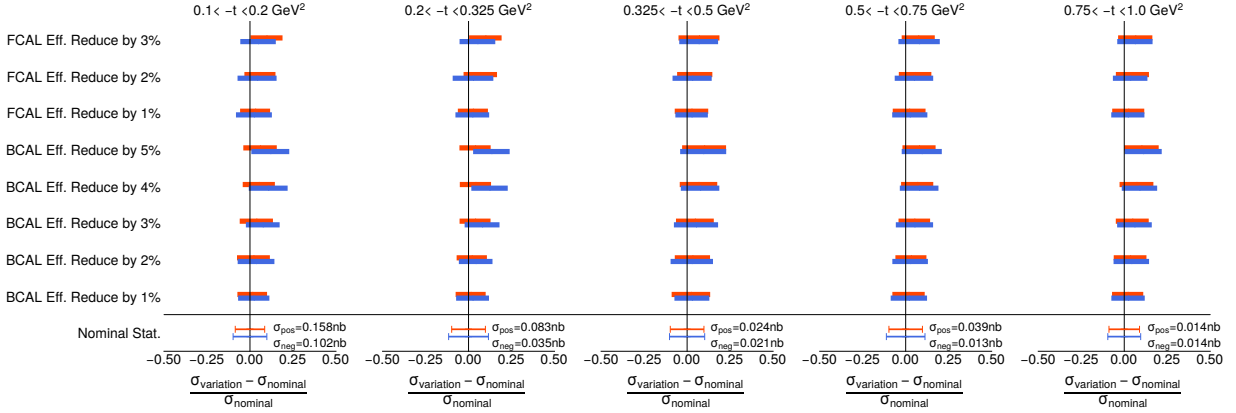
Figure 4.34: Systematics overview for variations of the FCAL/BCAL photon reconstruction efficiency. Each panel corresponds to a different t bin. The red/blue bars correspond to positive/negative reflectivity components. The x-axis is the percent deviation between the cross section for a particular (y-axis) variation, $\sigma_{\text{variation}}$, when compared to the nominal, σ_{nominal}. The width of each bar is the `Minuit` statistical uncertainty. For reference, the nominal `Minuit` statistical errors are also illustrated and are denoted by lines near the bottom of the graph.

The systematic uncertainty determined in the first method will be taken as the systematic uncertainty related to photon reconstruction efficiency. Table 4.6 shows the systematic uncertainties associated with the photon/proton reconstruction efficiency and the flux normalization.

External Systematic	Systematic Uncertainty
Photon Reconstruction	11.37%
Proton Reconstruction	3%
Flux Normalization	5%

Table 4.6: Table of external systematics.

4.7 Final Results

Figures 4.35 and 4.36 show the final results for the differential cross section and the parity asymmetry after adding the systematic uncertainties onto the bootstrapped statistical uncertainties in quadrature. The theory predictions for the differential cross-section tend to overestimate the measured values. It should be noted that the predicted differential cross section was renormalized by 60% to agree with the CLAS data[90]. This normalization factor could be a source of the underestimation.
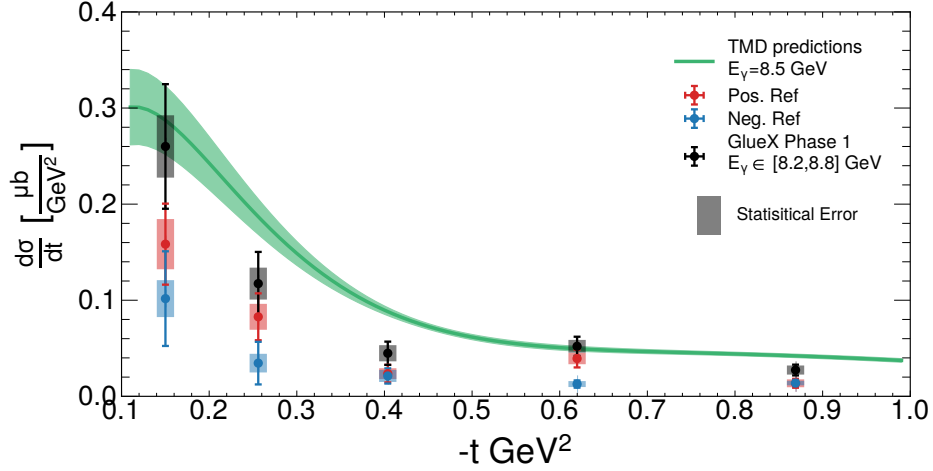
Figure 4.35: The differential cross section for the production of $a_2(1320)$ is shown in black. Incorporating polarization allows a separation of the cross section into positive and negative reflectivity states, which represents production through natural and unnatural parity exchange. Predictions from the TMD model is overlaid. Error bars contain both the statistical and systematic uncertainties added in quadrature. The rectangular shaded error bars are the statistical uncertainties.
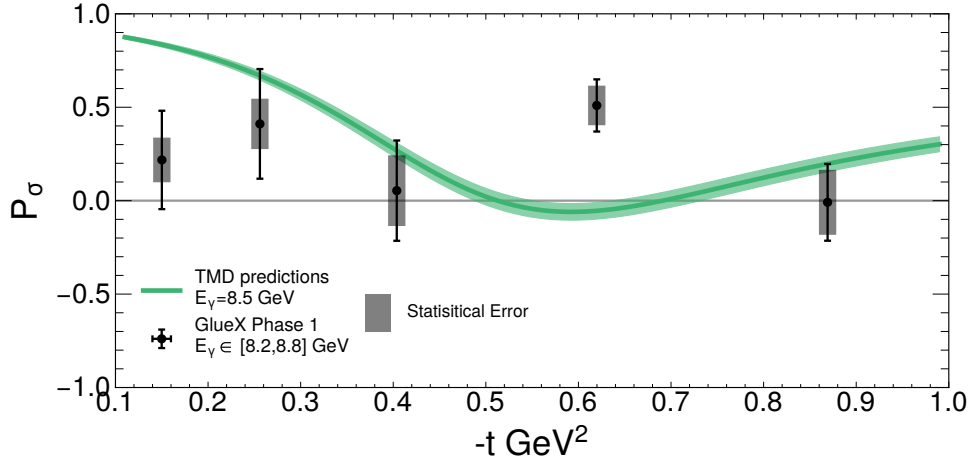
Figure 4.36: The parity asymmetry for the production of $a_2(1320)$ is shown in black. Values close to +1/-1 indicate a dominance of natural/unnatural exchange production. Predictions from the TMD model is overlaid. Error bars contain both the statistical and systematic uncertainties added in quadrature. The rectangular shaded error bars are the statistical uncertainties.

Figure 4.37 show the same differential cross section where the lower energy CLAS photoproduction data has been overlaid. The dip that is seen around 0.4 GeV is consistent in location with the CLAS data. Therefore, the dip appears to persist in photoproduction up to GlueX energies which
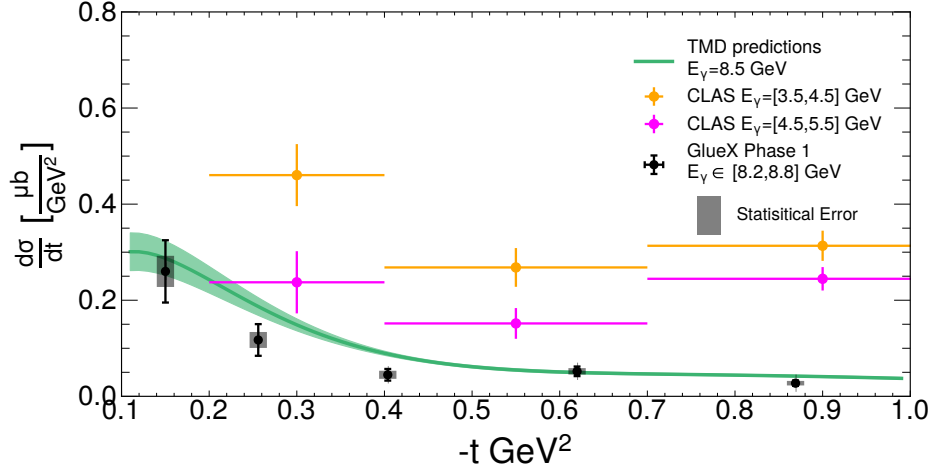
Figure 4.37: The differential cross section for the production of $a_2(1320)$ is shown in black. Incorporating polarization allows a separation of the cross section into positive and negative reflectivity states, which represents production through natural and unnatural parity exchange. Predictions from the TMD model are overlaid. Error bars contain both the statistical and systematic uncertainties added in quadrature. The rectangular shaded error bars are the statistical uncertainties. Low energy CLAS photoproduction data is also overlaid.

the current theory model does not display. This might not be a surprise as the TMD model predictions for the 5 GeV CLAS data has the dip that was already filled in the theory predictions[91]. An additional set of measurements are performed in Section B.8, where the differential cross section is determined in 4 t-bins spanning the mid points of the nominal 5 t-bins. This supplementary study shows a similar dip in the cross section.

t GeV^2	$\frac{d\sigma^+}{dt}$ $\left[\frac{\mu b}{\text{GeV}^2}\right]$	$\frac{d\sigma^-}{dt}$ $\left[\frac{\mu b}{\text{GeV}^2}\right]$	$\frac{d\sigma}{dt}$ $\left[\frac{\mu b}{\text{GeV}^2}\right]$
$0.1 < -t < 0.2$	$0.1584 \pm 0.0261 \pm 0.0331$	$0.1017 \pm 0.0192 \pm 0.0454$	$0.2600 \pm 0.0324 \pm 0.0561$
$0.2 < -t < 0.325$	$0.0828 \pm 0.0135 \pm 0.0203$	$0.0345 \pm 0.0097 \pm 0.0199$	$0.1173 \pm 0.0166 \pm 0.0285$
$0.325 < -t < 0.5$	$0.0236 \pm 0.0056 \pm 0.0072$	$0.0212 \pm 0.0063 \pm 0.0048$	$0.0448 \pm 0.0084 \pm 0.0087$
$0.5 < -t < 0.75$	$0.0393 \pm 0.0059 \pm 0.0071$	$0.0128 \pm 0.0031 \pm 0.0021$	$0.0521 \pm 0.0067 \pm 0.0074$
$0.75 < -t < 1.0$	$0.0136 \pm 0.0041 \pm 0.0021$	$0.0138 \pm 0.0023 \pm 0.0021$	$0.0274 \pm 0.0047 \pm 0.0030$

Table 4.7: Table of the $a_2(1320)$ differential cross section measurement split into different reflectivity components, $\frac{d\sigma^+}{dt}$ and $\frac{d\sigma^-}{dt}$. Statistical and systematic uncertainties are also shown following the central measurement.

t GeV^2	P_σ
$0.1 < t < 0.2$	$0.2180 \pm 0.1195 \pm 0.0920$
$0.2 < t < 0.325$	$0.4109 \pm 0.1349 \pm 0.1065$
$0.325 < t < 0.5$	$0.0537 \pm 0.1891 \pm 0.0906$
$0.5 < t < 0.75$	$0.5096 \pm 0.1059 \pm 0.0834$
$0.75 < t < 1.0$	$-0.0088 \pm 0.1739 \pm 0.0668$

Table 4.8: Table of the parity asymmetry for the production of the $a_2(1320)$. Statistical and systematic uncertainties are also shown following the central measurement.

4.8 Future Studies

4.8.1 Waveset Choice
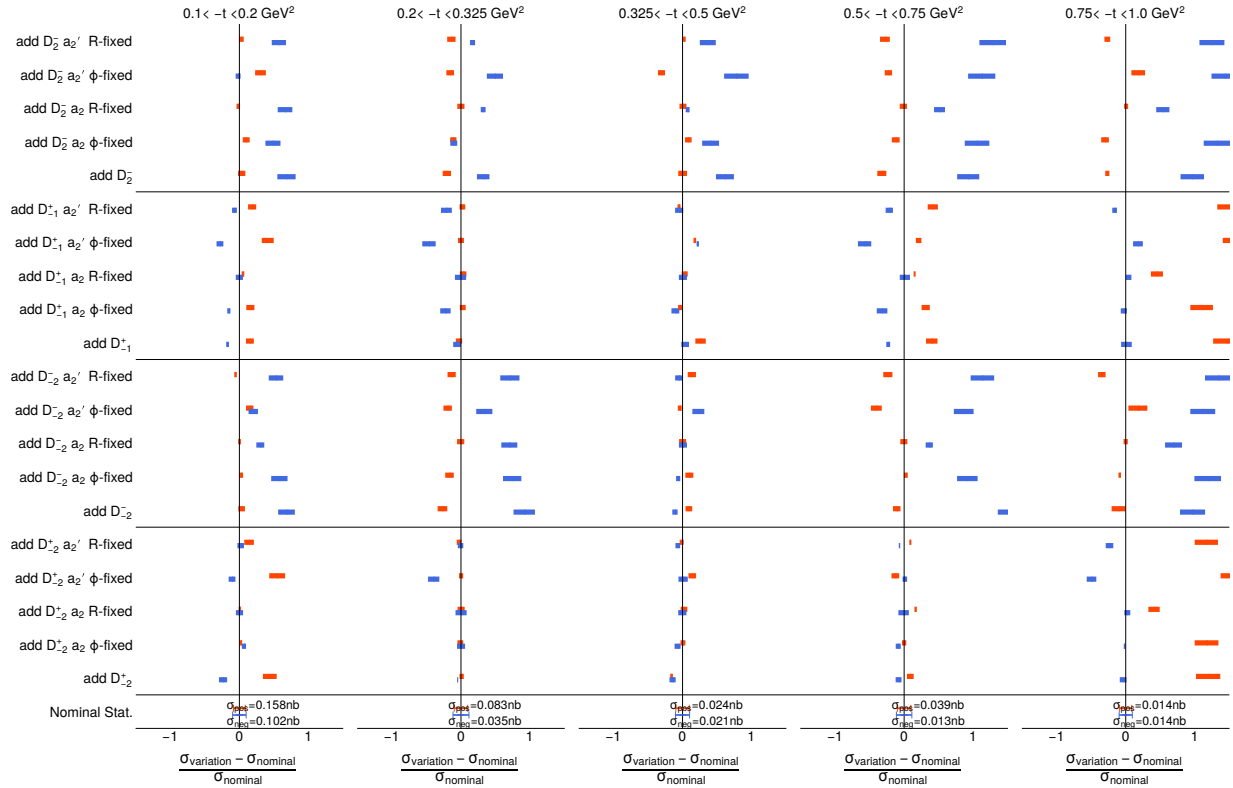
Figure 4.38: Waveset addition systematic for GlueX Phase 1 Data. Four potential waves are included. For each addition 5 total variations are tested. "add D" includes a specific D-wave. "ϕ-fixed" fixes the phase of all the nominal D-waves of the $a_2(1320)$ or $a_2(1700)$ resonance. "R-fixed" instead fixes the magnitude.

Part of the motivation to choose the TMD waveset as the nominal waveset was so that a

128

comparison to theory predictions can be made. The TMD waveset contains 6 specific waves out of the 10 possible D-wave/reflectivity combinations. To study the stability of the cross section results with respect to this waveset choice, an additional wave could be included in the fit. This leaves 4 potential options: D_2^-, D_{-1}^+, D_{-2}^-, and D_{-2}^+. These waves can be included with 0 intensity to a fit that was seeded with the nominal values. Four additional variations were performed for each potential wave addition to limit the flexibility that including an additional wave has. These variations fix the phase (or magnitude) of all the nominal $a_2(1320)$ (or $a_2(1700)$) waves. Figure 4.38 shows the significance of these variations. In general, the deviations can be large and significant for both reflectivity components. The middle t bin appears to be mostly well-behaved. There is an apparent bias that exists in that the varied cross sections never decrease as much as they can increase. This is likely due to interference effects and leakage of intensity out of the S-wave. It is clear that the waveset composition changes drastically as a function of t. Further studies are needed to determine how to consistently evaluate waveset choice for this sort of analysis.

4.8.2 Precision of the Likelihood and Multiple Solutions
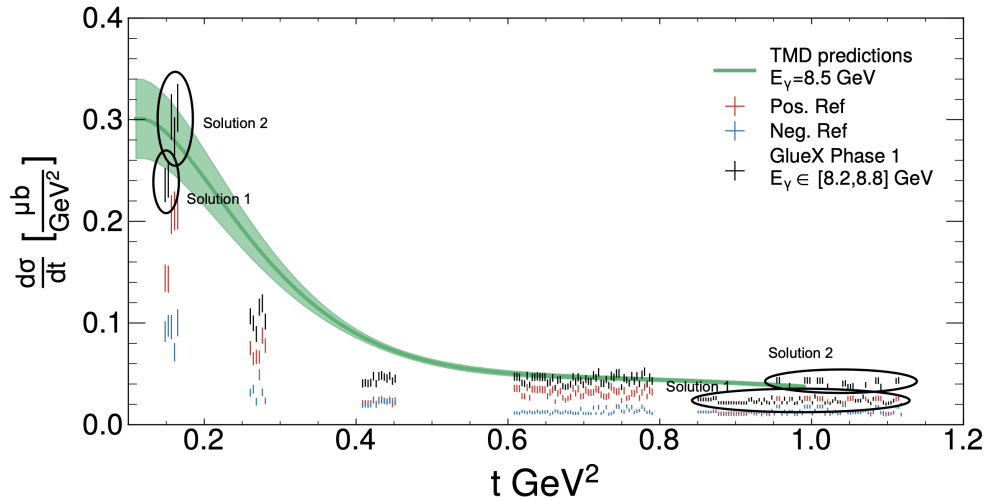
Figure 4.39: The differential cross section for the production of $a_2(1320)$ is shown in black. The positive and negative reflectivity components are shown in red/blue. The error bars denote the statistical uncertainties estimated by `Minuit`. The five cluster of data points correspond to the 5 different t-bins. Only fits within the 25 units of NLL are shown for each bin. The results in each cluster are organized from best to worse NLL where the left-most fit is the current nominal fit. Two obvious sets of solutions are observed in the lowest and highest bins.

129

A large ensemble of randomized-initial-parameter fits are initially performed in search for an approximate global minimum, see Section 4.5.1. Figure 4.39 shows all converged fits, scattered along in t, within 25 units of negative log-likelihood, NLL, for each t-bin. Multiple solutions clearly exist in the lowest and highest bins. The current selection of the nominal fit is simply a choice to pick the fit with the best likelihood. How much worse is one fit's likelihood compared to another? Is a second fit, that is worse by 5 units of NLL actually that much worse? Are we even sensitive to these differences? To study this, an alternative fit is additionally considered in the lowest and highest t-bins. The alternative fit is the best solution in the second cluster of solutions. Figure 4.40 shows these additional solutions.
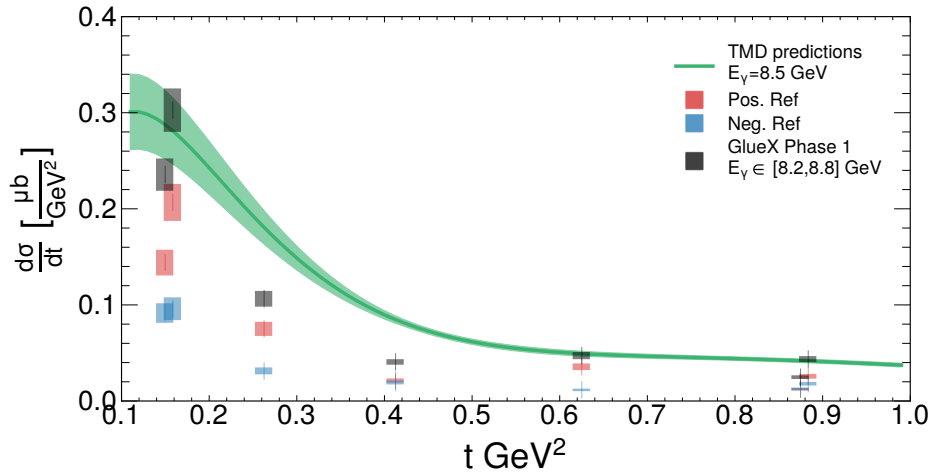
Figure 4.40: The differential cross section for the production of $a_2(1320)$ is shown in black. The positive and negative reflectivity components are shown in red/blue. The error bars denote the statistical uncertainties estimated by `Minuit`. For the lowest and highest t-bins, the alternative fit considered in this section is also shown. The alternative fits are shown shifted to the right of the nominal results.

The bootstrap procedure uses a random number generator to determine the indices of the dataset to sample. The sequence of the pseudo-random numbers depends on a seed argument that is passed to it. To compare two candidate nominal fit results, 100 bootstrap iterations are performed only on the `accmc` dataset with the same set of seeds. This is done so that each bootstrap fit sees the same underlying dataset. The distribution of the differences in NLL for each pair (paired on the seed) is the 'precision of the likelihood'.

Figure 4.41 shows a comparison of the likelihood precision for these pair of fits. The top row shows the precision of the likelihood which is around 8 and 6 for the lowest and highest t-bins
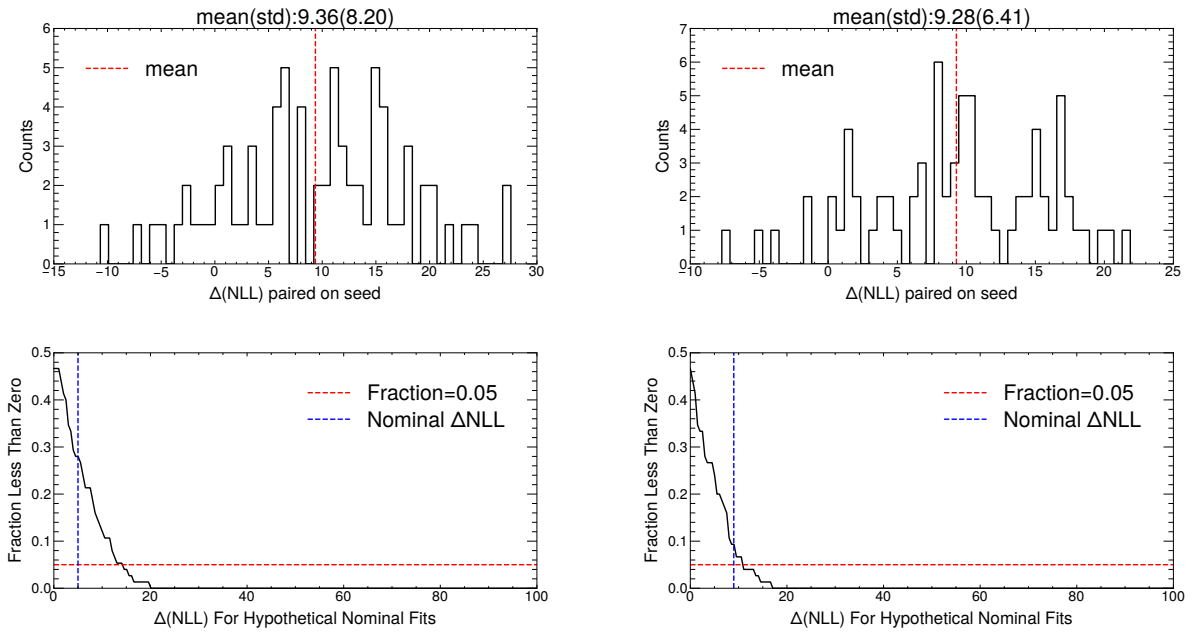
Figure 4.41: (Left-column) Precision the likelihood for two candidate nominal fits that differ by 5 units of NLL in the lowest t-bin. (Right-column) Precision of the likelihood for two candidate nominal fits that differ by 9 units of NLL in the highest t-bin. (Top-row) The difference in NLL for each pair of bootstrapped iterations. (Bottom-row) The probability distribution to accept the alternative candidate fit for hypothetical differences in NLL. With these estimates, the probability of accepting the alternative fit in the lowest/highest t-bin is around 30/10%.

respectively. If one assumes that the Δ(NLL) distribution is the same for all pairs of fits, then it is possible to estimate the probability to favor the alternative fit for hypothetical differences in initial candidate models. The probability that the alternative/worse fit becomes preferred is the integral of this distribution below 0. The bottom-row set of plots shows the fraction of fits (or probability) preferring the alternative fit vs hypothetical NLL differences. With this assumption, the probability of accepting the alternative fit in the lowest/highest t-bin is around 30/10%. Based on this analysis, an alternative solution exists in the lowest t-bin (and perhaps the highest t-bin) that is not distinguishable with the current data set statistics.

The method to handle these multiple solutions are still under investigation. One potential path forward is to look at the production phase[1] of the Breit-Wigner D-waves. The phase should be smooth across t bins. Figure 4.42 shows the phase of the production coefficient as a function of t for all Breit-Wigner D-waves split into the two reflectivity components and for the two a_2's. From these curves, it appears that the nominal solution and the alternative solution in the lowest and highest t bin, respectively, form the smoother set of solutions. Even though this is the case, the difference in likelihood between the nominal and alternative fit in the highest t-bin is quite significant. Further investigation is needed to understand how to deal with these multiple solutions.

---

[1]The production phase is obtained using atan2 which returns on the interval $[-\pi, \pi]$. The phase is invariant under 2π rotations which can lead to discontinuous-looking phases as a function of t. An algorithm is implemented to consider adding or subtracting 2π from each point. The combination of points that minimizes the total length is used as the best configuration.
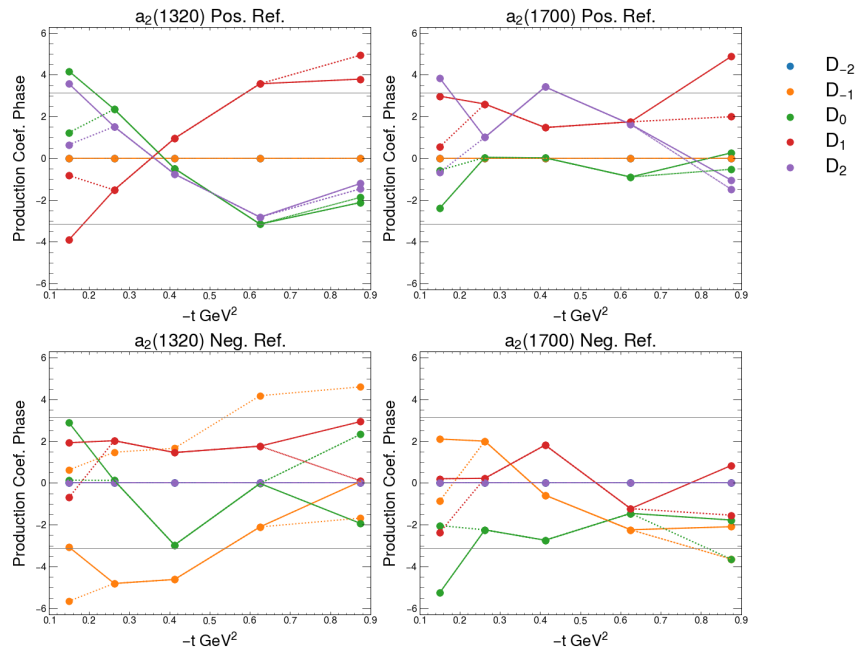
Figure 4.42: Plot of the production coefficient phase of all D-waves split into the different reflectivity components (top/bottom) and the different a_2s.

CHAPTER 5

DOUBLE REGGE EXCHANGE

5.1 Introduction

The current strategy to search for the lightest exotic hybrid meson, the π_1, requires an understanding of a wide range of the $M(\eta\pi)$ spectrum due to the small intensity and large width of the π_1. Chapter 4 studied the "resonance region", $M(\eta\pi) \lesssim 1.7$ GeV, and measured the differential cross section of the $a_2(1320)$. This is the largest feature in the spectrum and its characterization is essential in identifying the π_1. The second thrust of this dissertation is to characterize the high $M(\eta\pi)$ region, $1.6 < M(\eta\pi) < 2.8$, to help constrain other potential contributions that could contribute to exotic partial waves in the resonance region.

In Fig. 5.1, we show the distribuions of the cosine of the polar angle of the η in the Gottfried-Jackson frame ($\cos\theta_{GJ}$) versus the $\eta\pi$ invariant mass for exclusively reconstructed events, in order to illustrate their main features. This distribution includes the full t range with no additional selections on $M(\pi^0 p)$ nor $M(\eta p)$. In the resonance region clear vertical bands are seen which correspond to the production of the $a_0(980)$ and $a_2(1320)$ mesons. The lower-mass peak has a roughly uniform angular distribution, as one would expect from the S-wave decay of the $a_0(980)$. The $a_2(1320)$ does not appear to have any nodes in $\cos\theta_{GJ}$ which would suggest a mix of D-waves with different M projections. This is opposed to the low-t region where a dominant D_2 wave can be seen, see Figure 4.8 for the $M(4\gamma)$ vs $\cos(\theta)$ distribution and Section 4.5.4 for the partial wave amplitudes. A weaker signature can be seen for a broad resonance near $M(\eta\pi) \approx 1.7$ GeV, which can be the $a_2(1700)$. The partial wave analysis at low-t suggests that the $a_2(1700)$ can contribute significantly to the intensity, see Sections 4.5.4 and 4.5.2.

Events with $\eta\pi$ masses above the resonance region are increasingly dominated by events with ηs being produced predominantly forward or backward, which could be due to the production of baryon resonances, or non-resonant processes described by double-Regge exchange (DREx). These processes can produce asymmetries in the $\cos(\theta)$ angular distribution and can therefore contribute to the "exotic" odd-ℓ partial waves.
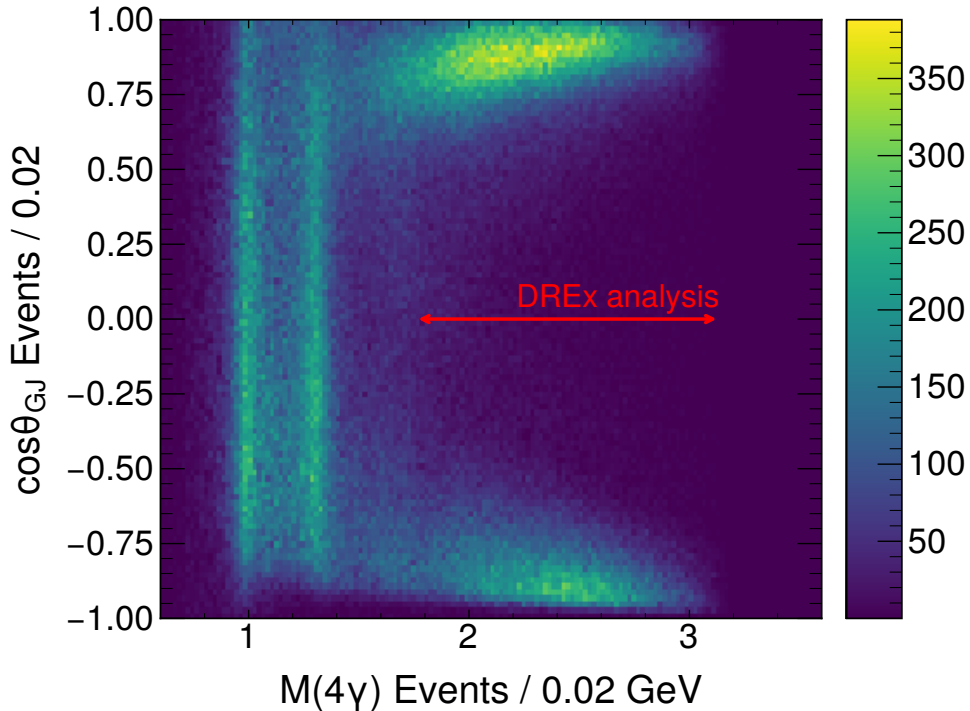
Figure 5.1: Distributions of η $\cos\theta_{\text{GJ}}$ vs. $M(\eta\pi)$ for the $\eta\pi^0$ channel

A recent measurement of the exotic π_1 resonance parameters gives a mass of $1564 \pm 24 \pm 86$ MeV and a width of $492 \pm 54 \pm 102$ MeV [33], which gives a very wide resonance that sits right between these two regions. Additionally, the amplitude of the π_1 contributions to the $\eta\pi$ channel is expected to be small, see Figures 1.10 and 1.13. It is therefore clear that understanding the processes in this high-mass "double Regge" region is crucial to robustly extract the contribution of $\eta\pi$ resonances in general, but especially the π_1.

The COMPASS experiment measured the $\eta\pi$ and $\eta'\pi$ partial waves in pion production off a nucleon target at 191 GeV/c up to $M(\eta^{(')}\pi) <$3 GeV [35]. A forward/backward asymmetry in the angular distribution can be seen in their data as was shown in Figure 1.12. This high-mass $\eta\pi$ region in the COMPASS $\pi^- p \to \eta^{(')}\pi^- p$ data was studied recently by the JPAC Collaboration, and a double-Regge exchange model was found to fit this data well. The GlueX data is similar to the COMPASS data in that the η's and π's are seen to be generated primarily in the forward/backward directions, so it seems reasonable that a similar model would fit the GlueX data as well. In addition to directly fitting this data with an amplitude model, we can also use our linearly polarized photon beam to measure polarization observables in this region, which yields complementary information

for the development of these multi-Regge models for polarized photoproduction. We report on the measurement of the Σ beam asymmetry for π and η mesons produced in these interactions.

5.2 Theoretical Model

As was described in Section 1.3.2, any reaction can be described as an infinite sum of partial waves in the s-channel or the t-channel. These are alternative or dual ways to describe the same dynamics [1]. Higher spin waves become successively more important as the center of mass energy increases and thus require that the s-channel partial wave expansion include higher L contributions. This becomes problematic as the total number of fit parameters to describe all these waves explodes making the minimization procedure significantly more difficult. It is then typical to work with a truncated set of partial waves which introduces effective background terms like the Deck effect which can be modeled by double Regge exchanges. Multi-Reggeon exchanges have been widely studied in the past [114][115][116][117][118][119]. The connection between resonances and Regge exchanges can be described by finite energy sum rules, FESR. Connecting these two domains with FESR has been done in References [120][121][122].

The DREx process has been used to describe central meson production in high-energy proton-proton collisions [123][124][125]. This process has also been studied in two pseudoscalar meson production in $K^{\pm} \to K^0 \pi^{\pm}$ [126]. Following their approach, JPAC constructed a DREx model for the COMPASS $\eta^{(')}\pi$ data [127]. The DREx model is described by an intensity of the form

$$I(m, \Omega) = k(m)|A(m, \Omega)| \tag{5.1}$$

where m is the invariant mass of the produced meson pair, Ω is the solid angle, $k(m) = \lambda^{1/2}(m^2, m_\eta, m_\pi)/2m$ is the break-up momentum, $\lambda_{x,y,z} = x^2 + y^2 + z^2 - 2(xy + xz + yz)$ is the triangle function, and

$$A(m, \Omega) = \sum_i c_i T_i(\alpha_1, \alpha_2; s_{12}, s_{23}) \tag{5.2}$$

where i runs over different double Reggeon exchanges, s_{12} is the $\eta\pi$ invariant mass squared, and s_{23} is the slow-pseudoscalar plus recoil baryon invariant mass. Fig. 5.2 shows the double Regge kinematic variables, where particle 1/2 would correspond to the fast/slow pseudoscalar meson. Also shown is the squared momentum transfer to the baryon u_3, the squared momentum transfer to the high-momentum meson t_1, and the squared center-of-mass energy s. T is a generic double Regge
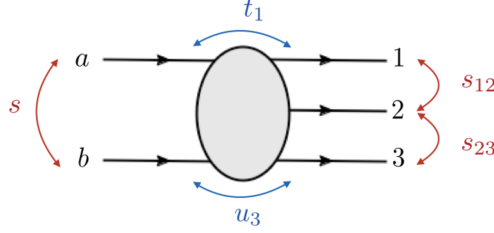
Figure 5.2: Double Regge kinematic variables.

exchange amplitude for five spinless particles with an odd number of pseudoscalars [115][126] and is given by

$$
\begin{aligned}
T(\alpha_1, \alpha_2; s_{12}, s_{23}) = {} & K\Gamma(1 - \alpha_1)\Gamma(1 - \alpha_2)\frac{(\alpha' s_1)^{\alpha_1}(\alpha' s_2)^{\alpha_2}}{\alpha' s} \\
& \times \left[\frac{\xi_1 \xi_{21}}{\kappa^{\alpha_1}} V(\alpha_1, \alpha_2, \kappa) + \frac{\xi_2 \xi_{12}}{\kappa^{\alpha_2}} V(\alpha_2, \alpha_1, \kappa) \right]
\end{aligned}
\tag{5.3}
$$

The nucleons play a spectator role at large total center of mass energies allowing their spins to be ignored. α is a scale parameter. The poles of T are at integer values of $\alpha = J$ and correspond to the exchange of a physical particle with spin J. ξ ensures that only poles with even signature $(-1)^J = +1$ are possible, as odd signature poles cannot couple to $\eta\pi$. V is a vertex function that incorporates all Reggeon-Reggeon-particle couplings (middle vertex). α_i refers to the exchange of a Regge trajectory and takes on a specific experimentally determined linear form that is dependent on the Reggeon that is exchanged, see Section 1.3.1.

With these trajectories, the intensity is completely specified by the c_i coefficients, as Regge theory predicts the dependence of the fast-η and fast-π amplitudes as a function of (s_{12}, s_{23}). This description can dramatically reduce the number of fit parameters when compared to a partial wave analysis (i.e. the JPAC analysis only has 3-4 amplitudes or c_i variables).

The potential Reggeons that are exchanged are reaction and energy-dependent. COMPASS included (L=1,..,6; M=1) and (L=2; M=2) partial waves for their $\eta\pi$ analysis and (L=1,...,6; M=1) for the $\eta'\pi$ analysis. Only positive reflectivity waves (which correspond to natural exchanges) were included due to the dominance of Pomeron exchange at COMPASS energies ($\sqrt{s}$=191 GeV). A single negative reflectivity wave can be included but was found to contribute $< 0.5\%$ to the intensity. At COMPASS there is a dominance of natural exchanges occurring which is also seen in the production of neutral particles at GlueX. Additionally, recall from Section 1.3.1, that a Regge trajectory corresponds to a particular infinite series of partial waves. By truncating their partial
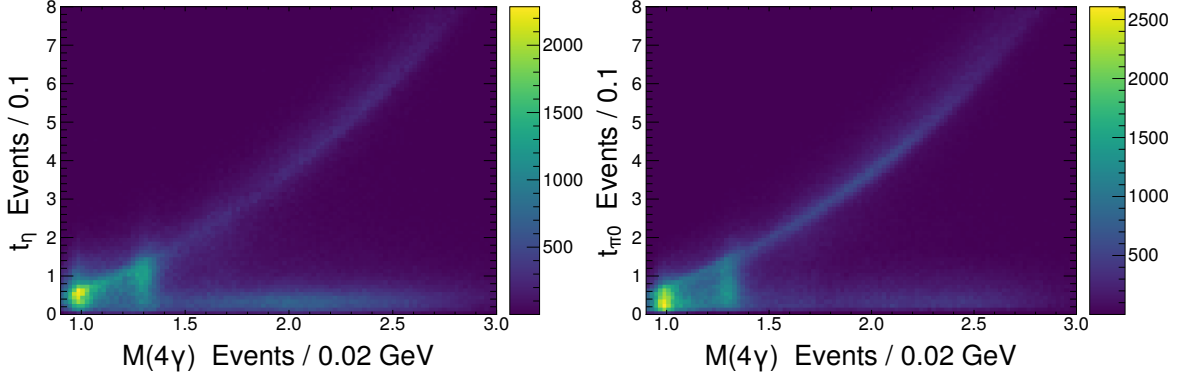
Figure 5.3: t_π and t_η as a function of $M(\eta\pi^0)$ as observed in the $\eta\pi^0$ channel.

wave series to the set of waves that COMPASS used (up to L=6), the JPAC model showed a significant loss in the modeled intensity around $M(\eta\pi) \sim 2.5$ GeV.

A similar model is being developed by the JPAC Collaboration to understand the potential contributions of double Regge exchanges in polarized photoproduction of the $\eta\pi$ system. Let t_η/t_π denote the momentum transfer at the top vertex which is t_1 in Figure 5.2. Fig. 5.3 show distributions for t_η/t_π as a function of $M(\eta\pi^0)$ from GlueX data. For $M(\eta\pi) \gtrsim 1.6$ GeV, it is clear that either low-t_η/high-t_π production or high-t_η/low-t_π production dominates this region.

Baryon production and DREx are similar in that one of the pseudoscalars is more forward-going as it recoils against the other pseudoscalar and the proton. This asymmetry is reflected in an asymmetry in the measured "decay" angular distributions of a candidate $\eta\pi$ resonance. Their similarities can make them difficult to separate. Figure 3.24 shows several photoproduction diagrams, including the signal in the diagram in the top-left, with an η and a π produced together in the final state. Two DREx and two baryon diagrams are shown. Figure 5.10 show contributions from multiple baryon resonances, i.e. the $\Delta^+(1232)$ and the $N(1535)$.

As input for the development of models to describe polarized photoproduction in this mass range at GlueX energies, the Σ beam asymmetry for individual η and π mesons are measured when one of the pseudoscalars is very forward-going. Σ is an observable that gives insight into the naturality of the exchange. For more information about naturality, see Section 1.2. Σ_η and Σ_π are measured in five bins of t_1 for $t_1 < 1$ GeV^2 and as functions of several kinematic variables including baryon-sensitive ones. This additional binning provides separation between the baryons and double Regge contributions. Σ takes on any value between -1 and 1. A value of 1(-1) corresponds to complete
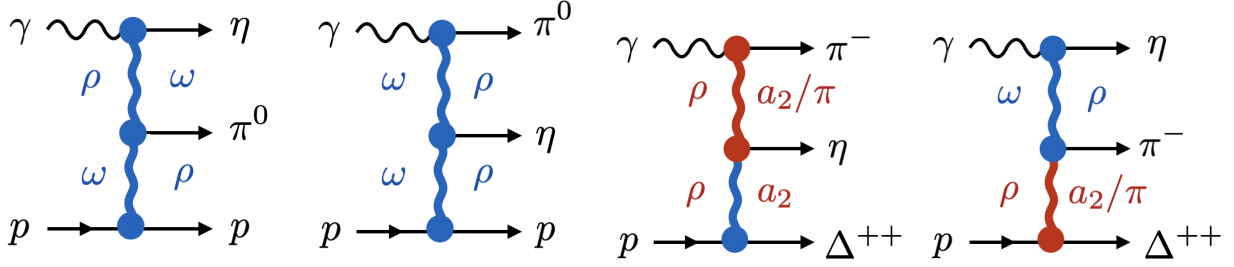
Figure 5.4: Example diagrams for double Reggeon exchange in the photoproduction of an η with a π. Exchanges of ρ, ω, and a_2 are all natural parity exchanges, whereas π is an unnatural parity exchange. Diagrams provided by Vincent Mathieu.

dominance of natural(unnatural) exchanges. Determining the relevant exchanges at the top vertex would also dictate the relevant exchanges at the bottom vertex.

The lowest-order Reggeon contributions to this double-Regge process are illustrated in Fig. 5.4. Generally, the neutral $\eta\pi$ channel is expected to be dominated by neutral ρ and ω exchange, while the charged $\eta\pi$ channel should have additional contributions from π and a_2 exchange in addition to charged ρ exchange. Sub-leading contributions are also known to contribute to polarization observables [121][128][129][130]. Measuring both the charged and neutral $\eta\pi$ decay modes provides complementary information. An analysis was performed in parallel on the reaction $\gamma p \to \eta\pi^-\Delta^{++}$ by another GlueX collaborator[1]. A comparison will be made between the channels.

5.3   Previous Beam Asymmetry Measurements at GlueX

GlueX has published beam asymmetry results for the production of several pseudoscalars, the very first being $\Sigma(t)$ for π^0 and η back in 2017 [131]. Figure 5.5 shows Σ as a function of momentum transfer, t, for the reactions $\gamma p \to \pi^0 p$ and $\gamma p \to \eta p$. Σ is both very nearly $+1$ in both cases over the range of t studied, suggesting that natural parity exchange is strongly dominant in this particular case. This turns out to be the general case for the photoproduction of other electrically neutral pseudoscalars at GlueX [132][133]. One exception is in the case of $\gamma p \to \pi^-\Delta^{++}$ [134]. The results are shown in Figure 5.6 where a striking t-dependence on Σ can be seen. At low-t unnatural exchanges dominate due to pion exchange whereas natural exchanges dominate at larger momentum transfer. In general, at GlueX, natural exchanges appear to dominate when pion exchange is not possible.

---

[1]The other collaborator is Colin Gleason.
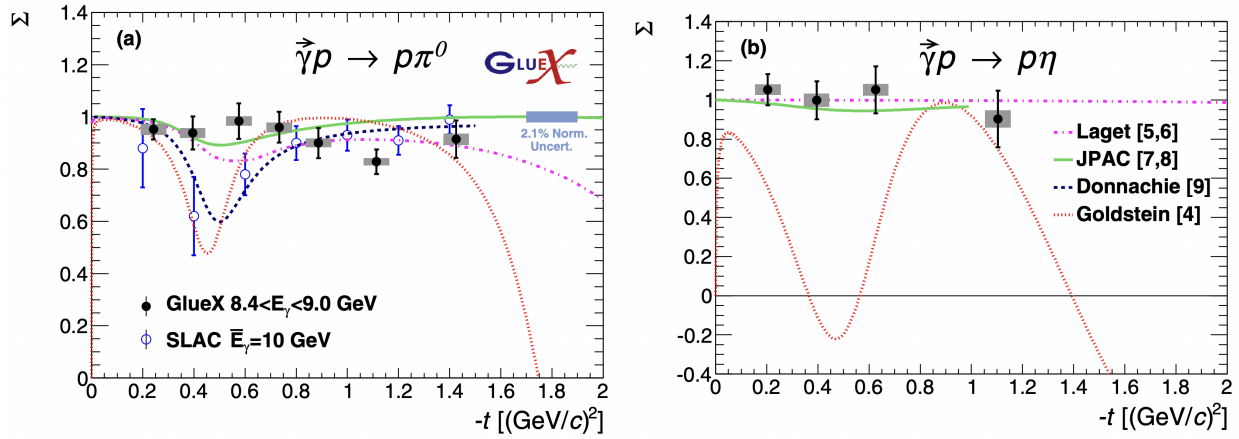
Figure 5.5: Beam asymmetry for (a) $\gamma p \to \pi^0 p$ and (b) $\gamma p \to \eta p$. SLAC measurements are also plotted along with various Regge theory predictions. Taken from [135].
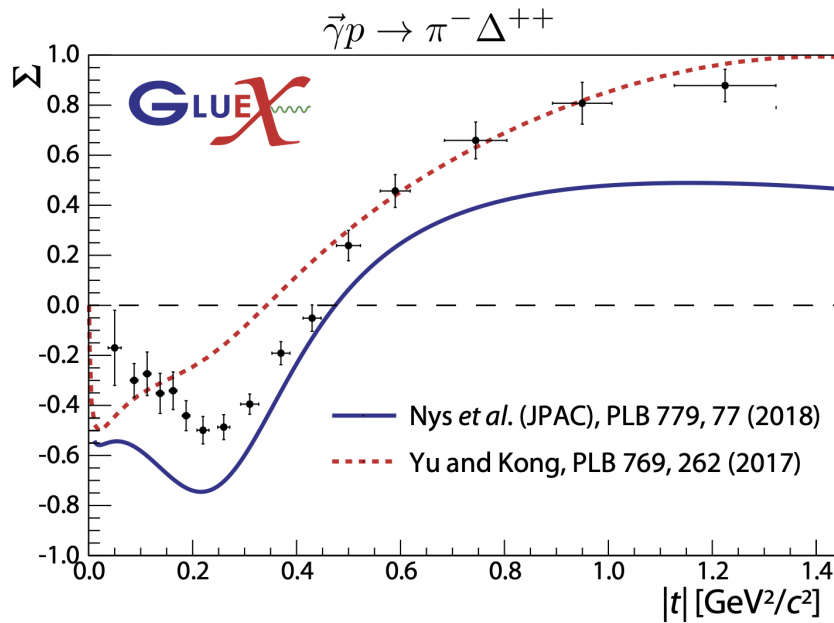
Figure 5.6: Σ vs |t| for $\gamma p \to \pi^- \Delta^{++}$ Errors include stat. and syst. uncertainties added in quadrature. Taken from [136].

5.4   Additional Event Selections

The discussion of event selection begins where Chapter 3 left off. All of the standard event selections have been applied and "accidentally" tagged beam photons have been subtracted. Recall that $\gamma_1\gamma_2$ form the candidate π^0 and that $\gamma_3\gamma_4$ form the candidate η. The invariant mass region of interest for this study is from $1.6 < M(\eta\pi^0) < 2.8$ GeV. There are limited statistics at higher masses, see Figure 5.3. The 1.6 GeV lower limit sits above the resonance region where most of the pronounced resonances and additional backgrounds live. To account for this difference in background contributions, the sideband subtraction procedure has been altered. Significant background underneath the invariant mass distribution of the candidate pion, $M(\pi^0)$, exists when looking inside the $\eta\pi$ resonance region. This is not the case in the double Regge region. Figure 5.7 shows the invariant mass distributions for the candidate π^0 and η in the double Regge region. No clear background exists underneath the $M(\gamma_1\gamma_2)$ peak and is no longer subtracted. The η signal and sideband regions are defined toward the end of the section in Table 5.1. The weights are determined in the same fashion as was done in Section 3.4.1.

In the presence of background, the asymmetries in the signal and sideband regions can be combined using the equation

$$\Sigma_{signal} = \frac{\Sigma_{total} - f\Sigma_{bkgnd}}{1 - f} \tag{5.4}$$

where f is the dilution factor and is related to purity as purity $= 1 - f$. If the data exhibits high purity and small background asymmetries, Σ_{bkgnd}, then the correction should be small.

To determine the purity, a fit was performed on the $M(\gamma_3\gamma_4)$ distributions. A double Gaussian was chosen as the signal distribution with a 2nd-order polynomial as the background distribution. The double Gaussian was formed by adding two Gaussians together but restricting their means to be the same. Fig. 5.8 shows the fit results. It can be seen that this sample is highly pure with $\approx 91\%$ purity.

To determine Σ_{bkgnd}, the asymmetry can be measured in the left and right sidebands of the $M(\gamma_3\gamma_4)$ distribution. Due to the low statistics with $t_\eta < 1$, only a single asymmetry measurement is made. The resulting Σ_{bkgnd} measurements are shown in 5.9. The asymmetries measured with each pair of orthogonal orientations are mostly consistent with each other. Σ_{bkgnd} is consistent with zero asymmetry within less than 2σ.

As the purity is high and Σ_{bkgnd} is small, the dilution factor correction will be small. Additionally, the left and right sidebands produce asymmetries that are consistent with each other. It is then
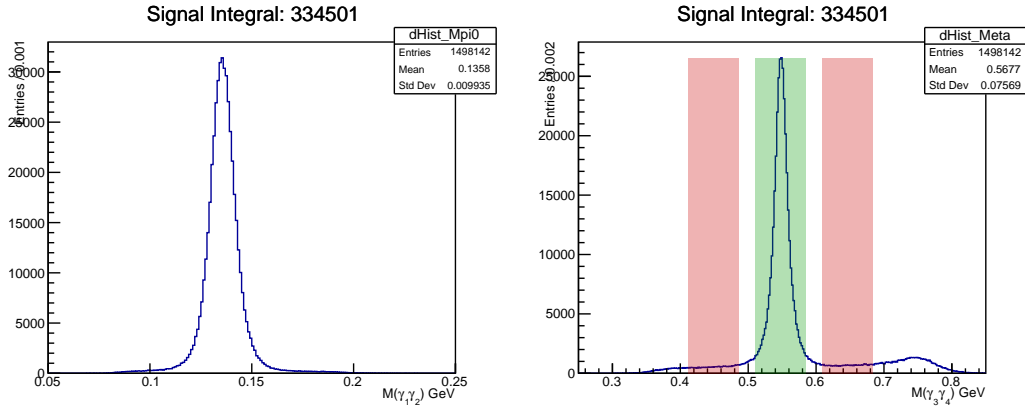
Figure 5.7: Distribution of $M(\gamma_1\gamma_2)$ and $M(\gamma_3\gamma_4)$ with all standard selections and accidental subtraction applied to data within the double Regge region. The highlighted region denotes the signal(green) and sideband(red) regions. No clear background exists underneath the $M(\gamma_1\gamma_2)$ peak.
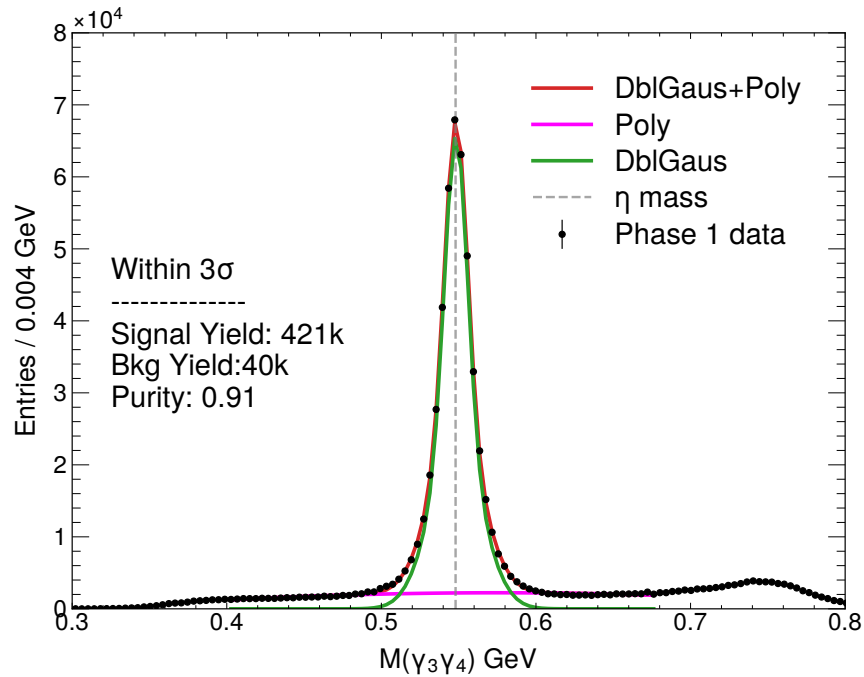
Figure 5.8: $M(\gamma_3\gamma_4)$ distribution with all standard selections and accidental subtraction applied to data within the double Regge region. Distribution is fitted to extract the purity of the signal peak.
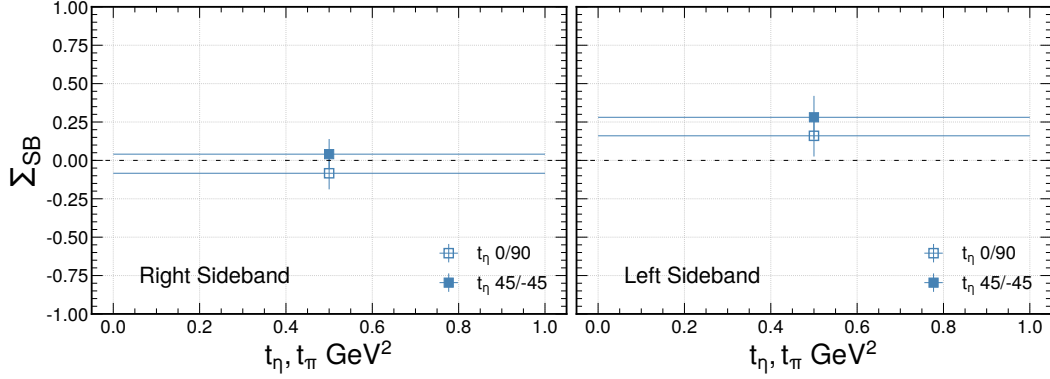
Figure 5.9: Left and right sideband asymmetry measurements for a fast-η measured in a single bin due to the lower statistics.

reasonable to simply sideband subtract the individual ϕ distributions that are fitted. All subsequent Σ asymmetry results will include sideband subtraction as a part of the measurement.

Fig. 5.10 shows t_1 and all its correlations with other kinematic variables. It can be seen in $M(\pi^0 p)$ that three πp baryon resonances populate the dataset with the strongest baryon signal coming from the $\Delta^+(1232)$ resonance. Similarly, there is an enhancement in the ηp baryon resonance close to its threshold. Figure 5.11 show a similar correlation plot for the $\eta \pi^0$ channel for fast-η and fast-π separately. The baryon contributions are more significant in these sets of plots, highlighting the overlap between the DREx and baryon processes. As we are primarily interested in the DREx process the prominent $\Delta^+(1232)$ is removed by requiring $M(\pi p) > 1.4$ GeV for most of the results. Table 5.1 summarizes the additional event selections.

$M(\eta\pi)$	[1.6, 2.8] GeV	
$M(\pi^0 p)$	>1.4 GeV	
Sideband	Signal Region	[0.5111, 0.5849] GeV
	Left Sideband	[0.4127, 0.4865] GeV
	Right Sideband	[0.6095, 0.6833] GeV

Table 5.1: Summary of additional event selections and the modifications to the sideband subtraction procedure. The specific $M(\gamma_3 \gamma_4)$ signal and sideband region are shown.

143
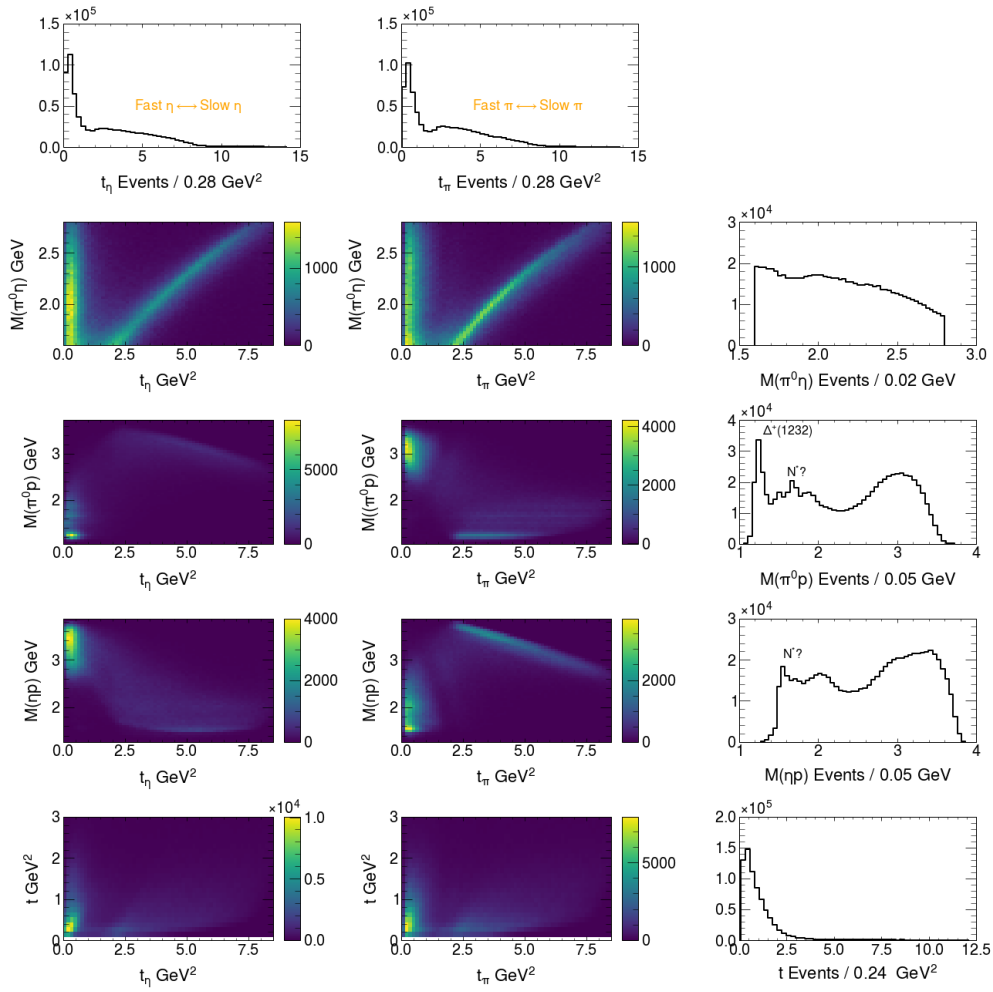
Figure 5.10: Shows all the relevant kinematic variables for the double Regge exchange process and some of their correlations. The x-axis is shared.

(a) Selected Fast-η

(b) Selected Fast-π

Figure 5.11: Correlation plots for the $\eta\pi^0$ channel. (a) shows the kinematic variables with a selection on fast-η's, $t_\eta < 1\text{GeV}^2$. (b) shows the kinematic variables with a selection on fast-π's, $t_\pi < 1\text{GeV}^2$.

5.5 Beam Asymmetry Measurement Methodology

For the photoproduction of a single pseudoscalar by a linearly polarized photon beam, the total cross section can be split up into two parts: one component of the cross section that is parallel to the reaction plane and another that is perpendicular. The reaction plane is determined by the incident beam photon and the recoiling proton. When the polarization is perpendicular(parallel) to the reaction plane only natural(unnatural) exchanges contribute to the cross section. This correspondence is known as *Stichel's Theorem* [137][138]. Although this separation of production processes has been shown in single pseudoscalar photoproduction, it should be accurate to leading order for the DREx process. Further theoretical development is needed to determine the scale of the correction at GlueX energies.

$$\frac{d\sigma}{dt} = \frac{d\sigma_\perp}{dt} + \frac{d\sigma_\parallel}{dt} \tag{5.5}$$

To quantify the strength of natural exchanges to that of unnatural exchanges, a useful quantity to look at is the beam asymmetry, Σ

$$\Sigma = \frac{\frac{d\sigma_\perp}{dt} - \frac{d\sigma_\parallel}{dt}}{\frac{d\sigma_\perp}{dt} + \frac{d\sigma_\parallel}{dt}} \tag{5.6}$$

The azimuthal dependence of the cross section in the photoproduction of psuedoscalars by a linearly polarized photon beam off an unpolarized target is given by

$$\sigma(\phi) = \sigma_0(1 - P_\gamma \Sigma \cos 2(\phi_p - \phi_\gamma)) \tag{5.7}$$

where σ_0 is the unpolarized cross section, Σ is the linearly polarized beam asymmetry, ϕ_γ is the polarization angle of the photon beam, and ϕ is the azimuthal angle of the fast pseudoscalar in the lab frame. Figure 5.12 show a diagram of the relevant variables. $\cos(2x)$ changes sign when $x \to x + \pi/2$ so that the yields in the different orientations take on the following forms

$$Y_\perp \propto N_\perp(1 + P_\gamma \Sigma \cos 2\phi) \tag{5.8}$$

$$Y_\parallel \propto N_\parallel(1 - P_\gamma \Sigma \cos 2\phi) \tag{5.9}$$

Potential ϕ-dependent detector acceptance effects cancel when considering the yield asymmetry given by

$$Y_A = \frac{Y_\perp - F_R Y_\parallel}{Y_\perp + F_R Y_\parallel} = \frac{(P_\perp + P_\parallel)\Sigma \cos 2\phi}{2 + (P_\perp - P_\parallel)\Sigma \cos 2\phi} \tag{5.10}$$

The Y_A is fitted to determine the Σ beam asymmetry.
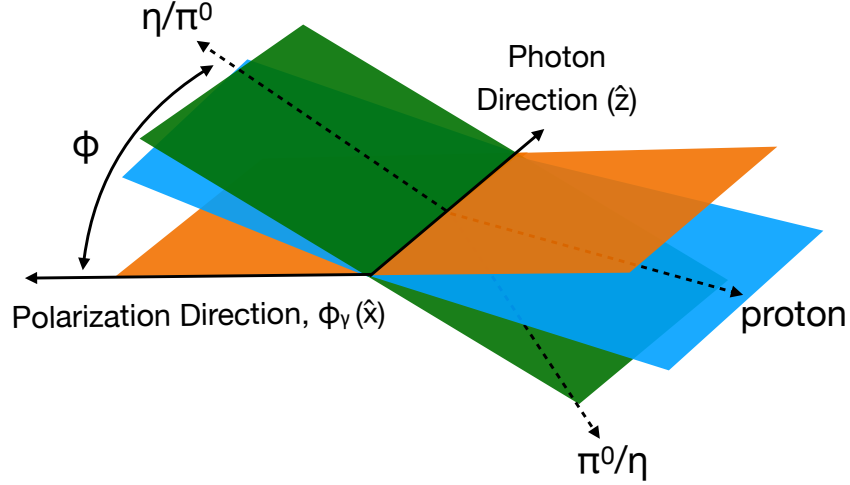
Figure 5.12: Diagram for the polarized production of a η/π^0 against a π^0/η and a proton. The reaction plane is shown in blue. The decay plane is shown in green. The orange plane contains the polarization direction.

Run Period	Flux Ratio 0/90	Flux Ratio 45/-45	Pol. Offset 0/90 (°)	Pol. Offset 45/-45 (°)
2017-01	1.038	0.995	3.13 ± 0.14	3.16 ± 0.17
2018-01	0.965	1.023	4.17 ± 0.14	3.01 ± 0.17
2018-08	0.919	1.032	3.07 ± 0.14	3.09 ± 0.17

Table 5.2: Photon beam flux ratios and polarization offsets for the beam asymmetry measurement for all three run periods analyzed. Offsets were taken from Reference [110].

5.5.1 Fit Procedure

The yield asymmetry, Y_A, will be fitted using Equation 5.10 to determine Σ. The beam properties used in this analysis are the photon flux and the amount and orientation of the linear polarization of the beam. The beam asymmetry measurement uses the ratio of the photon fluxes(N), $F_R = \frac{N_\perp}{N_\parallel}$, for each pair of orthogonal orientations. The photon fluxes were extracted with the standard `plot_flux_ccdb.py` program for each run period, and the corresponding ratios are given in Table 5.2. It is also known that the orientation of the linear photon polarization deviates by a few degrees from its nominal values. We use the standard offset for each polarization pair in each run period as determined in Ref. [110] by studying the photoproduction of $\rho^0 \to \pi^+\pi^-$ events, and

Run Period	0(°)	45(°)	90(°)	-45(°)
2017-01	0.3537 ± 0.0100	0.3484 ± 0.0102	0.3472 ± 0.0098	0.3512 ± 0.0102
2018-01	0.3458 ± 0.0055	0.3416 ± 0.0056	0.3448 ± 0.0055	0.3597 ± 0.0057
2018-08	0.3563 ± 0.0070	0.3403 ± 0.0075	0.3430 ± 0.0074	0.3523 ± 0.0077

Table 5.3: Photon polarization fractions for all three run periods analyzed [105].

reproduce these values in Table 5.2. The polarization magnitude for each polarization orientation and for each run period, as measured by the Triplet Polarimeter [105], is shown in Table 5.3. The above beam properties are fixed in the fit.

The ϕ distribution is determined for each polarization pair and for each kinematic bin. The yield asymmetry is formed for all pairs and is fitted by Equation 5.10. Since all the beam properties are fixed, only the Σ beam asymmetry is free to float. Figure 5.13 shows a sample fit in a particular bin to the yield asymmetry. p_2 is the measured Σ. Additional fits are performed to the $Y_\parallel$ and $Y_\perp$ yield and to the instrumental asymmetry which is given by $Y_\parallel + Y_\perp$. Y is fitted by Equation 5.7 where p_0 and p_1 are the normalization constant and $P_\gamma \Sigma$ respectively. Appendix C.2 shows all the fits to yield asymmetry for the GlueX Phase-I dataset.
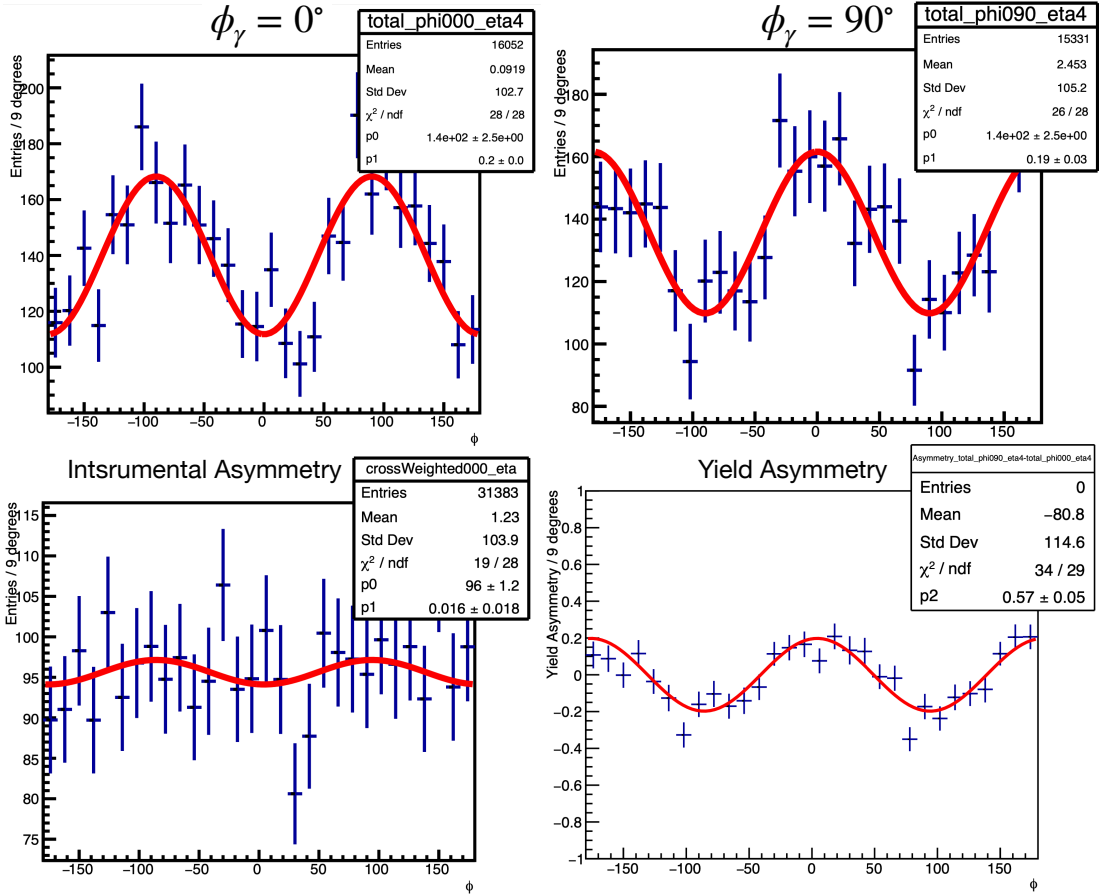
Figure 5.13: Sample fit of Equation 5.10 to the yield asymmetry for $t_\eta \in [0.8, 1.0]\text{GeV}^2$. The panels on the top correspond to $Y_\parallel$ and $Y_\perp$ for the 0 and 90 degree polarization orientation datasets. p_0 and p_1 are the normalization constant and $P\Sigma$ in Equation 5.7. The bottom-left plot shows the instrumental asymmetry which is equal to $Y_\parallel + Y_\perp$. The bottom-right plot is the yield asymmetry. $p2$ is the Σ beam asymmetry.

5.6 Consistency of Σ Between Datasets

For each kinematic bin, several measurements of Σ are made. A measurement is made for the 0/90 and 45/-45 degree polarization orientation pairs. A measurement is also made for each run period of the GlueX Phase-I dataset. The following sections will study the consistency between these datasets so that they can be combined in the final measurement. An additional consistency check is made by splitting $M(\eta)$ into two halves to form two almost independent datasets. The consistency between these datasets is quantified in the "integrated" case with no additional bins in u_3, s_{12}, or s_{23} as the statistical precision with additional bins would be limited. The below studies indicate that the independent measurements are consistent. The main results will use the weighted sum to combine the three datasets in GlueX Phase-I and the 0/90, 45/-45 datasets. Appendix C.3 contains plots for the Σ measurements in the additional kinematics bins.

5.6.1 Consistency Between Run Periods

Figure 5.14 shows Σ as a function of t_1 integrated over u_3, s_{12}, and s_{23} for the 3 datasets that make up the GlueX Phase-I dataset. Most of the data points are in agreement with each other. Some bins are statistically limited, showing large error bars, which are mainly seen from the Spring 2017 run period. Let S7, S8, F8 represent the Spring 2017, Spring 2018, and Fall 2018 datasets. Figure 5.15 shows the difference in Σ between the S7/S8 datasets with respect to the F8 dataset. Most points are consistent within 1.5σ with no apparent systematic trends. A reduced χ^2, can then be determined with these measurements to determine the overall consistency with 0 difference. The reduced χ^2 is roughly equal to 1.16. A value of 1 is expected when only statistical effects contribute to this difference. As the values are quite similar, the final results will be measured from the sum of the individual run periods.

5.6.2 Consistency Between Polarization Orientation Pairs

Σ is measured independently for both pairs of orthogonal orientations. The measured values are shown in Figure 5.16. The difference between each pair of measurements is taken for the five bins of t_η and t_π. The values are shown in Figure 5.17. A reduced χ^2 can then be determined with these 10 measurements to determine the overall consistency with 0. The reduced χ^2 is roughly equal to 0.96. A value of 1 is expected when only statistical effects contribute to this difference. As the values are quite similar, it is reasonable for the final results to be an average of the paired polarization measurements. The individual measurements can be found in Appendix C.3.1.
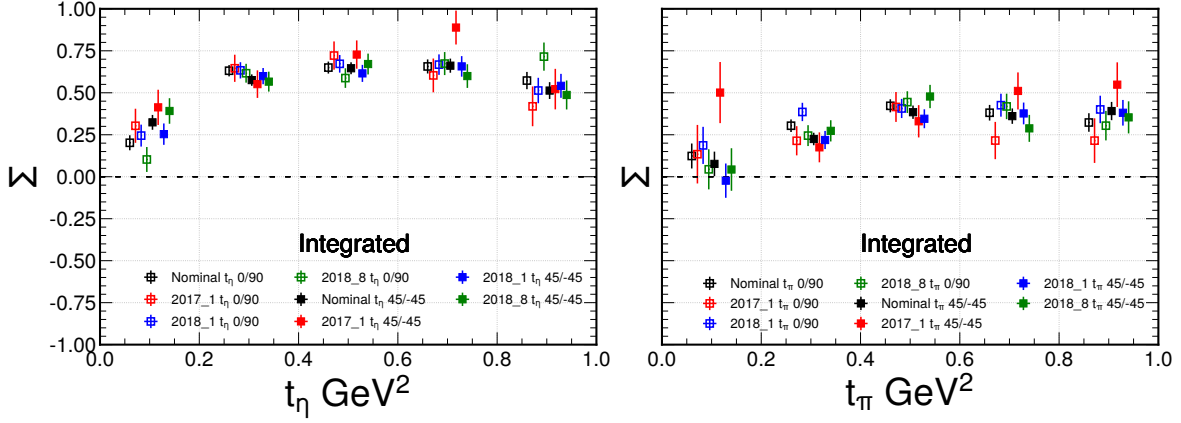
Figure 5.14: Asymmetries for t_η, t_π are measured in five bins split into separate run periods. Integrated over u_3, s_{12}, and s_{23}.
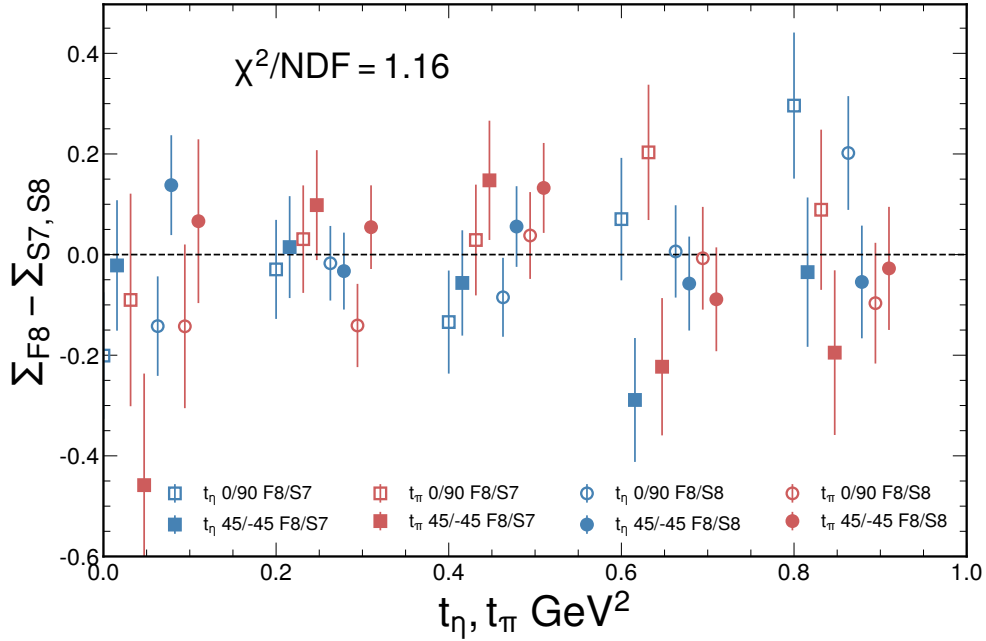
Figure 5.15: The difference in Σ between the S7/S8 datasets with respect to the F8 dataset is shown. A reduced χ^2 is then determined where the residuals for these data points are calculated with respect to 0.

5.6.3 Comparison of $M(\eta)$ halves

The $M(\eta)$ distribution can be split in half along the peak to obtain two independent datasets for an additional consistency check. See Figure. 5.8 for the mass distribution. The left and right halves can be sideband subtracted independently, and the resulting asymmetries for each half can
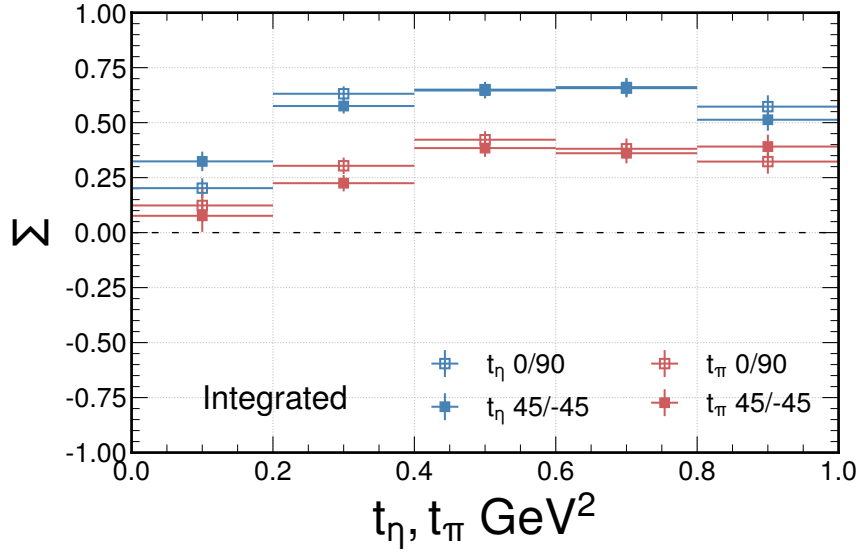
Figure 5.16: Σ measured in five bins of t_η and t_π. A measurement is made for each pair of polarization orientations. Integrated over u_3, s_{12}, and s_{23}.
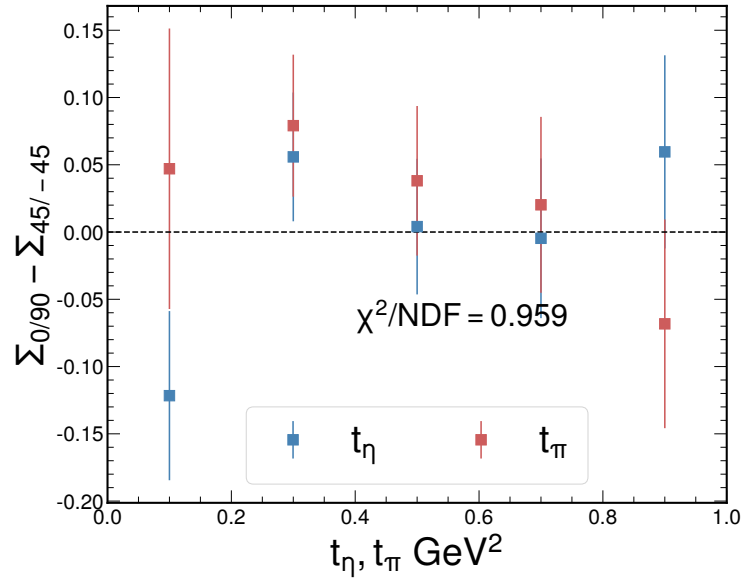
Figure 5.17: The difference between the measured Σ in the 0/90 and 45/-45 degree orientations are shown. A reduced χ^2 is then determined where the residuals for these data points are calculated with respect to 0.

be extracted. No changes in weights are needed as both the signal and sidebands are split in half. The measured values are shown in Figure 5.18. Figure 5.19 shows the difference in Σ between the left and right halves. A reduced χ^2, can then be determined with these measurements to determine

152

the overall consistency with 0. The reduced χ^2 is roughly equal to 0.756. A value of 1 is expected when only statistical effects contribute to this difference.
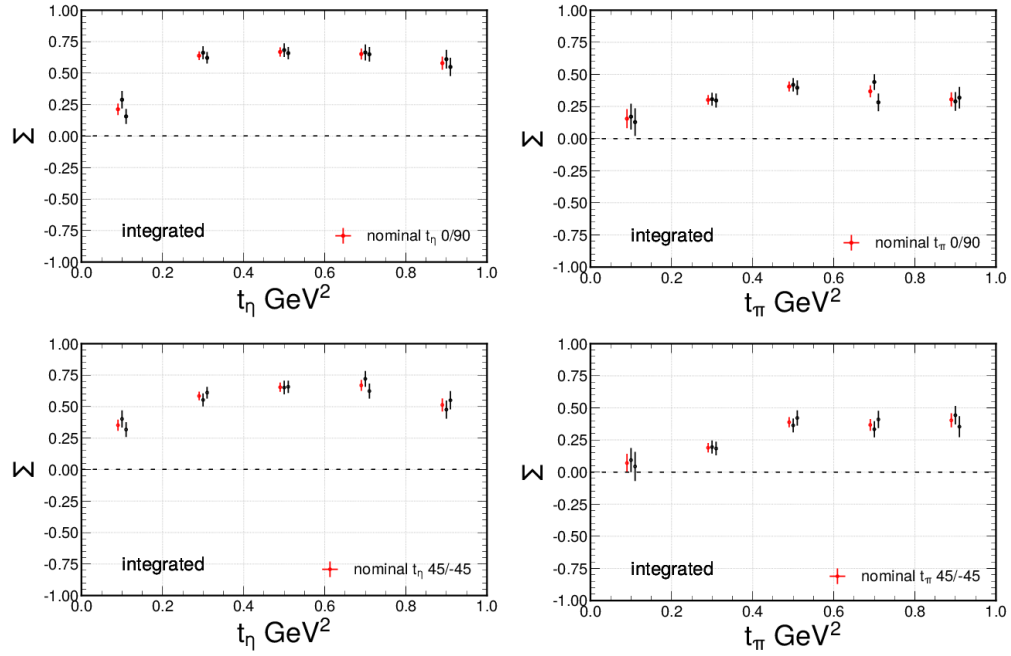
Figure 5.18: Systematic differences in Σ due to variations of $M(\eta)$ split halves for (Left) t_η, (Right) t_π are measured in five bins. Integrated over u_3, s_{12}, and s_{23}. (Top) Asymmetries from 0/90 pair. (Bot) Asymmetries from 45/-45 pair. Red is the nominal results, black points are from different variations of event selections.
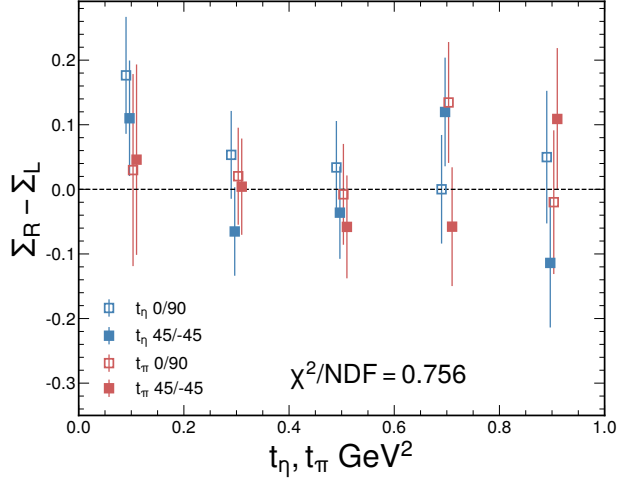
Figure 5.19: Let L and R represent the left and right halves $M(\eta)$. The difference in Σ between these two datasets is shown. A reduced χ^2 is then determined where the residuals for these data points are calculated with respect to 0.

5.7 Beam Asymmetry Results

Σ is extracted as a function of t_1 in bins of various kinematic variables: u_3, s_{12}, and s_{23}. Section 5.7.1 shows the dependence of Σ as a function of t_1 integrated over the other kinematic variables. Section 5.7.2 show the dependence of Σ as a function of t_1 binned in u_3. Section 5.7.3 show the dependence of Σ as a function of t_1 binned in s_{23}. For Σ_{t_η} vs $M(\pi p)$, the $M(\pi p) < 1.4$ GeV region is reincorporated to study the production of the $\Delta^+(1232)$. Section 5.7.4 show the dependence of Σ as a function of t_1 binned in s_{12}.

A comparison will be made between the asymmetries measured in the $\eta\pi^0$ and $\eta\pi^-$ channels. The estimated systematic uncertainties for the $\eta\pi^0$ channel are included in the results. The details for this estimation will be discussed further below in Section 5.8. For the $\eta\pi^-$ channel, only statistical uncertainties are shown.

As a general remark, the Σ measurements appear to saturate at smaller values compared to the single particle beam asymmetries discussed in Section 5.3. Comparatively, this would imply that the DREx process proceeds substantially through unnatural exchange. Another possibility is that the smaller Σ values are a consequence of only considering the top vertex. The exact interpretation of these measurements requires additional input from theory.

5.7.1 t_1

Fig. 5.20 shows Σ as a function of t_η and t_π integrated over u_3, s_{12}, and s_{23} for both $\eta\pi^0$ and $\eta\pi^-$ channels. Σ_{t_η} is seen to take on a similar shape and magnitude between the channels and appears to saturate around 0.6. In the neutral channel, Σ_{t_π} is seen to saturate around 0.3 and takes on a very similar profile. These asymmetries are dominated by natural exchanges. The measurements of Σ_{t_π} in the charged channel are initially dominated by unnatural exchanges. This is similar to the measurements in the $\gamma p \to \pi^- \Delta^{++}$, see Figure 5.6. It also appears that the theory predictions [139] for beam asymmetries in the $\gamma p \to \pi^- \Delta^{++}$ reaction seems to be in better agreement with the asymmetries measured in the double Regge region of the $\eta\pi^-$ channel.
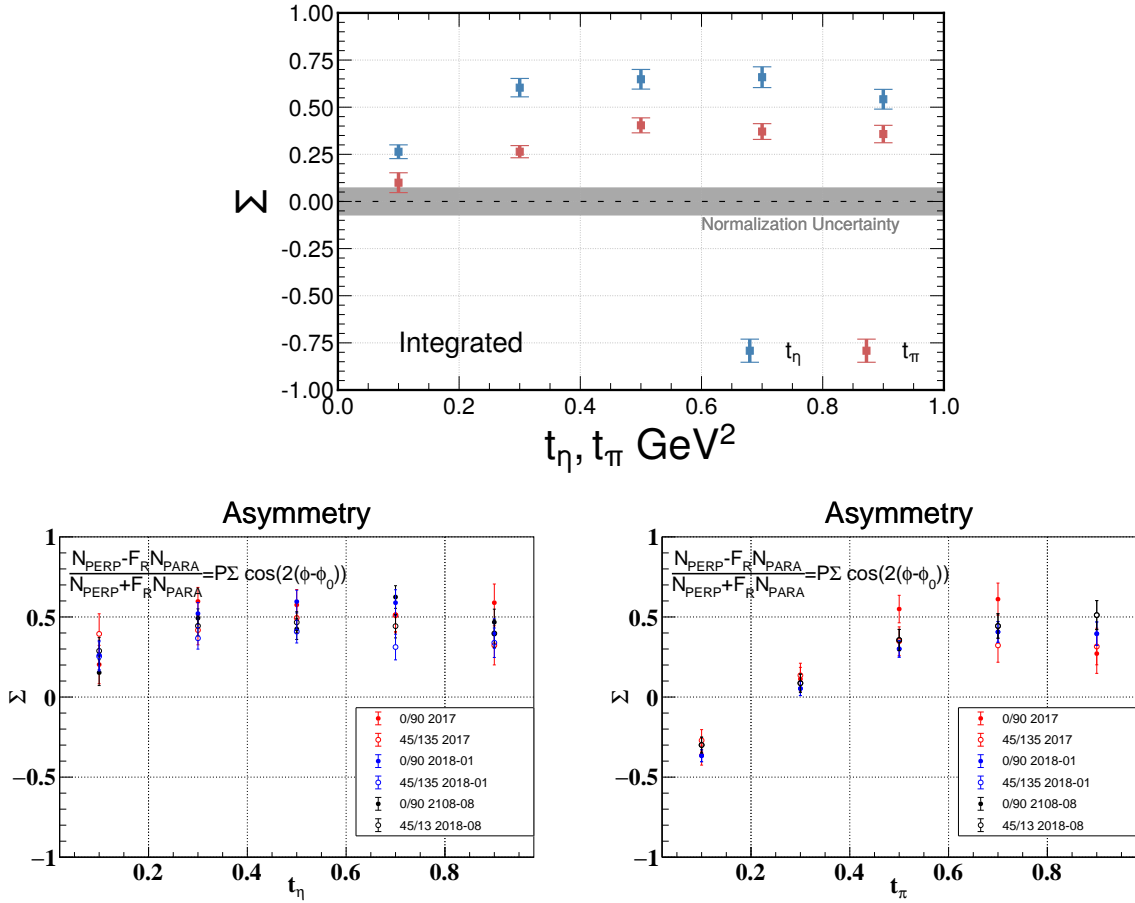
Figure 5.20: Σ measured in five bins of t_η and t_π. Integrated over u_3, s_{12}, and s_{23}. (Top) Measurements made from the $\eta\pi^0$ channel show error bars that are the total uncertainty, including both the statistical and systematic uncertainties. (Bottom) Measurements made from the $\eta\pi^-$ channel split into two plots for t_η and t_π with measurements for each run periods. Only statistical uncertainties are shown.

5.7.2 u_3, t_1

Fig. 5.21 shows Σ as a function of t_η and t_π in 3 bins of u_3 as measured in in the $\eta\pi^0$ and $\eta\pi^-$ channels. For the $\eta\pi^0$ channel, Σ as a function of t_1 has an overall trend of increasing asymmetry as u_3 increases. This is likely due to the increasing contributions from baryon resonances which get produced with larger u_3. The preference towards natural exchanges for baryon production can be seen in Figures 5.23 and 5.22. The reverse of this trend is seen in the $\eta\pi^-$ channel. In both channels, the asymmetry is larger for fast-η than it is for fast-π.

5.7.3 s_{23}, t_1

Fig. 5.22 shows the asymmetry as a function of t_η in bins of $M(\pi p)$ for the $\eta\pi^0$ and $\eta\pi^-$ channels. For the neutral channel, the 3 chosen $M(\pi p)$ bins correspond to regions dominated by the $\Delta^+(1232)$, the N^*s, and a region with little structure. These features can be seen in Figure 5.11. The asymmetries tend to decrease as $M(\pi p)$ increases. The beam asymmetry is strongly positive in the region dominated by the $\Delta^+(1232)$. The observed trends are similar to what is found in the $\eta\pi^-$ channel. The overall asymmetries tend to be smaller in the charged channel. In this case, no clear baryon resonances are observed the s_{23} distributions, see Appendix C.1.

Fig. 5.23 shows the asymmetry as a function of t_π in bins of $M(\eta p)$. In the $\eta\pi^0$ channel the asymmetries seem to increase before decreasing as $M(\eta p)$ increases and are dominated by natural exchanges. 3 bins of $M(\eta p)$ are made, where the first bin contains a prominent N^* resonance and the last two bins contain regions with little structures. This can be seen in Fig. 5.11. The $\eta\pi^-$ channel show a dependence on t_1 that is very similar in the low and high s_{23} bins. The asymmetries at very low t_π are dominated by unnatural exchanges and slowly transition to natural exchange dominance at higher t_π. The middle s_{23} bin is unique in that it saturates towards zero asymmetry.

5.7.4 s_{12}, t_1

Fig. 5.24 shows the asymmetry as a function of t_η and t_π in bins of $s_{12} = M(\eta\pi)$. Both channels appear to only weakly depend on the $\eta\pi$ invariant mass and is important to note as we wish to understand the contributions of the DREx process down into the resonance region. Σ_{t_η} show noticeable similarities between the two channels. In the charged channel, Σ_{t_π} always starts off dominated by unnatural exchanges and approaches similar values as the neutral channel at t_π increases. The statistics in the higher s_{12} bins are lower in both channels and are reflected in the larger error bars.
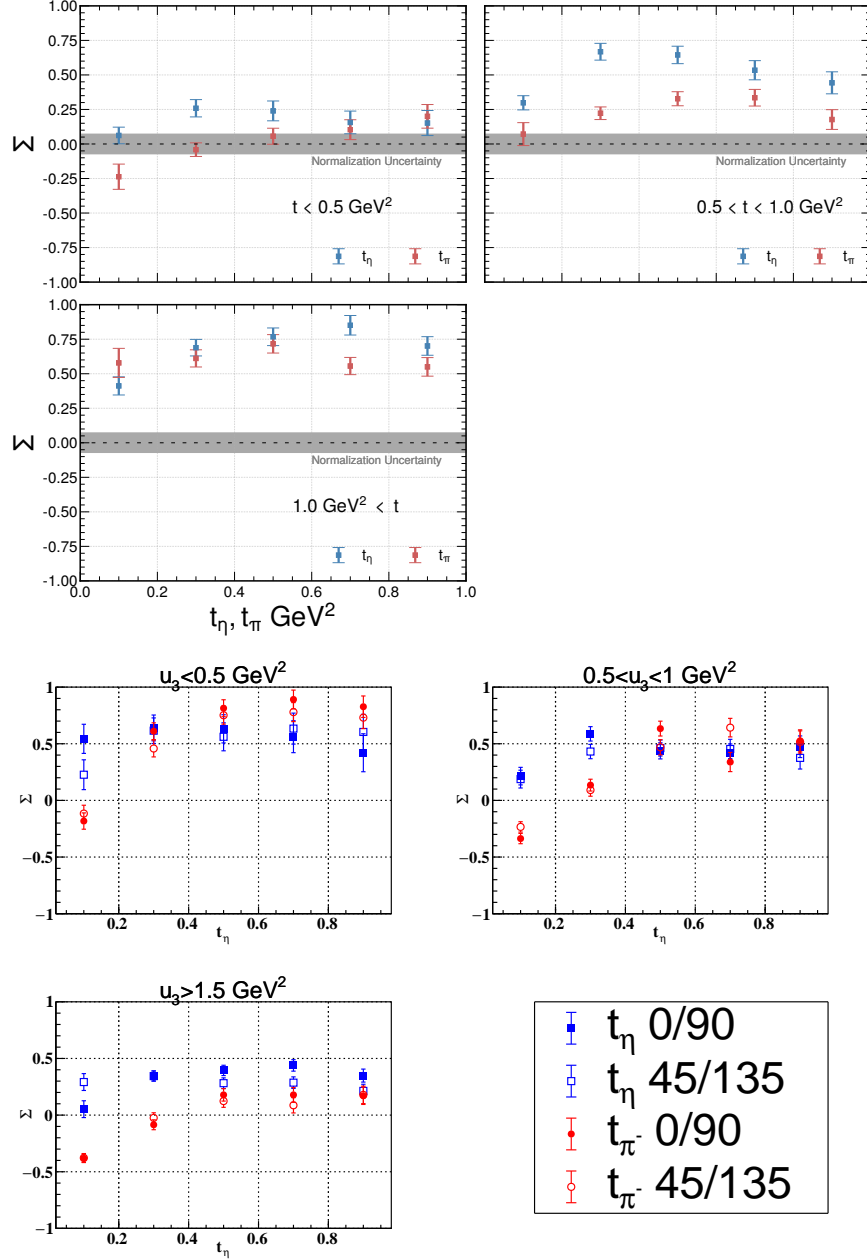
Figure 5.21: Σ measured in five bins of t_η and t_π with an additional 3 bins in u_3. Integrated over s_{12}, and s_{23}. (Top) Measurements made from the $\eta\pi^0$ channel show error bars that are the total uncertainty, including both the statistical and systematic uncertainties. (Bottom) Measurements made from the $\eta\pi^-$ channel. Only statistical uncertainties are shown.

5.7.5 Table of Results

Tables 5.4, 5.5, 5.6, 5.7, and 5.8 tabulates the final measurements for the "integrated" case, binned in u_3, binned in $M(\eta p)$, binned in $M(\pi p)$, and binned in $M(\eta\pi)$ respectively.
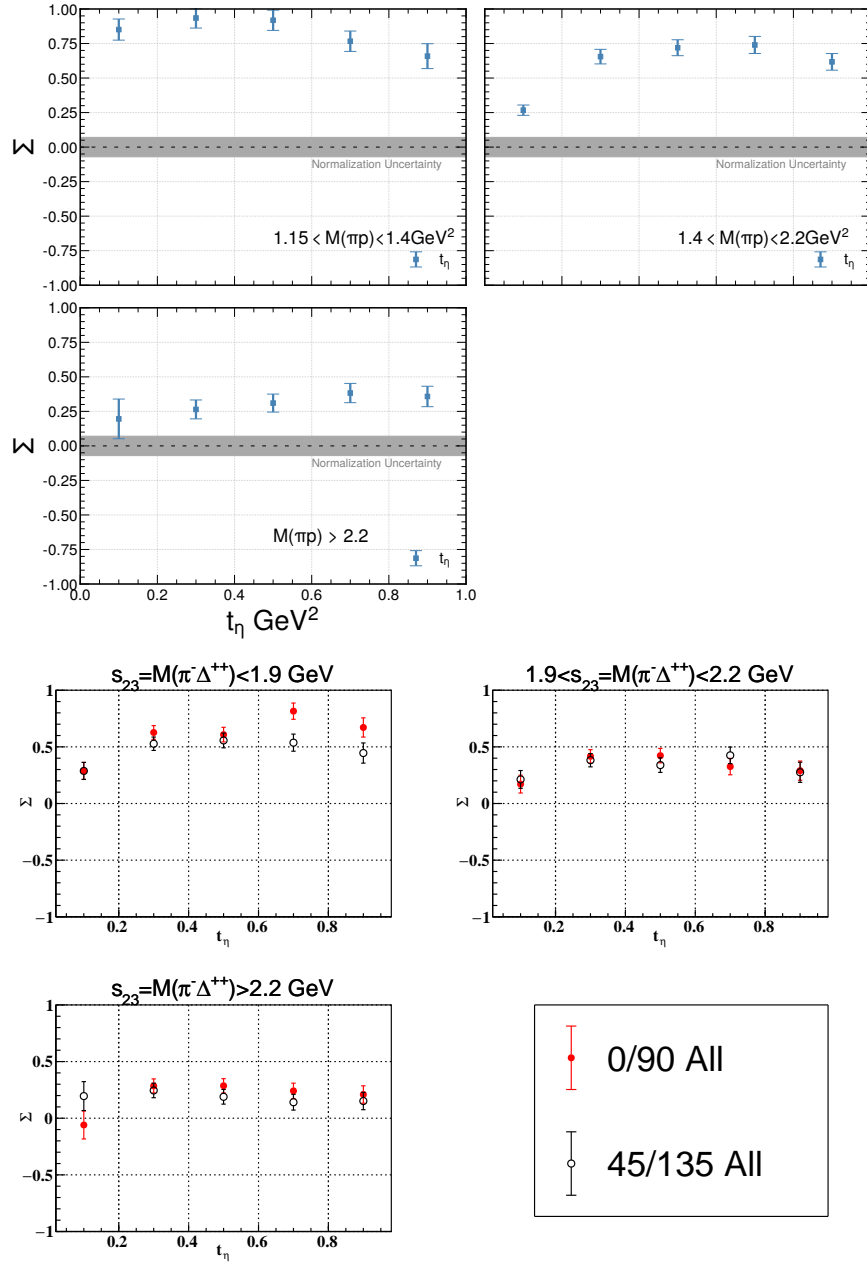
Figure 5.22: Σ measured in five bins of t_η with an additional 3 bins in $s_{23} = M(\pi p)$. Integrated over s_{12}, and u_3. (Top) Measurements made from the $\eta\pi^0$ channel show error bars that are the total uncertainty, including both the statistical and systematic uncertainties. The $1.15 < M(\pi p) < 1.4$ region, which was removed for the other Σ measurements in the $\eta\pi^0$ channel, is reincorporated to study the production of the $\Delta^+(1232)$. (Bottom) Measurements made from the $\eta\pi^-$ channel. Only statistical uncertainties are shown for the charged channel.
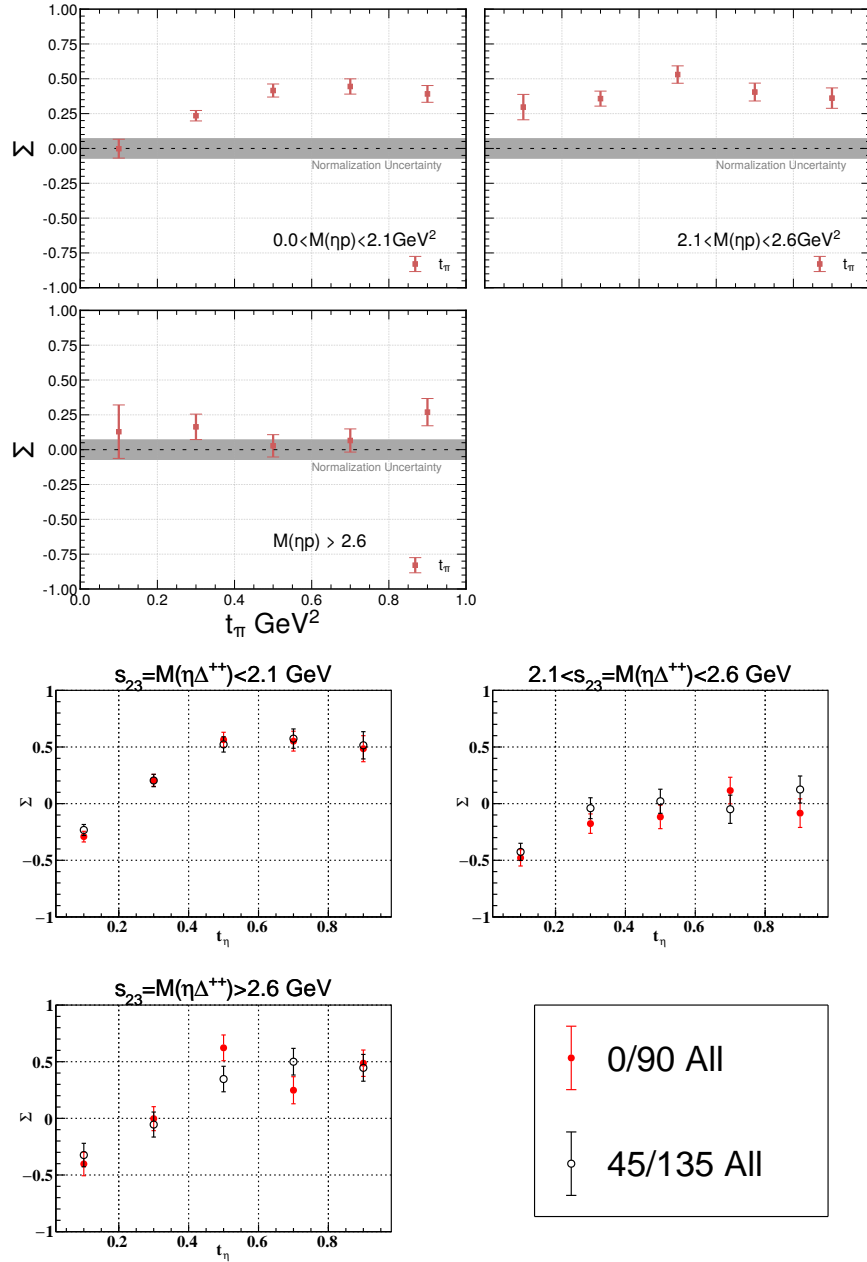
Figure 5.23: Σ measured in five bins of t_π with an additional 3 bins in $s_{23} = M(\eta p)$. Integrated over s_{12}, and u_3. (Top) Measurements made from the $\eta\pi^0$ channel show error bars that are the total uncertainty, including both the statistical and systematic uncertainties. (Bottom) Measurements made from the $\eta\pi^-$ channel. Only statistical uncertainties are shown.
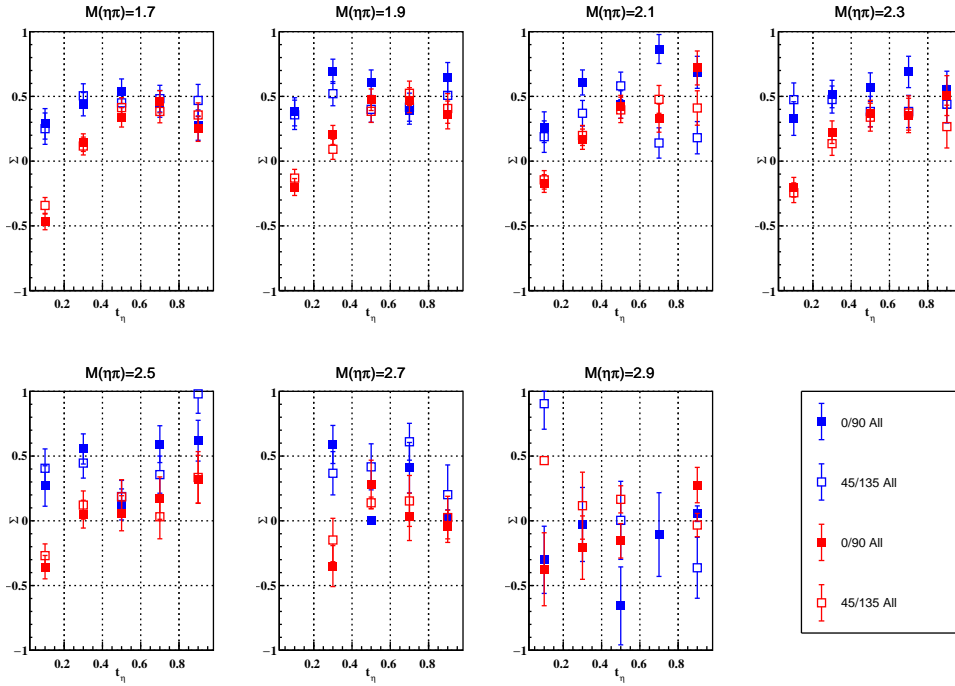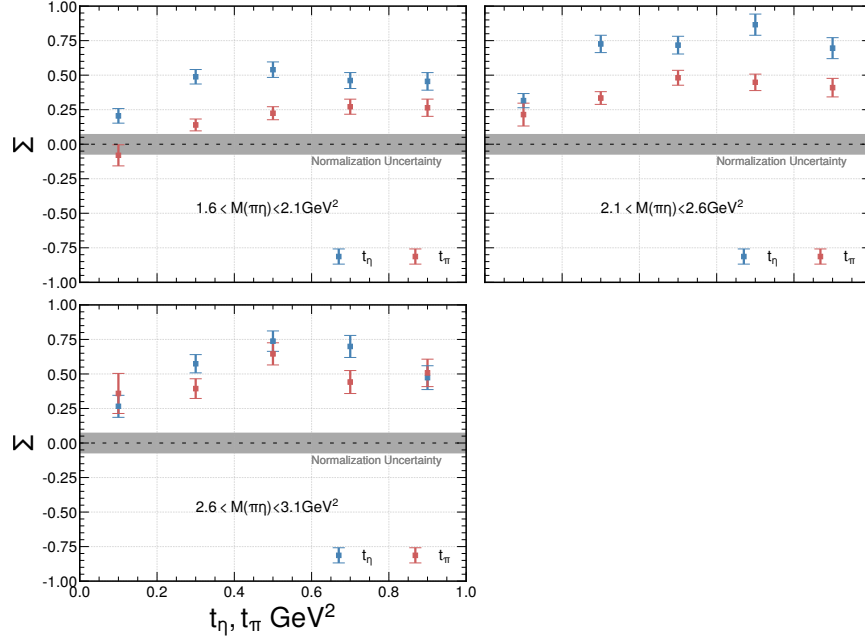
Figure 5.24: Σ measured in five bins of t_η, t_π with additional bins in s_{12}. Integrated over s_{23}, and u_3. (Top) Measurements made from the $\eta\pi^0$ channel show error bars that are the total uncertainty, including both the statistical and systematic uncertainties. (Bottom) Measurements made from the $\eta\pi^-$ channel. Only statistical uncertainties are shown.

Σ_{t_η}	Σ_{t_π}
0.264±0.031±0.019	0.100±0.052±0.007
0.604±0.024±0.042	0.264±0.026±0.019
0.648±0.025±0.046	0.404±0.028±0.028
0.659±0.030±0.046	0.371±0.033±0.026
0.542±0.036±0.038	0.358±0.039±0.025

Table 5.4: Table of "integrated" results. The three numbers in each cell correspond to the central asymmetry measurement followed by the statistical and systematic uncertainties. Each row corresponds to a t_1 bin in ascending order.

$-t < 0.5$ GeV^2		$0.5 < -t < 1.0$ GeV^2	
Σ_{t_η}	Σ_{t_π}	Σ_{t_η}	Σ_{t_π}
0.062±0.060±0.004	-0.237±0.090±-0.017	0.298±0.047±0.021	0.072±0.083±0.005
0.259±0.060±0.018	-0.041±0.049±-0.003	0.668±0.038±0.047	0.223±0.043±0.016
0.240±0.070±0.017	0.056±0.058±0.004	0.645±0.044±0.045	0.328±0.045±0.023
0.156±0.081±0.011	0.104±0.072±0.007	0.534±0.058±0.038	0.335±0.055±0.024
0.152±0.090±0.011	0.200±0.084±0.014	0.443±0.073±0.031	0.177±0.070±0.012
1.0 GeV$^2 < -t$			
Σ_{t_η}	Σ_{t_π}		
0.412±0.059±0.029	0.579±0.097±0.041		
0.689±0.035±0.048	0.611±0.045±0.043		
0.768±0.034±0.054	0.717±0.044±0.050		
0.851±0.038±0.060	0.556±0.049±0.039		
0.701±0.046±0.049	0.550±0.055±0.039		

Table 5.5: Σ measures binned in t_1 and u_3. The three numbers in each cell correspond to the central asymmetry measurement followed by the statistical and systematic uncertainties. Each row corresponds to a t_1 bin in ascending order.

$0.0 < M(\eta p) < 2.1$ GeV	$2.1 < M(\eta p) < 2.6$ GeV	$M(\eta p) > 2.6$ GeV
Σ_{t_η}	Σ_{t_η}	Σ_{t_η}
-0.002±0.068±-0.000	0.297±0.089±0.021	0.129±0.192±0.009
0.235±0.034±0.017	0.358±0.048±0.025	0.164±0.091±0.012
0.416±0.037±0.029	0.530±0.050±0.037	0.028±0.080±0.002
0.445±0.045±0.031	0.405±0.058±0.028	0.066±0.083±0.005
0.391±0.053±0.028	0.361±0.069±0.025	0.269±0.096±0.019

Table 5.6: Σ measures binned in t_1 and $M(\eta p)$. The three numbers in each cell correspond to the central asymmetry measurement followed by the statistical and systematic uncertainties. Each row corresponds to a t_1 bin in ascending order.

161

1.15 < $M(\pi p)$ < 1.4 GeV	1.4 < $M(\pi p)$ < 2.2 GeV	$M(\pi p)$ > 2.2 GeV
Σ_{t_π}	Σ_{t_π}	Σ_{t_π}
0.851±0.048±0.060	0.267±0.032±0.019	0.196±0.143±0.014
0.935±0.031±0.066	0.655±0.026±0.046	0.264±0.066±0.019
0.918±0.034±0.065	0.720±0.028±0.051	0.310±0.061±0.022
0.767±0.050±0.054	0.740±0.033±0.052	0.383±0.064±0.027
0.659±0.077±0.046	0.617±0.042±0.043	0.358±0.070±0.025

Table 5.7: Σ measures binned in t_1 and $M(\pi p)$. The three numbers in each cell correspond to the central asymmetry measurement followed by the statistical and systematic uncertainties. Each row corresponds to a t_1 bin in ascending order.

1.6 < $M(\pi\eta)$ < 2.1 GeV		2.1 < $M(\pi\eta)$ < 2.6 GeV	
Σ_{t_η}	Σ_{t_π}	Σ_{t_η}	Σ_{t_π}
0.205±0.051±0.014	-0.080±0.076±-0.006	0.315±0.046±0.022	0.215±0.081±0.015
0.488±0.040±0.034	0.140±0.042±0.010	0.726±0.036±0.051	0.334±0.040±0.024
0.540±0.041±0.038	0.224±0.044±0.016	0.717±0.040±0.051	0.481±0.042±0.034
0.461±0.048±0.032	0.272±0.051±0.019	0.866±0.047±0.061	0.448±0.051±0.032
0.455±0.055±0.032	0.264±0.060±0.019	0.696±0.058±0.049	0.410±0.061±0.029
2.6 < $M(\pi\eta)$ < 3.1 GeV			
Σ_{t_η}	Σ_{t_π}		
0.266±0.077±0.019	0.359±0.143±0.025		
0.574±0.052±0.040	0.394±0.066±0.028		
0.738±0.052±0.052	0.646±0.066±0.045		
0.699±0.063±0.049	0.442±0.077±0.031		
0.473±0.080±0.033	0.508±0.093±0.036		

Table 5.8: Σ measures binned in t_1 and s_{12}. The three numbers in each cell correspond to the central asymmetry measurement followed by the statistical and systematic uncertainties. Each row corresponds to a t_1 bin in ascending order.

5.8 Systematic Uncertainties in Σ Measurements

Systematic effects are studied by making a number of changes to the experimental methodology. For this analysis, the event selections, phase offset, flux ratio, instrumental asymmetry, choice of sideband subtraction regions, and the number of bins in ϕ to use will be studied in Sections 5.8.1, 5.8.2, 5.8.3, 5.8.4, 5.8.5, and 5.8.6 respectively. For each modification, a full analysis is performed and the results are compared to the nominal measurements. The statistics with additional bins in u_3, s_{12}, or s_{23} can be limiting. Therefore, the systematic uncertainties will be determined in the "integrated" case where Σ is only binned in t_1. These uncertainties will then be propagated to the measurements in additional kinematic bins. Appendix C.4 contains plots for the Σ measurements in the additional kinematics bins.

5.8.1 Event Selections

The specific set of event selections could potentially lead to systematic deviations to the asymmetry. Table 5.9 contains a list of the event selections that will be varied to study their systematic effects. The nominal selection is the one used in the main results section. Two other choices are made for most selections, one tight and the other looser. For some cases, making a tighter/looser selection would not make a significant difference, so, two looser/tighter bounds are tested. These selections attempt to make the yield vary by up to 10%. This yield is equal to the accidentally subtracted signal yield. Σ will be measured in bins of u_3 and show significant dependence on this variable. The proton momentum selection is directly related to u_3 and will not be varied.

To determine if a variation is significant, this analysis will again follow the prescription detailed by R. Barlow [109], as was done for the differential cross section measurement of the $a_2(1320)$ in Chapter 4. Suppose the nominal measurement returns a value of $x \pm \sigma_x$ and that a specific variation produces a measurement of $y \pm \sigma_y$. Since these two measurements are very similar, i.e. only varying one particular aspect, the values and uncertainties should also be very similar. Again, let us define $\Delta = y - x$ and $\sigma_\Delta^2 = \sigma_y^2 - \sigma_x^2$. A test of a variation's significance is to check the condition: $\frac{|\Delta|}{\sigma_\Delta} > X$. For discrepancies greater than $X = 4$, the variation can be included in the determination of the systematic uncertainty.

Figures 5.25 show the systematics for fast-η and fast-π for the integrated case. See the appendix for the results with additional sub-bins, i.e. Figures C.24 C.25, C.26, C.27. Figure 5.26 shows the results of the Barlow test due to event selection variations. Details on variations with $N\sigma_{barlow} > 2$

are tabulated in Tables 5.10, 5.11, 5.12, and 5.13. For Σ_η , no variation produces a $N_{\mathrm{Barlow}} > 4$. The most significant variations seem to be from exclusivity variables. For Σ_π, three variations appear to have a significant effect and again involve an exclusivity variable. At this point, no systematic uncertainty is placed on the choice of event selections. Any residual asymmetries will be covered by the instrumental asymmetry described further below.

Selection Variable	Tighter bound	Nominal	Looser bound
Vertex Position (cm)	$53 < z < 77$	$52 < z < 78$	$51 < z < 79$
Photon Energy (GeV)	$E > 0.11$, $E > 0.12$	$E > 0.1$	None
Photon θ beamline (degrees)	$\theta > 2.1$	$\theta > 2.5$	$\theta > 2.8$
Photon θ BCAL/FCAL (degrees)	$\theta < 10.0$ or $12.5 < \theta$	$\theta < 10.3$ or $11.9 < \theta$	Freed
Unused Energy (GeV)	None	$E < 0.01$	$E < 0.13$, $E < 0.17$
Missing Mass Squared GeV^2	None	$|\mathrm{MM}^2| < 0.05$	$|\mathrm{MM}^2| < 0.024$, $|\mathrm{MM}^2| < 0.03$
χ^2	$\chi^2 < 11.5$	$\chi^2 < 13.277$	$\chi^2 < 16$

Table 5.9: Variations of event selections to assess their systematics. Two variations are made for each event selection.

$N_{Barlow}\ \sigma$	% Diff.	$\Sigma_{nominal}$	$\Sigma_{variation}$	t_1 bin (GeV/c^2)	Cut Variation
3.200	-1.2	0.657 ± 0.0419	0.649 ± 0.0418	$0.6< t_\eta <0.8$	Unused Energy < 0.13 GeV
3.055	4.5	0.650 ± 0.0358	0.679 ± 0.0370	$0.4< t_\eta <0.6$	$|\mathrm{MM}^2| < 0.024$ GeV^2
3.037	-1.5	0.573 ± 0.0515	0.564 ± 0.0514	$0.8< t_\eta <1.0$	Unused Energy < 0.13 GeV
2.672	2.9	0.650 ± 0.0358	0.669 ± 0.0364	$0.4< t_\eta <0.6$	$|\mathrm{MM}^2| < 0.030$ GeV^2
2.651	2.9	0.650 ± 0.0358	0.669 ± 0.0365	$0.4< t_\eta <0.6$	$\chi^2 < 11.5$
2.622	-2.0	0.657 ± 0.0419	0.644 ± 0.0416	$0.6< t_\eta <0.8$	Unused Energy < 0.17 GeV
2.587	-1.6	0.631 ± 0.0337	0.621 ± 0.0335	$0.2< t_\eta <0.4$	Unused Energy < 0.17 GeV
2.354	-0.7	0.650 ± 0.0358	0.645 ± 0.0357	$0.4< t_\eta <0.6$	Unused Energy < 0.13 GeV
2.310	-1.1	0.631 ± 0.0337	0.624 ± 0.0336	$0.2< t_\eta <0.4$	Unused Energy < 0.13 GeV
2.197	5.0	0.573 ± 0.0515	0.601 ± 0.0531	$0.8< t_\eta <1.0$	$|\mathrm{MM}^2| < 0.024$ GeV^2

Table 5.10: For the Integrated case. Selections with N $\sigma_{barlow} > 2$ are shown for η in the 0/90 polarization pair.

$N_{Barlow}\ \sigma$	% Diff.	$\Sigma_{nominal}$	$\Sigma_{variation}$	t_1 bin (GeV/c^2)	Cut Variation
2.881	-1.4	0.575 ± 0.0340	0.567 ± 0.0339	$0.2< t_\eta <0.4$	Unused Energy < 0.13 GeV
2.627	-1.5	0.324 ± 0.0442	0.319 ± 0.0442	$0.0< t_\eta <0.2$	Unused Energy < 0.17 GeV
2.531	-0.9	0.646 ± 0.0355	0.640 ± 0.0354	$0.4< t_\eta <0.6$	Unused Energy < 0.13 GeV
2.449	-3.6	0.646 ± 0.0355	0.623 ± 0.0368	$0.4< t_\eta <0.6$	$2.5 < \theta < 10.0\ \theta > 12.5$ degrees
2.407	-1.5	0.646 ± 0.0355	0.637 ± 0.0353	$0.4< t_\eta <0.6$	Unused Energy < 0.17 GeV
2.152	2.3	0.661 ± 0.0420	0.676 ± 0.0426	$0.6< t_\eta <0.8$	$2.8 < \theta < 10.3\ \theta > 11.9$ degrees
2.035	-2.1	0.661 ± 0.0420	0.648 ± 0.0415	$0.6< t_\eta <0.8$	$\chi^2 < 16$

Table 5.11: For the Integrated case. Selections with N $\sigma_{barlow} > 2$ are shown for η in the 45/-45 polarization pair.

164

$N_{Barlow}\ \sigma$	% Diff.	$\Sigma_{nominal}$	$\Sigma_{variation}$	t_1 bin (GeV/c^2)	Cut Variation
5.073	-3.8	0.323±0.0552	0.311±0.0553	0.8< t_π <1.0	$\chi^2 < 16$
4.157	6.1	0.422±0.0389	0.448±0.0394	0.4< t_π <0.6	$2.5 < \theta < 10.0\ \theta > 12.5$ degrees
3.658	-23.1	0.124±0.0744	0.095±0.0740	0.0< t_π <0.2	$\chi^2 < 16$
3.246	-3.5	0.323±0.0552	0.312±0.0554	0.8< t_π <1.0	Unused Energy < 0.13 GeV
3.121	-2.6	0.422±0.0389	0.412±0.0388	0.4< t_π <0.6	$\chi^2 < 16$
3.050	4.0	0.422±0.0389	0.439±0.0393	0.4< t_π <0.6	$\chi^2 < 11.5$
2.964	-5.3	0.304±0.0374	0.288±0.0378	0.2< t_π <0.4	$\chi^2 < 11.5$
2.944	4.3	0.381±0.0466	0.398±0.0469	0.6< t_π <0.8	$\chi^2 < 11.5$
2.807	-3.3	0.422±0.0389	0.408±0.0392	0.4< t_π <0.6	$2.8 < \theta < 10.3\ \theta > 11.9$ degrees
2.699	-1.8	0.304±0.0374	0.298±0.0374	0.2< t_π <0.4	$\chi^2 < 16$
2.511	-3.9	0.304±0.0374	0.292±0.0371	0.2< t_π <0.4	$2.5 < \theta degrees$
2.028	-5.9	0.381±0.0466	0.359±0.0479	0.6< t_π <0.8	$|MM^2| < 0.024$ GeV^2

Table 5.12: For the Integrated case. Selections with N $\sigma_{barlow} > 2$ are shown for π^0 in the 0/90 polarization pair.

$N_{Barlow}\ \sigma$	% Diff.	$\Sigma_{nominal}$	$\Sigma_{variation}$	t_1 bin (GeV/c^2)	Cut Variation
6.568	54.9	0.076±0.0731	0.118±0.0733	0.0< t_π <0.2	$\chi^2 < 11.5$
3.567	4.2	0.384±0.0397	0.401±0.0400	0.4< t_π <0.6	$\chi^2 < 11.5$
3.500	3.5	0.391±0.0544	0.405±0.0543	0.8< t_π <1.0	$\chi^2 < 16$
3.180	3.6	0.384±0.0397	0.398±0.0399	0.4< t_π <0.6	Unused Energy < 0.13 GeV
3.095	-20.5	0.076±0.0731	0.061±0.0729	0.0< t_π <0.2	$\chi^2 < 16$
2.876	4.3	0.384±0.0397	0.401±0.0401	0.4< t_π <0.6	Unused Energy < 0.17 GeV
2.811	-5.0	0.225±0.0372	0.213±0.0370	0.2< t_π <0.4	$2.5 < \theta degrees$
2.567	-4.7	0.225±0.0372	0.214±0.0370	0.2< t_π <0.4	$\chi^2 < 16$
2.409	-2.5	0.361±0.0459	0.352±0.0457	0.6< t_π <0.8	$\chi^2 < 16$
2.363	-2.3	0.384±0.0397	0.375±0.0395	0.4< t_π <0.6	$2.1 < \theta < 10.3\ \theta > 11.9$ degrees
2.356	-3.7	0.391±0.0544	0.377±0.0548	0.8< t_π <1.0	$\chi^2 < 11.5$
2.324	4.2	0.384±0.0397	0.400±0.0403	0.4< t_π <0.6	$2.5 < \theta < 10.0\ \theta > 12.5$ degrees
2.213	23.7	0.076±0.0731	0.095±0.0735	0.0< t_π <0.2	Unused Energy < 0.13 GeV
2.102	3.6	0.361±0.0459	0.374±0.0463	0.6< t_π <0.8	Unused Energy < 0.13 GeV
2.081	23.7	0.076±0.0731	0.095±0.0736	0.0< t_π <0.2	Unused Energy < 0.17 GeV
2.033	2.8	0.384±0.0397	0.395±0.0401	0.4< t_π <0.6	$\gamma_E > 0.13 GeV$

Table 5.13: For the Integrated case. Selections with N $\sigma_{barlow} > 2$ are shown for π^0 in the 45/-45 polarization pair.

5.8.2 Phase Offset Systematic

For the standard results, the phase offset, ϕ_0 is fixed to the values determined in the analysis of ρ decay, see Section 5.5. The linear polarization axis should not change for any of these kinematic bins, but we can still assess the sensitivity of the fits to this specific choice of ϕ_0. ϕ_0 can be freed in the fit to vary within $\pm10°$ around the nominal value. Figure 5.27 shows the value of Σ when ϕ_0 is freed compared to the nominal measurement. To compare the asymmetries, the difference between the Σs with a freed-ϕ_0 and with the nominally fixed ϕ_0 can be studied. Figure 5.28 shows
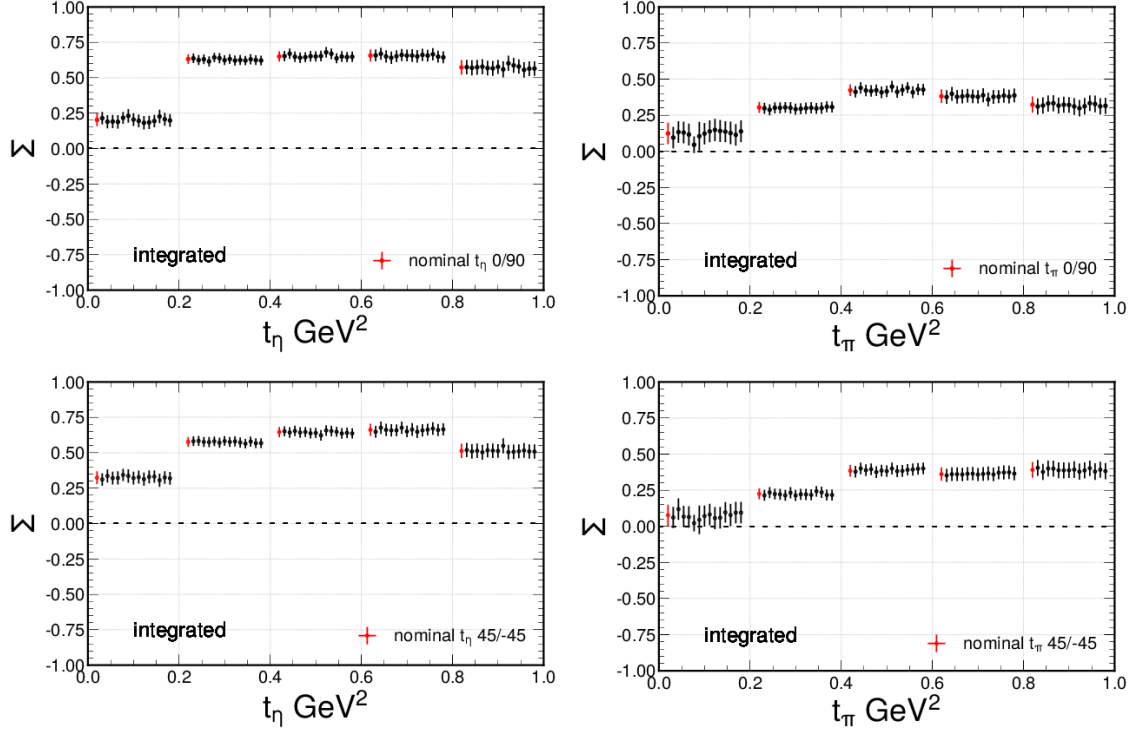
Figure 5.25: Σ measurements from the variations of the event selection for (Left) t_η, (Right) t_π are measured in five bins. Integrated over u_3, s_{12}, and s_{23}. (Top) Asymmetries from the 0/90 pair. (Bot) Asymmetries from the 45/-45 pairs. Red is the nominal results, black points are from different variations of event selections.

the distribution of this difference. A conservative estimate for the systematic uncertainty associated with the choice of ϕ_0 is chosen to be the standard deviation of this distribution, which 1%,

5.8.3 Flux Ratio Systematic

The flux is determined by the pair spectrometer. To propagate any systematic errors on Σ from the flux ratio, a conservative estimate for the uncertainty of F_R is taken to be 5%. Two additional fits are performed, scaling F_R to these bounds. Figure 5.29 shows the results of these variations and how they compare to the nominal Σ measurement. The difference between the variations and the nominal Σ measurement is plotted in Figure 5.30. The standard deviation of this distribution, 0.2%, is taken as the systematic uncertainty associated with this variation.

5.8.4 Sideband Subtraction Region

Performing a sideband subtraction requires the definition of a signal and a sideband region. The assignment of regions was originally estimated based on fits to separate the signal lineshape with
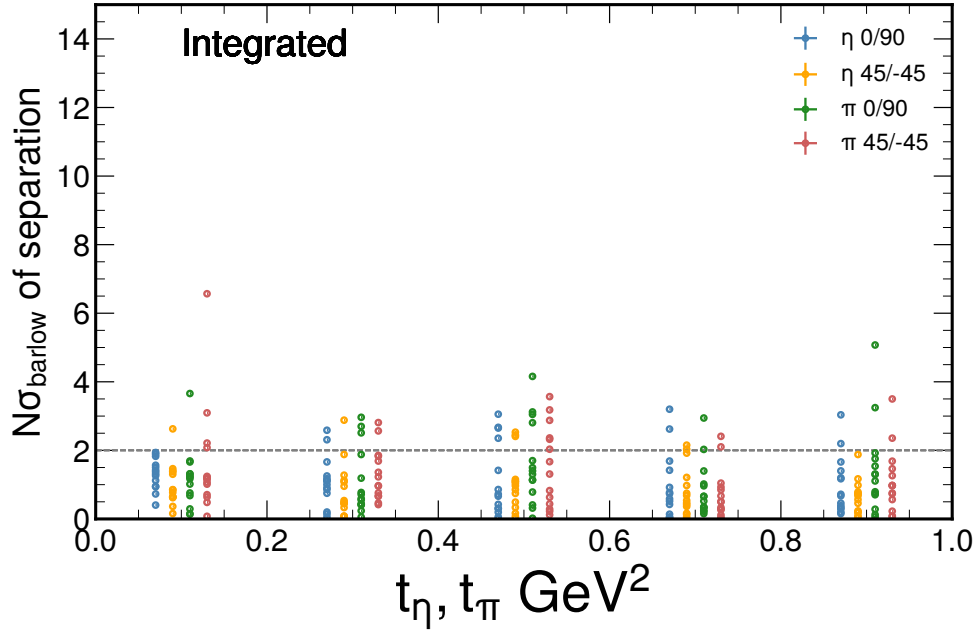
Figure 5.26: Barlow-test results for event selection systematics in 5 bins of t_1 integrated over u_3, s_{12}, s_{23}. Each t_1 bin consists of 4 sets of points for the 2 fast-particle and 2 paired-polarizations datasets.

that of the background, such that the signal region covers most of the peak and the sidebands are outside the peak region and are approximately linear. A narrower/wider set of region definitions are chosen and are depicted in Figure 5.31. Figure 5.32 compares Σ measured in these variations to the nominal measurement. Table 5.14 shows the variations where N_{barlow} is greater than 4. The systematic uncertainty associated with the choice of sideband regions is chosen to be the maximum deviation of these significant variations which is 0.036.

N_{Barlow} σ	% Diff.	$\Sigma_{nominal}$	$\Sigma_{variation}$	t_1 bin (GeV/c^2)	Cut Variation	Polarization
7.322	-1.19	0.631±0.0337	0.624±0.0337	0.2< t_η <0.4	Narrow Sidebands	0/90
5.311	2.86	0.573±0.0515	0.589±0.0515	0.8< t_η <1.0	Wide Sidebands	0/90
4.313	-2.52	0.573±0.0515	0.558±0.0516	0.8< t_η <1.0	Narrow Sidebands	0/90
5.119	-2.32	0.513±0.0501	0.501±0.0501	0.8< t_η <1.0	Wide Sidebands	45/-45
4.616	1.96	0.381±0.0466	0.389±0.0466	0.6< t_π <0.8	Narrow Sidebands	0/90
4.495	3.36	0.304±0.0374	0.314±0.0375	0.2< t_π <0.4	Wide Sidebands	0/90

Table 5.14: For the Integrated case. Selections with N σ_{barlow} > 4 are shown.
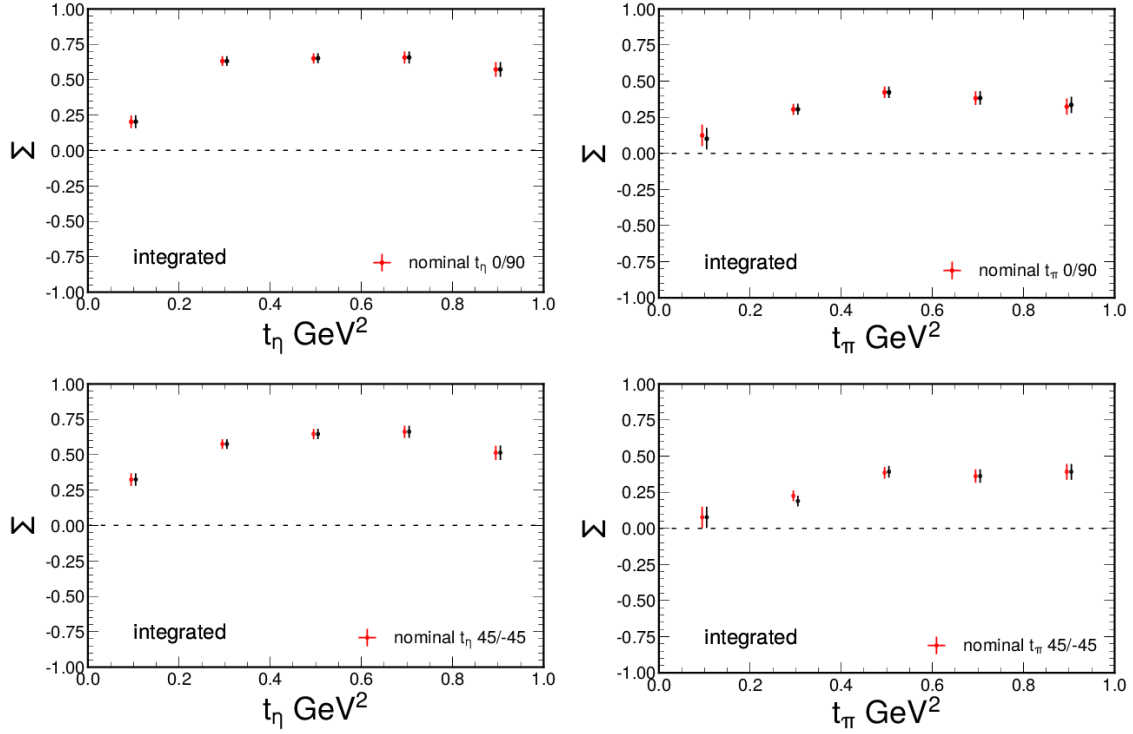
Figure 5.27: Σ measurements with a freed phase offset for (Left) t_η, (Right) t_π are measured in five bins. Integrated over u_3, s_{12}, and s_{23}. (Top) Asymmetries from the 0/90 pair. (Bot) Asymmetries from the 45/-45 pair. Red is the nominal results, black points are from different variations of event selections.
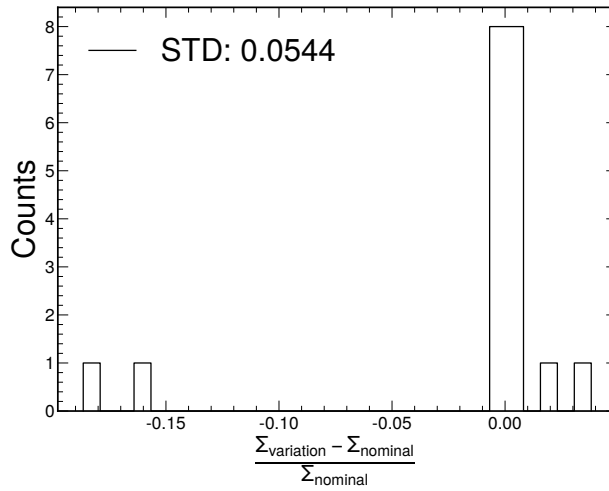
Figure 5.28: Distribution of the difference between $\Sigma_{\text{variation}}$ and the nominal Σ measurement where the phase offset, ϕ_0, is floated in the varied fit. The standard deviation of this distribution is the associated systematic error and is equal to 5.44%.

168
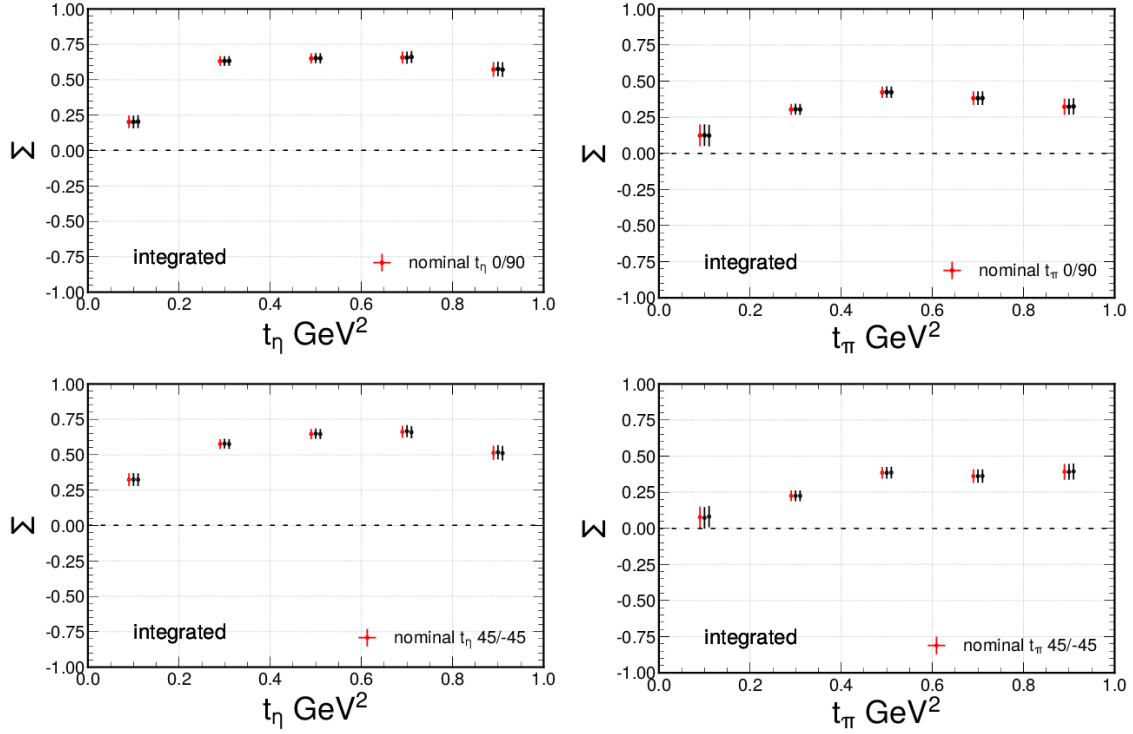
Figure 5.29: Systematic differences in Σ due to variations of $+/-5\%$ flux ratio for (Left) t_η, (Right) t_π are measured in five bins. Integrated over u_3, s_{12}, and s_{23}. (Top) Asymmetries from the 0/90 pair. (Bot) Asymmetries from the 45/-45 pair. Red is the nominal results, black points are from different variations of event selections.
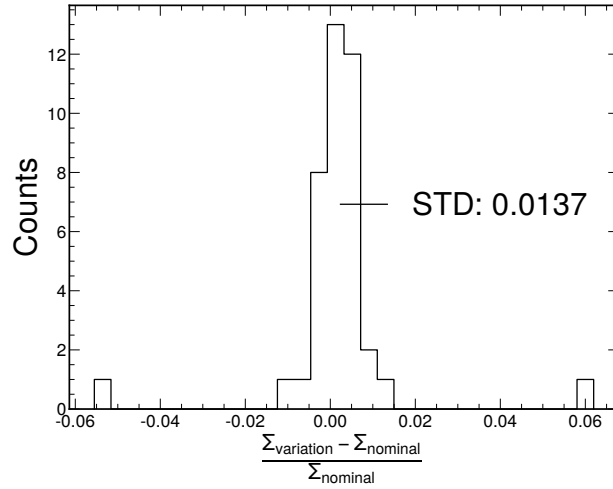
Figure 5.30: Distribution of the difference between $\Sigma_{\text{variation}}$ and the nominal Σ measurement where the flux ratio is varied. The standard deviation of this distribution is the associated systematic error and is equal to 1.37%.

169
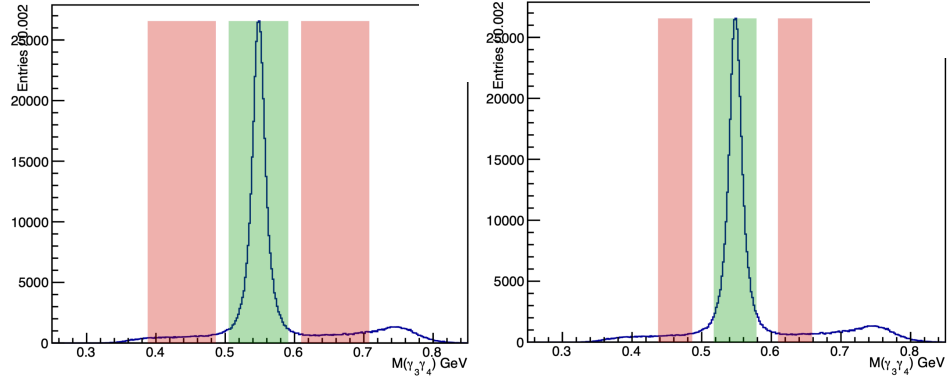
Figure 5.31: $M(\gamma_3\gamma_4)$ distribution is shown with "narrower" (left) and "tighter" (right) regions. Highlighted regions denote the signal (green) and background (red) regions.
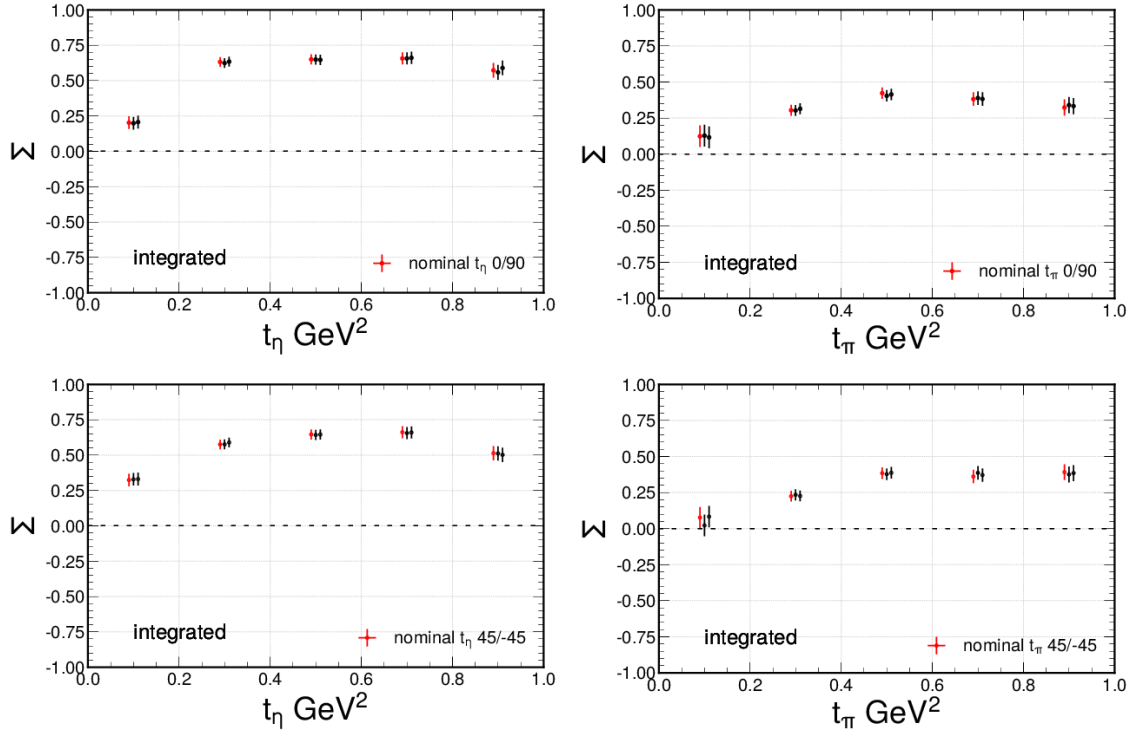
Figure 5.32: Systematic differences in Σ due to variations of the sideband subtraction regions for (Left) t_η, (Right) t_π are measured in five bins. Integrated over u_3, s_{12}, and s_{23}. (Top) Asymmetries from the 0/90 pair. (Bot) Asymmetries from the 45/-45 pair. Red is the nominal results, black points are from different variations of event selections.

5.8.5 Instrumental Asymmetry

Even after the event selections and background subtraction a residual asymmetry can exist. These instrumental asymmetries that are not canceled in the construction of the yield asymmetry can be extracted by fitting the polarization cross-weighted sum. This sum takes the following form:

$$P_{\parallel} Y_{\perp}(\phi) + P_{\perp} F_R Y_{\parallel}(\phi) = 2N_{\perp} P_{\text{avg}}[1 + \Sigma_{\text{inst}} cos2\phi] \tag{5.11}$$

This equation can be fitted to the following functional form:

$$f_{\text{inst}}(\phi) = C(1 + A_{\text{inst}} \cos2(\phi - \phi_0)) \tag{5.12}$$

where C is a normalization factor, A_{inst} is the instrumental asymmetry, and ϕ_0 is fixed to the same set of values as the yield asymmetry fit equation. These plots are shown in Figures 5.33. The results are mostly consistent with 0 instrumental asymmetry. To be more conservative and to cover other event selection related systematics, we assign a 2.5% systematic uncertainty for this residual instrumental asymmetry.
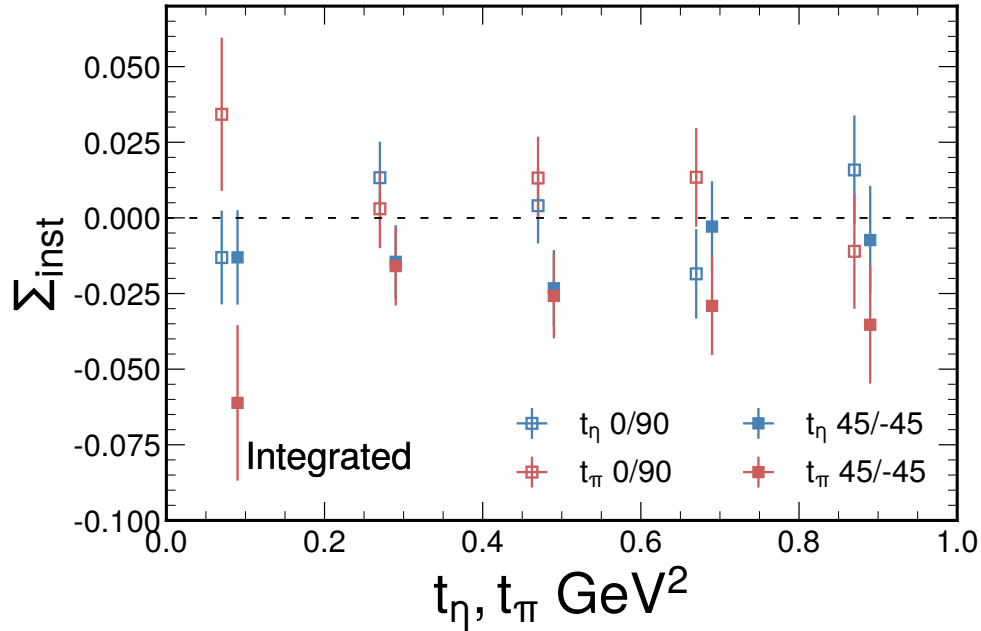
Figure 5.33: Instrumental asymmetry for t_η, t_π are measured in five bins. Integrated over u_3, s_{12}, and s_{23}.

5.8.6 Finite ϕ bin systematics

The number of bins in ϕ that can be chosen depends on the statistics. Large datasets can afford more bins which can more accurately describe the distribution of interest. A bias in the measurement can exist whose scale depends on the number of bins. The bias to the asymmetry can be determined numerically following the procedure outlined in Reference [140]. 500 ensembles distributed according to $1 + P\Sigma\cos(2\phi)$ are simulated with 1 million samples each. $P\Sigma$ is fixed to 0.4. Each ensemble is fit with the equation $p_0(1 + 0.4 * p_1\cos(2\phi)$ where p_1 is the correction factor. This is done as a function of the number of bins. For each bin, there would be 500 values of p_1 from which the mean and standard deviation could be extracted. The results are shown in Fig. 5.34. The correction factor rapidly asymptotes, reaching $<0.5\%$ at 40 bins. For this analysis, 30 bins in ϕ were used. A 0.75% systematic uncertainty is assigned to this particular choice of the number of bins.
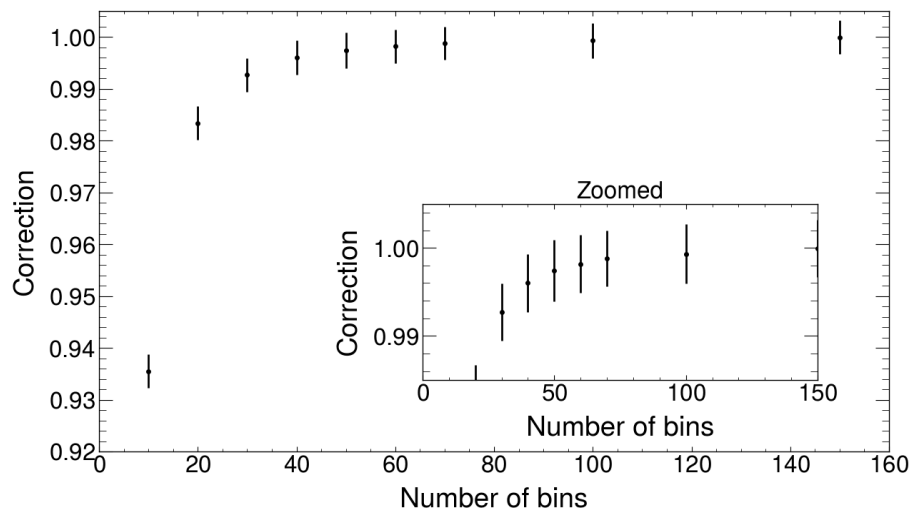
Figure 5.34: Mean and width of the *p1* parameter as a function of number of bins.

5.9 Summary of Systematic Uncertainties

Table 5.15 shows the estimated systematic uncertainties determined in the previous sections. These contributions are assumed to be uncorrelated and will thus be added in quadrature to determine the total systematic uncertainty.

Systematic Study	Systematic Uncertainty
Flux Ratio	1.37%
Finite Number of Bins	0.75%
Freed phase offset, ϕ_0	5.44%
Choice of Sideband Regions	3.36%
Instrumental Asymmetry	2.5%
Total Systematic Uncertainty	7.04%

Table 5.15: Summary of systematic uncertainties

CHAPTER 6

CONCLUSION

This dissertation studies the $\gamma p \to \eta \pi^0 p \to 4\gamma p$ reaction as observed by GlueX at $E_\gamma = 8.5$ GeV as part of the search for the spin-exotic π_1 hybrid meson. The observed $M(\eta \pi^0)$ spectrum is dominated by the $a_2(1320)$ resonance where the π_1 is expected to contribute only a few percent of the yield of the a_2. Additionally, the a_2 is a conventional meson that has been well-studied by other experiments. These aspects make understanding the $a_2(1320)$ a prerequisite to the π_1 search and allow the a_2 to act as a good phase reference to determine if any exotic signal is indeed resonant. Additionally, signatures of the π_1 can be mimicked by processes like the DREx process. This dissertation presented analyses of both of these features. These measurements build our knowledge of the photoproduction of tensor mesons and provide important information needed to build the detailed reaction models that are needed to search for exotics like the π_1. Here, we discuss some interesting observations and future prospects in regard to these studies.

A measurement of the differential photoproduction cross section of the $a_2^0(1320)$ in the four momentum transfer range 0.1 to $1.0\,\text{GeV}^2$ has been performed. A dip in the differential cross section exists in the GlueX data around $-t = 0.5$ GeV^2. This is in agreement with previous photoproduction experiments where the differential cross section of isovector mesons like the π^0 or a_2^0 also exhibits a dip at $t \approx 0.5$ GeV^2 [91]. This measurement is compared to a prediction from the TMD model which modifies a coupling factor that completely fills in this zero by $E_\gamma = 8.5$ GeV.

Additionally, the measured partial wave intensities differ significantly from the model predictions which is likely due to the fact that the TMD model was only fitted to the low energy differential cross section measurement made by CLAS where no partial wave analysis was performed nor was the beam polarized. Some of the difference between the measured and predicted parity asymmetries could be due to this. From these parity asymmetry measurements, it appears that natural parity exchange processes are only slightly dominant in the production of the neutral $a_2(1320)$ tensor meson. This is in contrast to previous asymmetry measurements of neutral pseudoscalar mesons where a strong dominance of natural parity exchange is observed. Preliminary asymmetry measurements of neutral vector mesons are also natural parity exchange dominant. Continued exchange with theory will help

guide future analyses, especially in regard to the choice of waveset which will be important for the exotic search.

In the presented analysis, both a_2's were described by a Breit-Wigner amplitude. A coherent sum of Breit-Wigner amplitudes, while it can provide a good description of the data, does not preserve unitarity and analyticity. These core S-matrix principles correspond to conservation of probability and causality. Unitarity is important as it constrains the resonance widths. A future analysis can use an alternative parameterization that has been previously applied to the COMPASS $\eta\pi$ channel which respects core S-matrix principles [141]. Their method uses the N/D method to construct an amplitude that provides a description of both the $a_2(1320)$ and $a_2(1700)$ mesons. Under certain conditions, their parameterization is equivalent to the standard K-matrix formalism as was done in Ref. [33]. This method constrains the form of the amplitude allowing for a more stable analysis. In this formalism, separating the contribution of the two a_2s would be more difficult but could benefit the π_1 search.

Additionally, the measured a_2 cross section can be used to constrain its contribution in the other "golden channel", the $\eta'\pi$, where a peak for the $a_2(1320)$ meson can be difficult to find to due to its proximity to the $\eta'\pi$ threshold. The $a_2(1320)$ can decay to $\omega\pi\pi$ with a branching fraction of around 10%. Theory predicts that the π_1 decays primarily to $b_1\pi$ which should also populate this final state. By studying $\omega\pi\pi$, the a_2 cross sections measured in this dissertation can help set an upper limit on the ratio between the π_1 and a_2 cross sections that can be observed at GlueX. Such upper limits are currently being studied at GlueX. This limit can then be used to estimate the yields of the $a_2(1320)$ and the π_1 in both the $\eta\pi^0$ and $\eta'\pi^0$ datasets which currently suggests that the $a_2(1320)$ is strongly dominant in the $\eta\pi^0$ channel, as we have already argued for in this dissertation, and that the π_1 is strongly dominant in the $\eta'\pi^0$ channel. Performing a coupled channel analysis of these channels, like what JPAC did to the COMPASS $\eta\pi$ and $\eta'\pi$ data, is a good pathway forward as the dominant contributions in one channel can help constrain the small contributions in the other.

Measurements have also been performed extracting the single particle beam asymmetries for $M(\eta\pi) > 1.6$ GeV in bins of several kinematic variables including baryon sensitive quantities. These measurements will be especially useful in separating DREx contributions from that of baryon production as these processes can share significant amounts of phase space. The measurements performed in this high-mass region can provide observational constraints to DREx contributions in the resonance region where we expect to see the π_1, for instance, by using finite energy sum rules. Results from the $\eta\pi^0$ channel were compared to that from the $\eta\pi^-$ channel.

When only binning in t_1, the beam asymmetry as a function of t_η is similar between channels. This is likely an averaging effect as the t_η dependence with additional kinematic bins shows significant differences between channels. The beam asymmetries as a function of t_π show significant differences since pion exchange is only possible in the charged channel. Similar to the production of $\pi^-\Delta^{++}$, the charged channel shows a dominance of unnatural parity exchange for t_1 less 0.3 but saturates to similar values as observed in the neutral channel.

When looking at the $\eta\pi^0$ channel, the current beam asymmetry measurements suggest that baryon resonances in the $\pi^0 p$ system could be produced mostly through natural parity exchange. It is unsure how much of this is due to baryon production as in the $\eta\pi^-$ channel there also exists a rather strong dependence of the asymmetry on the analogous quantity, $M(\pi^-\Delta^{++})$.

An unpolarized amplitude model is currently under development by another group at GlueX in collaboration with JPAC to model this process in the high mass region of the $\eta\pi^0$ channel. These amplitudes only contain the lowest order Reggeon contributions seen in 5.4 which are natural parity exchanges. If Σ_{t_1} can indeed be interpreted as an asymmetry between natural and unnatural parity exchanges, the current results suggest only a slight dominance of natural exchange indicating that unnatural parity exchanges may be important to describe the DREx process. These beam asymmetry measurements can be useful when the amplitude model begins to incorporate polarization.

APPENDIX A

ADDITIONAL STUDIES

A.1   dE/dx Selection Comparison

The nominal dE/dx selection, equation 3.8, is tighter than the one seen in the spring 2017 analysis launch [142]. Figure A.1 show a comparison of what the curves look like. The region between the orange and magenta curve is likely due to a charged kaon misidentified as a proton. The magenta curve is slightly better at rejecting this background. It can be seen that the actual yield difference between the two curves is small.
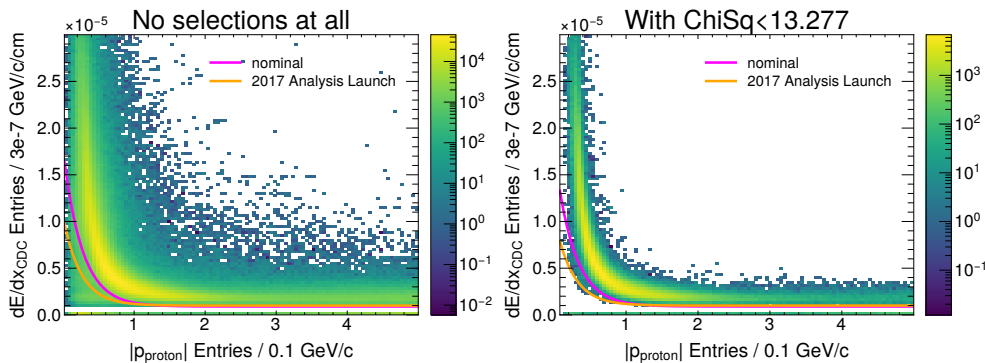
Figure A.1: (Left) Comparison of equation 3.8 to the selection for the spring 2017 analysis launch. The coherent peak has been selected and accidentals have been subtracted. (Right) Same setup but with an additional selection on the χ^2.

A.2   Comparison of Event Selections Between Run Periods

A comparison is made between the 3 different run periods of the GlueX Phase-I dataset for the charged track, neutral shower, and exclusivity-related event selection distributions. The plots representing the Spring 2017 dataset/MC are the same ones that were shown in Chapter 3. The following plots for the 2018 datasets include the same event selections that were used to generate the Spring 2017 distributions. This includes a selection on $8.2 < E_\gamma < 8.8$ GeV and the subtraction of accidental beam photons. The plots representing the Spring 2018 and Fall 2018 datasets contain a random subset that roughly matches in size to the Spring 2017 data and MC. Figures A.2, A.3,
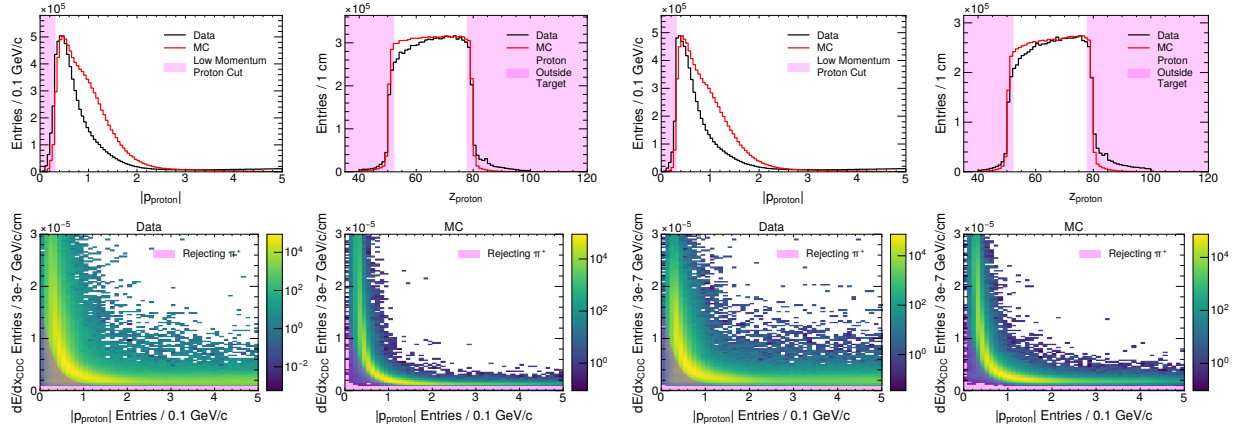
(a) Spring 2017

(b) Spring 2018
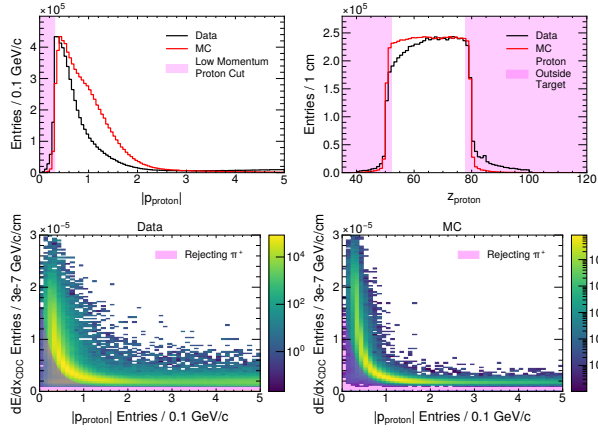
(c) Fall 2018

Figure A.2: Comparison of the charged track related event selection distributions between the GlueX Phase-I datasets.

A.4 shows the comparison between datasets for the charged track, neutral shower, and exclusivity-related event selection distributions, respectively.
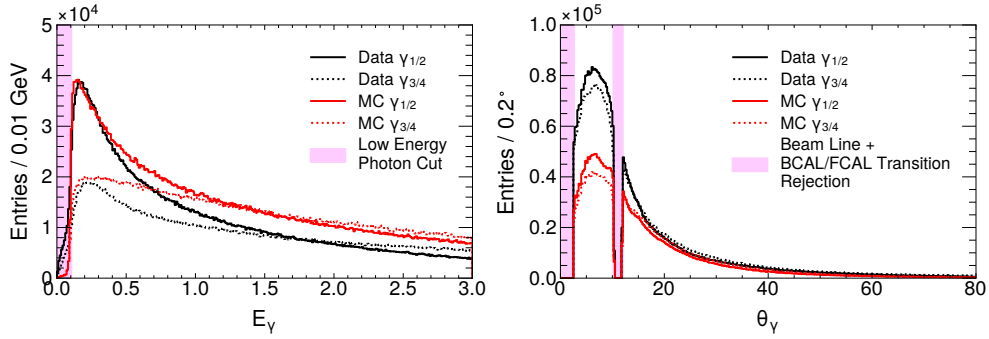
(a) Spring 2017
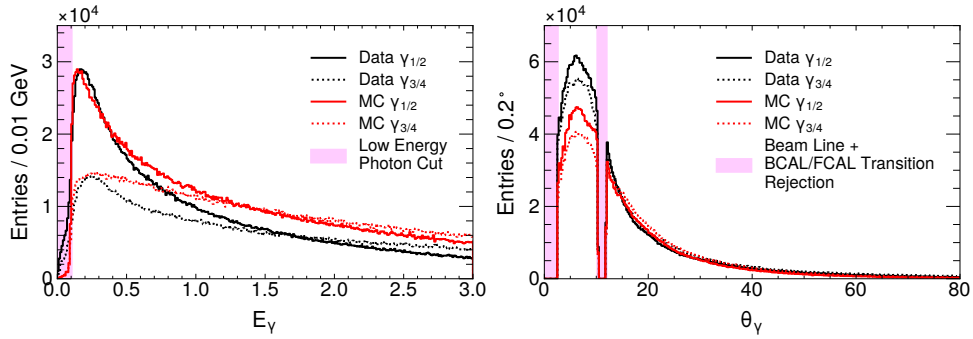
(b) Spring 2018
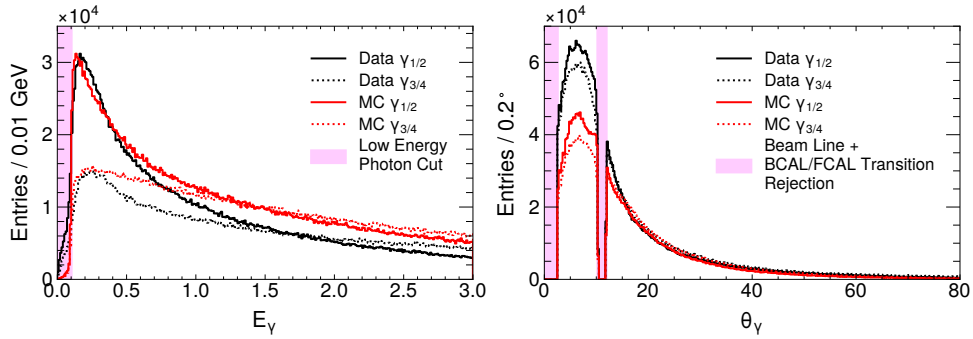
(c) Fall 2018

Figure A.3: Comparison of the neutral shower related event selection distributions between the GlueX Phase-I datasets.

179
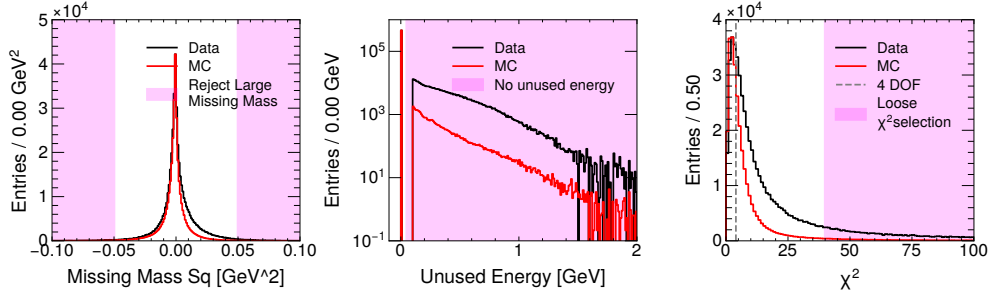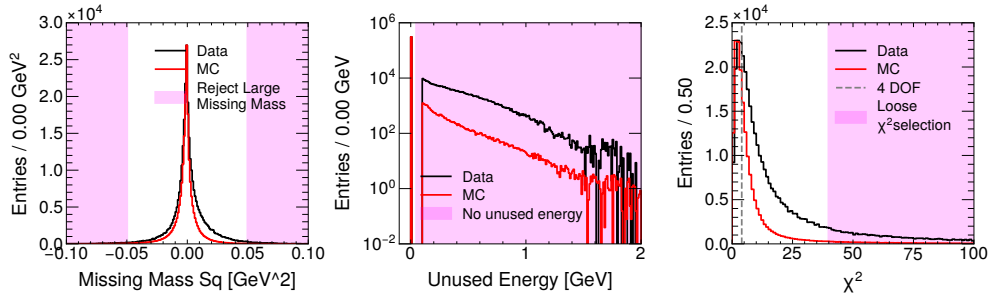
(a) Spring 2017

(b) Spring 2018
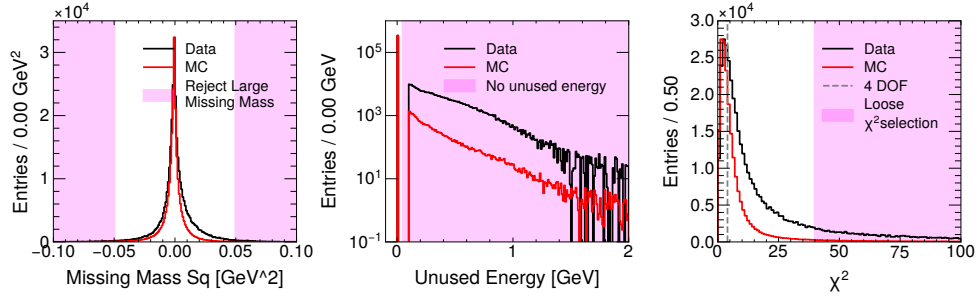
(c) Fall 2018

Figure A.4: Comparison of the exclusivity related event selection distributions between the GlueX Phase-I datasets.

A.3 Estimation of the $f_2(1270)$ Cross Section

An estimation of the $f_2(1270)$ photoproduction cross section is made at $E_\gamma \in [8.2, 8.8]$ GeV with $-t \in [0.1, 1.0]$ GeV^2. The value will be used to quantify the leakage from $f_2(1270) \to 2\pi^0 \to 4\gamma$ being improperly reconstructed as an $\eta\pi^0 \to 4\gamma$ hypothesis. Only the GlueX Spring 2017 dataset is used and corresponds to the version 20 analysis launch. Monte Carlo simulations are generated flat in $M(2\pi^0)$ mass from the same run period and analysis versions. These events are reconstructed in a similar fashion as the $\eta\pi^0$ data. Due to the similarity of these channels, the same event selections detailed in Section 3.3 have been applied to the GlueX $2\pi^0$ data. The π^0 sidebands from the $\eta\pi^0$ analysis are reused here.

There are significant baryon contributions to the $\pi^0\pi^0$ mass spectrum. Figure A.5 show the $M(4\gamma)$ and $M(\pi^0 p)$ mass distributions. There are three large resonances that contribute to the $M(\pi^0 p)$ spectrum including the $\Delta^+(1232)$. A sector selection on the Van Hove angle [99][73], ω_{VH}, is performed by requiring $238< \omega_{VH} <302$ degrees. The results are shown in red. A steep dropoff in yield can be seen where the $f_0(980)$ should be, suggesting potential destructive interference effects. A strong signal can be seen for the $f_2(1270)$. Much of the high $M(2\pi^0)$ is rejected by the Van Hove selection.
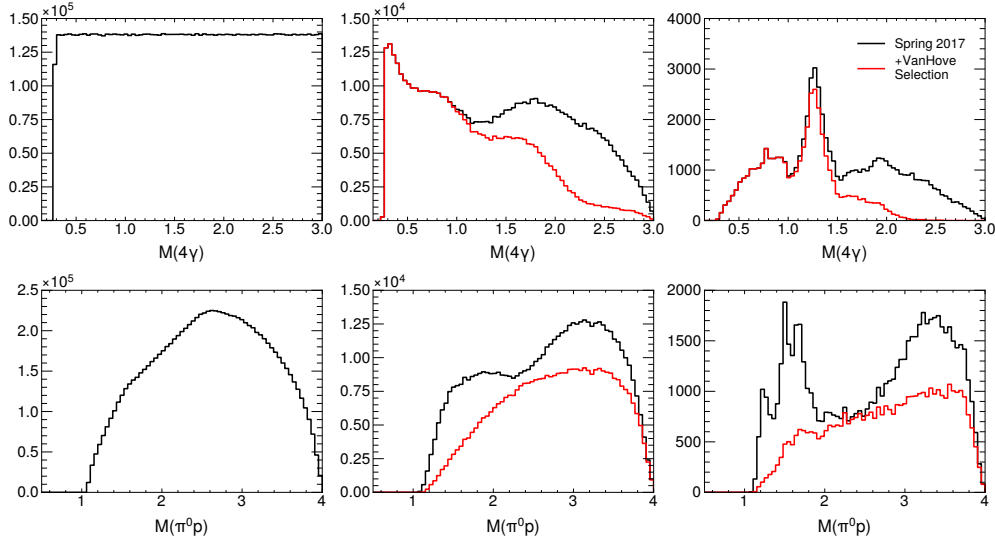
Figure A.5: (Left-Column) Generated Monte Carlo. (Middle-Column) Reconstructed Monte Carlo. (Right-Column) Spring 2017 Data. Black distributions include all standard event selections and are sideband subtracted. The red curves include a selection on the Van Hove angle.

Figure A.6 shows a fit to the acceptance corrected yield of the GlueX Spring 2017 data. The signal is described by a constant width relativistic Breit-Wigner. To be more accurate, an energy-dependent width could be used but we are only interested in an estimation. The Particle Data Group, PDG, mass and width for the $f_2(1270)$ are 1.2755 and 0.1867 GeV. The fits are initialized to the PDG values but are allowed to float freely. The background is a linear polynomial. After fitting, the resulting mass and width do not change significantly. The values can be seen in the figure text.
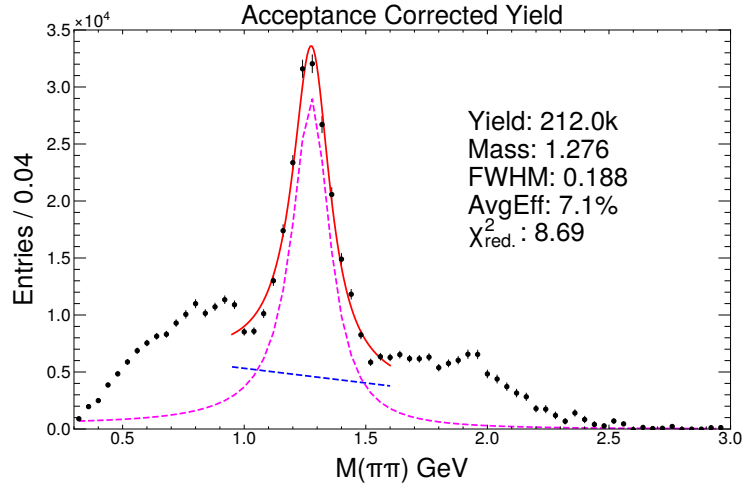
Figure A.6: Fit to the acceptance corrected yield of the GlueX Spring 2017 dataset. The signal is defined by a constant width relativistic Breit-Wigner. The background is a linear polynomial. The average efficiency to reconstruct a $\pi^0\pi^0$ event over this mass range is roughly 7%. The reduced χ^2 is ~ 9.

The branching ratio for $f_2(1270) \rightarrow 2\pi^0$ is taken from the PDG and is equal to 0.8429. In a similar fashion, the branching ratio of $\pi^0 \rightarrow 2\gamma$ is taken to be 0.988. The integrated flux is determined by using the `plot_flux_ccdb.py` script [143]. The target factor is equal to 1.22 nb^{-1}. This results in an estimate of the photoproduction cross section for $f_2(1270)$ between $E_\gamma \in [8.2, 8.8]$ GeV and $-t \in [0.1, 1.0]$ GeV^2 to be 12.48 ± 1.17 nb. The uncertainties are statistical only. This value is significantly smaller than the $a_2(1320)$ cross section measured in Chapter 4. Reference [91] shows a comparison between the f_2 and a_2 cross section predictions based on a Regge model fit to CLAS data.

A.4 Additional Details on the Quantification of Cross-Channel Leakages

Preliminary cross sections from other multi-photon final states have been measured at GlueX, see Section 3.5. Do these channels leak into the $\eta\pi^0 \to 4\gamma$ channel significantly? To answer this question, Monte Carlo simulations are made for the following reactions: $\omega \to \pi^0\gamma$, $f_2(1270) \to \pi^0\pi^0$, $b_1 \to \omega\pi^0$, $\eta \to 3\pi^0$, $\eta' \to \eta\pi^0\pi^0$, $f_1(1285) \to \eta\pi^0\pi^0$, and $a_2\pi^0 \to \eta\pi^0\pi^0$. These simulations are reconstructed under the $\eta\pi^0 \to 4\gamma$ hypothesis to determine the "efficiency" of this cross-channel leakage.

Decay	Branching Ratio
$\pi^0 \to 2\gamma$	0.988
$\eta \to 2\gamma$	0.3936
$\omega \to \pi^0\gamma$	0.0835
$\eta \to 3\pi^0$	0.3257
$f_1(1285) \to \eta\pi^0\pi^0$	0.522
$\eta' \to \eta\pi^0\pi^0$	0.224
$f_2(1270) \to \pi^0\pi^0$	0.842
$a_2(1320) \to \eta\pi^0$	0.145

Table A.1: Table of select particle branching ratios taken from the Particle Data Group

Table A.1 shows the select particle branching ratios relevant to the reactions above. The branching ratio of the decay chain can then be determined. The integrated flux and target thickness are known. These values can then be plugged into Equation 3.13. Table A.2 shows a summary of values used to determine the cross-channel leakage and the amount of leakage itself. Information for each channel, weighting scheme, and energy bin is detailed. Figure A.7 shows the cross section, efficiency, and expected leakages for the $b_1(1235) \to \omega\pi^0$ channel as a function of the beam energy where only accidentals have been subtracted.

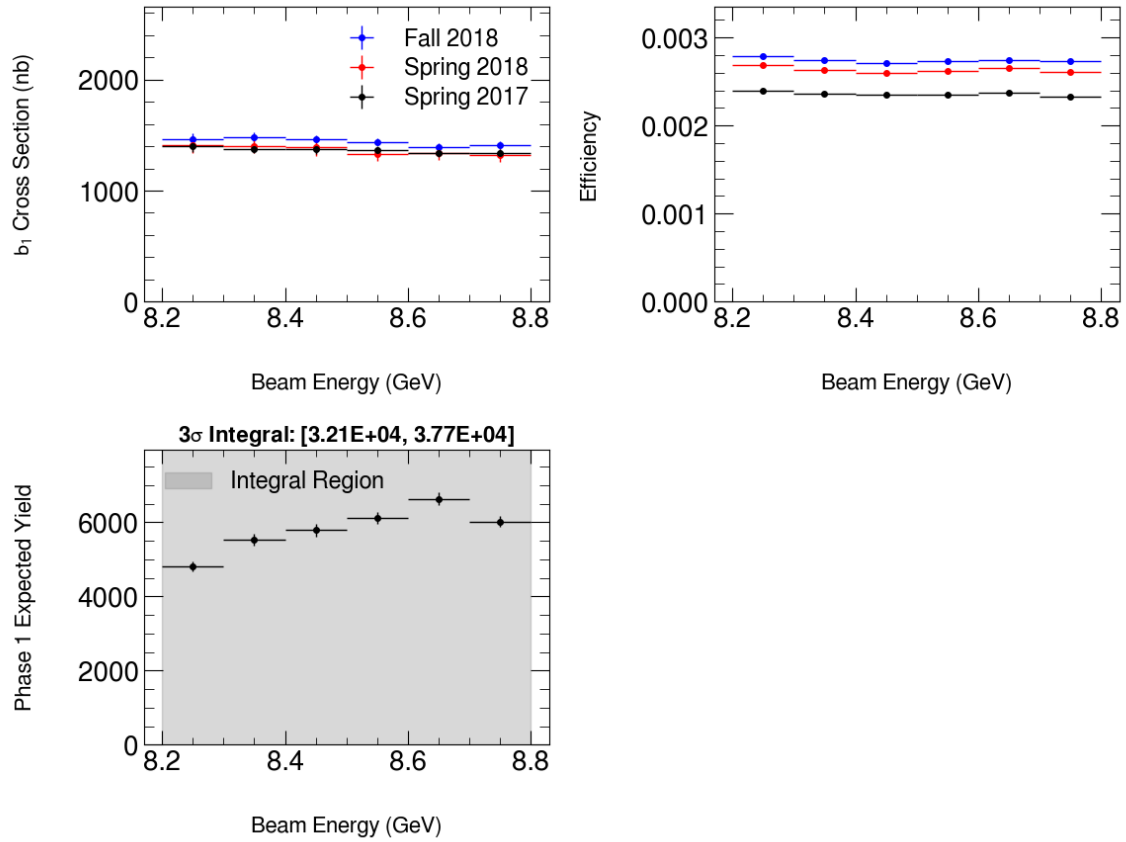Figure A.7: Figure showing the b_1 differential cross section, efficiency estimates of $b_1 \rightarrow \omega\pi^0 \rightarrow 2\pi^0\gamma \rightarrow 5\gamma$ reconstructed under a $\eta\pi^0 \rightarrow 4\gamma$ hypothesis, and the resulting expected yields in bins of energy. The upper and lower 3σ bounds are also given and are shown in the title of the bottom left plot. Only accidentals have been subtracted.

Channel	Weight	E [GeV]	$Yield \times 10^{-1}$	$XSec$ [nb]	$Flux \times 10^{12}$	$Eff. \times 10^{-3}$	Γ
$b_1 \to \omega\pi^0$	AS	8.25 ± 0.05	48039.15 ± 1368.91	1398.00 ± 47.00	2.29 ± 0.00	2.40 ± 0.02	0.082
$b_1 \to \omega\pi^0$	AS	8.35 ± 0.05	55274.41 ± 1503.16	1378.00 ± 41.00	2.59 ± 0.00	2.36 ± 0.02	0.082
$b_1 \to \omega\pi^0$	AS	8.45 ± 0.05	57825.33 ± 1625.23	1372.00 ± 42.00	2.71 ± 0.00	2.35 ± 0.02	0.082
$b_1 \to \omega\pi^0$	AS	8.55 ± 0.05	61250.07 ± 1564.14	1367.00 ± 37.00	2.91 ± 0.00	2.35 ± 0.02	0.082
$b_1 \to \omega\pi^0$	AS	8.65 ± 0.05	66247.81 ± 1744.16	1336.00 ± 36.00	3.37 ± 0.00	2.37 ± 0.02	0.082
$b_1 \to \omega\pi^0$	AS	8.75 ± 0.05	60209.88 ± 1473.91	1341.00 ± 37.00	2.90 ± 0.00	2.33 ± 0.02	0.082
$\omega \to \pi^0\gamma$	AS	8.30 ± 0.10	305.56 ± 25.78	1331.00 ± 80.00	4.88 ± 0.00	0.01 ± 0.00	0.082
$\omega \to \pi^0\gamma$	AS	8.50 ± 0.10	314.22 ± 26.06	1293.00 ± 80.00	5.63 ± 0.00	0.01 ± 0.00	0.082
$\omega \to \pi^0\gamma$	AS	8.70 ± 0.10	298.78 ± 24.56	1275.00 ± 80.00	6.27 ± 0.00	0.01 ± 0.00	0.082
$\eta \to 3\pi^0$	AS	8.25 ± 0.25	7.04 ± 2.75	37.90 ± 0.00	11.68 ± 0.00	0.00 ± 0.00	0.31
$\eta \to 3\pi^0$	AS	8.75 ± 0.25	9.81 ± 2.96	34.50 ± 0.00	10.85 ± 0.00	0.00 ± 0.00	0.31
$\eta' \to \eta\pi^0\pi^0$	AS	8.25 ± 0.25	1636.34 ± 32.86	30.96 ± 0.23	11.68 ± 0.00	0.75 ± 0.02	0.086
$\eta' \to \eta\pi^0\pi^0$	AS	8.75 ± 0.25	1410.72 ± 27.92	27.92 ± 0.23	10.85 ± 0.00	0.74 ± 0.02	0.086
$f_1 \to \eta\pi^0\pi^0$	AS	8.25 ± 0.25	2060.18 ± 61.71	37.90 ± 0.00	11.68 ± 0.00	0.33 ± 0.02	0.2
$f_1 \to \eta\pi^0\pi^0$	AS	8.75 ± 0.25	1824.36 ± 52.99	34.50 ± 0.00	10.85 ± 0.00	0.33 ± 0.02	0.2
$a_2 \to \eta\pi^0\pi^0$	AS	8.25 ± 0.25	216.83 ± 10.08	37.90 ± 0.00	11.68 ± 0.00	0.13 ± 0.01	0.056
$a_2 \to \eta\pi^0\pi^0$	AS	8.75 ± 0.25	166.85 ± 7.71	34.50 ± 0.00	10.85 ± 0.00	0.11 ± 0.01	0.056
$f_2 \to \pi^0\pi^0$	AS	8.50 ± 0.50	305.27 ± 27.88	12.73 ± 1.13	22.53 ± 0.00	0.02 ± 0.00	0.82
$b_1 \to \omega\pi^0$	ASBS	8.25 ± 0.05	-3355.85 ± 126.29	1398.00 ± 47.00	2.29 ± 0.00	-0.16 ± -0.01	0.082
$b_1 \to \omega\pi^0$	ASBS	8.35 ± 0.05	-4208.14 ± 143.64	1378.00 ± 41.00	2.59 ± 0.00	-0.14 ± -0.01	0.082
$b_1 \to \omega\pi^0$	ASBS	8.45 ± 0.05	-5366.47 ± 152.93	1372.00 ± 42.00	2.71 ± 0.00	-0.28 ± -0.01	0.082
$b_1 \to \omega\pi^0$	ASBS	8.55 ± 0.05	-4423.44 ± 126.04	1367.00 ± 37.00	2.91 ± 0.00	-0.19 ± -0.01	0.082
$b_1 \to \omega\pi^0$	ASBS	8.65 ± 0.05	-4119.94 ± 130.77	1336.00 ± 36.00	3.37 ± 0.00	-0.17 ± -0.01	0.082
$b_1 \to \omega\pi^0$	ASBS	8.75 ± 0.05	-5055.43 ± 146.88	1341.00 ± 37.00	2.90 ± 0.00	-0.18 ± -0.01	0.082
$\omega \to \pi^0\gamma$	ASBS	8.30 ± 0.10	-224.00 ± 21.50	1331.00 ± 80.00	4.88 ± 0.00	-0.01 ± -0.00	0.082
$\omega \to \pi^0\gamma$	ASBS	8.50 ± 0.10	120.27 ± 15.00	1293.00 ± 80.00	5.63 ± 0.00	0.00 ± 0.00	0.082
$\omega \to \pi^0\gamma$	ASBS	8.70 ± 0.10	72.36 ± 11.00	1275.00 ± 80.00	6.27 ± 0.00	0.00 ± 0.00	0.082
$\eta \to 3\pi^0$	ASBS	8.25 ± 0.25	-2.58 ± 1.67	37.90 ± 0.00	11.68 ± 0.00	-0.00 ± -0.00	0.31
$\eta \to 3\pi^0$	ASBS	8.75 ± 0.25	0.19 ± 0.41	34.50 ± 0.00	10.85 ± 0.00	0.00 ± 0.00	0.31
$\eta' \to \eta\pi^0\pi^0$	ASBS	8.25 ± 0.25	71.98 ± 6.71	30.96 ± 0.23	11.68 ± 0.00	0.03 ± 0.00	0.086
$\eta' \to \eta\pi^0\pi^0$	ASBS	8.75 ± 0.25	-20.07 ± 3.21	27.92 ± 0.23	10.85 ± 0.00	-0.01 ± -0.00	0.086
$f_1 \to \eta\pi^0\pi^0$	ASBS	8.25 ± 0.25	-395.50 ± 27.04	37.90 ± 0.00	11.68 ± 0.00	-0.06 ± -0.01	0.2
$f_1 \to \eta\pi^0\pi^0$	ASBS	8.75 ± 0.25	-387.65 ± 24.42	34.50 ± 0.00	10.85 ± 0.00	-0.07 ± -0.01	0.2
$a_2 \to \eta\pi^0\pi^0$	ASBS	8.25 ± 0.25	-43.88 ± 4.54	37.90 ± 0.00	11.68 ± 0.00	-0.03 ± -0.00	0.056
$a_2 \to \eta\pi^0\pi^0$	ASBS	8.75 ± 0.25	-67.10 ± 4.89	34.50 ± 0.00	10.85 ± 0.00	-0.04 ± -0.01	0.056
$f_2 \to \pi^0\pi^0$	ASBS	8.50 ± 0.50	-111.96 ± 14.81	12.73 ± 1.13	22.53 ± 0.00	-0.01 ± -0.00	0.82

Table A.2: Expected leakage from a variety of multi-photon final states are calculated in various energy bins. The channel and the weighting scheme(AS=Accidentally Subtracted, BS=Mass sideband subtracted) that was used to statistically select good events are also included. Photoproduction cross sections were determined in various GlueX analyses. From these cross sections (XSec), it is possible to estimate the expected background leakage yields (Yields) into the $\eta\pi^0 \to 4\gamma$ channel. Reconstruction efficiencies (Eff) are determined by reconstructing and analyzing simulations of these channels with an $\eta\pi^0$ hypothesis. All event selections are the same when determining the expected cross-channel background. The Branching ratio (Γ) for the reaction chain is calculated based on the branching ratios of each sub-decay. All these are determined in the same (E)nergy binning as the cross section measurements with bin centers and width. The flux spectrum for the Phase-I dataset is known. The flux column is the integrated flux in each energy bin with a minimum and maximum E_γ from 8.2-8.8 GeV.

APPENDIX B

ADDITIONAL STUDIES FOR THE $a_2(1320)$ CROSS SECTION MEASUREMENT

B.1 Unused Energy Data/MC Comparison

Unused energy loosely determines the number of additional photon hypotheses in an event that can be used for combination forming. This quantity allows more fine-grained control over the data yield as opposed to the number of unused showers. In this section, we probe the scale of the potential differences that exist between data and MC. This study uses the data and MC samples that were restricted to the $1.04 < M(\eta\pi) < 1.72$ GeV domain.

Figure B.1 shows the invariant mass distribution of the candidate η, $M(\eta)$, as a function of the unused energy selection threshold. The signal is described by two Gaussian that share the same mean. The background is described by a linear polynomial. The MC is scaled to match the data signal yield in the nominal no unused energy case. It is apparent that the signal MC underestimates the η signal yield in data. No fits were performed in the final two bins as the signal has significantly degraded.

Figure B.2 shows the invariant mass distribution of the candidate π^0, $M(\pi^0)$, as a function of the unused energy selection threshold. The MC is scaled to match the data signal yield in the nominal no unused energy case as determined by fitting $M(\eta)$. When freeing the unused energy selection, the majority of the events come from the $b_1 \to \omega\pi \to 5\gamma$ reaction. The signature of this reaction is a real π with a fake η.

Figure B.3 shows the percent signal yield growth vs the unused energy selection threshold. The yield growth is normalized to the nominal no unused energy selection. When freeing the unused energy selection to 200 MeV, the data experiences a signal yield growth of around 3% whereas the MC grows by about 1%. It should also be apparent, from B.1, that the **total** yield grows much more as a significant background is let in. These two features can both contribute to the drift seen when varying the unused energy selection threshold when probing the effect of its systematic effect.
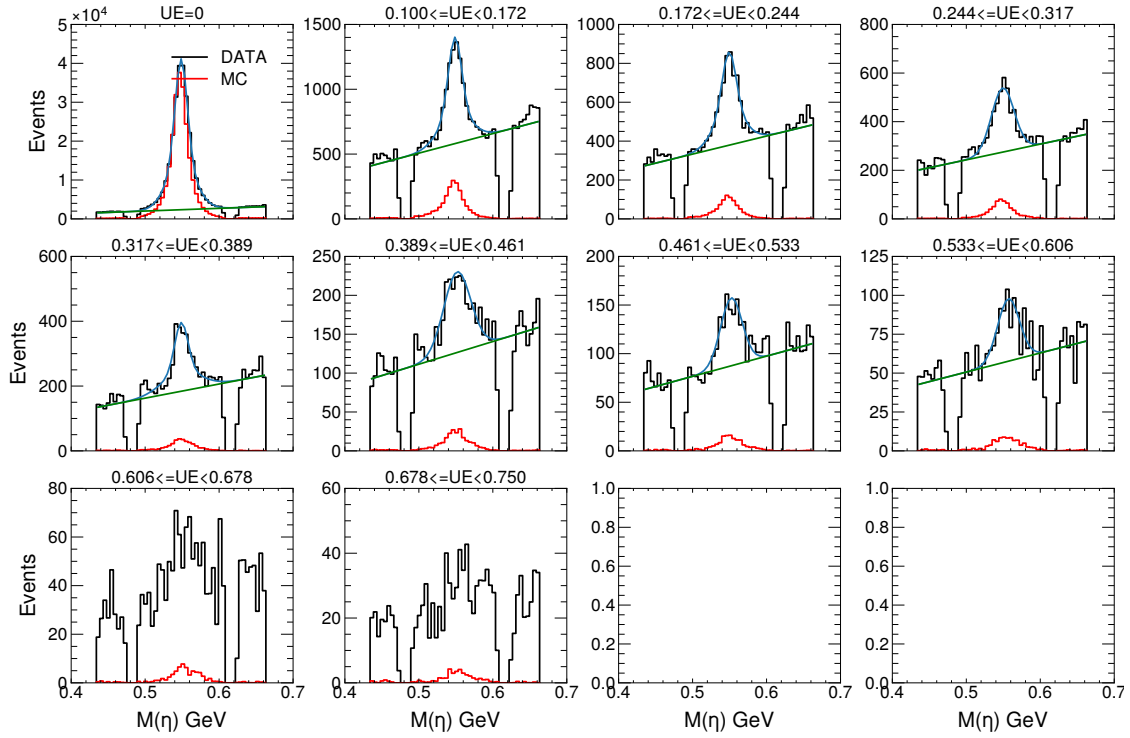
Figure B.1: Invariant mass distribution of the candidate η, $M(\eta)$, as a function of the unused energy selection threshold. The signal is described by two Gaussian that share the same mean. The background is described by a linear polynomial. The MC is scaled to match the data signal yield in the nominal no unused energy case.
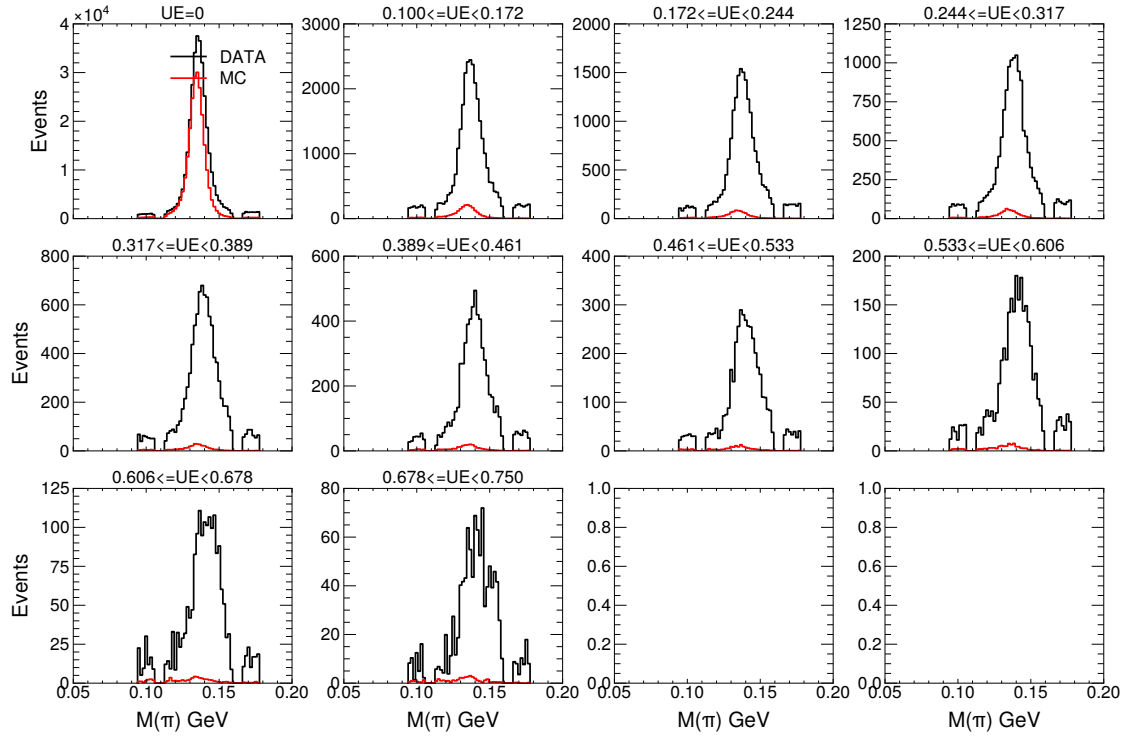
Figure B.2: Invariant mass distribution of the candidate π^0, $M(\pi^0)$, as a function of the unused energy selection threshold. The MC is scaled to match the data signal yield in the nominal no unused energy case as determined by fitting $M(\eta)$.
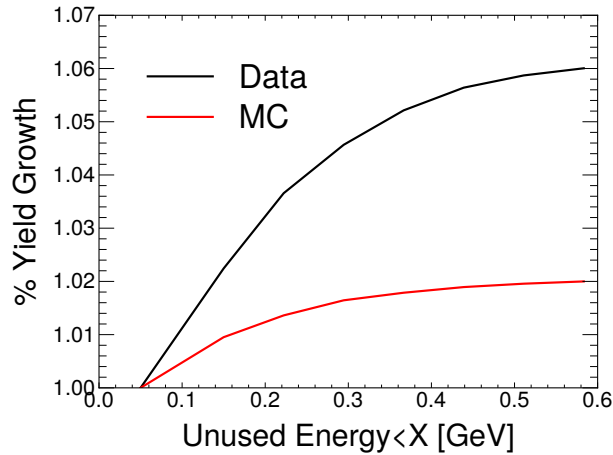

Figure B.3: The percent yield growth, normalized to the nominal no unused energy yield, as a function of the unused energy selection threshold.

B.2 Commands to Extract the Integrated Luminosity

```
plot_flux_ccdb.py --begin-run=30274 --end-run=31057 --num-bins=1 --energy-min=8.2 --
    energy-max=8.8 [--pol=AMO]}

plot_flux_ccdb.py --begin-run=40856 --end-run=42577 --num-bins=1 --energy-min=8.2 --
    energy-max=8.8 [--pol=AMO] -rcdb-query='@is_2018production and
    @status_approved'

plot_flux_ccdb.py --begin-run=50677 --end-run=51768 --num-bins=1 --energy-min=8.2 --
    energy-max=8.8 [--pol=AMO] --rcdb-query='@is_2018production and @status_approved and
    beam_on_current > 49'
```

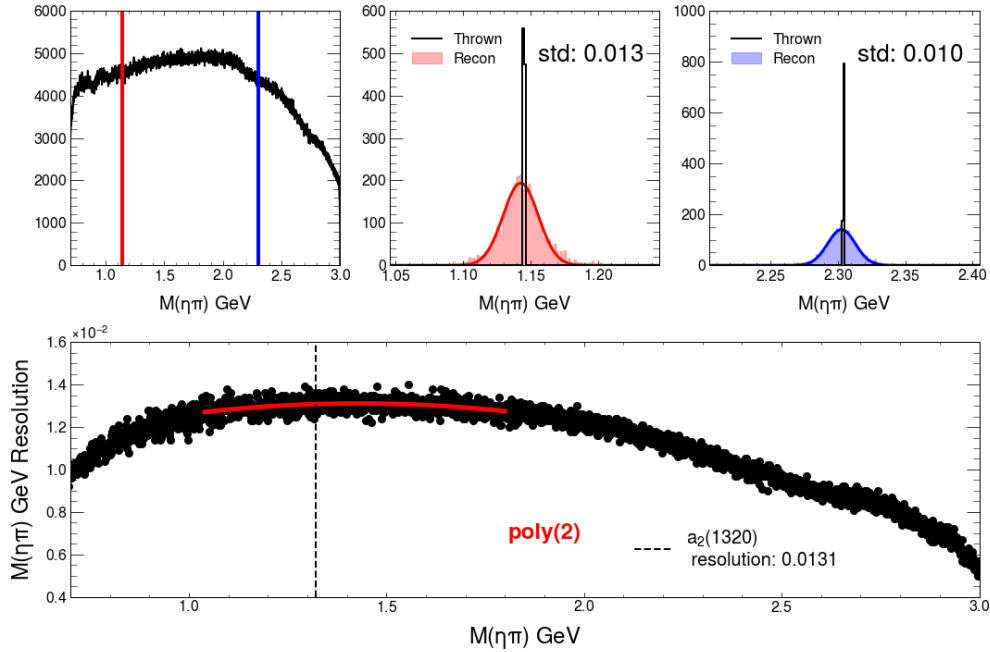## B.3 GlueX $M(\eta\pi)$ Resolution

Figure B.4: Determining mass resolution from Monte-Carlo. (Top-Left) Histogram of the reconstructed $M(\eta\pi)$ in 1 MeV bins. (Top-Middle/Top-Left) 1 MeV window selection on the generated $M(\eta\pi)$ values. The red/blue histograms correspond to the reconstructed $M(\eta\pi)$ values. The overlaid distribution is from a Gaussian fit to the histogram. (Bottom) Mass resolution as a function of $M(\eta\pi)$. Red curve denotes a polynomial fit to the data. The mass resolution at the $a_2(1320)$ mass is around 13 MeV.

The mass resolution can be estimated from the large Monte-Carlo sample that is used to model the acceptance. Each reconstructed event has an associated set of generated kinematics. For this study, the data is split into 1 MeV bins of generated masses. For each bin a histogram of the

reconstructed masses can be made. These histograms can be fit to a Gaussian to extract the resolution. This is shown for two masses on the top row of plots of Figure B.4. The standard deviation of the reconstructed masses can also be used as the distribution is highly Gaussian. The bottom-row plot shows the mass resolution as a function of mass. The resolution at the $a_2(1320)$ mass is around 13 MeV. The Breit-Wigner width is the full width at half maximum(FWHM). The Gaussian mass resolution can be converted to FWHM by dividing by 2.355, which turns out to be roughly 5.5 MeV.

B.4   Convergence of bootstrap

The number of bootstrap iterations to perform is dependent on the complexity of the model and data. One way to assess the convergence of the bootstrap procedure is to evaluate your metric of interest (i.e. standard deviation) as a function of sample size. Figure B.5 shows the standard deviation of the acceptance corrected yield vs the sample size for select coherent sums. The metric should stabilize after some number of steps.

Another factor to consider is the shape of the distribution. Standard deviation is a good metric for distributions that are roughly Gaussian in shape. Alternatively if the resulting bootstrap distribution is irregular/asymmetric then percentiles can give a better representation. Figure B.6 shows the bootstrap acceptance corrected yield distribution for select coherent sums which are mostly symmetric and Gaussian-like. The standard deviation of $D^+_{a_2(1320)}$ and $D^+_{a_2(1320)}$ is proportional to the uncertainty on positive/negative reflectivity cross sections.

It is also insightful to quantify the difference between the uncertainties estimated by `Minuit` with the ones estimated through the bootstrap procedure. Figure B.7 shows the ratio of the bootstrapped uncertainties to the `Minuit` uncertainties. The bootstrapped uncertainties for the acceptance corrected yields appear to roughly [2-5]x larger for the positive and negative reflectivity coherent sums for the $a_2(1320)$. Note that this factor does not translate directly to a [2-5]x larger uncertainty to the cross section as it's uncertainty will include contributions from the uncertainty on the branching fraction, for instance.
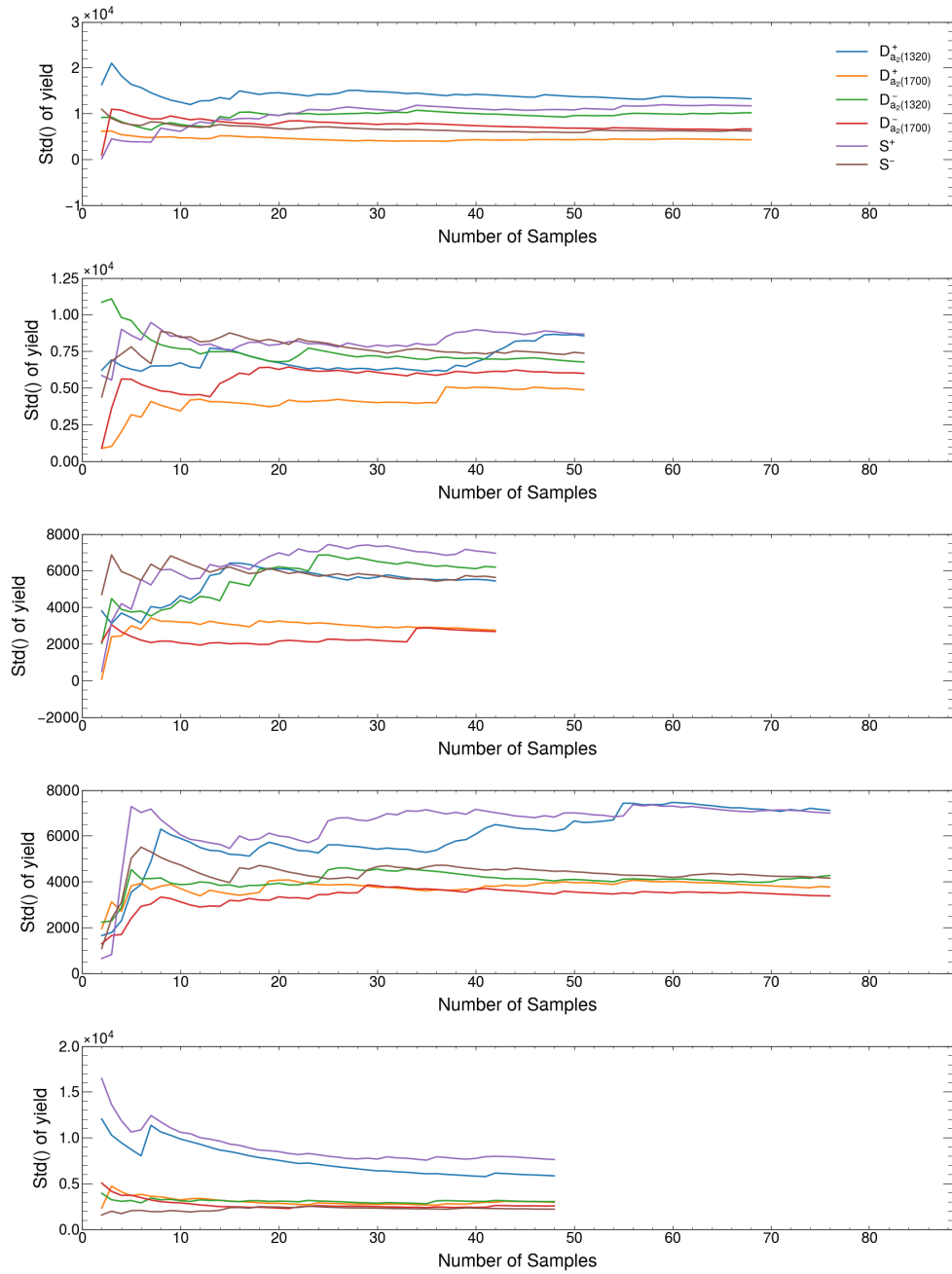
Figure B.5: Standard deviation of the bootstrap samples vs the sample size. $D^+_{a_2(1320)}$ is the coherent sum of all amplitudes that describe the $a_2(1320)$ produced with positive reflectivity.
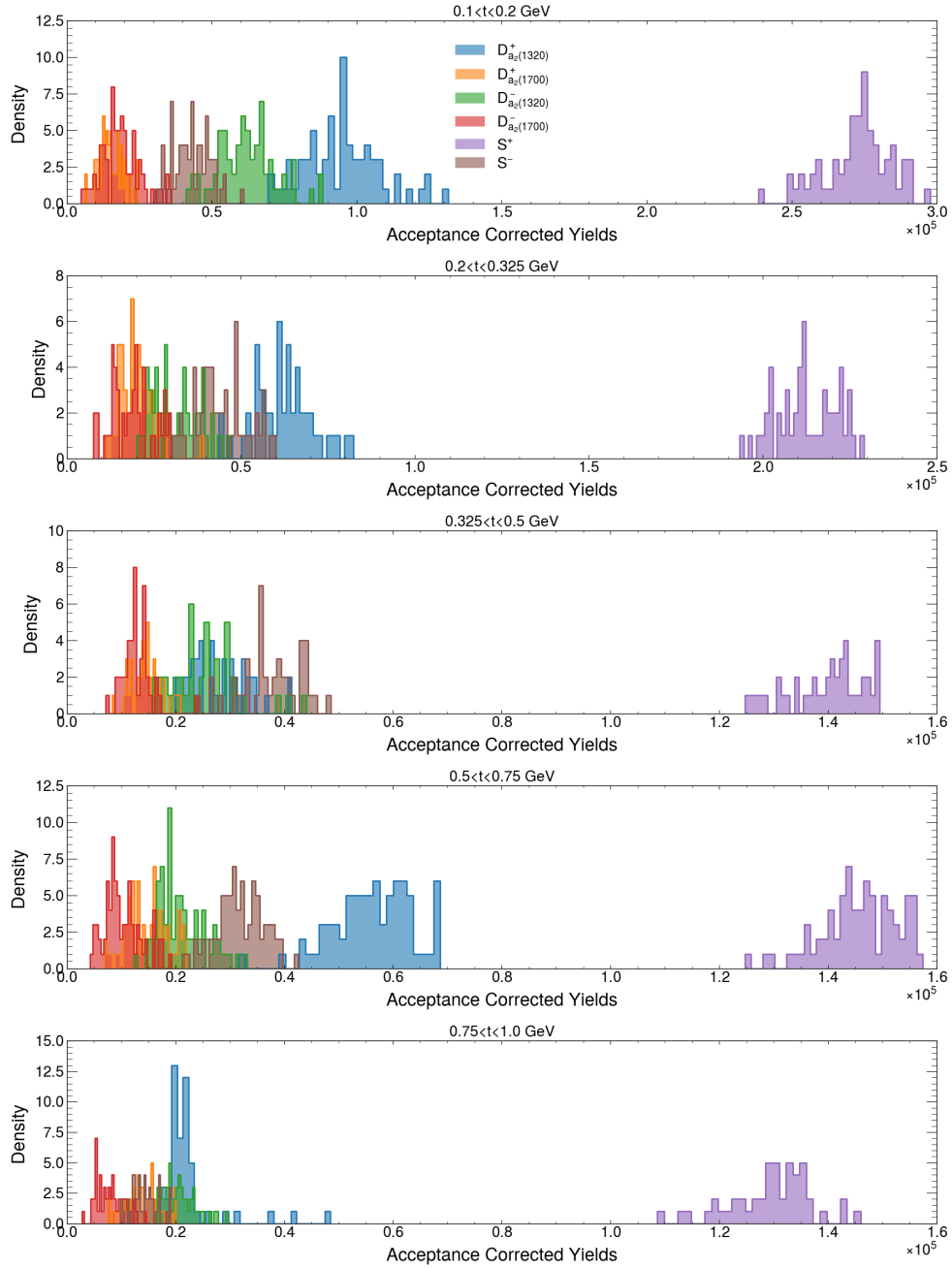
Figure B.6: Bootstrapped distribution for the acceptance corrected yield for select coherent sums. $D^+_{a_2(1320)}$ is the coherent sum of all amplitudes that describe the $a_2(1320)$ produced with positive reflectivity.
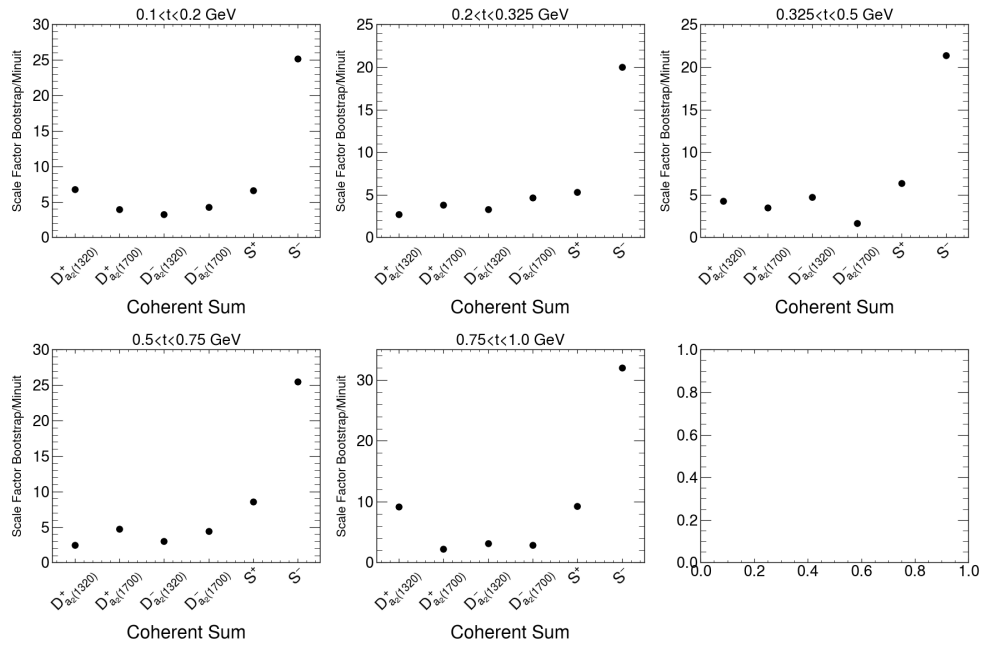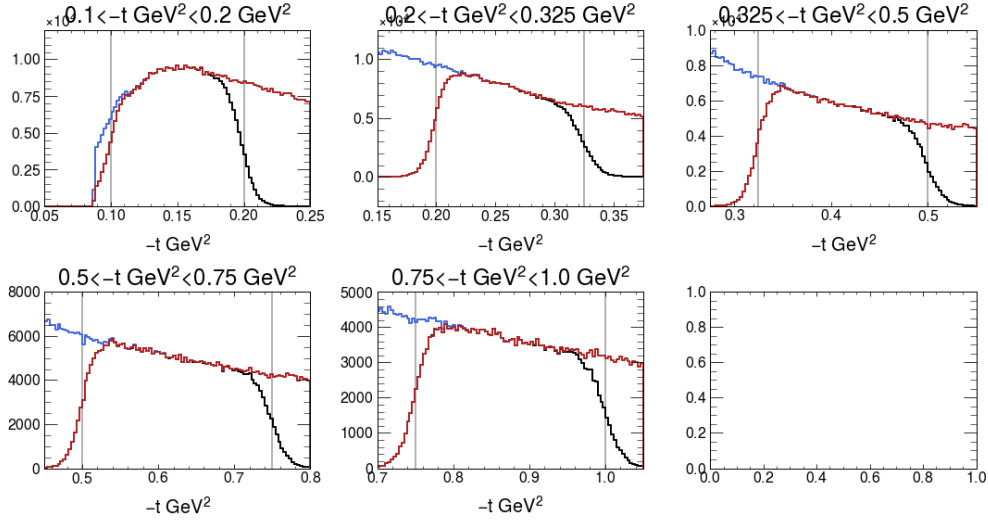
Figure B.7: Ratio between the bootstrapped uncertainties and `Minuit` uncertainties. $D^+_{a_2(1320)}$ is the coherent sum of all amplitudes that describe the $a_2(1320)$ produced with positive reflectivity.

B.5   Quantifying Bin Migration

Figure B.8: Histogram showing migration in and out of each $-t$ bin in simulation. (Blue) Generated $-t$ is selected to be less than the right bin edge, reconstructed values are plotted. (Red) Generated $-t$ is selected to be greater than the left bin edge, reconstructed values are plotted. (Black) Generated $-t$ is selected to be with the left and right bin edges, reconstructed values are plotted.
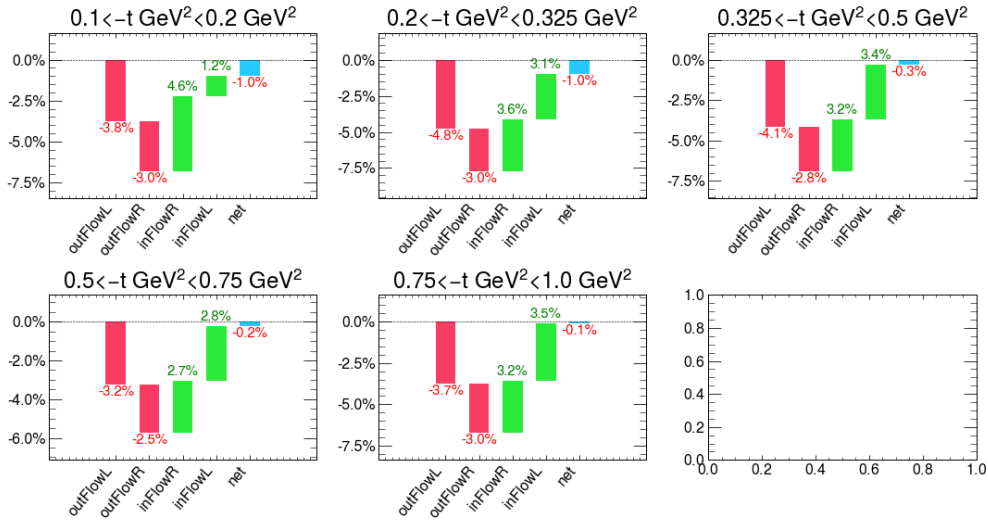
Figure B.9: Waterfall plot of the inflows and outflows (migration) for the 5 different t-bins. Outflow are events that are generated within the bin boundary but reconstructed outside. Inflow are the opposite.

A large Monte-Carlo sample is used in the fit procedure to include the acceptance of the GlueX detector. We can reuse this dataset to quantify the effects of bin migration. High level kinematic

variables, like $M(\eta\pi)$, can significantly migrate in complicated ways. Monte-Carlo simulations give a way to quantify the effects of bin migration since both the generated and reconstructed values are known. Figure B.8 shows the reconstructed t-distribution in the 5 t-bins where various selections have been applied on the generated values. Outflow from a bin is equal to integral of the black curve outside the bin boundaries. Inflow from the left is the difference between the integral of the blue and black curves inside the bin boundaries. Inflow from the right is the difference between the integral of the red and black curves inside the bin boundaries.

Figure B.9 shows a waterfall plot denoting the inflow/outflow from the left/right sides of the bin boundary. If the Monte-Carlo sample that is used during the partial wave analysis procedure contains only events where the generated t is within the bin boundaries, then only outflow can occur. For example, based on the top-left plot of the Figure, if the generated t distribution is bounded by [0.1,0.2] GeV^2 , then about 7% of the events would migrate outside the region of interest. This should lead to an underestimation of the efficiency that is used in the cross section measurement. The effect of bin migration can be incorporated in the fit by simulating over a larger kinematic range and not performing additional selections on the generated quantities for the `accmc` dataset. The `genmc` dataset is still filtered to select in the relevant t-bin as it is the region we wish to extrapolate into. Inflows and outflows are not always symmetric and there appears to be a small overall net migration left over.

B.6   Fit Fractions of Systematic Variations

The presented measurements are of the differential cross section and the parity asymmetry. Systematic uncertainties have been extracted for a wide set of variations. It is insightful to see how each partial wave contribution changes when variations are made. Perhaps the variation seen in the cross section is completely driven by one partial wave.

Figures B.10, B.11, B.12, B.13, B.14 contains a set of plots that show the fit fraction of particular sums of coherent waves for the 5 different t bins for variations shown in Section 4.6.2. The standard Barlow significance plot is shown on the left panel. Percent deviation is on the x-axis and the specific variation is along the y-axis. Red/Blue denote positive and negative reflectivity components respectively. The second panel from the left show the fit fractions of partial waves that make up the $a_2(1320)$. The third panel shows the fit fractions of partial waves of both a_2's coherently summed. The S-wave fit fraction has been scaled by 1/3 for better visual comparisons. The fourth panel shows the difference between the incoherent sum of the partial waves and the coherent sum.

A similar set of plots is made for the variations shown in Section 4.6.3. These variations were related to the model parameterization. Figures B.15, B.16, B.17, B.18, B.19 shows the results.
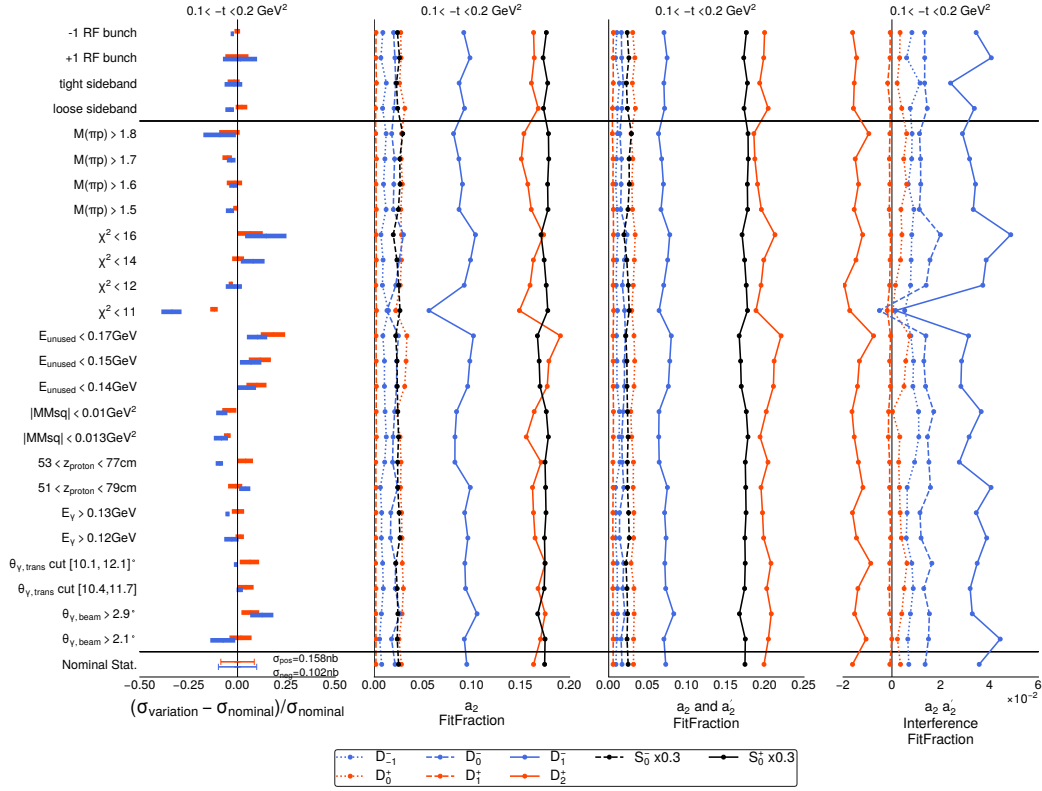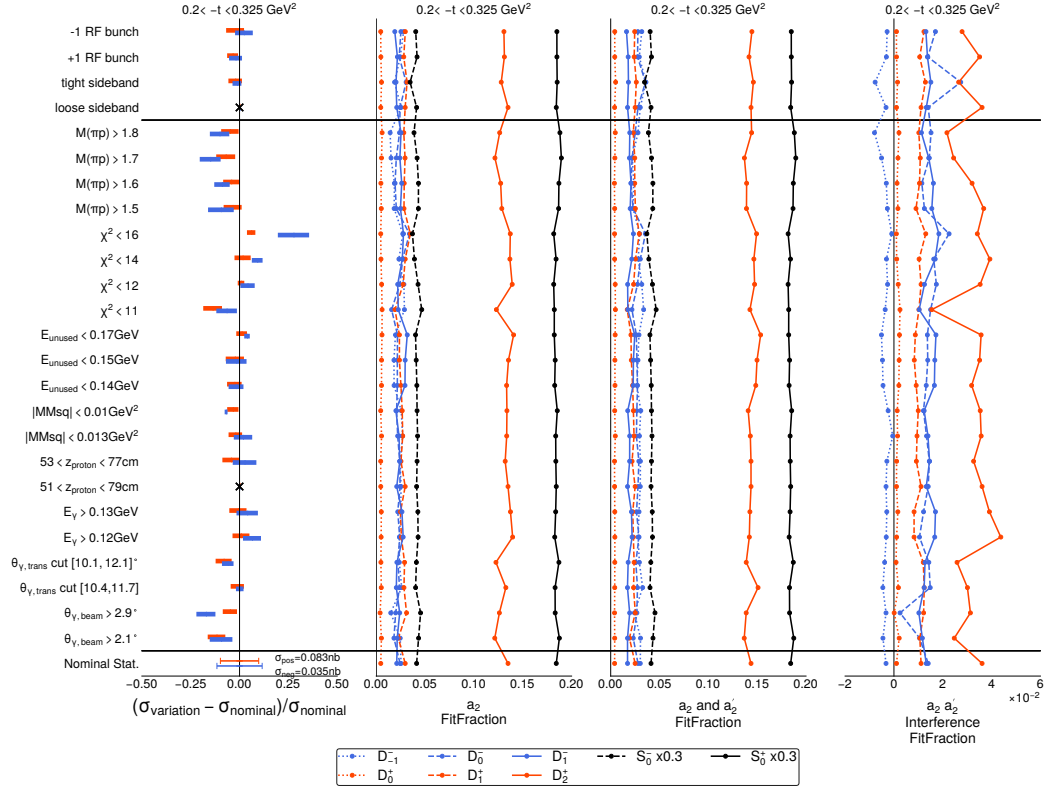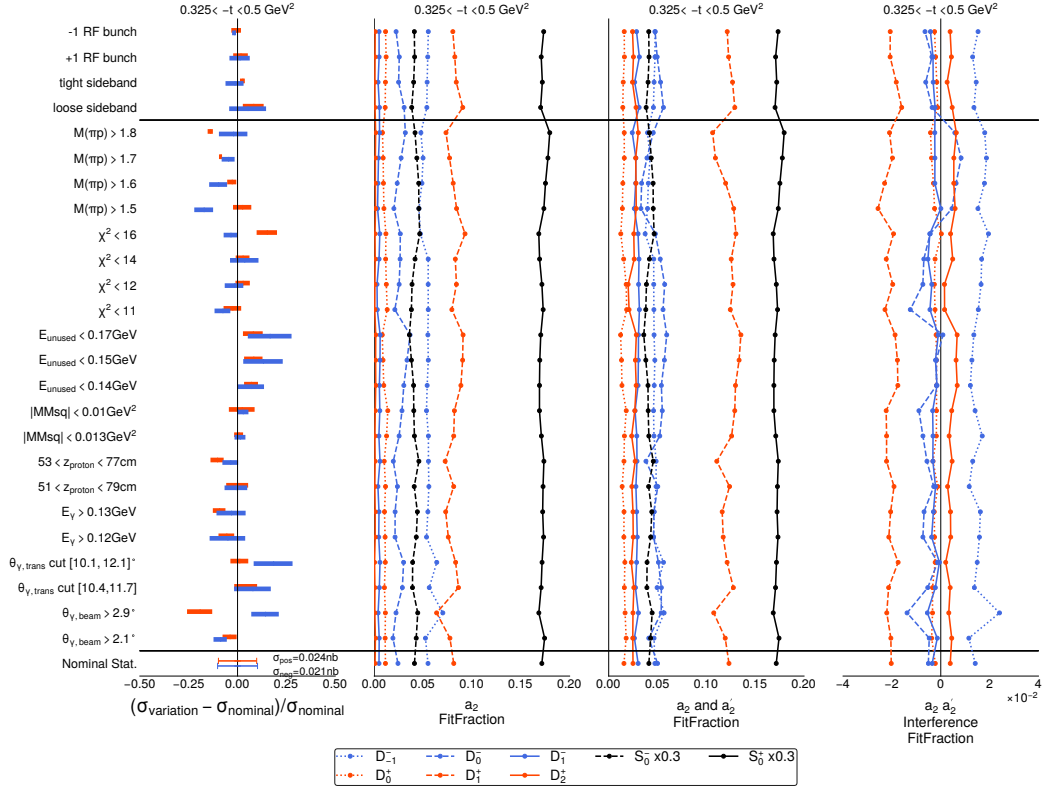

Figure B.10: $(0.1 < -t < 0.2)$ GeV^2) Plot detailing the significance of specific variations and the associated fit fractions of the partial waves of the $a_2(1320)$, coherent sum of both a_2's, and the interference between the a_2's. Red/Blue denote positive and negative reflectivity components respectively.
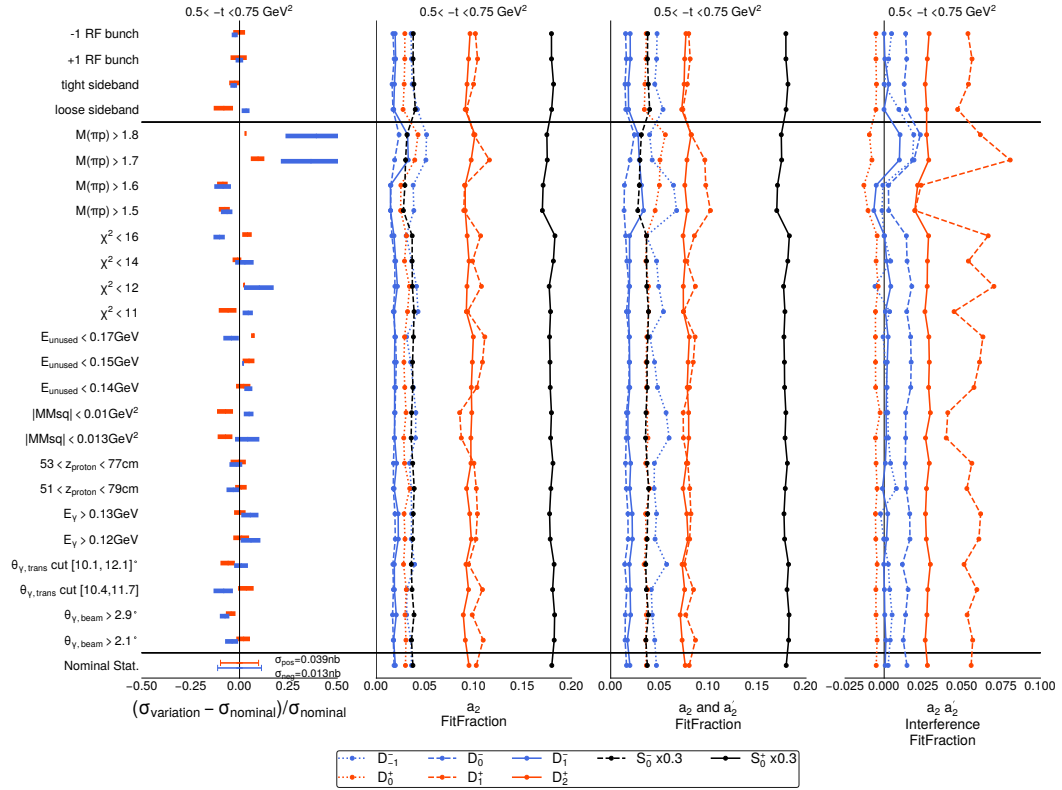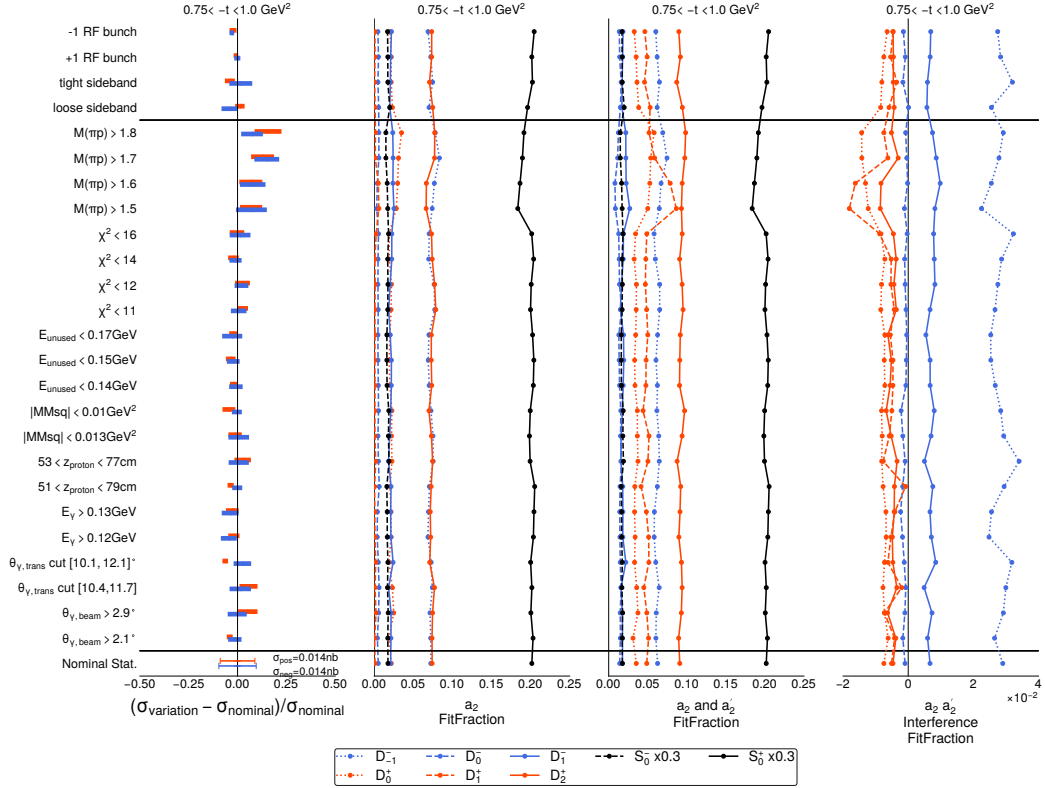
Figure B.11: $(0.2 < -t < 0.325)$ GeV^2) Plot detailing the significance of specific variations and the associated fit fractions of the partial waves of the $a_2(1320)$, coherent sum of both a_2's, and the interference between the a_2's. Red/Blue denote positive and negative reflectivity components respectively.
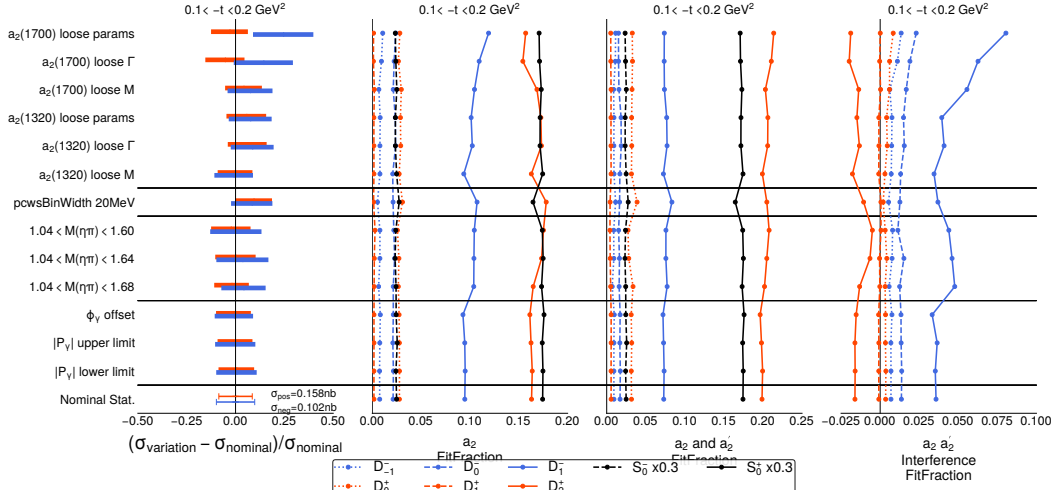
Figure B.12: $(0.325 < -t < 0.50)$ GeV^2) Plot detailing the significance of specific variations and the associated fit fractions of the partial waves of the $a_2(1320)$, coherent sum of both a_2's, and the interference between the a_2's. Red/Blue denote positive and negative reflectivity components respectively.

Figure B.13: $(0.50 < -t < 0.75)$ GeV^2) Plot detailing the significance of specific variations and the associated fit fractions of the partial waves of the $a_2(1320)$, coherent sum of both a_2's, and the interference between the a_2's. Red/Blue denote positive and negative reflectivity components respectively.
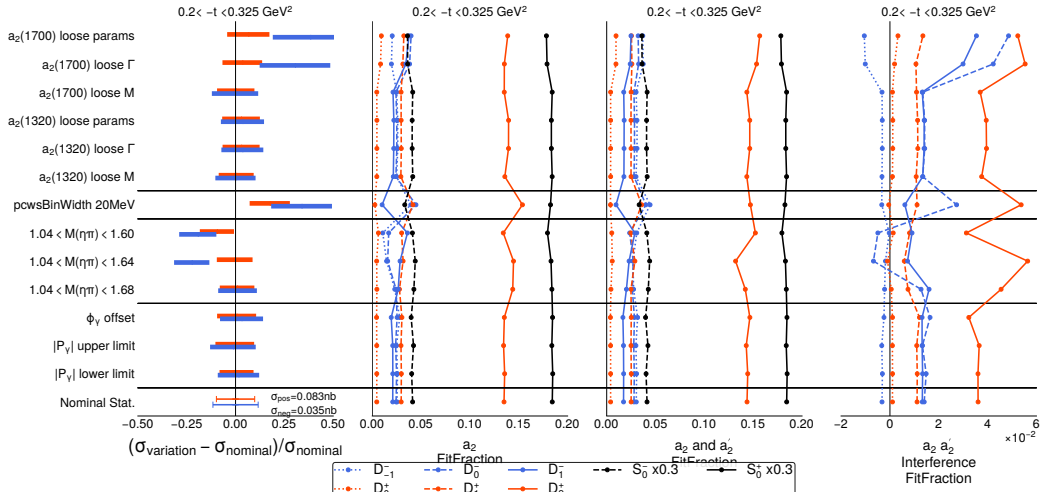
199

Figure B.14: $(0.75 < -t < 1.0)$ GeV^2) Plot detailing the significance of specific variations and the associated fit fractions of the partial waves of the $a_2(1320)$, coherent sum of both a_2's, and the interference between the a_2's. Red/Blue denote positive and negative reflectivity components respectively.
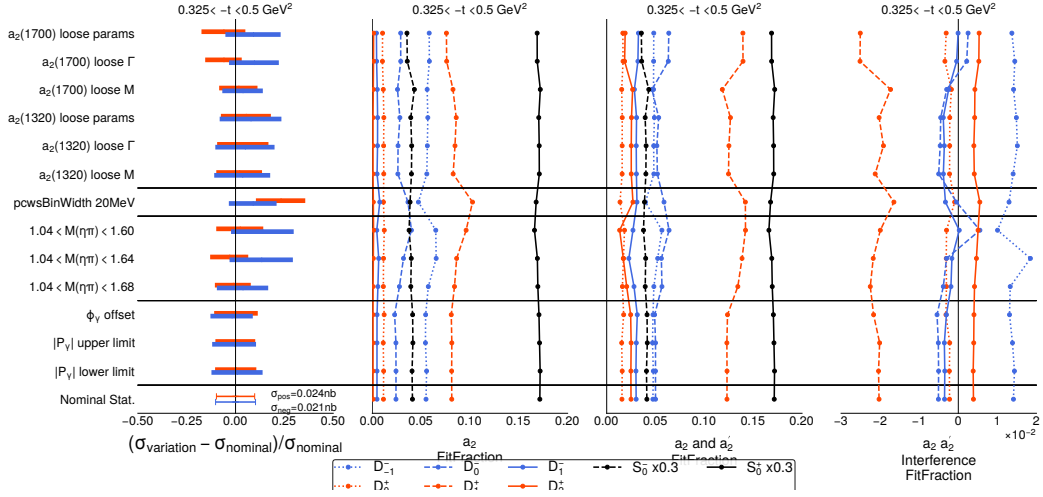
Figure B.15: $(0.1 < -t < 0.2)$ GeV^2) Plot detailing the deviations of specific variations and the associated fit fractions of the partial waves of the $a_2(1320)$, coherent sum of both a_2's, and the interference between the a_2's. Red/Blue denote positive and negative reflectivity components respectively.
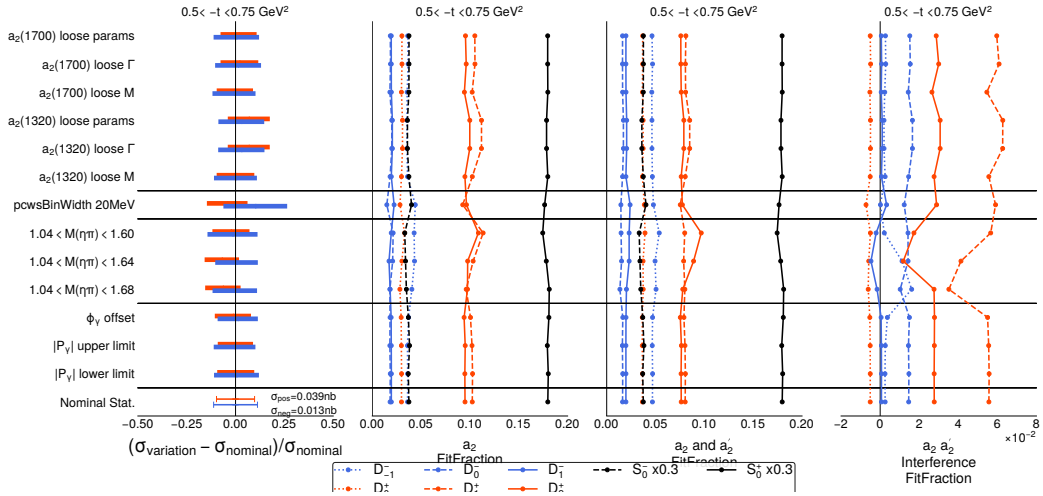

Figure B.16: $(0.2 < -t < 0.325)$ GeV^2) Plot detailing the deviations of specific variations and the associated fit fractions of the partial waves of the $a_2(1320)$, coherent sum of both a_2's, and the interference between the a_2's. Red/Blue denote positive and negative reflectivity components respectively.
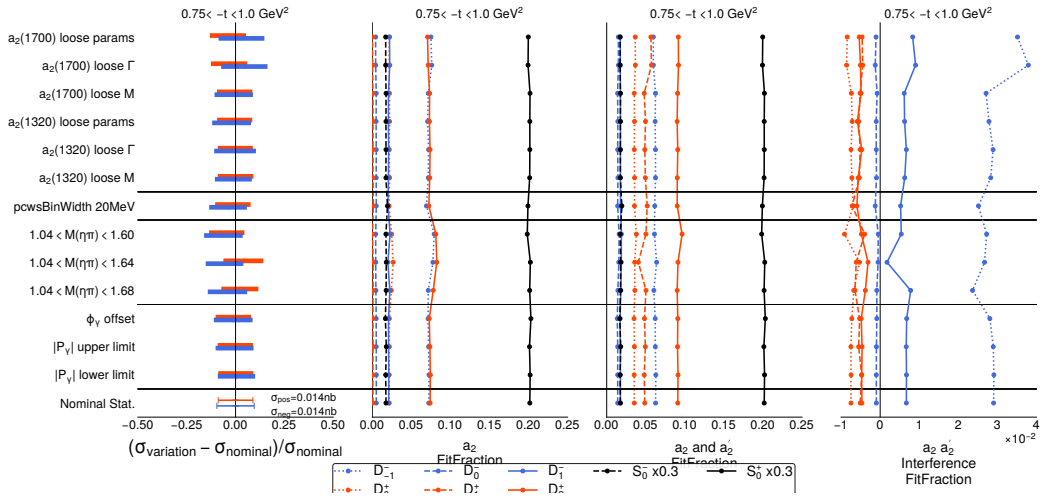
Figure B.17: $(0.325 < -t < 0.50)$ GeV^2) Plot detailing the deviations of specific variations and the associated fit fractions of the partial waves of the $a_2(1320)$, coherent sum of both a_2's, and the interference between the a_2's. Red/Blue denote positive and negative reflectivity components respectively.

Figure B.18: $(0.50 < -t < 0.75)$ GeV^2) Plot detailing the deviations of specific variations and the associated fit fractions of the partial waves of the $a_2(1320)$, coherent sum of both a_2's, and the interference between the a_2's. Red/Blue denote positive and negative reflectivity components respectively.

Figure B.19: $(0.75 < -t < 1.0)$ GeV^2) Plot detailing the deviations of specific variations and the associated fit fractions of the partial waves of the $a_2(1320)$, coherent sum of both a_2's, and the interference between the a_2's. Red/Blue denote positive and negative reflectivity components respectively.

B.7 Input/Output Test

It is important to conduct an input/output, I/O, test to study whether the experimental methodology extracts results that are consistent with generated inputs. The simulated data is based on the results of a K-matrix fit to GlueX data allowing it to have realistic angular distributions and allows for a sophisticated description of the $a_0(980)$ which is known to take on a more complicated lineshape compared to the standard Breit-Wigner distribution. A fixed K-matrix parameterization for S and D-waves with isospin 1 is used to describe the dynamics of the $a_0(980)$, $a_2(1320)$, and the $a_2(1700)$. In this approach, the Breit-Wigner distribution gets replaced with $(I - iK\rho)^{-1}P$ where

$$K_{ij} = \sum_{\alpha} \frac{g_{\alpha i}(m) g_{\alpha_j}(m)}{(m_\alpha^2 - m^2)\sqrt{\rho_i \rho_j}} \quad P_i = \sum_{\alpha} \frac{\beta_\alpha g_{\alpha i}}{(m_\alpha^2 - m^2)\sqrt{\rho_i}} \tag{B.1}$$

m_α and β_α are fixed to the results from the coupled channel analysis of $p\bar{p}$ annihilation data for the $\pi^0 \pi^0 \eta, \pi^0 \eta\eta$ and $K^+ K^- \pi^0$ channels from Crystal Barrel, with additional $\pi\pi$-scattering datasets, and with the P and D-wave amplitudes of the $\eta\pi$ and $\eta'\pi$ systems produced by a pion beam at COMPASS. m_α^{bare} is the mass of the resonance α. g_{α_j} is the coupling strength to channel j. β_α is the strength of the produced resonance that is fitted for. ρ are phase space factors. A reduced waveset was used for this study: $S_0^\pm, D_0^\pm, D_2^\pm$.

B.7.1 I/O Test and Calibrated Uncertainties using Mass-Independent Fits

The simulations made from the K-Matrix fit are reconstructed and filtered using the same procedure outlined in Chapter 3. The mass-independent fit is performed in 40 MeV bins from $M(\eta\pi)$ = 0.8 to 1.8 GeV using the same waveset that generated the data. Reconstructed phase space Monte-Carlo, described in Section 3.2.1, is used to incorporate the GlueX acceptance and is corrected for. Figure B.20 shows the results of the mass independent fits with vertical bars whose length represents the 1σ bootstrapped uncertainties. The dashed line is the generated wave contributions. Positive and negative reflectivity components are shown in red and blue, respectively. The pull distribution is shown in the bottom right plot, where the blue distribution uses the Minuit errors and the orange distribution uses the bootstrapped uncertainties. A standard normal is overlaid in black. The Minuit uncertainties appear to be underestimated, whereas the bootstrapped uncertainties are better calibrated than the Minuit ones. Mass independent fits are used for this particular study because they are significantly cheaper to run which compensates for the costly bootstrap resampling procedure.
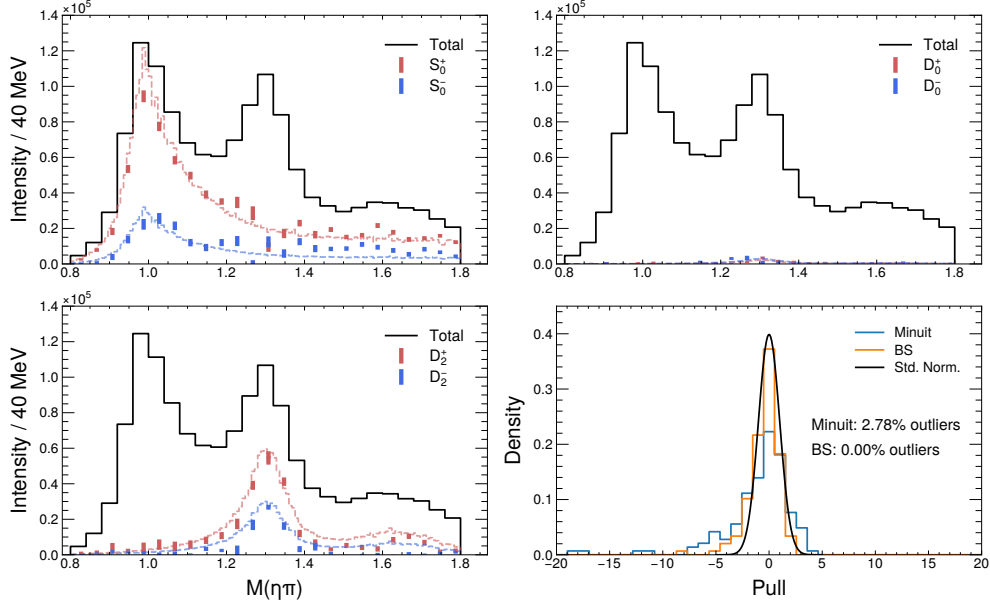
Figure B.20: Input/output study with K-Matrix simulated data for $\eta\pi^0$. Dashed line is the generated spectra. Vertical bars are the mass-independent fit results with bootstrapped errors. The bottom right plot shows the pull distribution with bootstrapped errors and with errors from Minuit. Minuit has <3% of the points outside the shown range.

B.7.2   I/O Test of Systematics

This study performs a subset of the variations that was detailed in the main analysis of the GlueX data. Since the "data" and MC are both simulated there should exist little significant variations. Note, some small fraction of variations are expected to be significant simply by sampling randomness. Figure B.21 shows how significant each variation is to a measurement of a simulated differential cross section. For each event selection a looser and tighter selection is made, if possible. If the nominal selection is already considerably loose/tight then two tighter/looser selections are made. A more detailed scan is performed over the χ^2, unused energy, and $M(\pi p)$. Each panel corresponds to a different t bin. The red/blue bars correspond to positive/negative reflectivity components. The x-axis is the percent deviation of a particular variation when compared to the nominal. The width of each bar is the normalized uncertainty, $\frac{\sigma_\Delta}{x}$. The discrepancy of a variation, N, is then the distance it's corresponding bar is away from 0. For reference, the nominal statistical errors are also included and is denoted by lines near the x-axis. Overall, the variations are consistent with the nominal measurement. Note, tightening the $M(\eta\pi)$ selection can make it more difficult to constrain the contributions from the $a_2(1700)$. Some variation could be expected due to this.
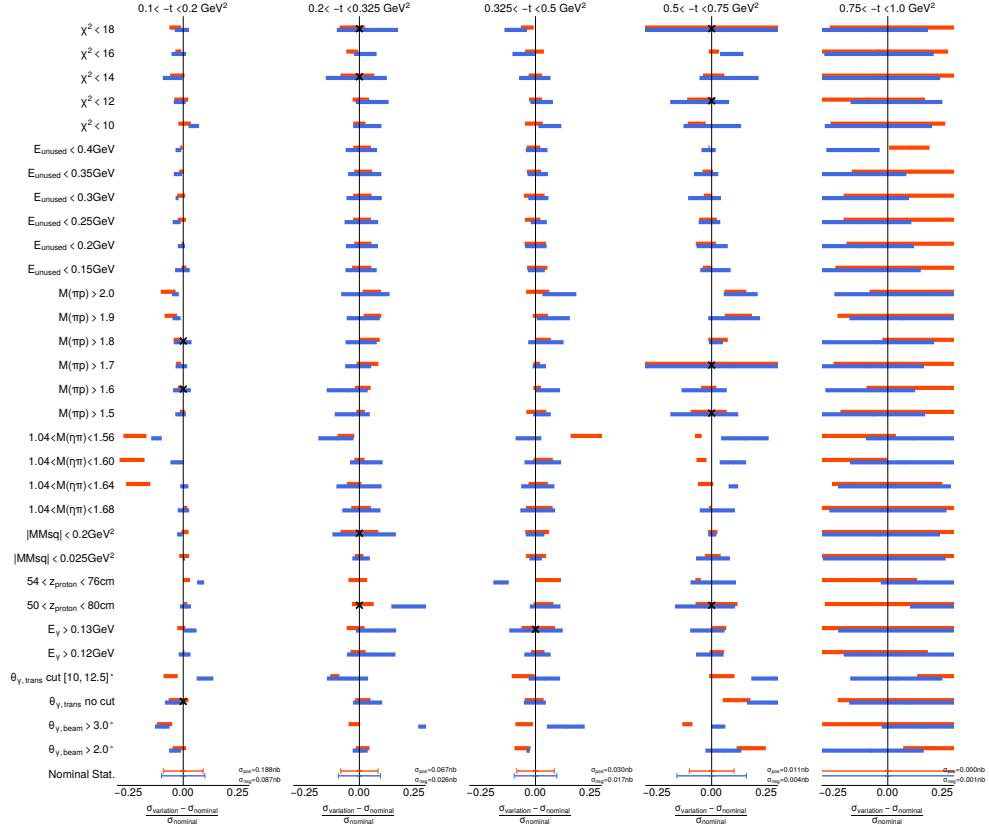
Figure B.21: Systematics overview for K-matrix MC

B.8 Measurements with Alternative t-Binning

An alternative t-binning scheme is analyzed to determine whether the results depend on the particular t-binning scheme that was chosen in the nominal procedure. For this analysis, 4 t-bins were chosen to span the region in between the 5 nominal t-bins. Figure B.22 shows a comparison between the nominal t-binning and this alternative t-binning format. The bottom row overlays the low energy CLAS data. The measurements do not show a significant dip in the analysis with 4 t-bins. This could be due to binning effects. Comparing the two analyses, a dip in the differential cross section could exist between $t \in [0.4, 0.5] \text{GeV}^2$.
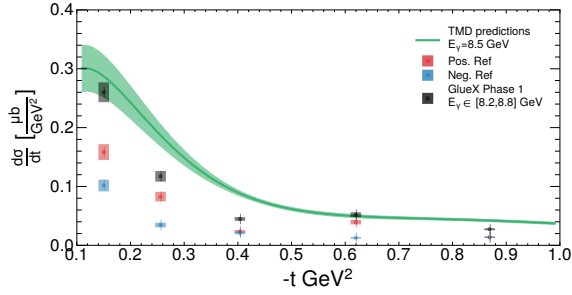
(a) Differential cross section measured in t t-bins
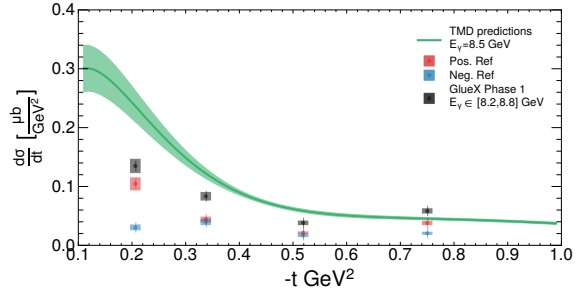
(b) Differential cross section measured in 4 t-bins
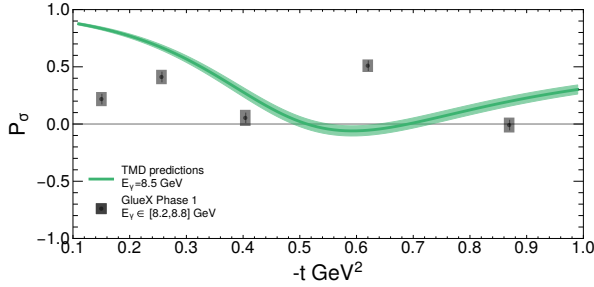
(c) Parity asymmetry measured in 5 t-bins
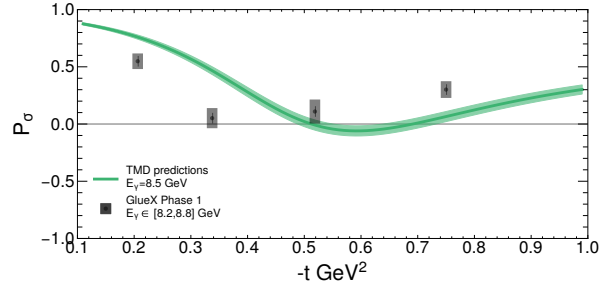
(d) Parity asymmetry measured in 4 t-bins
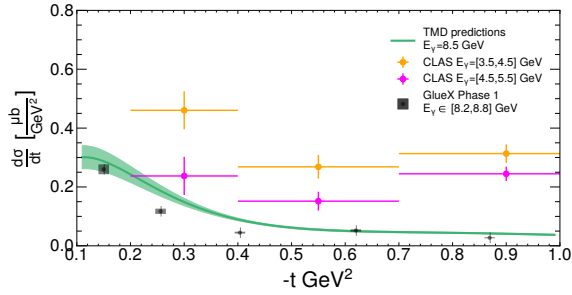
(e) Differential cross section measured in 5 t-bins with CLAS data comparison
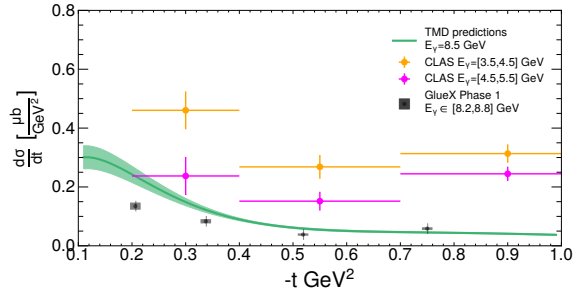
(f) Differential cross section measured in 4 t-bins with CLAS data comparison

Figure B.22: Figures comparing measurements of the differential cross section and parity asymmetry in (left-column) 5 t-bins and (right-column) 4 t-bins. Predictions from the JPAC TMD model are shown shaded in green. Only statistical uncertainties are shown and are estimated by `Minuit`. The bottom-row plots overlay the low energy CLAS data points.

APPENDIX C

ADDITIONAL STUDIES FOR THE MEASUREMENT OF SINGLE PARTICLE BEAM ASYMMETRIES

C.1   Kinematic Distributions for $\gamma p \to \eta \pi^- \Delta^{++}$
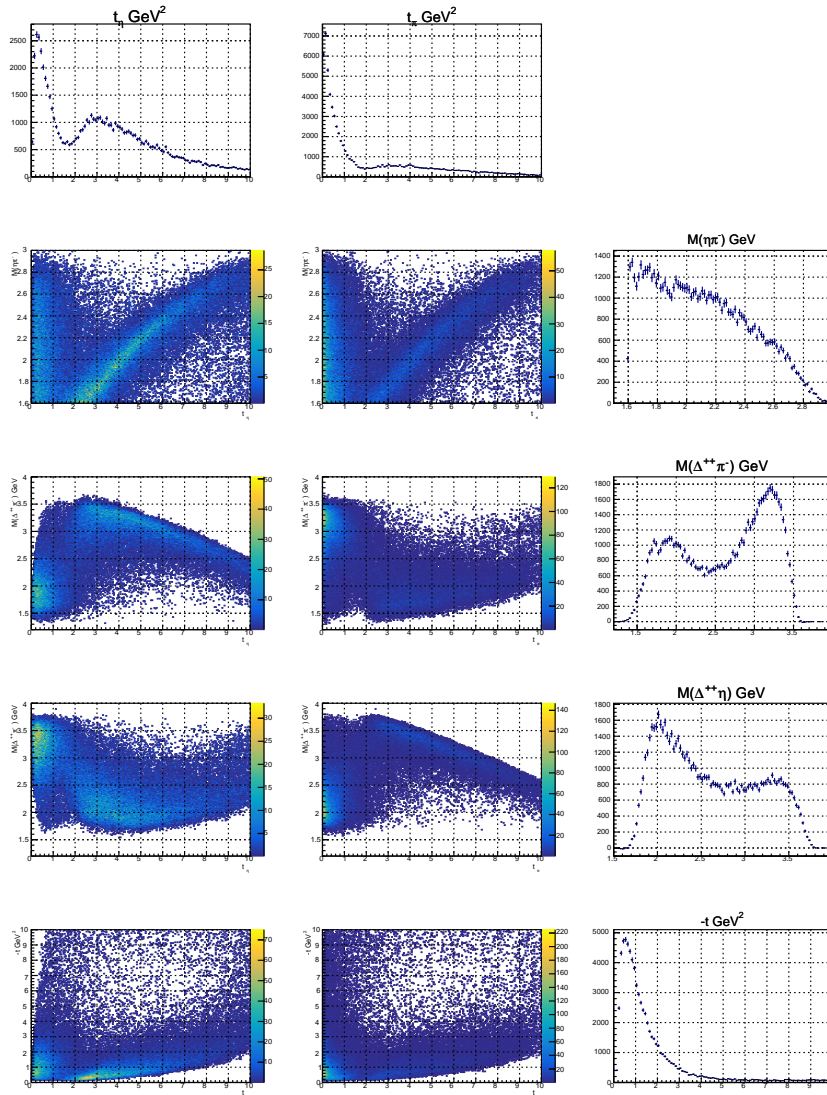
Figure C.1: Correlations of the relevant kinematic variables. Courtesy of Colin Gleason.

C.2   Yield Asymmetry Fits

This section shows the fits to the yield asymmetry for the GlueX Phase-I dataset. The particular bin in u_3, s_{12}, or s_{23} a Figure belongs to is tabulated in Table C.1.

Kinematic Bin	Figure
$0 < u_3 < 0.5$ GeV^2	C.2
$0.5 < u_3 < 1.0$ GeV^2	C.3
$1.0 < u_3$ GeV^2	C.4
$0 < u_3$ GeV^2	C.5
$1.6 < s_{12} < 2.1$ GeV	C.6
$2.1 < s_{12} < 2.6$ GeV	C.7
$2.6 < s_{12} < 3.1$ GeV	C.8
$s_{\eta p} < 2.1$ GeV and $1.15 < s_{\pi p} < 1.4$ GeV	C.9
$2.1 < s_{\eta p} < 2.6$ GeV and $1.4 < s_{\pi p} < 2.2$ GeV	C.10
$2.2 < s_{\eta p}$ GeV and $2.2 < s_{\pi p} < 1.4$ GeV	C.11

Table C.1: Table of yield asymmetry fits organized into the additional binning that was performed u_3, s_{12}, or s_{23}. For all figures, the yield asymmetry fit for each pair of orthogonal orientations for both fast-η are shown in the left two columns, and fast-π, are shown in the right two columns. The rows correspond to the 5 different t_1 bins.
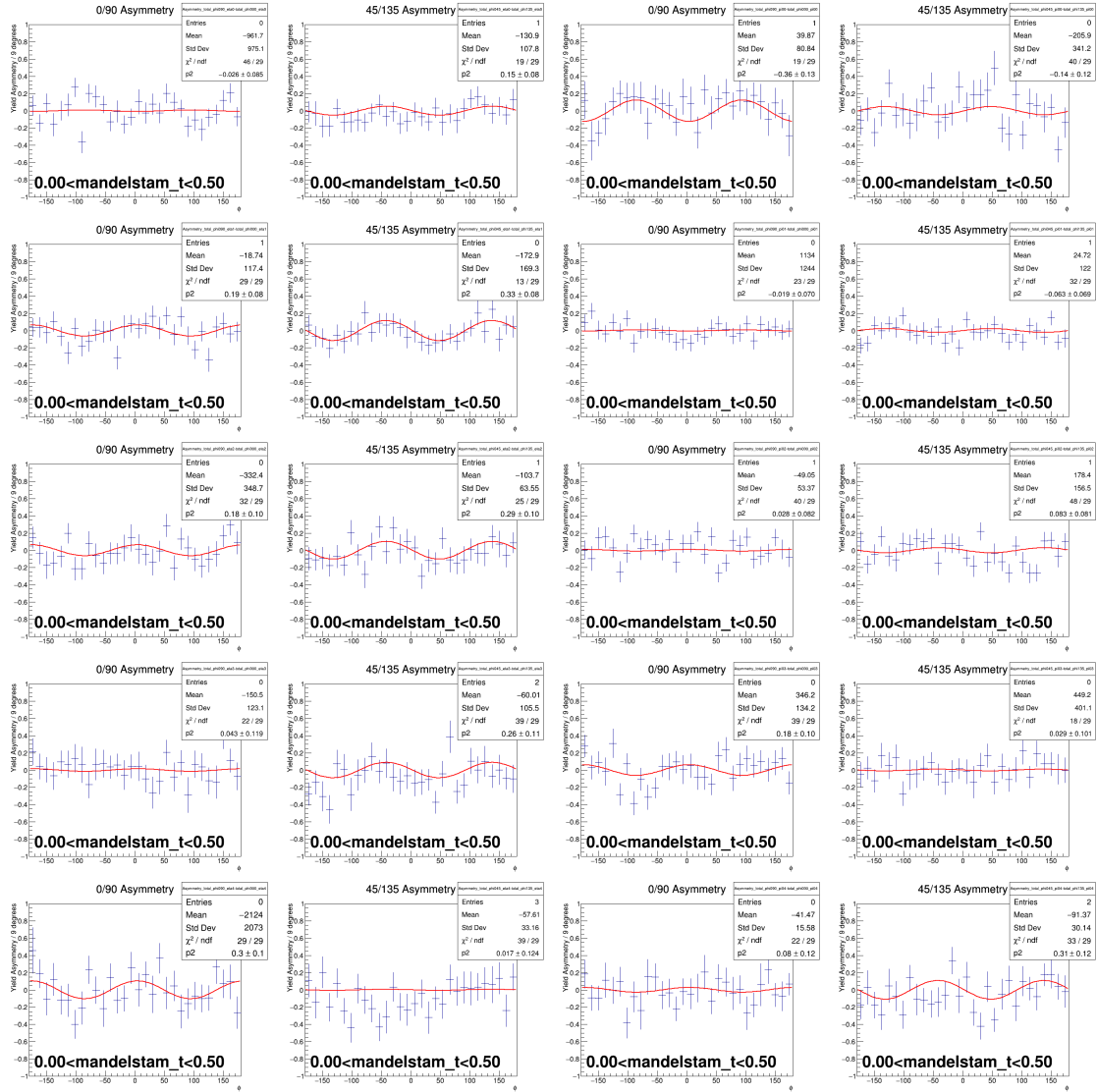
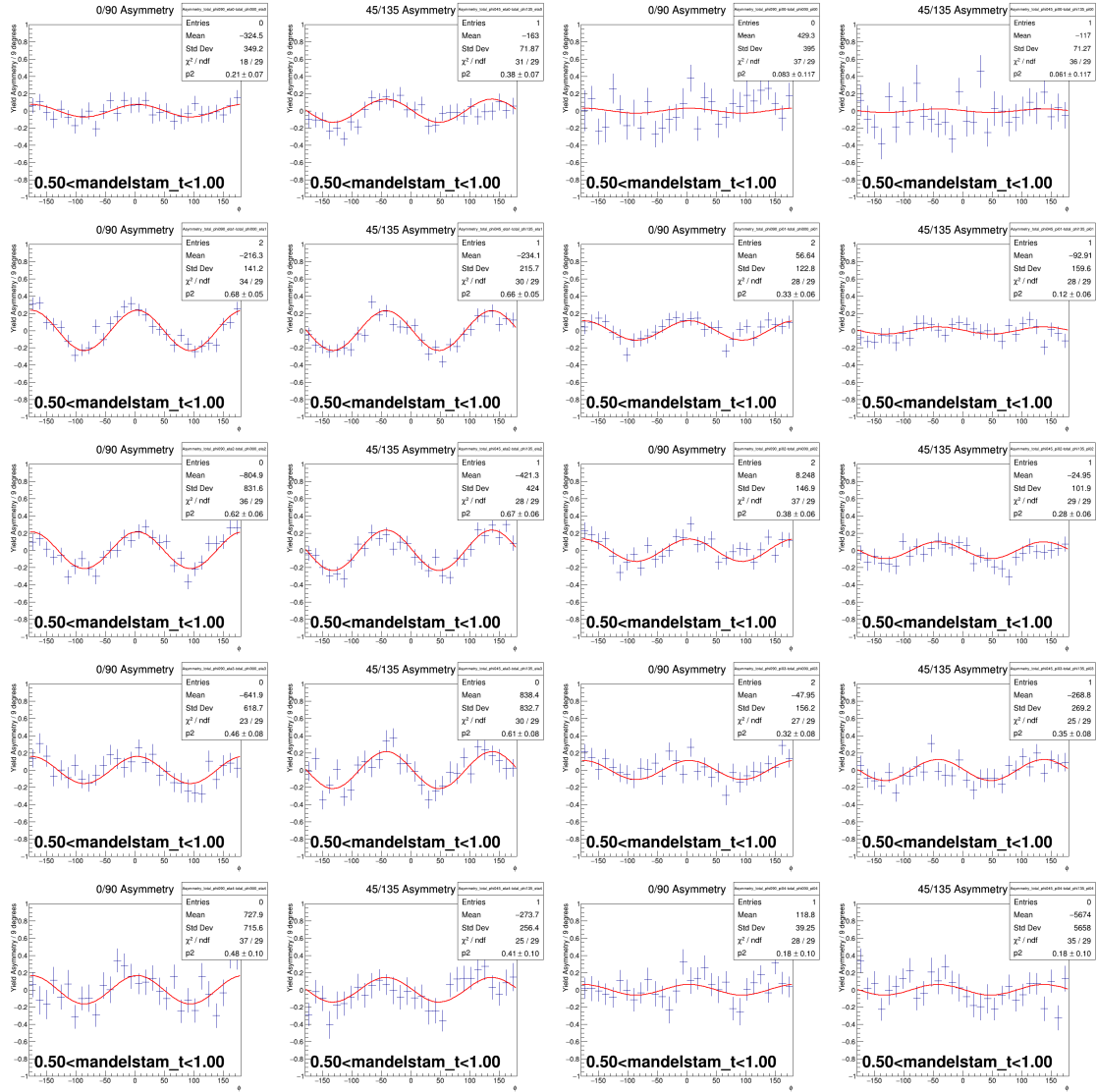Figure C.2: Yield asymmetry fits in $0 < u_3 < 0.5$ GeV^2.

Figure C.3: Yield asymmetry fits in $0.5 < u_3 < 1.0$ GeV^2.
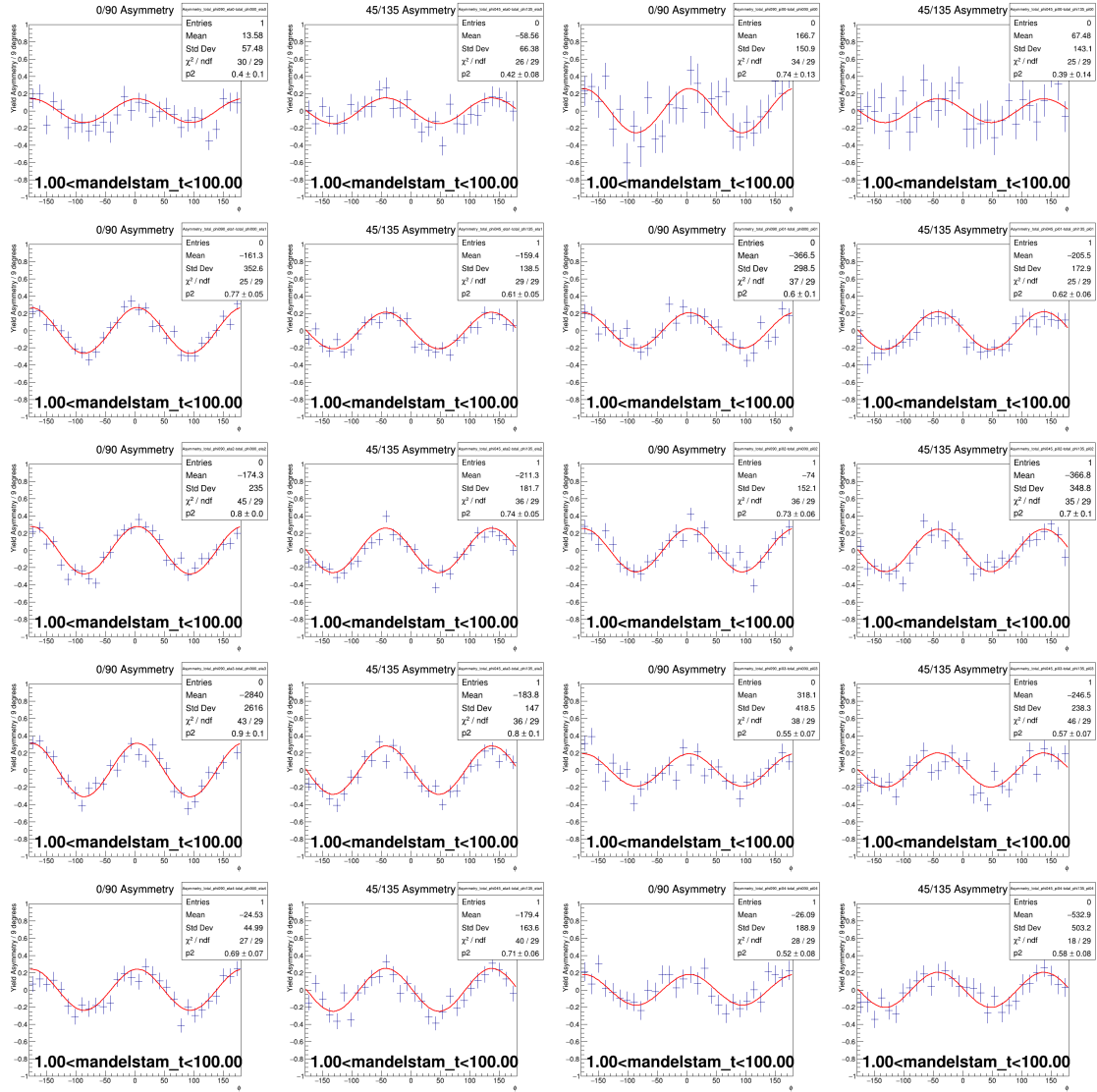
Figure C.4: Yield asymmetry fits in $1.0 < u_3$ GeV^2.
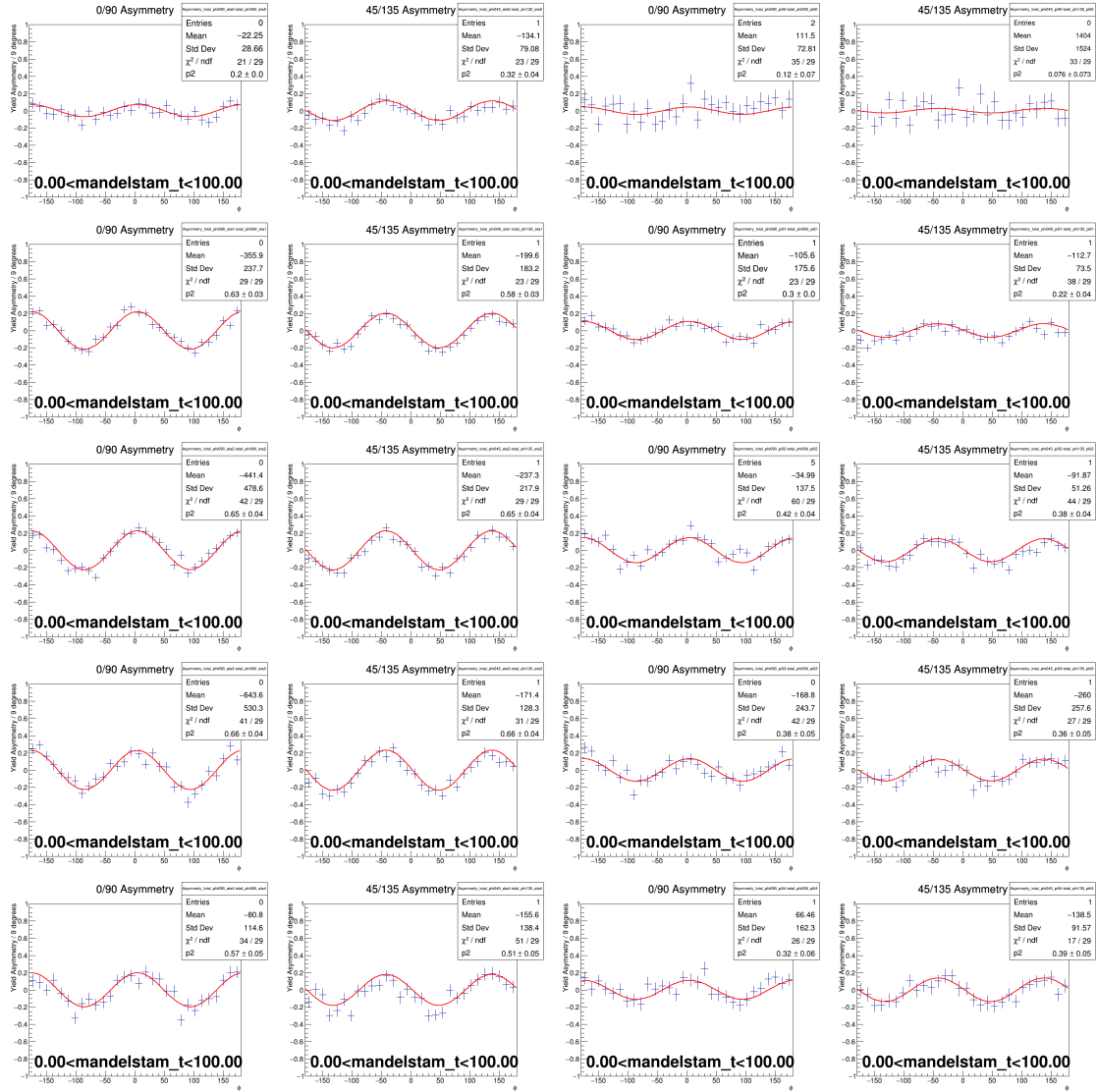
Figure C.5: Yield asymmetry fits in $0 < u_3$ GeV^2.
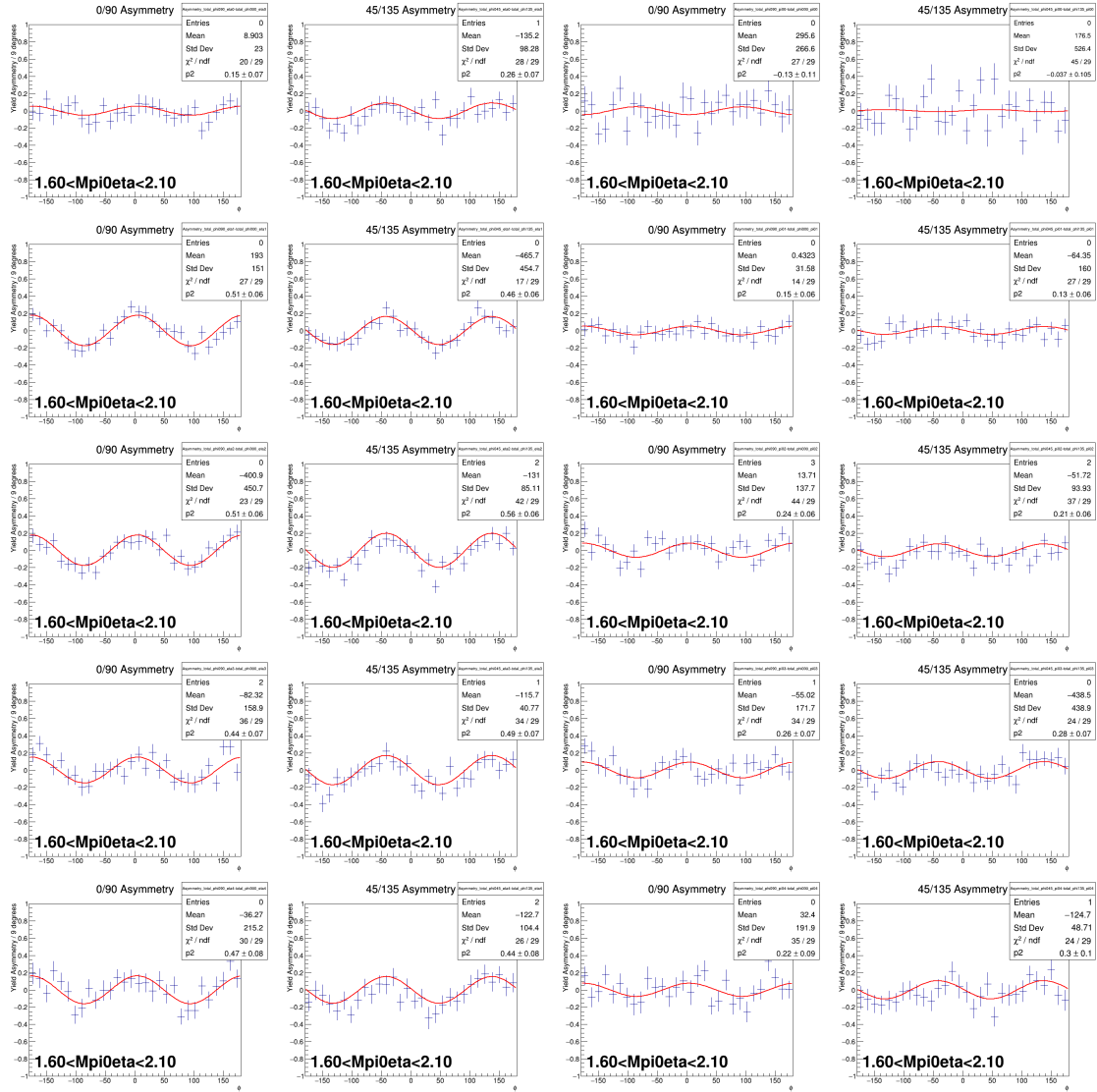
Figure C.6: Yield asymmetry fits in $1.6 < s_{12} < 2.1$ GeV.
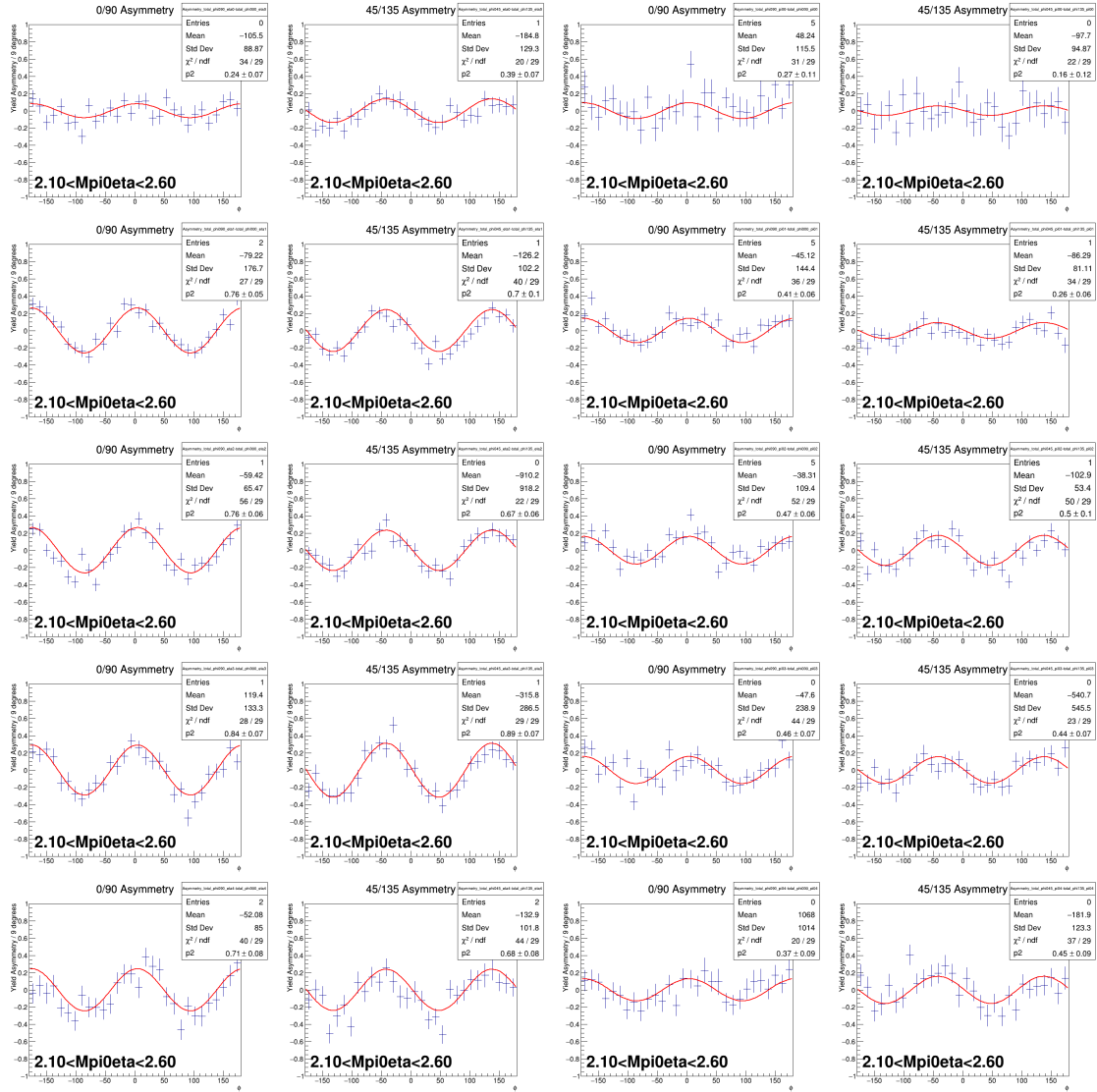
Figure C.7: Yield asymmetry fits in $2.1 < s_{12} < 2.6$ GeV.
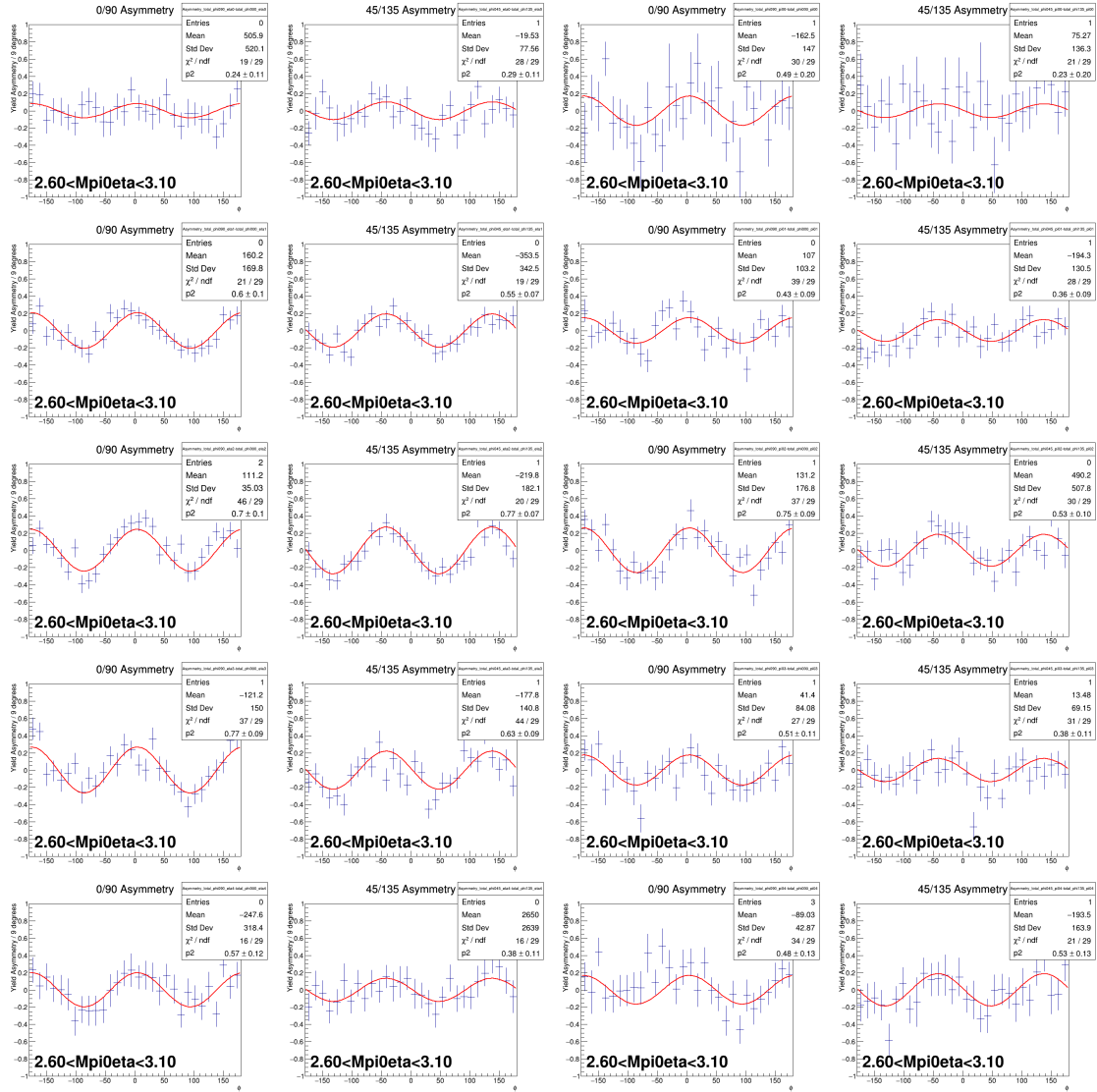
Figure C.8: Yield asymmetry fits in $2.6 < s_{12} < 3.1$ GeV.
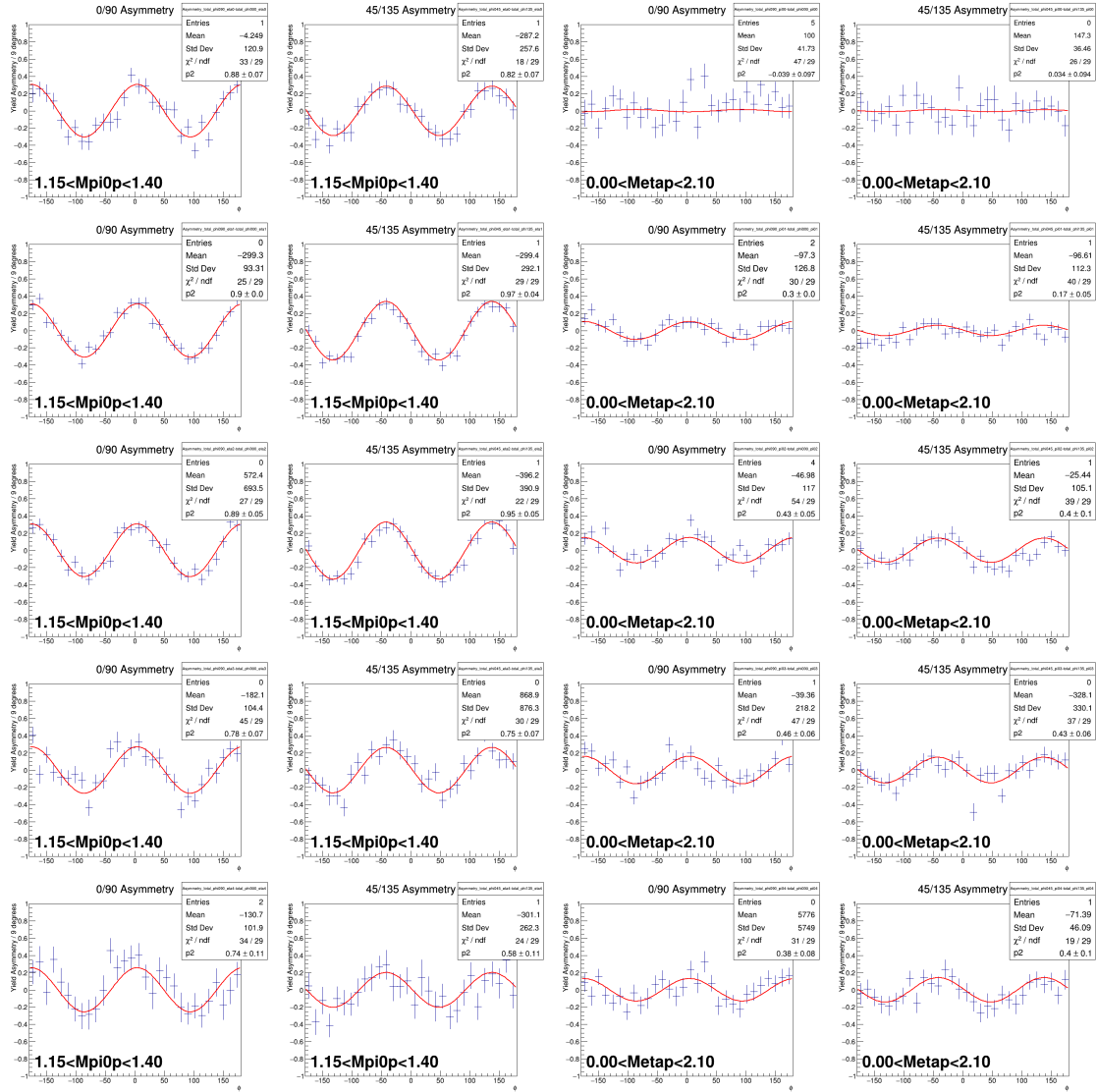
Figure C.9: Yield asymmetry fits in $s_{\eta p} < 2.1$ GeV and $1.15 < s_{\pi p} < 1.4$ GeV.
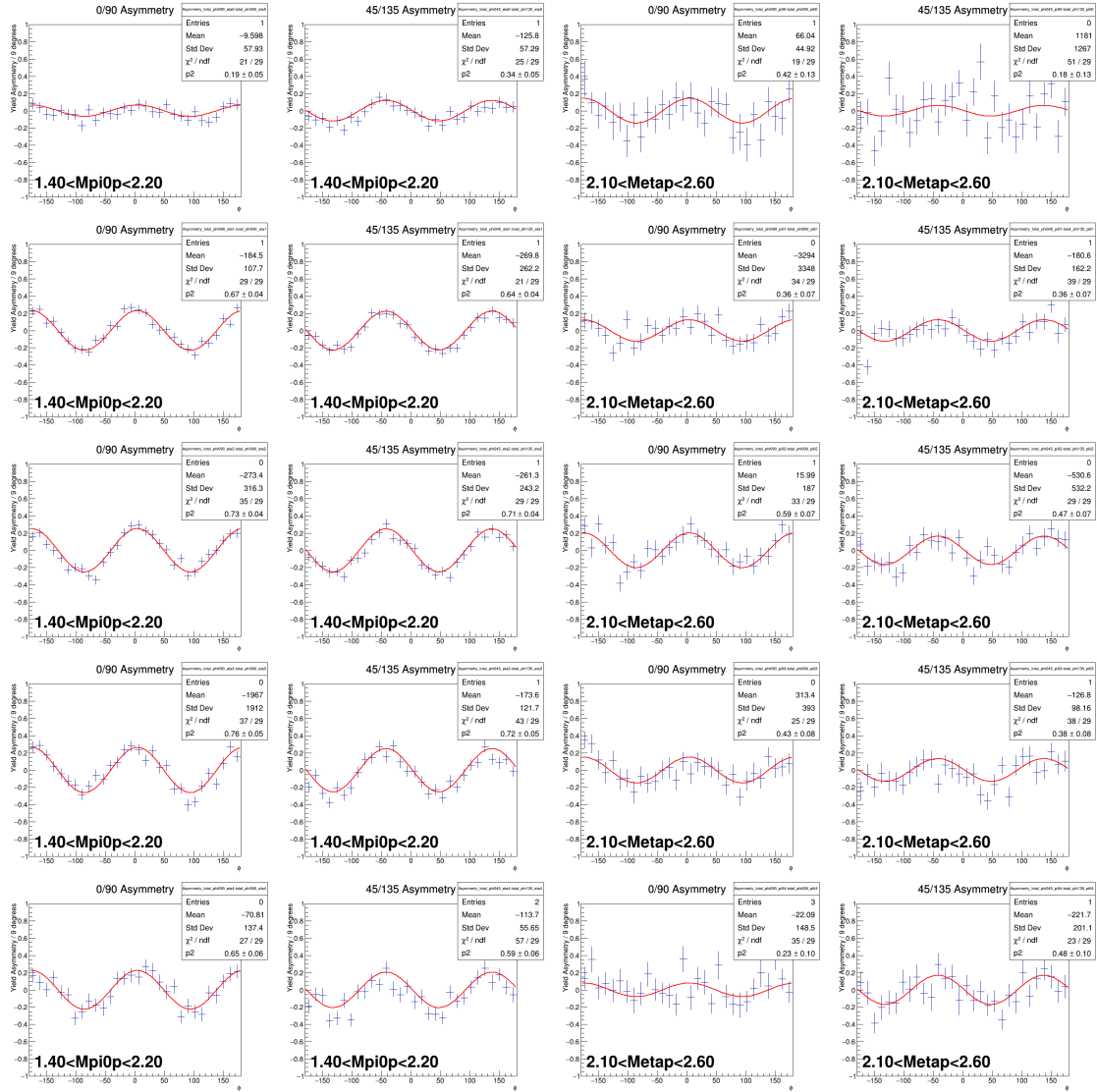
Figure C.10: Yield asymmetry fits in $2.1 < s_{\eta p} < 2.6$ GeV and $1.4 < s_{\pi p} < 2.2$ GeV.
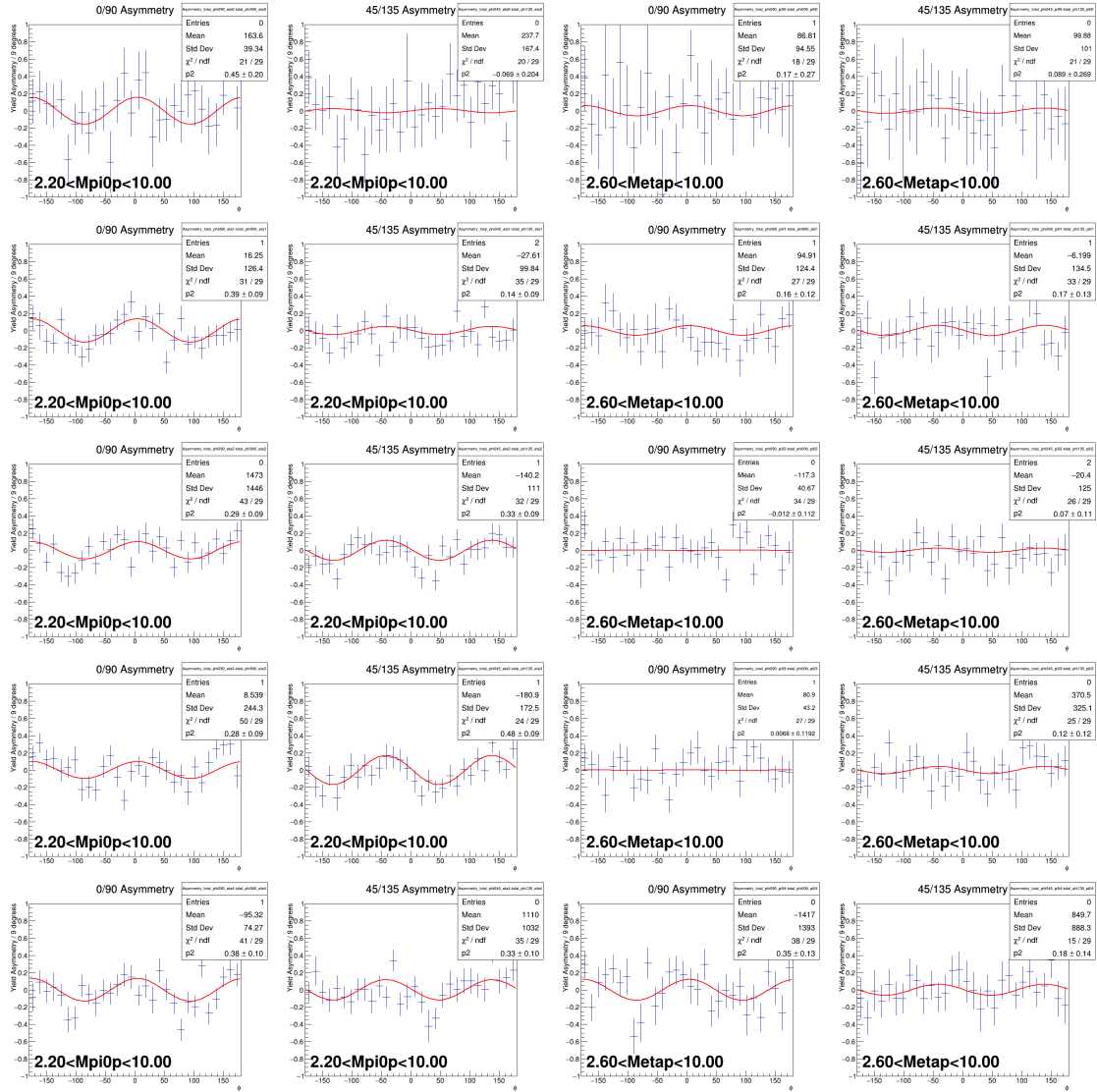
Figure C.11: Yield asymmetry fits in $2.2 < s_{\eta p}$ GeV and $2.2 < s_{\pi p} < 1.4$ GeV.

C.3   Consistency of Datasets

C.3.1   Consistency Between Paired Orientations - Additional Kinematic Bins

Figures C.12, C.13,C.14,C.15 shows the measured Σ as a function of t_1 in bins of various kinematic variables for both 0/90 and 45/-45 polarization orientation pairs. It can be seen that Σ measured with 0/90 and 45/-45 degree polarization pairs mostly agree with each other.

C.3.2   Consistency Between Run Periods

Figures C.16, C.17, C.18,C.19 shows the measured Σ as a function of t_1 in bins of various kinematic variables for both 0/90 and 45/-45 polarization orientation pairs for the three different run periods.
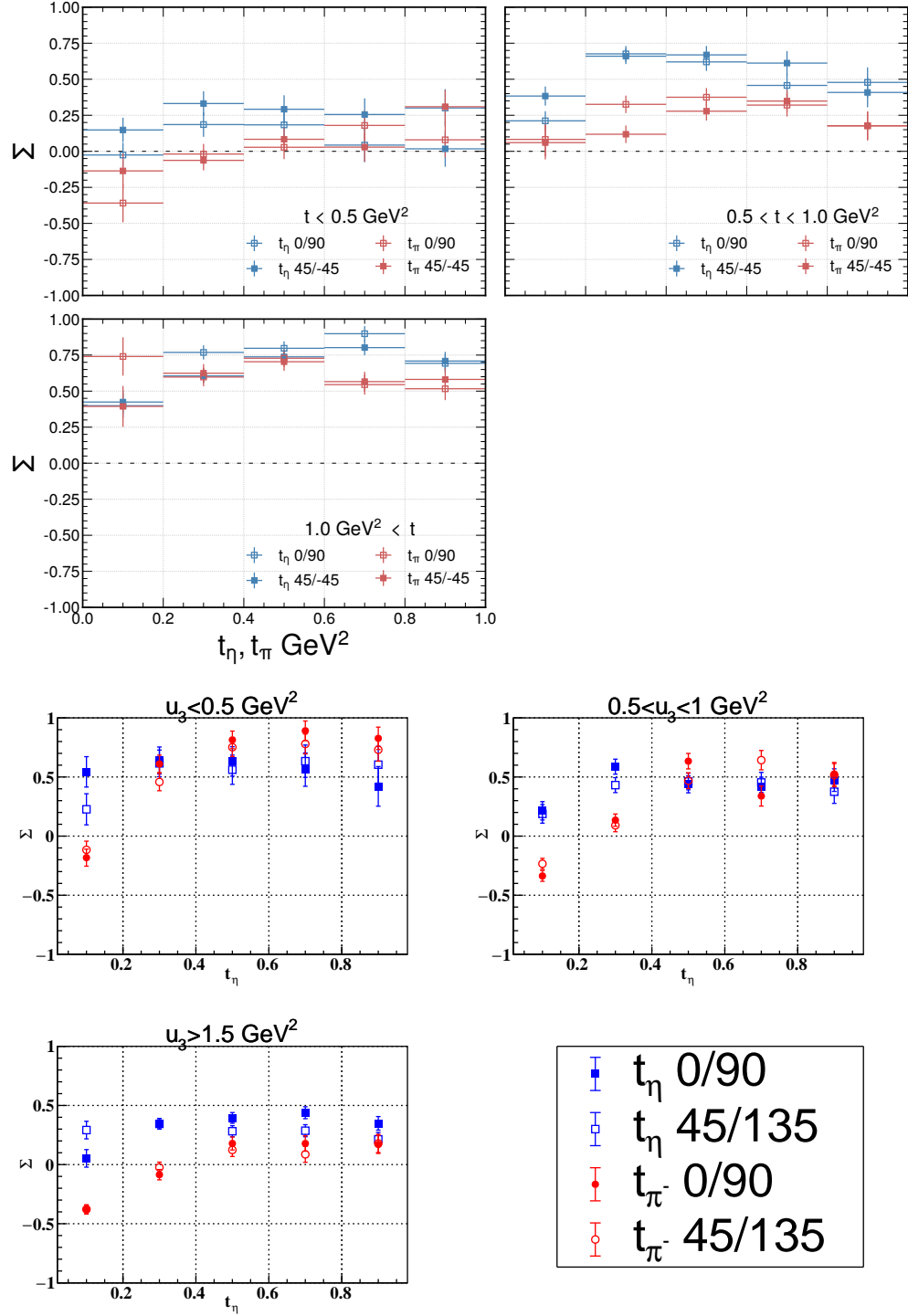
Figure C.12: Σ measured in five bins of t_η and t_π with an additional 3 bins in u_3. A measurement is made for each pair of polarization orientations. Integrated over s_{12}, and s_{23}.
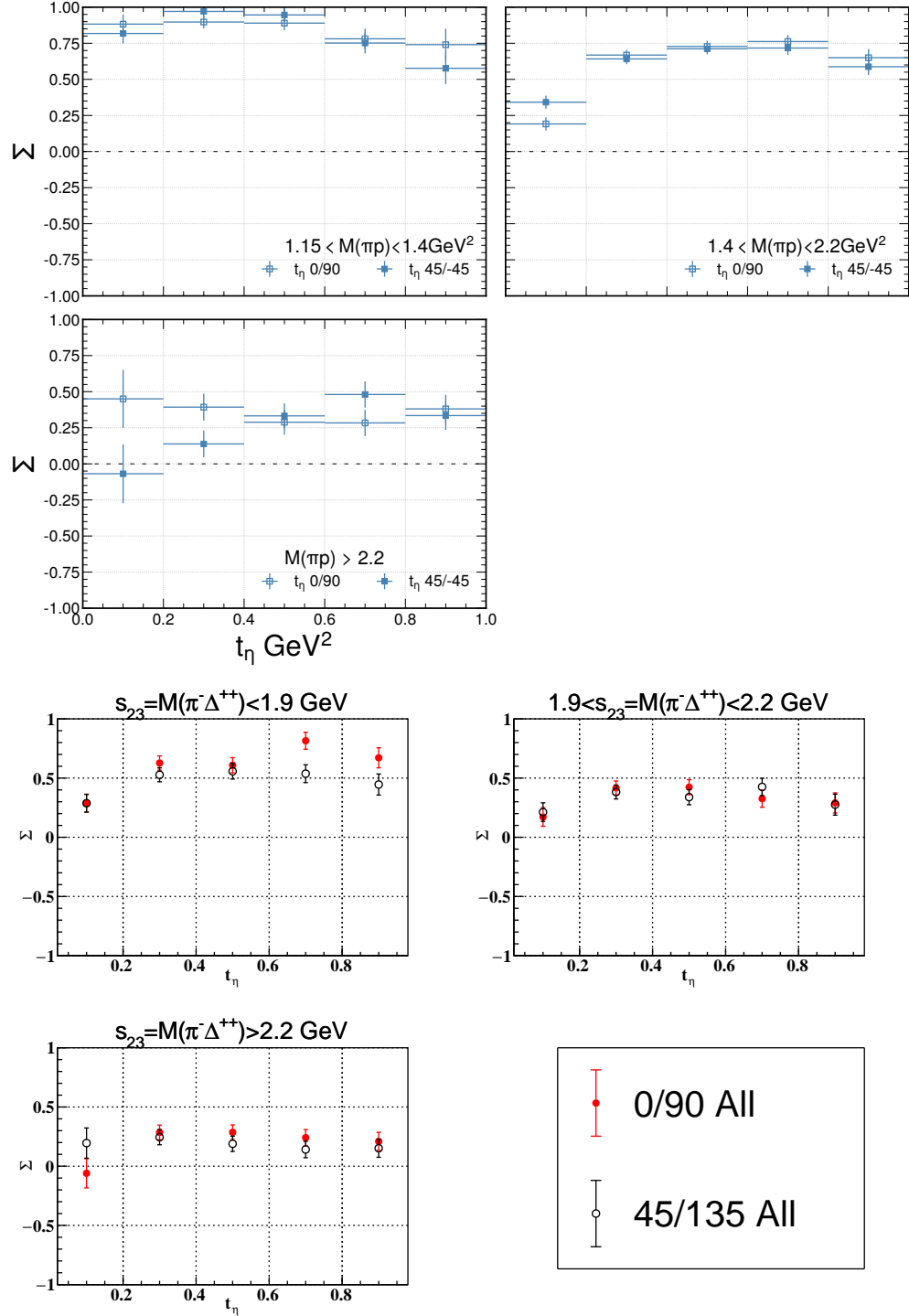
Figure C.13: Σ measured in five bins of t_η with an additional 3 bins in $s_{23} = M(\pi p)$. A measurement is made for each pair of polarization orientations. Integrated over s_{12}, and u_3. (Top) Measurements made from the $\eta\pi^0$ channel. (Bottom) Measurements made from the $\eta\pi^-$ channel.

Figure C.14: Σ measured in five bins of t_π with an additional 3 bins in $s_{23} = M(\eta p)$. A measurement is made for each pair of polarization orientations. Integrated over s_{12}, and u_3. (Top) Measurements made from the $\eta\pi^0$ channel. (Bottom) Measurements made from the $\eta\pi^-$ channel.
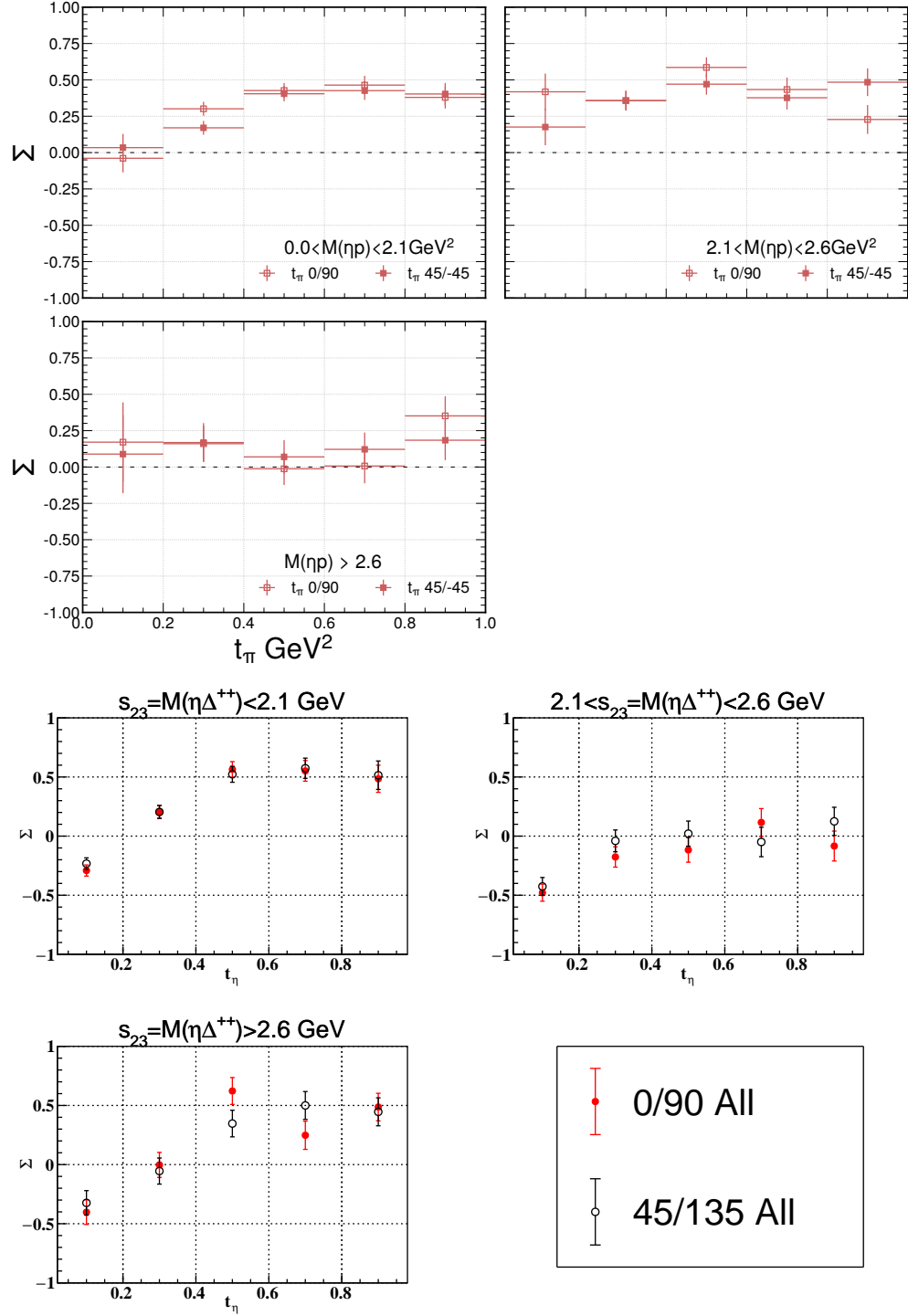
223

Figure C.15: Σ measured in five bins of t_η, t_π with additional binning in s_{12}. A measurement is made for each pair of polarization orientations. Integrated over s_{23}, and u_3. (Top) Measurements made from the $\eta\pi^0$ channel. (Bottom) Measurements made from the $\eta\pi^-$ channel.
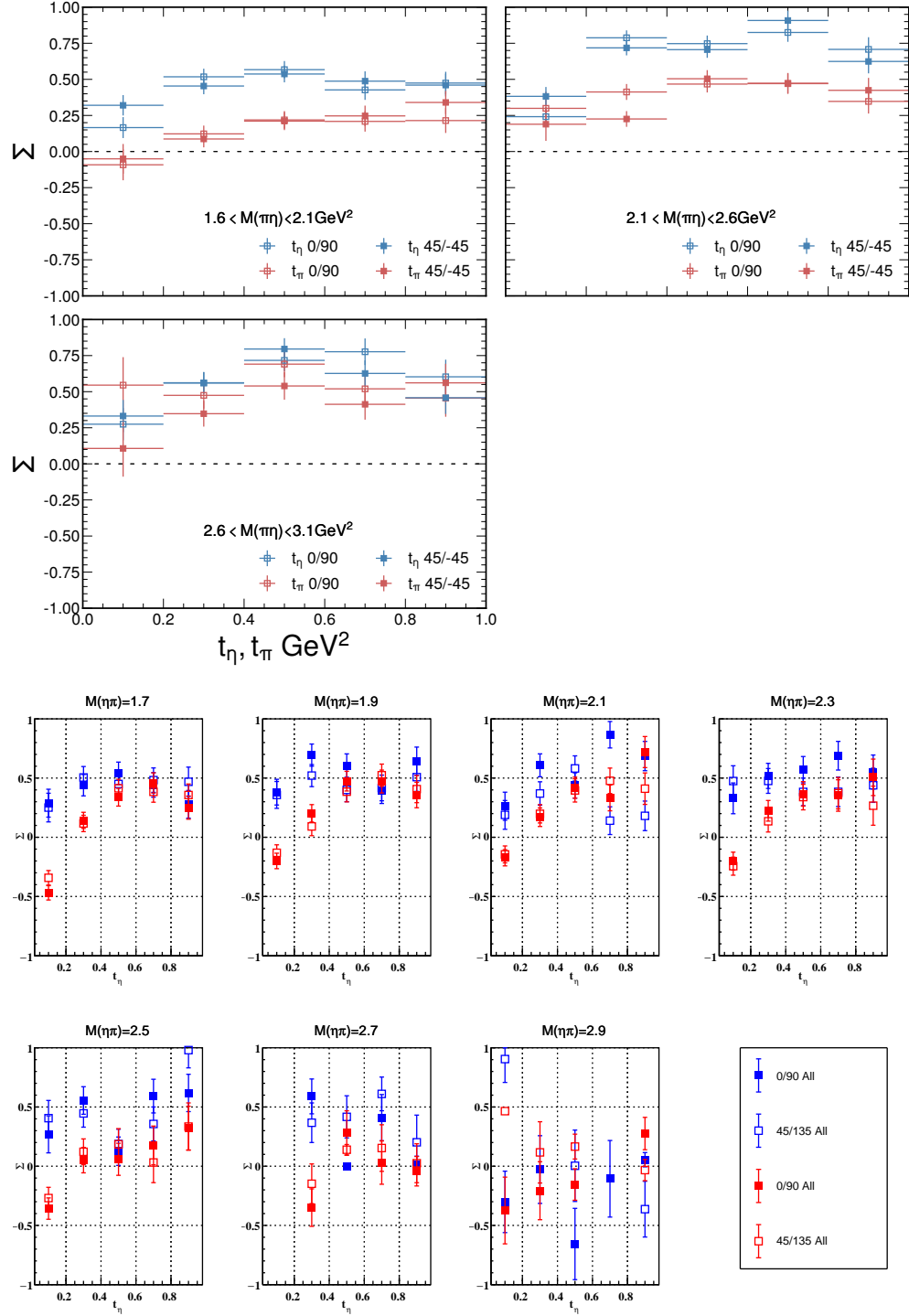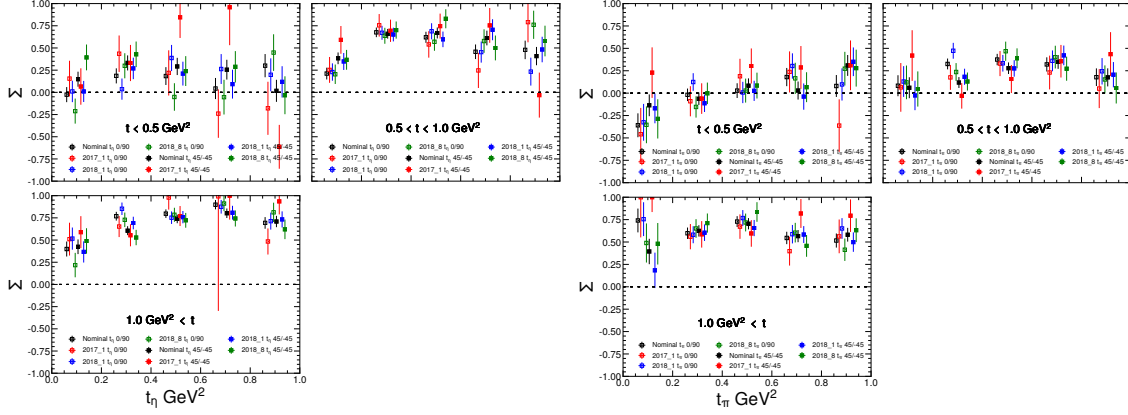
Figure C.16: Run dependent measurements of Σ for (Left) t_η, (Right) t_π measured in five bins. Additionally binned in u_3.
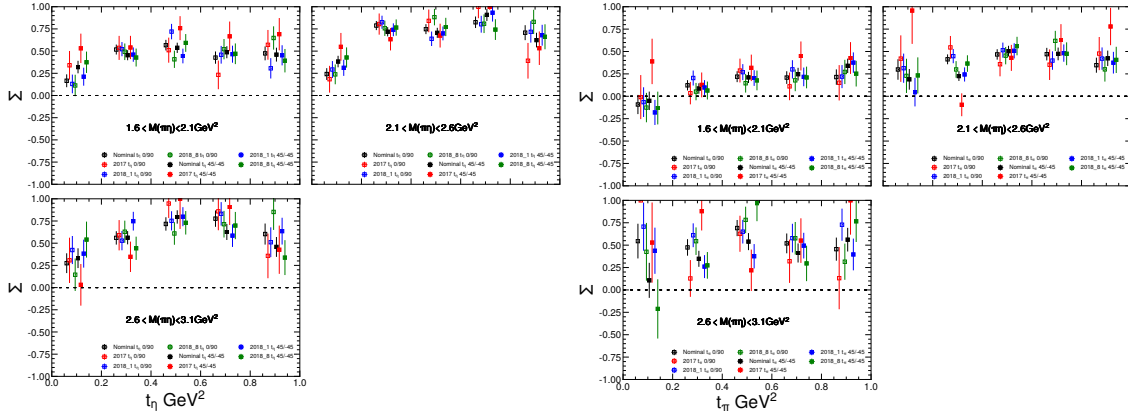

Figure C.17: Run dependent measurements of Σ for (Left) t_η, (Right) t_π measured in five bins. Additionally binned in s_{12}.
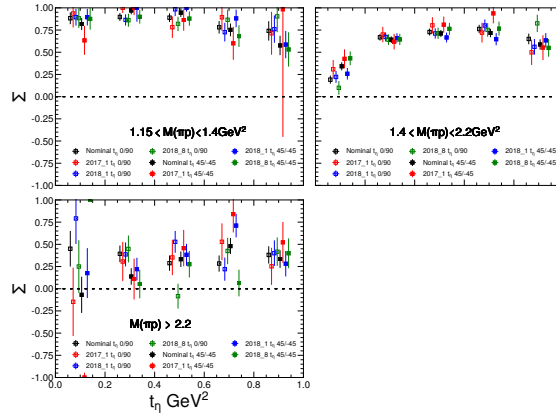

Figure C.18: Run dependent measurements of Σ for (Left) t_η, (Right) t_π measured in five bins. Additionally binned in $M(\pi^0 p)$.
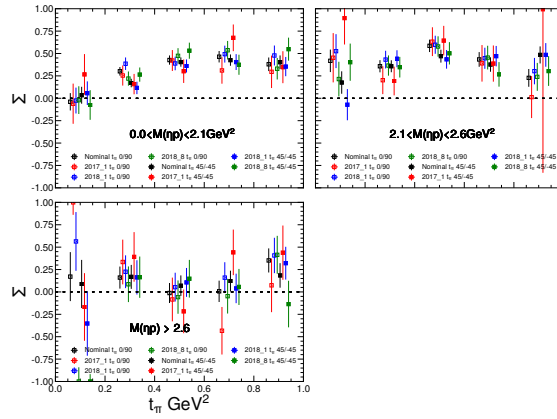
225

Figure C.19: Run dependent measurements of Σ for (Left) t_η, (Right) t_π measured in five bins. Additionally binned in $M(\eta p)$.

C.3.3 Consistency Between $M(\eta)$ halves

Figures C.16,C.17, C.18,C.19 shows the measured Σ as a function of t_1 in bins of various kinematic variables for both 0/90 and 45/-45 polarization orientation pairs for the three different run periods.

Figure C.20: Systematic differences in Σ due to variations of $M(\eta)$ split halves for (Left) t_η, (Right) t_π are measured in five bins. Binned in u_3. (Top) Asymmetries from 0/90 pair. (Bot) Asymmetries from 45/-45 pair. Red is the nominal results, black points are from different variations of event selections.

Figure C.21: Systematic differences in Σ due to variations of $M(\eta)$ split halves for (Left) t_η, (Right) t_π are measured in five bins. Binned in s_{12}. (Top) Asymmetries from 0/90 pair. (Bot) Asymmetries from 45/-45 pair. Red is the nominal results, black points are from different variations of event selections.
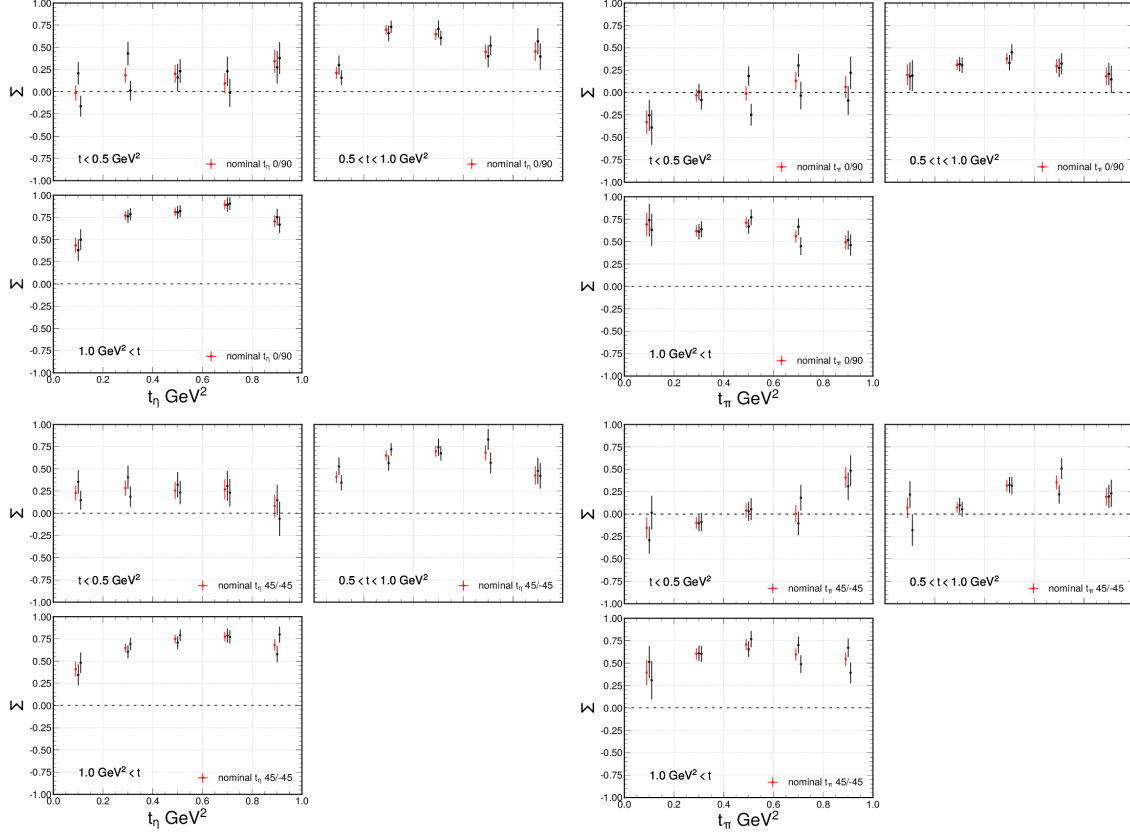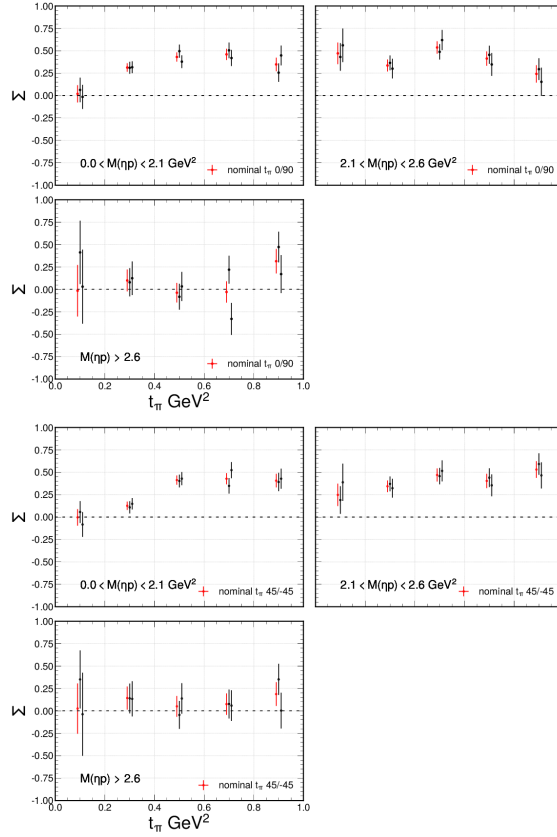
Figure C.22: Systematic differences in Σ due to variations of $M(\eta)$ split halves for t_π are measured in five bins. Binned in $M(\eta p)$. (Top) Asymmetries from 0/90 pair. (Bot) Asymmetries from 45/-45 pair. Red is the nominal results, black points are from different variations of event selections.
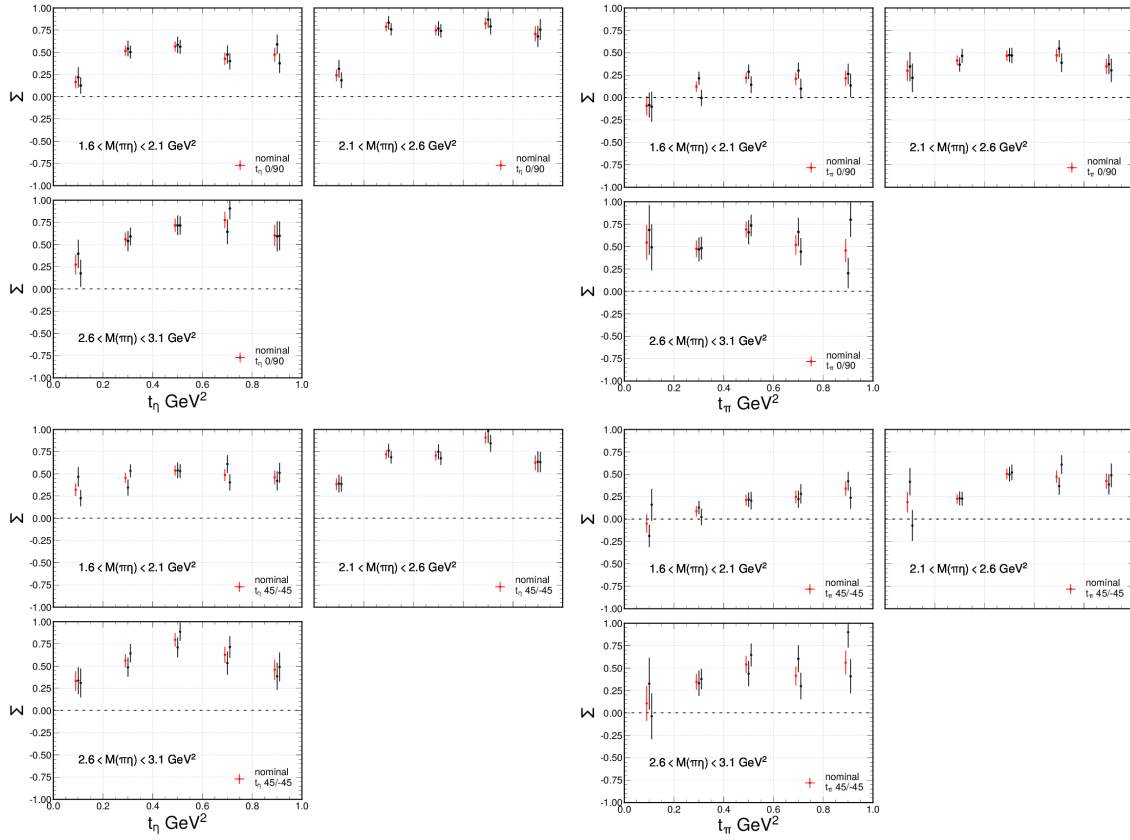
Figure C.23: Systematic differences in Σ due to variations of $M(\eta)$ split halves for t_η are measured in five bins. Binned in $M(\pi^0 p)$. (Top) Asymmetries from 0/90 pair. (Bot) Asymmetries from 45/-45 pair. Red is the nominal results, black points are from different variations of event selections.

C.4   Measurement of Systematic Uncertainties - Additional Kinematic Bins

C.4.1   Event Selection Systematics

Figure C.24: Systematic differences in Σ due to variations of the event selection for t_η are measured in five bins. Binned in $M(\pi^0 p)$. (Top) Asymmetries from 0/90 pair. (Bot) Asymmetries from 45/-45 pair. Red is the nominal results, black points are from different variations of event selections.
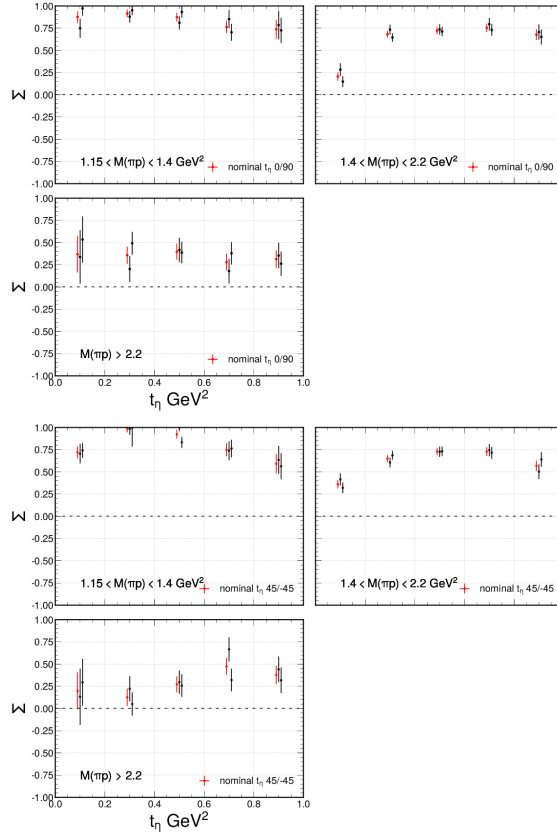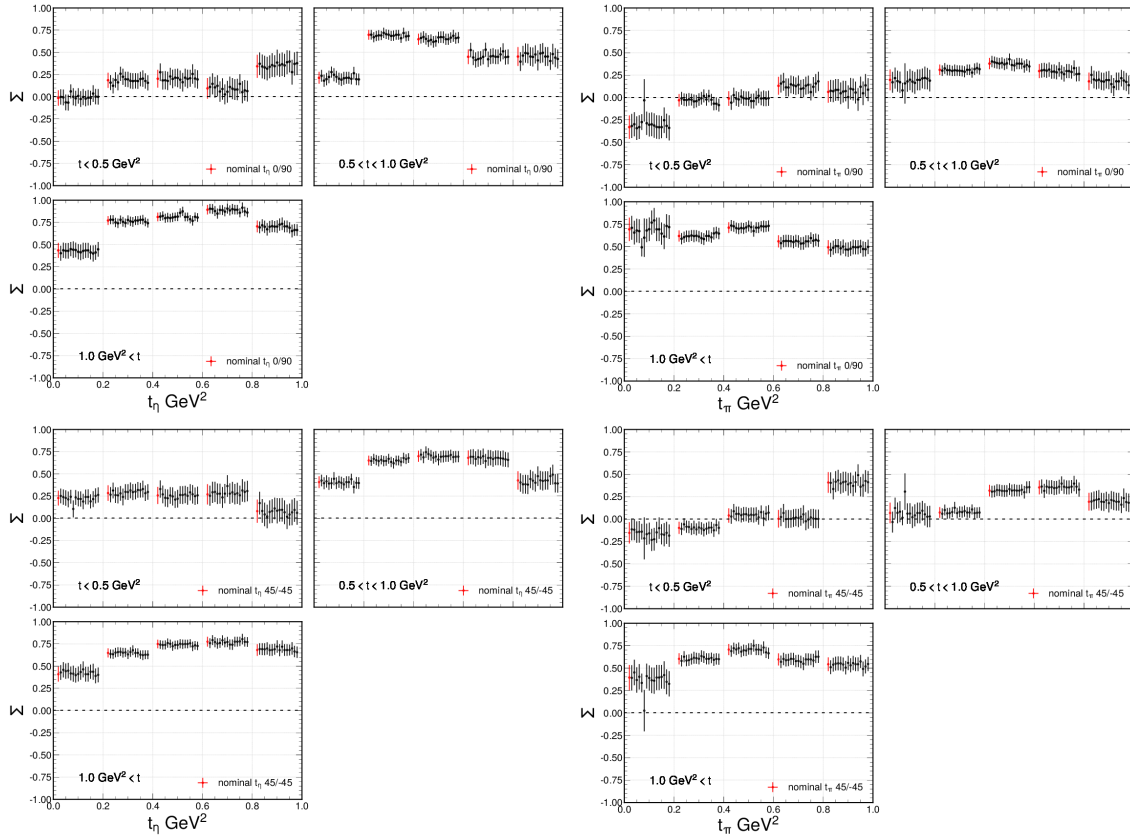
Figure C.25: Systematic differences in Σ due to variations of the event selection for (Left) t_η, (Right) t_π are measured in five bins. Binned in u_3. (Top) Asymmetries from 0/90 pair. (Bot) Asymmetries from 45/-45 pair. Red is the nominal results, black points are from different variations of event selections.

Figure C.26: Systematic differences in Σ due to variations of the event selection for (Left) t_η, (Right) t_π are measured in five bins. Binned in s_{12}. (Top) Asymmetries from 0/90 pair. (Bot) Asymmetries from 45/-45 pair. Red is the nominal results, black points are from different variations of event selections.
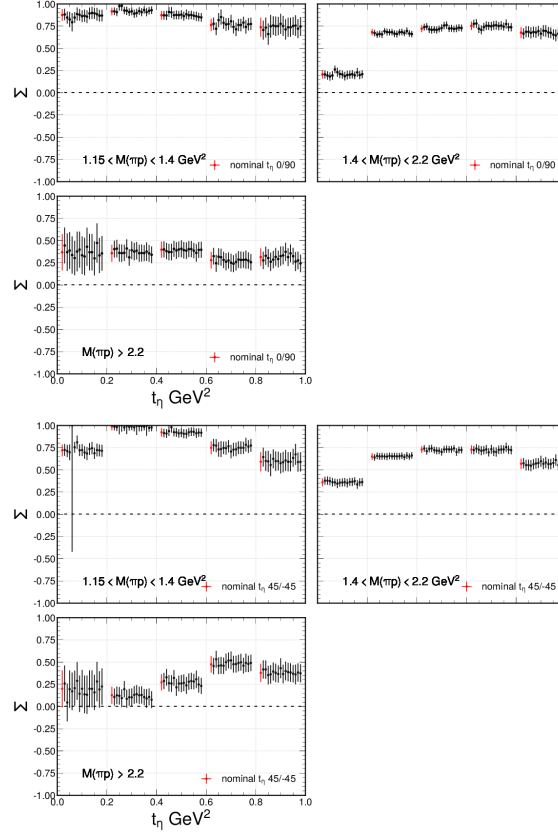
Figure C.27: Systematic differences in Σ due to variations of the event selection for t_π are measured in five bins. Binned in $M(\eta p)$. (Top) Asymmetries from 0/90 pair. (Bot) Asymmetries from 45/-45 pair. Red is the nominal results, black points are from different variations of event selections.

C.4.2 Freed phase offset systematics

Figure C.28: Systematic differences in Σ due to variations with freed phase offset for t_η are measured in five bins. Binned in $M(\pi^0 p)$. (Top) Asymmetries from 0/90 pair. (Bot) Asymmetries from 45/-45 pair. Red is the nominal results, black points are from different variations of event selections.
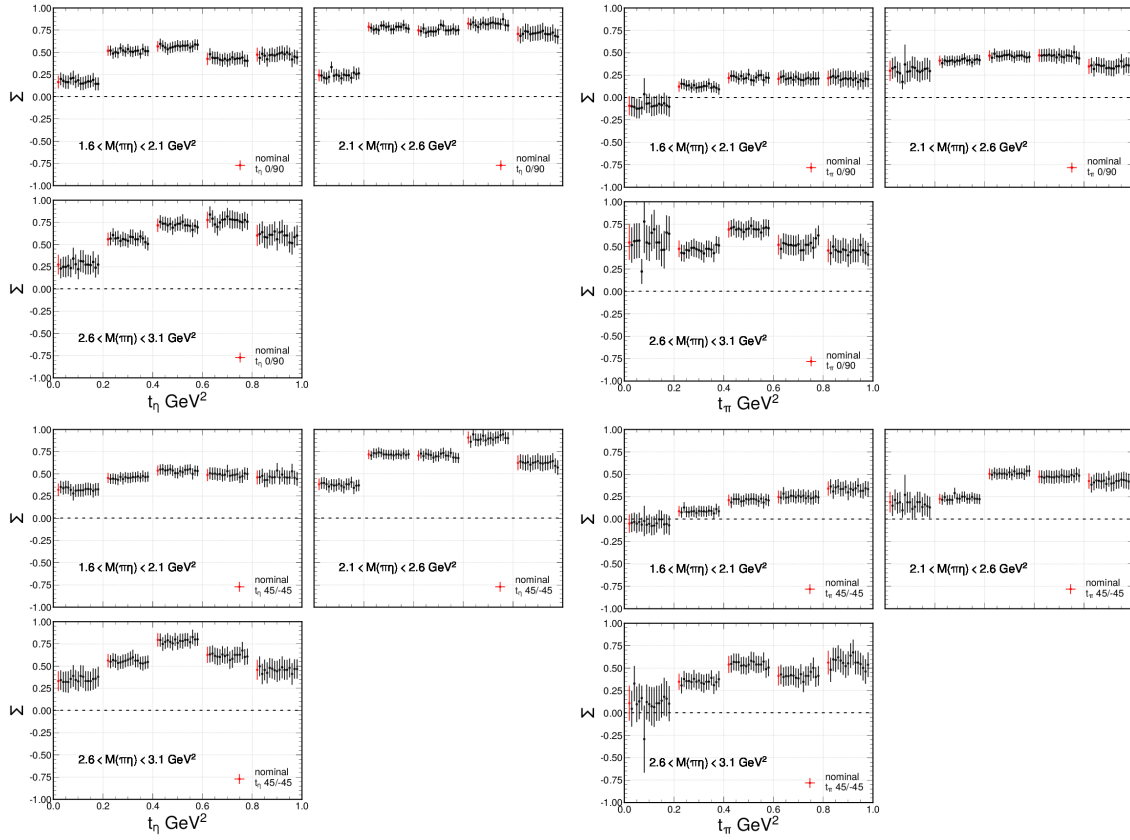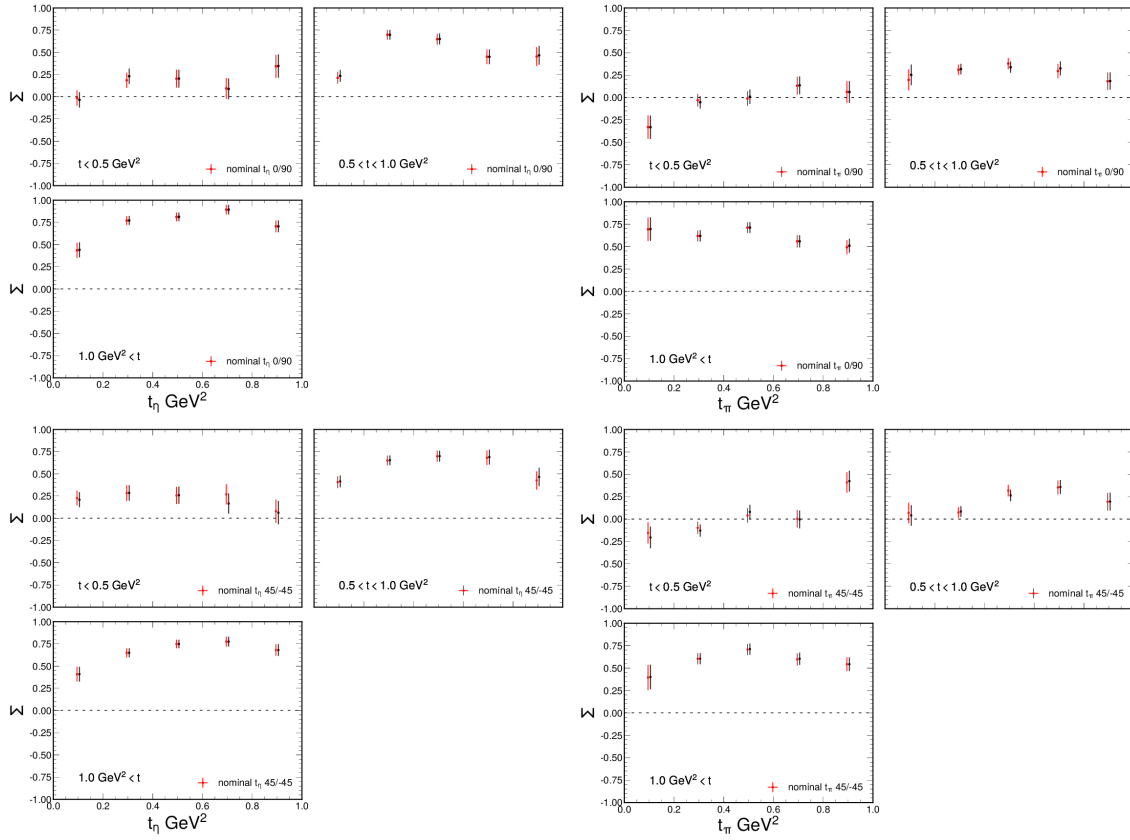
Figure C.29: Systematic differences in Σ due to variations with freed phase offset for (Left) t_η, (Right) t_π are measured in five bins. Binned in u_3. (Top) Asymmetries from 0/90 pair. (Bot) Asymmetries from 45/-45 pair. Red is the nominal results, black points are from different variations of event selections.
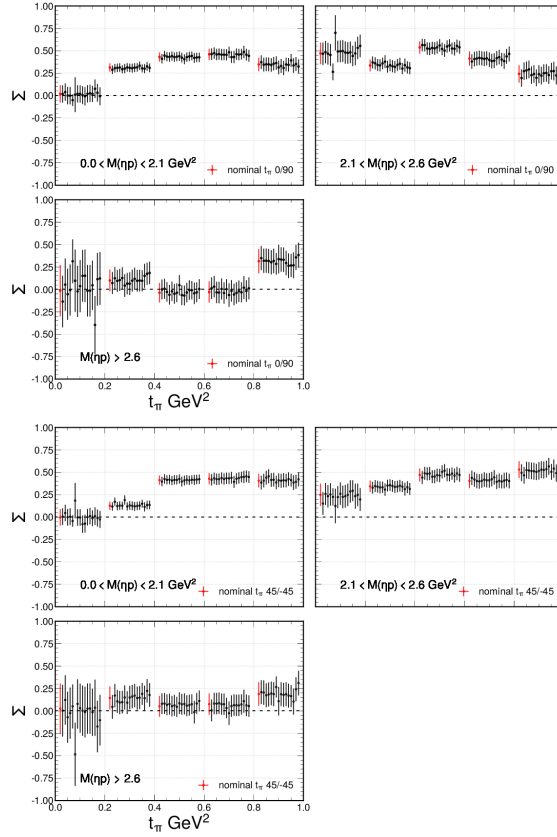
Figure C.30: Systematic differences in Σ due to variations with freed phase offset for (Left) t_η, (Right) t_π are measured in five bins. Binned in s_{12}. (Top) Asymmetries from 0/90 pair. (Bot) Asymmetries from 45/-45 pair. Red is the nominal results, black points are from different variations of event selections.
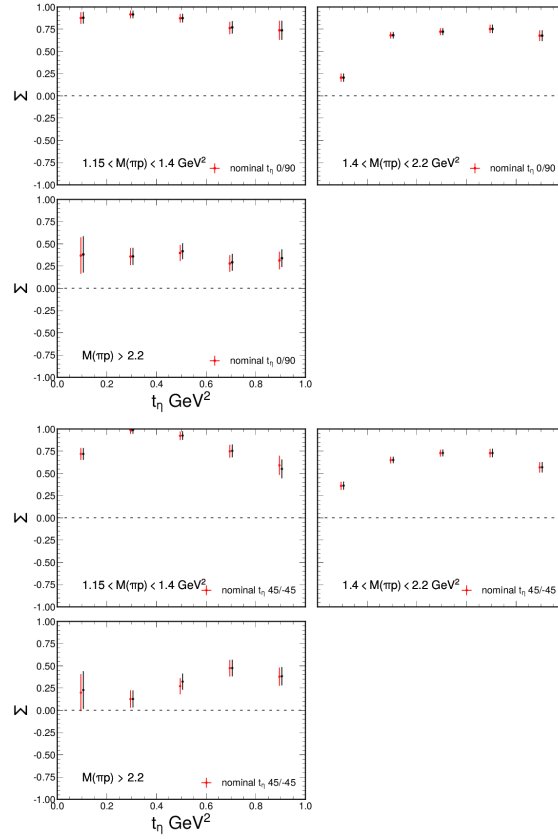
Figure C.31: Systematic differences in Σ due to variations with freed phase offset for t_π are measured in five bins. Binned in $M(\eta p)$. (Top) Asymmetries from 0/90 pair. (Bot) Asymmetries from 45/-45 pair. Red is the nominal results, black points are from different variations of event selections.

C.4.3   Flux Normalization systematics
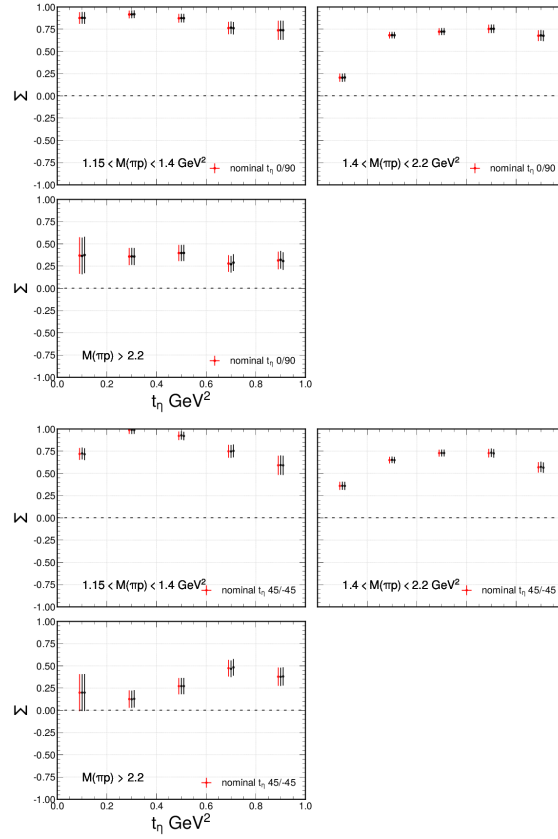
Figure C.32: Systematic differences in Σ due to variations of $+/\text{-}5\%$ flux normalization for t_η are measured in five bins. Binned in $M(\pi^0 p)$. (Top) Asymmetries from 0/90 pair. (Bot) Asymmetries from 45/-45 pair. Red is the nominal results, black points are from different variations of event selections.
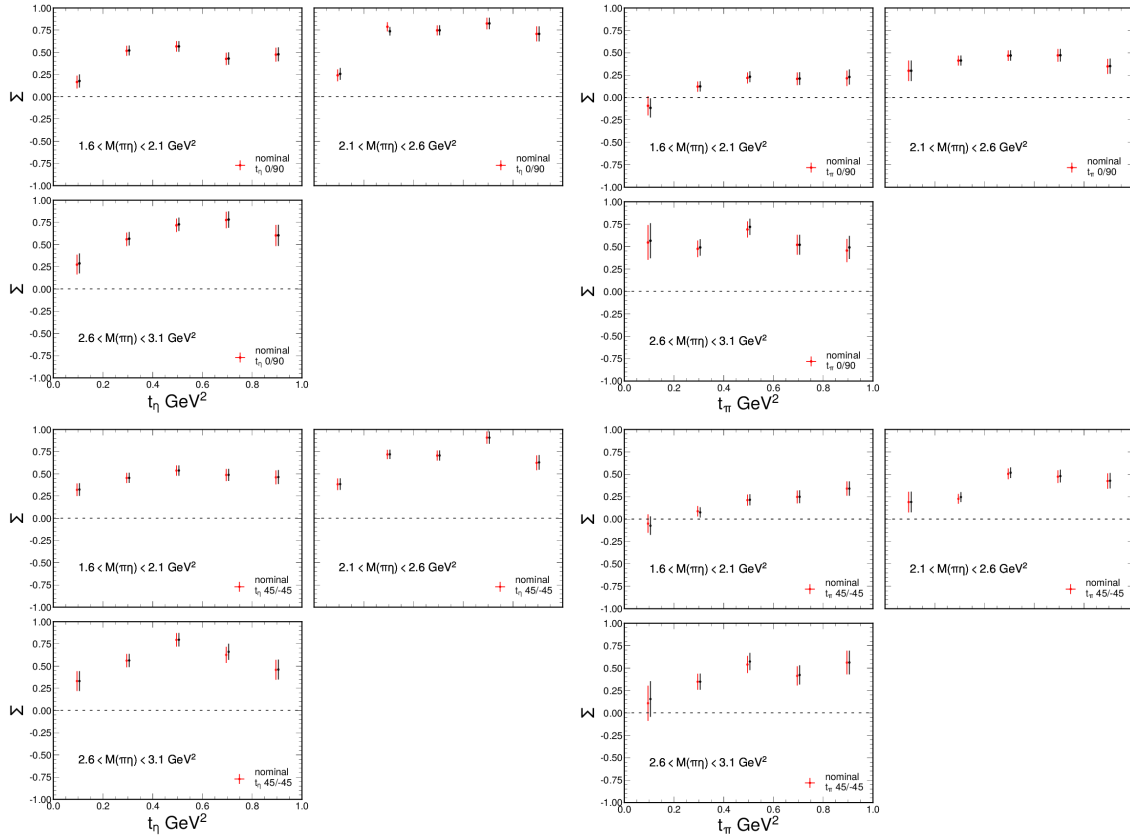
Figure C.33: Systematic differences in Σ due to variations of $+/$-5% flux normalization for (Left) t_η, (Right) t_π are measured in five bins. Binned in u_3. (Top) Asymmetries from 0/90 pair. (Bot) Asymmetries from 45/-45 pair. Red is the nominal results, black points are from different variations of event selections.

Figure C.34: Systematic differences in Σ due to variations of $+/$-5% flux normalization for (Left) t_η, (Right) t_π are measured in five bins. Binned in s_{12}. (Top) Asymmetries from 0/90 pair. (Bot) Asymmetries from 45/-45 pair. Red is the nominal results, black points are from different variations of event selections.
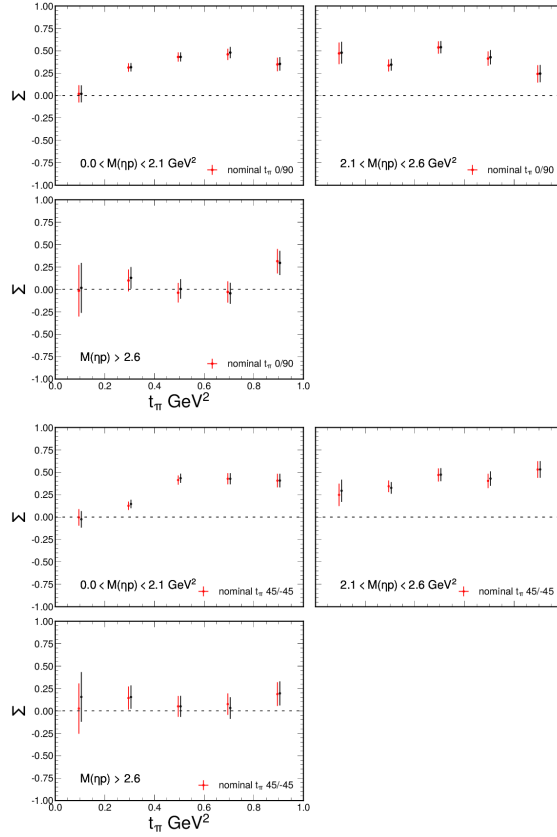
Figure C.35: Systematic differences in Σ due to variations of +/-5% flux normalization for t_π are measured in five bins. Binned in $M(\eta p)$. (Top) Asymmetries from 0/90 pair. (Bot) Asymmetries from 45/-45 pair. Red is the nominal results, black points are from different variations of event selections.

C.4.4   Sideband systematics
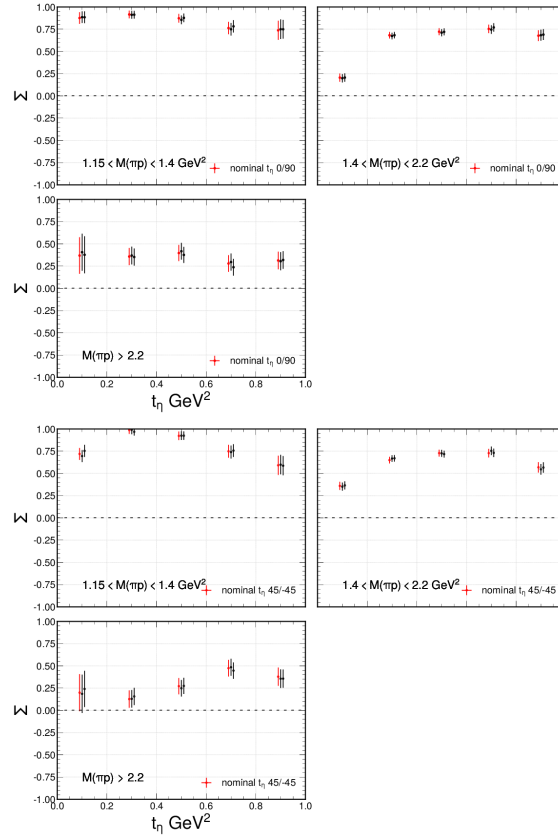
Figure C.36: Systematic differences in Σ due to variations of the sideband subtraction regions for t_η are measured in five bins. Binned in $M(\pi^0 p)$. (Top) Asymmetries from 0/90 pair. (Bot) Asymmetries from 45/-45 pair. Red is the nominal results, black points are from different variations of event selections.
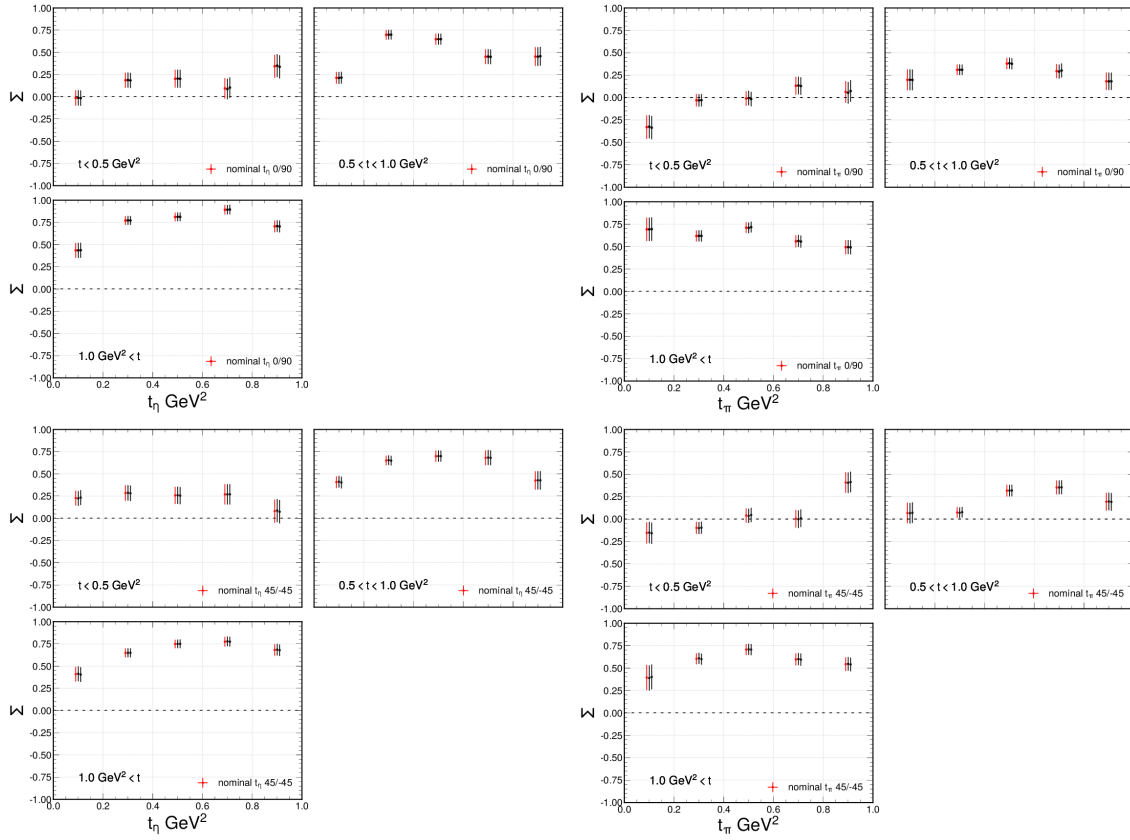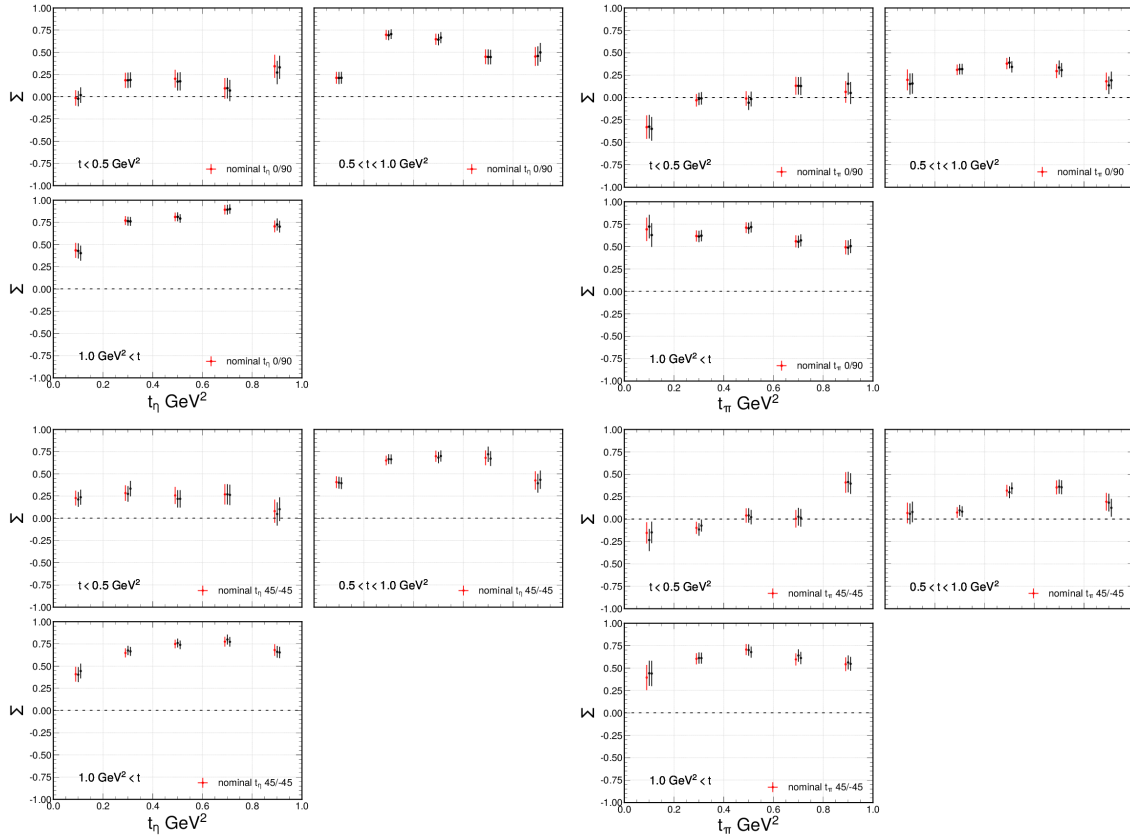
Figure C.37: Systematic differences in Σ due to variations of the sideband subtraction regions for (Left) t_η, (Right) t_π are measured in five bins. Binned in u_3. (Top) Asymmetries from 0/90 pair. (Bot) Asymmetries from 45/-45 pair. Red is the nominal results, black points are from different variations of event selections.
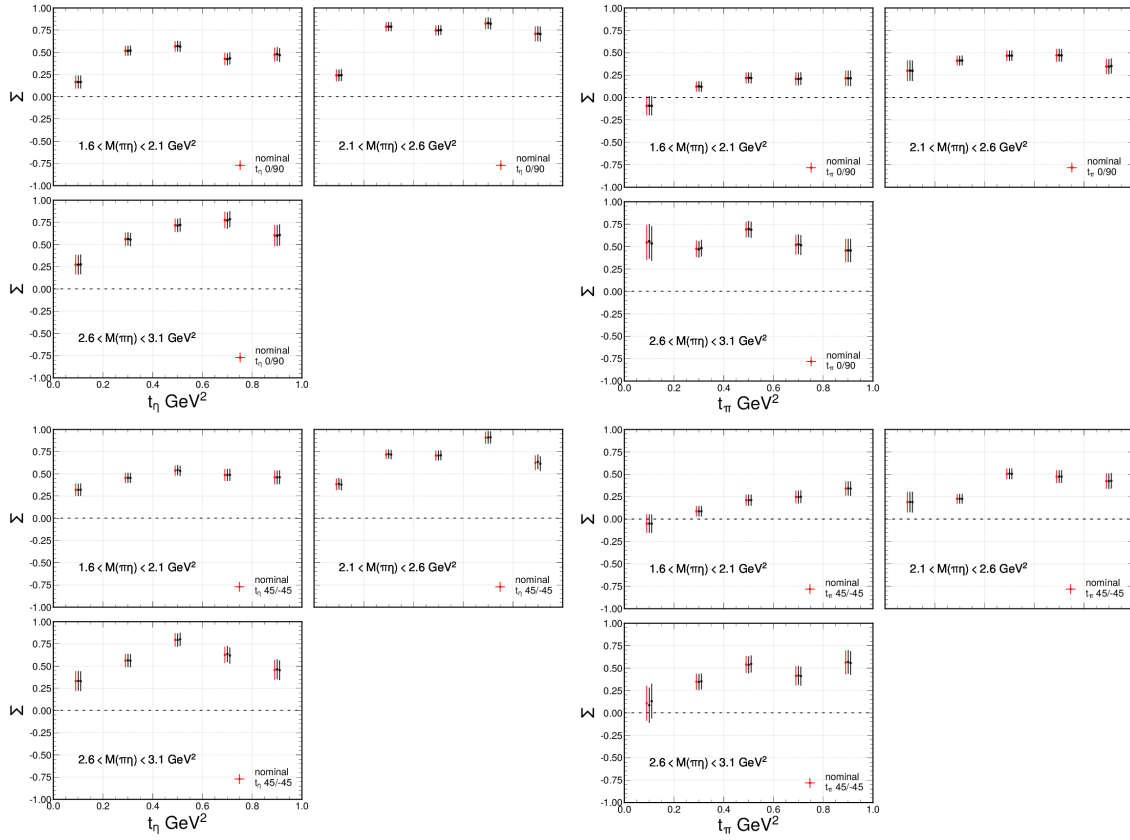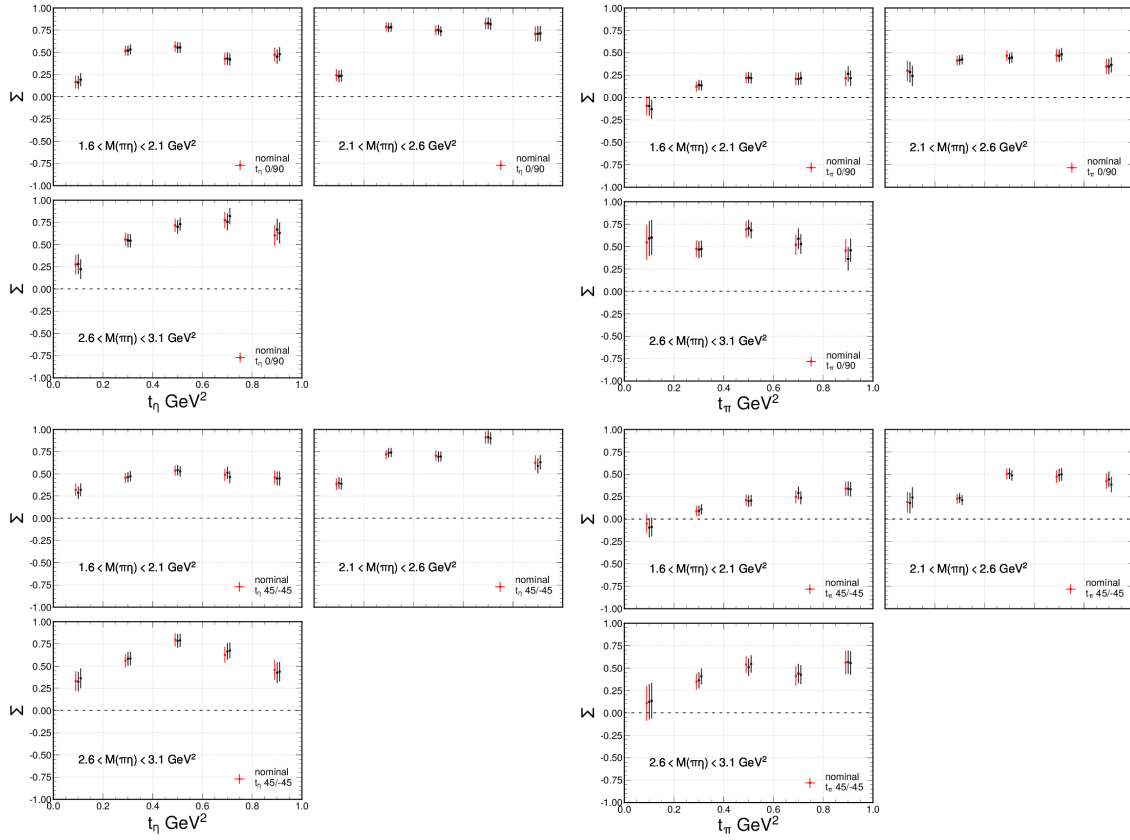
Figure C.38: Systematic differences in Σ due to variations of the sideband subtraction regions for (Left) t_η, (Right) t_π are measured in five bins. Binned in s_{12}. (Top) Asymmetries from 0/90 pair. (Bot) Asymmetries from 45/-45 pair. Red is the nominal results, black points are from different variations of event selections.
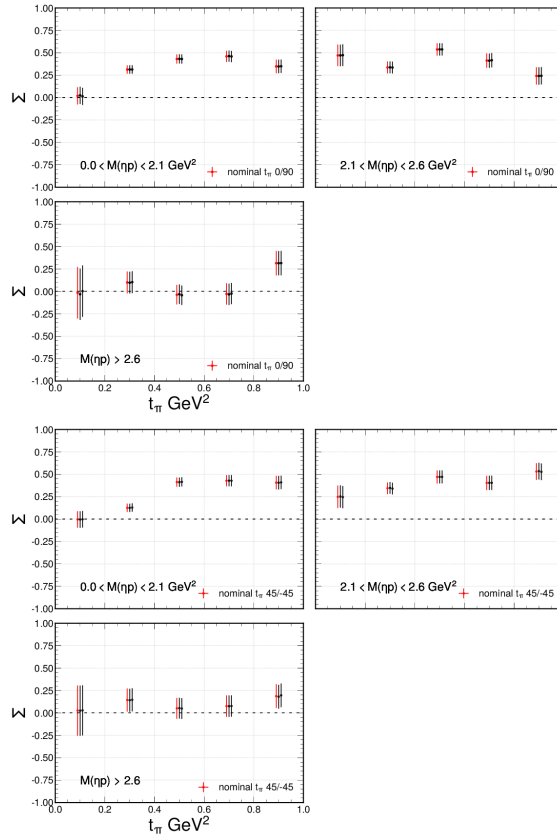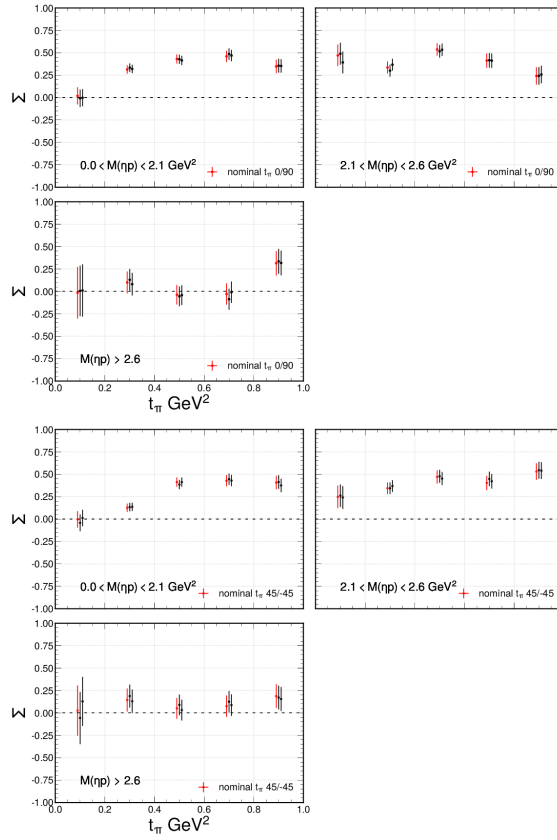
Figure C.39: Systematic differences in Σ due to variations of the sideband subtraction regions for t_π are measured in five bins. Binned in $M(\eta p)$. (Top) Asymmetries from 0/90 pair. (Bot) Asymmetries from 45/-45 pair. Red is the nominal results, black points are from different variations of event selections.

C.4.5 Instrumental asymmetry systematics
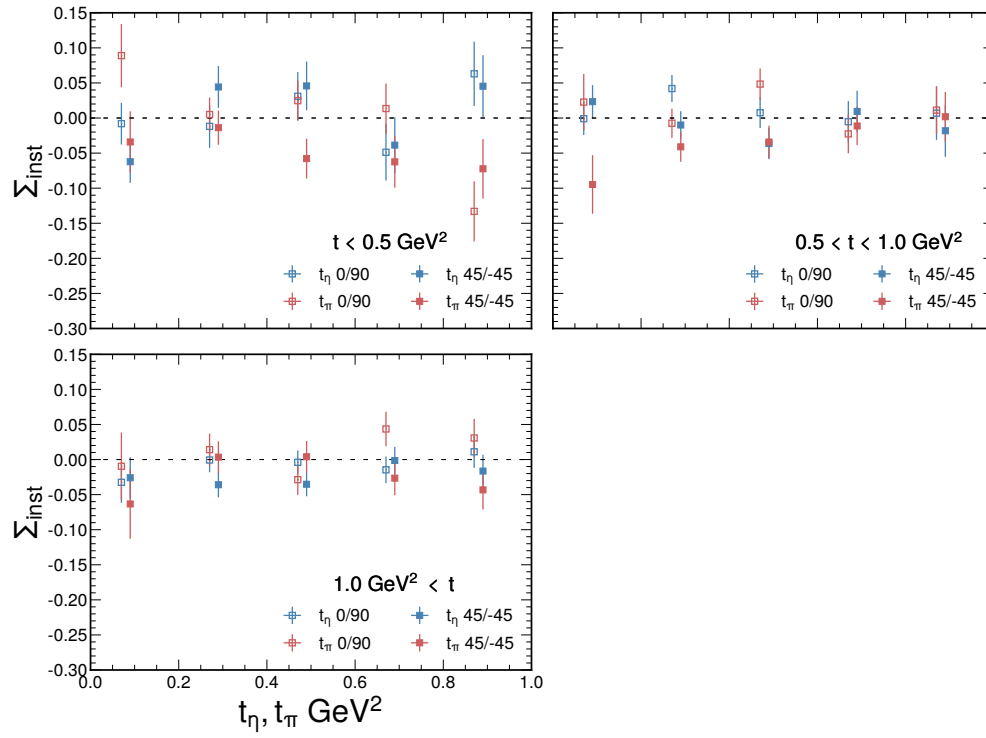

Figure C.40: Instrumental asymmetry for t_η, t_π are measured in five bins. Binned in u_3.
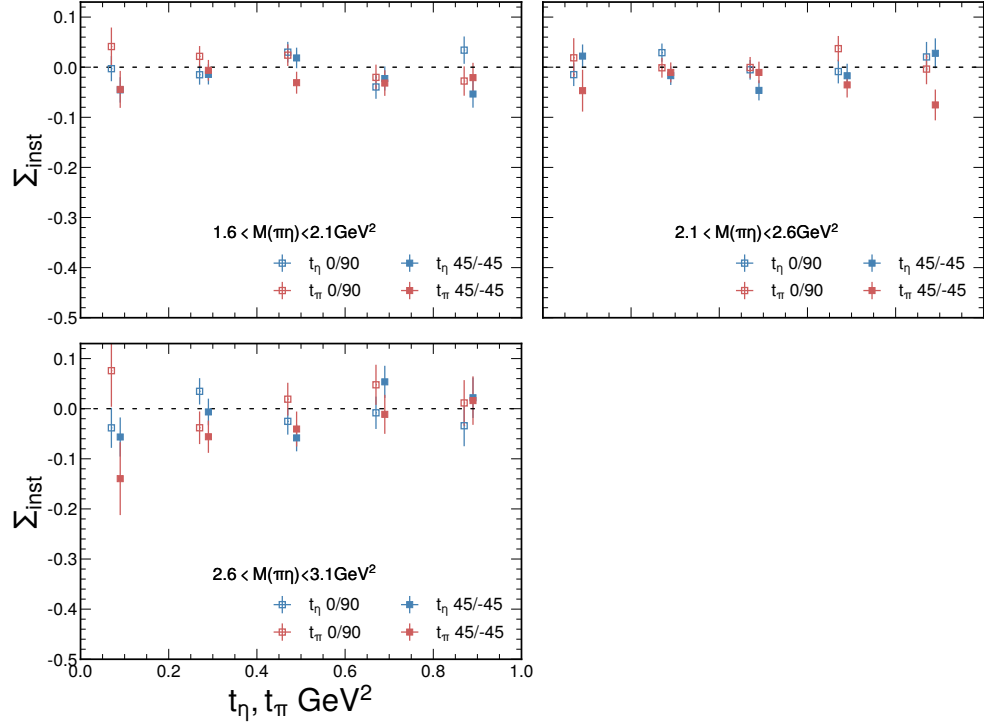
Figure C.41: Instrumental asymmetry for t_η, t_π are measured in five bins. Binned in s_{12}.
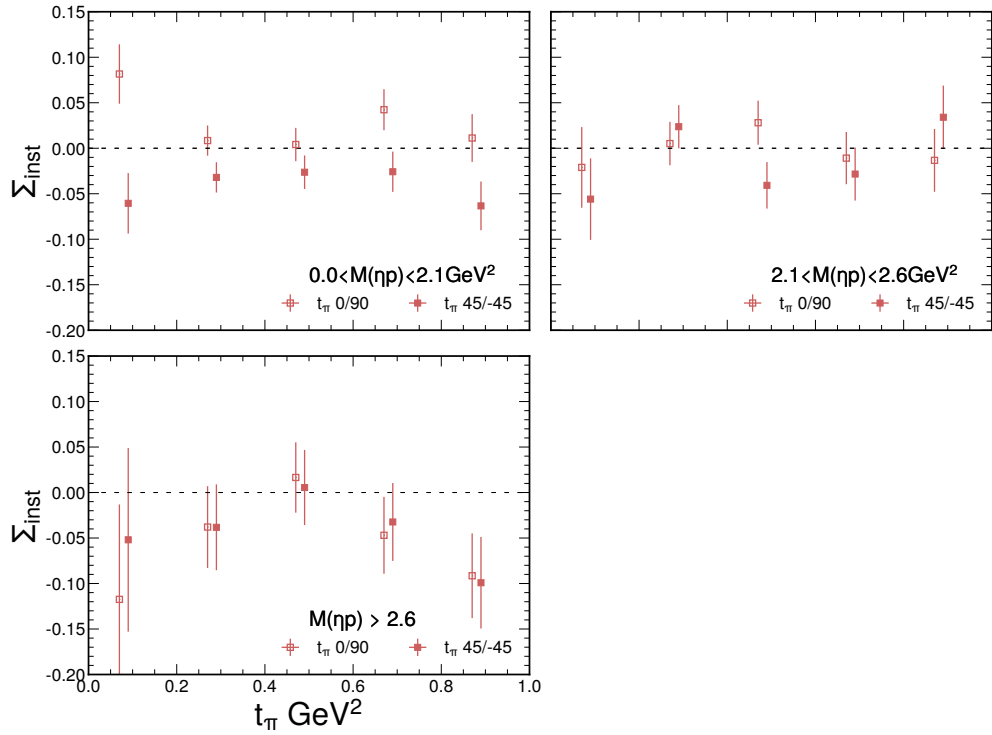
Figure C.42: Instrumental asymmetry for t_η, t_π are measured in five bins. Binned in $M(\eta p)$.

248
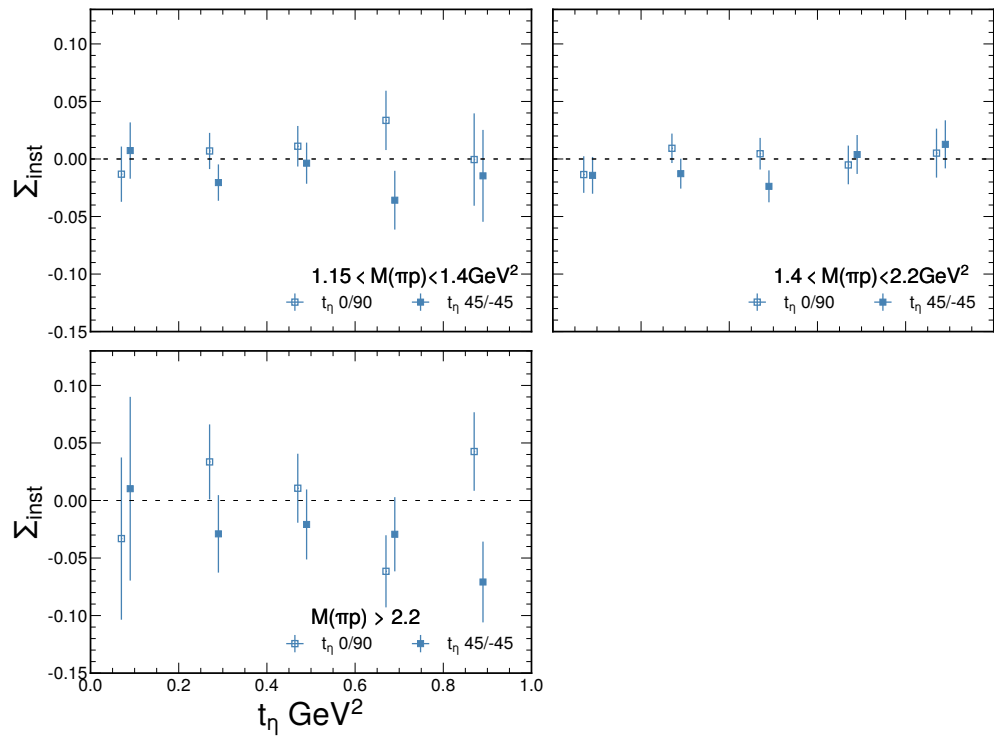
Figure C.43: Instrumental asymmetry for t_η, t_π are measured in five bins. Binned in $M(\pi 0 p)$.

REFERENCES

[1] Bernhard Ketzer, Boris Grube, and Dmitry Ryabchikov. "Light-Meson Spectroscopy with COMPASS". In: (Sept. 2019). DOI: 10.1016/j.ppnp.2020.103755. arXiv: 1909.06366 [hep-ex].

[2] David J. Gross and Frank Wilczek. "Ultraviolet Behavior of Nonabelian Gauge Theories". In: *Phys. Rev. Lett.* 30 (1973). Ed. by J. C. Taylor, pp. 1343–1346. DOI: 10.1103/PhysRevLett.30.1343.

[3] R. L. Workman et al. "Review of Particle Physics". In: *PTEP* 2022 (2022), p. 083C01. DOI: 10.1093/ptep/ptac097.

[4] E. Eichten et al. "The Spectrum of Charmonium". In: *Phys. Rev. Lett.* 34 (1975). [Erratum: Phys.Rev.Lett. 36, 1276 (1976)], pp. 369–372. DOI: 10.1103/PhysRevLett.34.369.

[5] V. E. Barnes et al. "Observation of a Hyperon with Strangeness Minus Three". In: *Phys. Rev. Lett.* 12 (1964), pp. 204–206. DOI: 10.1103/PhysRevLett.12.204.

[6] R.L. Jaffe and K. Johnson. "Unconventional states of confined quarks and gluons". In: *Physics Letters B* 60.2 (1976), pp. 201–204. ISSN: 0370-2693. DOI: https://doi.org/10.1016/0370-2693(76)90423-8. URL: https://www.sciencedirect.com/science/article/pii/0370269376904238.

[7] Y. Nambu. "The Confinement of Quarks". In: *Sci. Am.* 235N5 (1976), pp. 48–70. DOI: 10.1038/scientificamerican1176-48.

[8] Nathan Isgur, Richard Kokoski, and Jack Paton. "Gluonic excitations of mesons: Why they are missing and where to find them". In: *Phys. Rev. Lett.* 54 (9 Mar. 1985), pp. 869–872. DOI: 10.1103/PhysRevLett.54.869. URL: https://link.aps.org/doi/10.1103/PhysRevLett.54.869.

[9] Frank E. Close and Philip R. Page. "The Production and decay of hybrid mesons by flux tube breaking". In: *Nucl. Phys. B* 443 (1995), pp. 233–254. DOI: 10.1016/0550-3213(95)00085-7. arXiv: hep-ph/9411301.

[10] C. Meyer. "LIGHT AND EXOTIC MESONS". In: (). URL: http://www.curtismeyer.com/material/lecture.pdf.

[11] Geoffrey F. Chew and Steven C. Frautschi. "Regge Trajectories and the Principle of Maximum Strength for Strong Interactions". In: *Phys. Rev. Lett.* 8 (1 Jan. 1962), pp. 41–44. DOI: 10.1103/PhysRevLett.8.41. URL: https://link.aps.org/doi/10.1103/PhysRevLett.8.41.

[12] C. Patrignani et al. "Review of Particle Physics". In: *Chin. Phys. C* 40.10 (2016), p. 100001. DOI: 10.1088/1674-1137/40/10/100001.

[13] A. Donnachie and P. V. Landshoff. "Total cross-sections". In: *Phys. Lett. B* 296 (1992), pp. 227–232. DOI: 10.1016/0370-2693(92)90832-O. arXiv: hep-ph/9209205.

[14] Laurent Lellouch and Martin Luscher. "Weak transition matrix elements from finite volume correlation functions". In: *Commun. Math. Phys.* 219 (2001), pp. 31–44. DOI: 10.1007/s002200100410. arXiv: hep-lat/0003023.

[15] Raul A. Briceno et al. "Isoscalar $\pi\pi, K\overline{K}, \eta\eta$ scattering and the σ, f_0, f_2 mesons from QCD". In: *Phys. Rev. D* 97.5 (2018), p. 054513. DOI: 10.1103/PhysRevD.97.054513. arXiv: 1708.06667 [hep-lat].

[16] Jozef J. Dudek et al. "Toward the excited isoscalar meson spectrum from lattice QCD". In: *Phys. Rev. D* 88.9 (2013), p. 094505. DOI: 10.1103/PhysRevD.88.094505. arXiv: 1309.2608 [hep-lat].

[17] P. Lacock et al. "Hybrid mesons from quenched QCD". In: *Phys. Lett. B* 401 (1997), pp. 308–312. DOI: 10.1016/S0370-2693(97)00384-5. arXiv: hep-lat/9611011.

[18] C. Bernard et al. "Lattice Determination of Heavy-Light Decay Constants". In: *Phys. Rev. Lett.* 81 (22 Nov. 1998), pp. 4812–4815. DOI: 10.1103/PhysRevLett.81.4812. URL: https://link.aps.org/doi/10.1103/PhysRevLett.81.4812.

[19] C. Bernard et al. "Lattice calculation of 1^{-+} hybrid mesons with improved Kogut-Susskind fermions". In: *Phys. Rev. D* 68 (7 Oct. 2003), p. 074505. DOI: 10.1103/PhysRevD.68.074505. URL: https://link.aps.org/doi/10.1103/PhysRevD.68.074505.

[20] J. N. Hedditch et al. "1^{-+} exotic meson at light quark masses". In: *Phys. Rev. D* 72 (11 Dec. 2005), p. 114507. DOI: 10.1103/PhysRevD.72.114507. URL: https://link.aps.org/doi/10.1103/PhysRevD.72.114507.

[21] P. Lacock and K. Schilling. "Hybrid and orbitally excited mesons in full QCD". In: *Nuclear Physics B - Proceedings Supplements* 73.1 (1999), pp. 261–263. ISSN: 0920-5632. DOI: https://doi.org/10.1016/S0920-5632(99)85042-7. URL: https://www.sciencedirect.com/science/article/pii/S0920563299850427.

[22] C. McNeile and C. Michael. "Decay width of light quark hybrid meson from the lattice". In: *Phys. Rev. D* 73 (7 Apr. 2006), p. 074506. DOI: 10.1103/PhysRevD.73.074506. URL: https://link.aps.org/doi/10.1103/PhysRevD.73.074506.

[23] Jozef J. Dudek et al. "Toward the excited meson spectrum of dynamical QCD". In: *Phys. Rev. D* 82 (2010), p. 034508. DOI: 10.1103/PhysRevD.82.034508. arXiv: 1004.4930 [hep-ph].

[24]   C. A. Meyer and Y. Van Haarlem. "The Status of Exotic-quantum-number Mesons". In: *Phys. Rev. C* 82 (2010), p. 025208. DOI: 10.1103/PhysRevC.82.025208. arXiv: 1004.5516 [nucl-ex].

[25]   Antoni J. Woss et al. "Decays of an exotic 1−+ hybrid meson resonance in QCD". In: *Phys. Rev. D* 103.5 (2021), p. 054502. DOI: 10.1103/PhysRevD.103.054502. arXiv: 2009.10034 [hep-lat].

[26]   Jozef J. Dudek, Robert G. Edwards, and David J. Wilson. "An a_0 resonance in strongly coupled $\pi\eta$, $K\overline{K}$ scattering from lattice QCD". In: *Phys. Rev. D* 93.9 (2016), p. 094506. DOI: 10.1103/PhysRevD.93.094506. arXiv: 1602.05122 [hep-ph].

[27]   G.S. Adams et al. "Confirmation of a pi(1)0 Exotic Meson in the eta pi0 System". In: *Phys. Lett. B* 657 (2007), pp. 27–31. DOI: 10.1016/j.physletb.2007.07.068. arXiv: hep-ex/0612062.

[28]   A. R. Dzierba et al. "Study of the $\eta\pi^0$ spectrum and search for a $J^{\mathrm{PC}} = 1^{-+}$ exotic meson". In: *Phys. Rev. D* 67 (9 May 2003), p. 094015. DOI: 10.1103/PhysRevD.67.094015. URL: https://link.aps.org/doi/10.1103/PhysRevD.67.094015.

[29]   A. Abele et al. "Evidence for a pi eta P wave in anti-p p annihilations at rest into pi0 pi0 eta". In: *Phys. Lett. B* 446 (1999), pp. 349–355. DOI: 10.1016/S0370-2693(98)01544-5.

[30]   D. Alde et al. "Evidence for a 1-+ Exotic Meson". In: *Phys. Lett. B* 205 (1988). Ed. by R. Kotthaus and Johann H. Kuhn, p. 397. DOI: 10.1016/0370-2693(88)91686-3.

[31]   D.R. Thompson et al. "Evidence for exotic meson production in the reaction pi- p —> eta pi-p at 18-GeV/c". In: *Phys. Rev. Lett.* 79 (1997), pp. 1630–1633. DOI: 10.1103/PhysRevLett.79.1630. arXiv: hep-ex/9705011.

[32]   E852 Collaboration. "Observation of Exotic Meson Production in the Reaction $\pi^-p \to \eta^{'}\pi^-p$ at 18GeV/c". In: *Phys. Rev. Lett.* 86 (18 Apr. 2001), pp. 3977–3980. DOI: 10.1103/PhysRevLett.86.3977. URL: https://link.aps.org/doi/10.1103/PhysRevLett.86.3977.

[33]   A. Rodas et al. "Determination of the Pole Position of the Lightest Hybrid Meson Candidate". In: *Phys. Rev. Lett.* 122 (4 Jan. 2019), p. 042002. DOI: 10.1103/PhysRevLett.122.042002. URL: https://link.aps.org/doi/10.1103/PhysRevLett.122.042002.

[34]   C.A. Meyer and E.S. Swanson. "Hybrid Mesons". In: *Prog. Part. Nucl. Phys.* 82 (2015), pp. 21–58. DOI: 10.1016/j.ppnp.2015.03.001. arXiv: 1502.07276 [hep-ph].

[35]   C. Adolph et al. "Odd and even partial waves of $\eta\pi^-$ and $\eta'\pi^-$ in $\pi^-p \to \eta^{(')}\pi^-p$ at 191 GeV/c". In: *Phys. Lett. B* 740 (2015), pp. 303–311. DOI: 10.1016/j.physletb.2014.11.058. arXiv: 1408.4286 [hep-ex].

[36] B. Kopf et al. "Investigation of the lightest hybrid meson candidate with a coupled-channel analysis of $\bar{p}p$-, π^-p- and $\pi\pi$-Data". In: *Eur. Phys. J. C* 81.12 (2021), p. 1056. DOI: 10.1140/epjc/s10052-021-09821-2. arXiv: 2008.11566 [hep-ph].

[37] M. Ablikim et al. "Observation of an Isoscalar Resonance with Exotic JPC=1-+ Quantum Numbers in J/$\psi\rightarrow\gamma\eta\eta$'". In: *Phys. Rev. Lett.* 129.19 (2022), p. 192002. DOI: 10.1103/PhysRevLett.129.192002. arXiv: 2202.00621 [hep-ex].

[38] GlueX Collaboration. "A Search for QCD Exotics Using a Beam of Photons". In: 4 (2002).

[39] Adam P. Szczepaniak and Maciej Swat. "Role of photoproduction in exotic meson searches". In: *Phys. Lett. B* 516 (2001), pp. 72–76. DOI: 10.1016/S0370-2693(01)00905-4. arXiv: hep-ph/0105329.

[40] DOE/NSF Nuclear Science Advisory Committee et al. "Report of the NSAC Ad Hoc Subcommittee on a 4 GeV, CW Electron Accelerator for Nuclear Physics". In: *September* 27 (1984), pp. 320–21.

[41] Christoph W. Leemann, David R. Douglas, and Geoffrey A. Krafft. "THE CONTINUOUS ELECTRON BEAM ACCELERATOR FACILITY: CEBAF at the Jefferson Laboratory". In: *Annual Review of Nuclear and Particle Science* 51.1 (2001), pp. 413–450. DOI: 10.1146/annurev.nucl.51.101701.132327. eprint: https://doi.org/10.1146/annurev.nucl.51.101701.132327. URL: https://doi.org/10.1146/annurev.nucl.51.101701.132327.

[42] M. F. Spata. "12 GeV CEBAF Initial Operational Experience and Challenges". In: *Proc. 9th International Particle Accelerator Conference (IPAC'18), Vancouver, BC, Canada, April 29-May 4, 2018* (Vancouver, BC, Canada). International Particle Accelerator Conference 9. https://doi.org/10.18429/JACoW-IPAC2018-WEYGBD1. Geneva, Switzerland: JACoW Publishing, June 2018, pp. 1771–1775. ISBN: 978-3-95450-184-7. DOI: doi:10.18429/JACoW-IPAC2018-WEYGBD1. URL: http://jacow.org/ipac2018/papers/weygbd1.pdf.

[43] M. Vretenar. "Linear Accelerators". In: *CERN Accelerator School: Advanced Accelerator Physics Course*. 2014, pp. 295–329. DOI: 10.5170/CERN-2014-009.295. arXiv: 1601.05210 [physics.acc-ph].

[44] S. Adhikari et al. "The GLUEX beamline and detector". In: *Nucl. Instrum. Meth. A* 987 (2021), p. 164807. DOI: 10.1016/j.nima.2020.164807. arXiv: 2005.14272 [physics.ins-det].

[45] D. Elsner et al. "Linearly polarised photon beams at ELSA and measurement of the beam asymmetry in pi0-photoproduction off the proton". In: *Eur. Phys. J. A* 39 (2009), pp. 373–381. DOI: 10.1140/epja/i2008-10708-1. arXiv: 0810.1849 [nucl-ex].

[46] F. Barbosa et al. "Pair spectrometer hodoscope for Hall D at Jefferson Lab". In: *Nucl. Instrum. Meth. A* 795 (2015), pp. 376–380. DOI: 10.1016/j.nima.2015.06.012.

[47] *Total Absorption Counter*. https://halldweb1.jlab.org/wiki/index.php/Total_Absorption_Counter.

[48] K. J. Mork. "Pair Production by Photons on Electrons". In: *Phys. Rev.* 160 (5 Aug. 1967), pp. 1065–1071. DOI: 10.1103/PhysRev.160.1065. URL: https://link.aps.org/doi/10.1103/PhysRev.160.1065.

[49] M. Dugger et al. "Design and construction of a high-energy photon polarimeter". In: *Nuclear Instruments and Methods in Physics Research Section A: Accelerators, Spectrometers, Detectors and Associated Equipment* 867 (2017), pp. 115–127. ISSN: 0168-9002. DOI: https://doi.org/10.1016/j.nima.2017.05.026. URL: https://www.sciencedirect.com/science/article/pii/S0168900217305715.

[50] Eric Pooser et al. "The GlueX Start Counter Detector". In: *Nucl. Instrum. Meth. A* 927 (2019), pp. 330–342. DOI: 10.1016/j.nima.2019.02.029. arXiv: 1901.02759 [physics.ins-det].

[51] N. S. Jarvis et al. "The Central Drift Chamber for GlueX". In: *Nucl. Instrum. Meth. A* 962 (2020), p. 163727. DOI: 10.1016/j.nima.2020.163727. arXiv: 1910.07602 [physics.ins-det].

[52] L. Pentchev et al. "Studies with cathode drift chambers for the GlueX experiment at Jefferson Lab". In: *Nuclear Instruments and Methods in Physics Research Section A: Accelerators, Spectrometers, Detectors and Associated Equipment* 845 (2017). Proceedings of the Vienna Conference on Instrumentation 2016, pp. 281–284. ISSN: 0168-9002. DOI: https://doi.org/10.1016/j.nima.2016.04.076. URL: https://www.sciencedirect.com/science/article/pii/S0168900216302893.

[53] Lubomir Pentchev and Benedikt Zihlmann. "Forward Drift Chamber for the GlueX Experiment at the 12 GeV CEBAF Machine". In: *AIP Conference Proceedings* 1336.1 (2011), pp. 565–568. DOI: 10.1063/1.3586164. eprint: https://aip.scitation.org/doi/pdf/10.1063/1.3586164. URL: https://aip.scitation.org/doi/abs/10.1063/1.3586164.

[54] R. E. Kalman. "A New Approach to Linear Filtering and Prediction Problems". In: *Journal of Basic Engineering* 82.1 (Mar. 1960), pp. 35–45. ISSN: 0021-9223. DOI: 10.1115/1.3662552. eprint: https://asmedigitalcollection.asme.org/fluidsengineering/article-pdf/82/1/35/5518977/35_1.pdf. URL: https://doi.org/10.1115/1.3662552.

[55] Tegan D. Beattie et al. "Construction and Performance of the Barrel Electromagnetic Calorimeter for the GlueX Experiment". In: *Nucl. Instrum. Meth. A* 896 (2018), pp. 24–42. DOI: 10.1016/j.nima.2018.04.006. arXiv: 1801.03088 [physics.ins-det].

[56] R.R. Crittenden et al. "A 3000 element lead-glass electromagnetic calorimeter". In: *Nuclear Instruments and Methods in Physics Research Section A: Accelerators, Spectrometers, Detectors and Associated Equipment* 387.3 (1997), pp. 377–394. ISSN: 0168-9002. DOI: https://doi.org/10.1016/S0168-9002(97)00101-0. URL: https://www.sciencedirect.com/science/article/pii/S0168900297001010.

[57] R.T. Jones et al. "Performance of the radphi detector and trigger in a high rate tagged photon beam". In: *Nuclear Instruments and Methods in Physics Research Section A: Accelerators, Spectrometers, Detectors and Associated Equipment* 570.3 (2007), pp. 384–398. ISSN: 0168-9002. DOI: https://doi.org/10.1016/j.nima.2006.09.039. URL: https://www.sciencedirect.com/science/article/pii/S0168900206015798.

[58] K. Moriya et al. "A measurement of the energy and timing resolution of the GlueX Forward Calorimeter using an electron beam". In: *Nuclear Instruments and Methods in Physics Research Section A: Accelerators, Spectrometers, Detectors and Associated Equipment* 726 (2013), pp. 60–66. ISSN: 0168-9002. DOI: https://doi.org/10.1016/j.nima.2013.05.109. URL: https://www.sciencedirect.com/science/article/pii/S0168900213007201.

[59] "Spring 2017 Analysis Launch Cuts". In: (). URL: https://halldweb.jlab.org/wiki/index.php/Spring_2017_Analysis_Launch_Cuts.

[60] Daniel Lersch. *Kinematic Fitting in Hadron Physics*. http://hadron.physics.fsu.edu/~dlersch/kfit_slides/Kinematic_Fitting.pdf.

[61] B. Zihlmann. *Tagger Accidentals and Scaling*. https://halldweb.jlab.org/DocDB/0041/004122/004/tagger_accidentals_doc.pdf.

[62] Glen Cowan et al. "Asymptotic formulae for likelihood-based tests of new physics". In: *Eur. Phys. J. C* 71 (2011). [Erratum: Eur.Phys.J.C 73, 2501 (2013)], p. 1554. DOI: 10.1140/epjc/s10052-011-1554-0. arXiv: 1007.1727 [physics.data-an].

[63] Mark Dalton. https://halldweb.jlab.org/DocDB/0050/005028/001/Dalton_20210404_CrossSection.pdf.

[64] M. Williams, M. Bellis, and C.A. Meyer. "Multivariate side-band subtraction using probabilistic event weights". In: *JINST* 4 (2009), P10003. DOI: 10.1088/1748-0221/4/10/P10003. arXiv: 0809.2548 [nucl-ex].

[65] M. Albrecht et al. "Coupled channel analysis of $\bar{p}p \to \pi^0\pi^0\eta$, $\pi^0\eta\eta$ and $K^+K^-\pi^0$ at 900 MeV/c and of $\pi\pi$-scattering data". In: *Eur. Phys. J. C* 80.5 (2020), p. 453. DOI: 10.1140/epjc/s10052-020-7930-x. arXiv: 1909.07091 [hep-ex].

[66] M. Ablikim et al. "Observation of $\eta_c \to \omega\omega$ in $J/\psi \to \gamma\omega\omega$". In: *Phys. Rev. D* 100.5 (2019), p. 052012. DOI: 10.1103/PhysRevD.100.052012. arXiv: 1905.10318 [hep-ex].

[67] P. Roy et al. "Measurement of the beam asymmetry Σ and the target asymmetry T in the photoproduction of ω mesons off the proton using CLAS at Jefferson Laboratory". In: *Phys. Rev. C* 97.5 (2018), p. 055202. DOI: 10.1103/PhysRevC.97.055202. arXiv: 1711.05176 [nucl-ex].

[68] Z. Akbar et al. "Measurement of the helicity asymmetry E in $\omega \to \pi^+\pi^-\pi^0$ photoproduction". In: *Phys. Rev. C* 96.6 (2017), p. 065209. DOI: 10.1103/PhysRevC.96.065209. arXiv: 1708.02608 [nucl-ex].

[69] M. Williams et al. "Partial wave analysis of the reaction gamma p —> p omega and the search for nucleon resonances". In: *Phys. Rev. C* 80 (2009), p. 065209. DOI: 10.1103/PhysRevC.80.065209. arXiv: 0908.2911 [nucl-ex].

[70] Lawrence Ng. *Q-Factors*. https://github.com/lan13005/QFactors.

[71] Lawrence Ng. *Q-Factors*. https://www.overleaf.com/read/tjkpgxsnmwvt.

[72] Carlos W. Salgado and Dennis P. Weygand. "On the Partial-Wave Analysis of Mesonic Resonances Decaying to Multiparticle Final States Produced by Polarized Photons". In: *Phys. Rept.* 537 (2014), pp. 1–58. DOI: 10.1016/j.physrep.2013.11.005. arXiv: 1310.7498 [nucl-ex].

[73] L. Van Hove. "Longitudinal phase-space plots of multiparticle hadron collisions at high energy". In: *Nuclear Physics B* 9.3 (1969), pp. 331–348. ISSN: 0550-3213. DOI: https://doi.org/10.1016/0550-3213(69)90133-3. URL: https://www.sciencedirect.com/science/article/pii/0550321369901333.

[74] Stuart Fegan. "Beam asymmetries from light scalar meson photoproduction on the proton at GlueX". In: *AIP Conference Proceedings* 2249.1 (2020), p. 030007. DOI: 10.1063/5.0009377. eprint: https://aip.scitation.org/doi/pdf/10.1063/5.0009377. URL: https://aip.scitation.org/doi/abs/10.1063/5.0009377.

[75] Simon Taylor. *Multi-particle final state survey*. https://halldweb.jlab.org/DocDB/0038/003818/001/surveyOct18.pdf.

[76] Ahmed Foda. https://halldweb.jlab.org/DocDB/0052/005210/001/XWG_12Jul2021.pdf.

[77] Jonathan Zarling. https://halldweb.jlab.org/DocDB/0055/005581/001/EtaXSec_5.13.22.pdf.

[78] Georgios Vasileiadis. https://halldweb.jlab.org/DocDB/0046/004687/002/presentation_46.pdf.

[79] D. Barberis et al. "A Study of the centrally produced eta pi0 and eta pi- systems in p p interactions at 450-GeV/c". In: *Phys. Lett. B* 488 (2000), pp. 225–233. DOI: 10.1016/S0370-2693(00)00894-7. arXiv: hep-ex/0007019.

[80] S. U. Chung et al. "Exotic and q anti-q resonances in the pi+ pi- pi- system produced in pi- p collisions at 18-GeV/c/". In: *Phys. Rev. D* 65 (2002), p. 072001. DOI: 10.1103/PhysRevD.65.072001.

[81] Curtis A. Meyer. *Translating Old Meson Names*. https://halldweb.jlab.org/DocDB/0055/005555/004/meson-names.pdf.

[82] G. Bellini et al. "Pion Diffraction Dissociation on Carbon Nuclei at 6.1 and 18.1 GeV/c". In: *Nuovo Cim.* 29 (1963), p. 896. DOI: 10.1007/BF02827952.

[83] S. U. Chung et al. "Analysis of the 1.0-1.4 BeV pi p Enhancement". In: *Phys. Rev. Lett.* 12 (1964), p. 621. DOI: `10.1103/PhysRevLett.12.621`.

[84] G. Goldhaber et al. "Evidence for a pi rho Interaction Produced in the pi+ p Reaction at 3.65 BeV". In: *Phys. Rev. Lett.* 12 (1964), p. 336. DOI: `10.1103/PhysRevLett.12.336`.

[85] M. Aguilar-Benitez et al. "Review of Particle Properties. Particle Data Group". In: *Phys. Lett. B* 170 (1986), pp. 1–350.

[86] D. R. Thompson et al. "Evidence for exotic meson production in the reaction pi- p —> eta pi-p at 18-GeV/c". In: *Phys. Rev. Lett.* 79 (1997), pp. 1630–1633. DOI: `10.1103/PhysRevLett.79.1630`. arXiv: `hep-ex/9705011`.

[87] C. Amsler et al. "Observation of a new I(G) (J(PC)) = 1- (O++) resonance at 1450-MeV". In: *Phys. Lett. B* 333 (1994), pp. 277–282. DOI: `10.1016/0370-2693(94)91044-8`.

[88] A. Abele et al. "Observation of resonances in the reaction anti-p p –> pi0 eta eta at 1.94-GeV/c". In: *Eur. Phys. J. C* 8 (1999), pp. 67–79. DOI: `10.1007/s100520050445`.

[89] Claude Amsler et al. "Proton anti-proton annihilation at 900-MeV/c into pi0 pi0 pi0, pi0 pi0 eta and pi0 eta eta". In: *Eur. Phys. J. C* 23 (2002), pp. 29–41. DOI: `10.1007/s100520100860`.

[90] A. Celentano et al. "First measurement of direct photoproduction of the $a_2(1320)^0$ meson on the proton". In: *Phys. Rev. C* 102.3 (2020), p. 032201. DOI: `10.1103/PhysRevC.102.032201`. arXiv: `2004.05359 [nucl-ex]`.

[91] V. Mathieu et al. "Exclusive tensor meson photoproduction". In: *Phys. Rev. D* 102.1 (2020), p. 014003. DOI: `10.1103/PhysRevD.102.014003`. arXiv: `2005.01617 [hep-ph]`.

[92] Ju-Jun Xie, Eulogio Oset, and Li-Sheng Geng. "Photoproduction of the $f_2'(1525), a_2(1320)$, and $K_2^*(1430)$". In: *Phys. Rev. C* 93.2 (2016), p. 025202. DOI: `10.1103/PhysRevC.93.025202`. arXiv: `1509.06469 [nucl-th]`.

[93] Jassem Ajaka et al. "Simultaneous Photoproduction of η and π^0 Mesons on the Proton". In: *Physical Review Letters* 100 (Feb. 2008). DOI: `10.1103/PhysRevLett.100.052003`.

[94] V. L. Kashevarov et al. "Photoproduction of pi0 eta on protons and the Delta(1700)D(33) resonance". In: *Eur. Phys. J. A* 42 (2009), pp. 141–149. DOI: `10.1140/epja/i2009-10868-4`. arXiv: `0901.3888 [hep-ex]`.

[95] The Collaboration et al. "Study of the reaction $\gamma p \to p\pi^0\eta$". In: *European Physical Journal A* 38 (Nov. 2008), pp. 173–186. DOI: `10.1140/epja/i2008-10657-7`.

[96] V. et al Sokhoyan. "Experimental study of the $\gamma p \to p\pi^0\eta p$ reaction with the A2 setup at the Mainz Microtron". In: *Physical Review C* 97.5 (May 2018). DOI: `10.1103/PhysRevC.97.055212`.

[97]   M. Battaglieri et al. "Photoproduction of pi+ pi- meson pairs on the proton". In: *Phys. Rev. D* 80 (2009), p. 072005. DOI: 10.1103/PhysRevD.80.072005. arXiv: 0907.1021 [hep-ex].

[98]   Mahiko Suzuki. "Tensor-meson dominance: Phenomenology of the f_2 meson". In: *Phys. Rev. D* 47 (3 Feb. 1993), pp. 1043–1047. DOI: 10.1103/PhysRevD.47.1043. URL: https://link.aps.org/doi/10.1103/PhysRevD.47.1043.

[99]   L. Van Hove. "Final state classification and new phase space plot for many-body hadron collisions". In: *Physics Letters B* 28.6 (1969), pp. 429–431. ISSN: 0370-2693. DOI: https://doi.org/10.1016/0370-2693(69)90343-8. URL: https://www.sciencedirect.com/science/article/pii/0370269369903438.

[100] M. Shi et al. "Double-Regge exchange limit for the $\gamma p \to K^+ K^- p$ reaction". In: *Phys. Rev. D* 91 (3 Feb. 2015), p. 034007. DOI: 10.1103/PhysRevD.91.034007. URL: https://link.aps.org/doi/10.1103/PhysRevD.91.034007.

[101] P. Pauli et al. "Mass-dependent cuts in longitudinal phase space". In: *Phys. Rev. C* 98.6 (2018), p. 065201. DOI: 10.1103/PhysRevC.98.065201. arXiv: 1809.02009 [nucl-ex].

[102] V. Mathieu et al. "Moments of angular distribution and beam asymmetries in $\eta\pi^0$ photoproduction at GlueX". In: *Phys. Rev. D* 100 (5 Sept. 2019), p. 054017. DOI: 10.1103/PhysRevD.100.054017. URL: https://link.aps.org/doi/10.1103/PhysRevD.100.054017.

[103] Matt Shepherd. "AmpTools Implementation of Polarized Production". In: (2019). eprint: https://halldweb.jlab.org/DocDB/0040/004094/003/amptools_polarization.pdf.

[104] M. R. Shepherd. *AmpTools User Guide v0.11.0.* https://github.com/mashephe/AmpTools/blob/master/AmpTools_User_Guide.pdf.

[105] M. Dugger. https://userweb.jlab.org/~dugger/triPol/makePolValsV9.tar.

[106] GlueX. *Github link for hd_utilities.* https://github.com/JeffersonLab/hd_utilities.

[107] R. L. Workman et al. "Review of Particle Physics". In: *PTEP* 2022 (2022), p. 083C01. DOI: 10.1093/ptep/ptac097.

[108] Tim C Hesterberg. "What teachers should know about the bootstrap: Resampling in the undergraduate statistics curriculum". In: *The american statistician* 69.4 (2015), pp. 371–386.

[109] Roger Barlow. "Systematic errors: Facts and fictions". In: *Conference on Advanced Statistical Techniques in Particle Physics.* July 2002, pp. 134–144. arXiv: hep-ex/0207026.

[110] A. Austregesilo. *Orientations of the Photon Beam Polarization from $\rho(770)$ Decay Asymmetries.* https://halldweb.jlab.org/DocDB/0039/003977/005/note.pdf.

[111] A Somov et al. "Commissioning of the Pair Spectrometer of the GlueX experiment". In: *Journal of Physics: Conference Series* 798.1 (Jan. 2017), p. 012175. DOI: 10.1088/1742-6596/798/1/012175. URL: https://dx.doi.org/10.1088/1742-6596/798/1/012175.

[112] A. Somov. Private communication.

[113] GlueX. https://halldweb.jlab.org/DocDB/0040/004025/011/fcal_bcal_efficiency.pdf.

[114] Naren F. Bali, Geoffrey F. Chew, and Alberto Pignotti. "Multiple-Production Theory Via Toller Variables". In: *Phys. Rev. Lett.* 19 (10 Sept. 1967), pp. 614–618. DOI: 10.1103/PhysRevLett.19.614. URL: https://link.aps.org/doi/10.1103/PhysRevLett.19.614.

[115] R.C Brower, C.E DeTar, and J.H Weis. "Regge theory for multiparticle amplitudes". In: *Physics Reports* 14.6 (1974), pp. 257–367. ISSN: 0370-1573. DOI: https://doi.org/10.1016/0370-1573(74)90012-X. URL: https://www.sciencedirect.com/science/article/pii/037015737490012X.

[116] P. D. B. Collins. *An Introduction to Regge Theory and High-Energy Physics*. Cambridge Monographs on Mathematical Physics. Cambridge, UK: Cambridge Univ. Press, May 2009. ISBN: 978-0-521-11035-8. DOI: 10.1017/CBO9780511897603.

[117] I.T. Drummond, P.V. Landshoff, and W.J. Zakrzewski. "Signature in production amplitudes". In: *Physics Letters B* 28.10 (1969), pp. 676–678. ISSN: 0370-2693. DOI: https://doi.org/10.1016/0370-2693(69)90220-2. URL: https://www.sciencedirect.com/science/article/pii/0370269369902202.

[118] I.T. Drummond, P.V. Landshoff, and W.J. Zakrzewski. "The two-Reggeon/particle coupling". In: *Nuclear Physics B* 11.2 (1969), pp. 383–405. ISSN: 0550-3213. DOI: https://doi.org/10.1016/0550-3213(69)90088-1. URL: https://www.sciencedirect.com/science/article/pii/0550321369900881.

[119] J. H. Weis. "Singularities in Complex Angular Momentum and Helicity". In: *Phys. Rev. D* 6 (10 Nov. 1972), pp. 2823–2841. DOI: 10.1103/PhysRevD.6.2823. URL: https://link.aps.org/doi/10.1103/PhysRevD.6.2823.

[120] R. Dolen, D. Horn, and C. Schmid. "Finite-Energy Sum Rules and Their Application to πN Charge Exchange". In: *Phys. Rev.* 166 (5 Feb. 1968), pp. 1768–1781. DOI: 10.1103/PhysRev.166.1768. URL: https://link.aps.org/doi/10.1103/PhysRev.166.1768.

[121] J. Nys et al. "Finite-energy sum rules in eta photoproduction off a nucleon". In: *Phys. Rev. D* 95.3 (2017), p. 034014. DOI: 10.1103/PhysRevD.95.034014. arXiv: 1611.04658 [hep-ph].

[122] Miguel Albaladejo et al. "Novel approaches in hadron spectroscopy". In: *Prog. Part. Nucl. Phys.* 127 (2022), p. 103981. DOI: 10.1016/j.ppnp.2022.103981. arXiv: 2112.13436 [hep-ph].

[123] Piotr Lebiedowicz, Otto Nachtmann, and Antoni Szczurek. "Central exclusive diffractive production of $K^+K^-K^+K^-$ via the intermediate $\phi\phi$ state in proton-proton collisions". In: *Phys. Rev. D* 99.9 (2019), p. 094034. DOI: 10.1103/PhysRevD.99.094034. arXiv: 1901.11490 [hep-ph].

[124] Piotr Lebiedowicz et al. "Central exclusive diffractive production of axial-vector $f_1(1285)$ and $f_1(1420)$ mesons in proton-proton collisions". In: *Phys. Rev. D* 102.11 (2020), p. 114003. DOI: 10.1103/PhysRevD.102.114003. arXiv: 2008.07452 [hep-ph].

[125] Anna Cisek and Antoni Szczurek. "Two-gluon production of ϕ and η' mesons in proton-proton collisions at high energies". In: *Phys. Rev. D* 103 (2021), p. 114008. DOI: 10.1103/PhysRevD.103.114008. arXiv: 2103.08954 [hep-ph].

[126] T. Shimada, A.D. Martin, and A.C. Irving. "Double Regge exchange phenomenology". In: *Nuclear Physics B* 142.3 (1978), pp. 344–364. ISSN: 0550-3213. DOI: https://doi.org/10.1016/0550-3213(78)90209-2. URL: https://www.sciencedirect.com/science/article/pii/0550321378902092.

[127] L. Bibrzycki et al. "$\pi^-p \to \eta^{(\prime)}\pi^-p$ in the double-Regge region ". In: *Eur. Phys. J. C* 81 (2021). [Erratum: Eur.Phys.J.C 81, 915 (2021)], p. 647. DOI: 10.1140/epjc/s10052-021-09594-8. arXiv: 2104.10646 [hep-ph].

[128] V. Mathieu, G. Fox, and A. P. Szczepaniak. "Neutral Pion Photoproduction in a Regge Model". In: *Phys. Rev. D* 92.7 (2015), p. 074013. DOI: 10.1103/PhysRevD.92.074013. arXiv: 1505.02321 [hep-ph].

[129] V. Mathieu et al. "Structure of Pion Photoproduction Amplitudes". In: *Phys. Rev. D* 98.1 (2018), p. 014041. DOI: 10.1103/PhysRevD.98.014041. arXiv: 1806.08414 [hep-ph].

[130] V. Mathieu et al. "Toward Complete Pion Nucleon Amplitudes". In: *Phys. Rev. D* 92.7 (2015), p. 074004. DOI: 10.1103/PhysRevD.92.074004. arXiv: 1506.01764 [hep-ph].

[131] H. Al Ghoul et al. "Measurement of the beam asymmetry Σ for π^0 and η photoproduction on the proton at $E_\gamma = 9$ GeV". In: *Phys. Rev. C* 95.4 (2017), p. 042201. DOI: 10.1103/PhysRevC.95.042201. arXiv: 1701.08123 [nucl-ex].

[132] S. Adhikari et al. "Beam Asymmetry $\boldsymbol{\Sigma}$ for the Photoproduction of η and η' Mesons at $\mathbf{E}_\gamma = \mathbf{8.8}$GeV". In: *Phys. Rev. C* 100.5 (2019), p. 052201. DOI: 10.1103/PhysRevC.100.052201. arXiv: 1908.05563 [nucl-ex].

[133] S. Adhikari et al. "Measurement of the photon beam asymmetry in $\vec{\gamma}p \to K^+\Sigma^0$ at $E_\gamma = 8.5$ GeV". In: *Phys. Rev. C* 101.6 (2020), p. 065206. DOI: 10.1103/PhysRevC.101.065206. arXiv: 2003.08038 [nucl-ex].

[134] S. Adhikari et al. "Measurement of beam asymmetry for $\pi^-\Delta^{++}$ photoproduction on the proton at E_γ=8.5 GeV". In: *Phys. Rev. C* 103.2 (2021), p. L022201. DOI: 10.1103/PhysRevC.103.L022201. arXiv: 2009.07326 [nucl-ex].

[135] GlueX Collaboration. "Measurement of the beam asymmetry Σ for π^0 and η photoproduction on the proton at E_γ=9 GeV". English (US). In: *Physical Review C* 95.4 (Apr. 2017). ISSN: 2469-9985. DOI: 10.1103/PhysRevC.95.042201.

[136] The GlueX Collaboration. "Measurement of beam asymmetry for $\pi^-\Delta^{++}$ photoproduction on the proton at $E_\gamma = 8.5\,\mathrm{GeV}$". In: *Phys. Rev. C* 103 (2 Feb. 2021), p. L022201. DOI: 10.1103/PhysRevC.103.L022201. URL: https://link.aps.org/doi/10.1103/PhysRevC.103.L022201.

[137] G Kramer and P Stichel. "PHOTOPRODUCTION OF PIONS IN FORWARD DIRECTION AND REGGE POLES". In: *Z. Physik* Vol: 178 (Jan. 1964). DOI: 10.1007/BF01379479. URL: https://www.osti.gov/biblio/4051847.

[138] F. Ravndal. "Polarization Theorems in Pion Photoproduction". In: *Phys. Rev. D* 2 (7 Oct. 1970), pp. 1278–1280. DOI: 10.1103/PhysRevD.2.1278. URL: https://link.aps.org/doi/10.1103/PhysRevD.2.1278.

[139] J. Nys et al. "Features of $\pi\Delta$ Photoproduction at High Energies". In: *Phys. Lett. B* 779 (2018), pp. 77–81. DOI: 10.1016/j.physletb.2018.01.075. arXiv: 1710.09394 [hep-ph].

[140] Dave Mack et al. "GlueX Analysis Note (DocDB #3118)". In: (). URL: https://halldweb.jlab.org/DocDB/0031/003118/017/pseudoBeamAsymNote_v1.6.pdf.

[141] A. Jackura et al. "New analysis of $\eta\pi$ tensor resonances measured at the COMPASS experiment". In: *Phys. Lett. B* 779 (2018), pp. 464–472. DOI: 10.1016/j.physletb.2018.01.017. arXiv: 1707.02848 [hep-ph].

[142] https://halldweb.jlab.org/wiki/index.php/Spring_2017_Analysis_Launch_Cuts.

[143] Justin Stevens. https://github.com/JeffersonLab/hd_utilities/blob/master/psflux/README.md.

BIOGRAPHICAL SKETCH

Lawrence Ng

Education

Florida State University Tallahassee, FL
Doctor of Philosophy in Physics *Aug. 2016 – April 2023*

University of Connecticut Storrs, CT
Bachelor of Science in Physics *Aug. 2013 – May 2015*

Summary

Experienced in physics analyses with a wide range of interest. Extensive use of statistical analysis tools and competent in integrating machine learning into a workflow. Worked in multiple collaborations, two of which are outside immediate research field, both generating published results. Convener of two analysis working groups of more than 6 people.

Experience

Graduate Research Assistant Aug. 2016 – Present
Florida State University (FSU) *Tallahassee, FL*

- (Advsior: Sean Dobbs) Searching for photoproduced exotic hybrid mesons in the $\eta\pi^0$ system at GlueX
  - (Project 1) Measuring the $a_2(1320)$ differential cross-section via a partial wave analysis of $\gamma p \to \eta\pi^0 p$. *Publication in prep.*
  - (Project 2) Measuring the single particle beam asymmetry in the double Regge region in $\gamma p \to \eta\pi^0 p$ and $\gamma p \to \eta\pi^- \Delta^{++}$
  - Computation and statistical techniques used in above projects
    - Proficient in using Monte Carlo to study backgrounds and in understanding event selection and fit/model performance
    - Implemented a computationally expensive background subtraction technique known as Q-Factors/Q-Values with multi-threaded support. Mostly written in C++ with python/bash driving scripts - https://github.com/lan13005/QFactors
    - Experienced in maximum likelihood optimization, Markov Chain Monte Carlo (PyMC), statistic estimation(bootstrap), model selection(information criteria), Hypothesis testing, sampling techniques, time series analysis, data mining, classification, regression
- (Advisor: Rachel Yohay) Conducted research with the Compact Muon Solenoid (CMS) group at FSU from Fall 2016 to January 2018
  - Irradiating silicon photomultipiers as R&D for the Large Hadron Collider (LHC) upgrade
  - Maintained equipment for the refrigeration system, measured CV/IV curves of the diodes (programmed in LabView), and prepped vaccum chambers

Undergraduate Research Assistant Aug. 2013 – May 2015
University of Connecticut (UConn) *Storrs, CT*

- (Advisor: Vasili Kharchenko) Studied cometary spectra observed by Chandra X-ray observatory to determine elemental abundances with a mixture of Gaussian lineshapes. Programmed in Mathematica and MATLAB

Machine Learning Experience

Professional Experience

- Developed a prescription to determine the nature of exotic hadrons from their spectra using neural networks, in collaboration with the Joint Physics Analysis Center. Explainable AI - using game theory's Shapely values to determine feature impact. Hyperparameters are optimized using Hyperopt. Implemented in PyTorch[1]

- Collaboration with astronomers from the Carnegie Supernova Project to develop a conditional variational autoencoder neural network to generate template supernova spectra[2]

- Monitoring consistency in run quality and run parameters by web-scraping GlueX wiki pages using lxml+python

Hackathons and ML Workshops

- (Summer 2019) Deep Learning for Science Summer School at Lawrence Berkeley National Lab

- (Summer 2019) FRIB TA Summer School - Machine Learning Applied to Nuclear Physics at Michigan State University

- (October 2019) HackFSU - Major League Hacking event at Florida State University - centralizing graduate school requirements/expectations by web-scraping using lxml

- (June 2021) JLab AI Town Hall Hackathon - Group competition to solve several problems

  - 3rd place for predicting number of particle showers and their associated energies using two dense neural networks: one to classify the number of showers and another to predict their energies.

- (July 2021) Quarks to Cosmos Hackathon - Group project to solve inverse problems using variational inference - normalizing flow variational autoencoder

- (November 2021) Machine Learning for Science (ML4SCI)

  - Planetary albedo challenge (1st place) Determining elemental composition from moon images using a U-Net+GAN model architecture
  - Gravitational lensing challenge (2nd place) – Predicting the properties of cosmic dark matter halo
  - Circumgalactic Medium Challenge (2nd place) – Extracting important features in the generation of circumgalactic media using an autoencoder to match the low-dimensional physical process

TECHNICAL SKILLS

Languages: C++, Python (Scientific python software stack + Pytorch), Bash/zsh, Mathematica/MatLab
Tools: Jupyter/Colab, Vim, Git, *nix operating systems, SQL, Frequentist+Bayesian Statistics / Fitting, LaTex / Overleaf

PRESENTATIONS

- (May 2019) $\eta\pi$ photoproduction at GlueX @ HUGS Summer School
- (Oct 2020) Double Regge Physics @ APS
- (Mar 2021) Quarkonia at GlueX Invited Talk
- (Oct 2021) Deep Learning Exotic Hadrons @ Division of Nuclear Physics
- (Jan 2022) Deep Learning Exotic Hadrons Seminar
- (Feb 2020, May 2020, Oct 2020, Sept 2021) GlueX Collaboration meetings

PUBLICATIONS

[1] **L. Ng**, L. Bibrzycki, J. Nys, C. Fernández-Ramírez, A. Pilloni, V. Mathieu, A.J. Rasmusson, and A.P. Szczepaniak (Joint Physics Analysis Center), "Deep Learning Exotic Hadrons", Phys. Rev. D 105 (2022) L091501
[2] J. Lu, **L. Ng**, et al. (Carnegie Supernova Project), "Carnegie Supernova Project-II: Near-infrared spectral diversity and template of Type Ia Supernovae", arXiv 2211.05998
[3] A. Ali (Darmstadt, GSI), **L. Ng**, et al. "First Measurement of Near-Threshold J/ψ Exclusive Photoproduction off the Proton", Phys.Rev.Lett. 123 (2019) 7, 072001
[4] S. Adhikari, **L. Ng**, et al., "Beam asymmetry Σ for the photoproduction of η and η' mesons at $E_\gamma = 8.8$ GeV", Phys. Rev. C 100, 052201(R)

[5] S. Adhikari, **L. Ng**, et al., "Measurement of the photon beam asymmetry in $\vec{\gamma}p \to K^+\Sigma^0$ at $E_\gamma = 8.5$ GeV", Phys.Rev.C 101 (2020) 6, 065206

[6] S. Adhikari, **L. Ng**, et al., "The GlueX beamline and detector", Nucl.Instrum.Meth.A 987 (2021) 164807

[7] S. Adhikari, **L. Ng**, et al., "Measurement of beam asymmetry for $\pi^-\Delta^{++}$ photoproduction on the proton at $E_\gamma = 8.5$ GeV", Phys.Rev.C 103 (2021) 2, L022201

[8] S. Adhikari, **L. Ng**, et al., "Measurement of spin density matrix elements in $\Lambda(1520)$ photoproduction at 8.2–8.8 GeV", Phys.Rev.C 105 (2022) 3, 035201

[9] S. Adhikari, **L. Ng**, et al., "Search for photoproduction of axionlike particles at GlueX", Phys.Rev.D 105 (2022) 5, 052007